APPENDIX L
SIMPLIFIED TSPA

L1. INTRODUCTION

This appendix presents the Simplified Total System Performance Assessment (TSPA) Analysis to corroborate the Total System Performance Assessment for the License Application (TSPA-LA Model). The Simplified TSPA Analysis was developed as a stand-alone computer program written in FORTRAN 90 and compiled/linked using Compaq Visual Fortran as unqualified software. Unqualified software can be used to corroborate analysis or calculation results per Section 6.2.1M of SCI-PRO-006, *Model.*

This appendix is divided into two major sections. The first section presents the details of the Simplified TSPA Analysis. It discusses the approach taken for modeling each of the model areas included, the mathematical equations used in the FORTRAN computer program, and the input data used. The second section discusses the simulations that were conducted using this Simplified TSPA Analysis and discusses the results in comparison with the TSPA-LA Model.

L2. SIMPLIFIED TSPA MODELING APPROACH

The Simplified TSPA Analysis is a higher-level abstraction than the TSPA-LA Model. In general, it includes the same features, events, and processes (FEPs) that are considered in the TSPA, but the manner in which they are modeled is simpler. This simplification primarily involves removing a considerable amount of detail included in the TSPA-LA to capture spatial and temporal variability and treating the repository system with a more 'average' representation. In addition, process-level modeling results are further abstracted for inclusion in this Simplified TSPA instead of being directly included as in the TSPA-LA Model.

The Simplified TSPA Analysis has its bases in the process- and abstraction-level modeling captured in the supporting analysis and/or model reports. Thus, its technical bases are identical to those of the TSPA-LA Model. However, the Simplified TSPA is different from the TSPA-LA Model, both in its structure and computational method.

This section discusses each model area and how it is included in the Simplified TSPA.

L2.1. SEISMIC EVENTS

Seismic activity is modeled in *Seismic Consequence Abstraction* (SNL 2007 [DIRS 176828], Section 6.12.2) as a Poisson process with a mean frequency of 4.287×10^{-4} per year. This simplified model also assumes that seismic activity follows a Poisson process for those modeling cases that include seismic events. The probability of 'n' events occurring in a timestep is shown in Equation L-1.

$$P(n) = \frac{(\lambda \Delta t)^n e^{(-\lambda \Delta t)}}{n!} \qquad \text{(Eq. L-1)}$$

where

P(n) = the probability of 'n' events occurring during a timestep

λ = the mean frequency of the Poisson process, 4.287×10^{-4} per year

Δt = the timestep size (yr).

A random number (between 0 and 1) is drawn and compared to a cumulative probability distribution developed using Equation L-1 to determine whether 0, 1, 2, or 3 seismic events occur in a given timestep. No more than three events are assumed to occur because the probability of even three events occurring in a timestep becomes exceedingly small. For example, the probability of greater than three events occurring within a 1,000-year timestep is 0.0025. The use of a smaller timestep further reduces this probability.

The annual exceedance frequency, λ_j, is sampled for each seismic event that occurs during a timestep from a uniform distribution that varies from 10^{-8} per year and 4.287×10^{-4} per year (SNL 2007 [DIRS 176828], Section 6.12.2). The peak ground velocity (PGV) is then determined using the bounded hazard curve shown in Table L-1 for use in subsequent mechanical damage calculations. In addition, a random number is also drawn from a uniform distribution ranging from 0 to 1 for each seismic event that occurs for use in subsequent rock fall and mechanical damage calculations.

L2.2. ROCK FALL

The amount of rock that falls into the emplacement drifts is evaluated and modeled in *Seismic Consequence Abstraction* (SNL 2007 [DIRS 176828]). A similar approach is used in this simplified model.

For each seismic event, the probability of rock fall in the lithophysal and nonlithophysal zones is determined using Equation L-2 (SNL 2007 [DIRS 176828], Section 6.12.2). If the random number drawn for the seismic event, discussed above, is less than the calculated rock fall probability, then rock fall occurs.

$$P_{rockfall,Lith} = MIN(1.0, MAX(0.0, (1.288)PGV - 0.353)). \quad \text{(Eq. L-2)}$$

Seismic Consequence Abstraction (SNL 2007 [DIRS 176828]) treats the volume of rock that falls in a seismic event as a gamma distribution with the mean and variance of the distribution being functions of the PGV. This simplified model assumes that the volume of rock that falls is simply the mean value of the gamma distribution in order to model the 'average' evolution of the repository. For the lithophysal volume, an effective PGV for rock fall is used as shown in Equation L-3 (SNL 2007 [DIRS 176828], Section 6.12.2). The mean value of the gamma distributions, in terms of m^3 per meter of emplacement drift, is shown in Equations L-4 and L-5 for the lithophysal and nonlithophysal zones (SNL 2007 [DIRS 176828], Section 6.12.2):

$$PGV_{rf} = MAX(PGV, 0.4m/s) \quad \text{(Eq. L-3)}$$

$$\mu_{lith} = (20.307)\left(PGV_{rf}\right)^2 - (18.023)PGV_{rf} + 4.0102 \quad \text{(Eq. L-4)}$$

$$\mu_{non-lith} = (-0.0142)\left(PGV\right)^2 + (0.2064)PGV + 0.0387. \quad \text{(Eq. L-5)}$$

Rock fall accumulates within the drift in both the lithophysal and nonlithophysal zone and the maximum total rockfall volume of the two is assumed to be the total volume of rock in the drift. The fraction of the drift filled with fallen rock is then calculated as the ratio between the total volume of rock that has fallen and the total amount of rock required to fill the drift. The total amount of rock required to fill the drift is assumed to be a uniform distribution ranging between 30 m^3 per meter to 120 m^3 per meter of drift length (SNL 2007 [DIRS 176828], Section 6.12.2).

L2.3. CLIMATE

Future climate analyses were conducted that cover 10,000 years following closure of the repository and are documented in *Future Climate Analysis* (BSC 2004 [DIRS 170002]). Based on the results of this analysis, the present-day climate is assumed to occur for 600 years following repository closure. A monsoon climate then occurs until 2,000 years following repository closure. A glacial-transition climate then occurs until 10,000 years following repository closure.

A fourth climate state is assumed to occur beyond 10,000 years after repository closure. This climate state is assumed to be 'constant' with increased percolation flux through the repository as required by the NRC draft rule in 10 CFR 63.342(c) [DIRS 178394].

Changes from one climate state to another result in increased percolation fluxes across the repository horizon. This leads to higher seepage rates, a larger number of waste packages (WPs) that could potentially be contacted by seeping water (provided the drip shields [DSs] fail), and larger advective flow rates through any failed WPs and the invert. Increased percolation fluxes also correspond to faster groundwater flow rates in both the unsaturated zone (UZ) and saturated zone (SZ).

L2.4. INFILTRATION AND UNSATURATED ZONE FLOW ABOVE THE REPOSITORY

Infiltration rates over the surface of the repository for the present-day, monsoon, and glacial-transition climate states were presented in *Simulation of Net Infiltration for Present-Day and Potential Future Climates* (SNL 2007 [DIRS 182145]). Spatially varying infiltration rates, in the form of infiltration rate maps, were determined for four different infiltration uncertainty scenarios. These infiltration rate maps were used as boundary conditions in the modeling of groundwater flow through the UZ as discussed in *UZ Flow Models and Submodels* (SNL 2007 [DIRS 184614]).

The UZ Flow Model, discussed in detail in *UZ Flow Models and Submodels* (SNL 2007 [DIRS 184614]), produced flow field information for each infiltration uncertainty scenario for the present-day, monsoon, and glacial-transition climate states. A scaling technique was utilized to develop flow fields for the post-10,000-year climate. The flow field information was used to determine the spatial distribution of the percolation flux and the average percolation flux over the

repository area for each of the infiltration uncertainty scenarios and each climate state (DTN: SN0703PAEBSPCE.006_R2 [DIRS 181571]). These parameters were used in this simplified model. The distribution of percolation flux over the repository area is shown on Figure L-1 and the average percolation rates over the repository area for the different climate states and infiltration scenarios are shown in Table L-2.

Weighting factors were also developed for each of the infiltration scenarios in *UZ Flow Models and Submodels* (SNL 2007 [DIRS 184614]). These weighting factors are shown in Table L-2.

L2.5. EMPLACEMENT DRIFT SEEPAGE

The seepage model is described in detail in *Abstraction of Drift Seepag*e (SNL 2007 [DIRS 181244]). The key factors that affect the seepage model are:

- **Local Percolation Flux**—The local percolation flux is represented by a two-dimensional map over the repository area. It is an output of the three-dimensional UZ Flow Model. The magnitude of the percolation flux depends on the infiltration rate at the repository surface. The percolation flux is spatially variable across the area of the repository.

- **Flow focusing**—Intermediate-scale heterogeneity may lead to focusing of flow on a scale smaller than the resolution of the three dimensional UZ Flow Model. This may increase the site-scale fluxes in some areas, while reducing them in other areas. The additional variability and uncertainty of percolation flux stemming from this effect can be accounted for by using appropriate flow focusing factors, to be multiplied with the percolation flux distribution from the three dimensional UZ Flow Model.

- **Capillary strength**—The local capillary-strength parameter ($1/\alpha$) of the fractured rock is one of the key parameters affecting the capillary barrier behavior at the drift crown. The larger this parameter, the stronger the capillary force, which holds water in the fractures and prevents it from seeping into the drift. A value of zero is the lower limit for the capillary-strength parameter, corresponding to a fractured rock with zero capillary forces.

- **Fracture permeability**—The second key parameter affecting the diversion of water around drifts is the tangential fracture permeability in the boundary layer near the drift wall. The larger this parameter, the more likely is the water-flow around the drift, and the less likely is seepage.

Seepage is modeled using a multi-dimensional response surface (in the form of a look-up table) that gives the seepage rate as a function of local percolation flux, capillary-strength, and fracture permeability. This simplified model utilizes the mean value for seepage rate from the response surfaces for:

- Noncollapsed drifts (DTN: LB0702PASEEP01.001_R0 [DIRS 179511])
- Collapsed drifts (DTN: LB0702PASEEP01.001_R0 [DIRS 179511]).

Abstraction of Drift Seepage (SNL 2007 [DIRS 181244]) provides ranges for the capillary strength and fracture permeability parameters. Table L-3 shows the ranges for the capillary-strength parameter and Table L-4 shows the ranges for the fracture permeability parameter for lithophysal and nonlithophysal units. The areal average fracture permeability is determined assuming 85 percent of the repository residing in lithophysal units and 15 percent in nonlithophysal units (SNL 2007 [DIRS 181244], Section 6.3.1). The distribution values for the areal average fracture permeability used in this simplified model are shown in Table L-4.

Abstraction of Drift Seepage (SNL 2007 [DIRS 181244], Section 6.7.1.1) also provides a probability distribution of the flow focusing factor to be applied at each location. The flow focusing factor probability distribution is shown in Table L-5 and is used in this simplified model.

This simplified approach determines the fraction of the repository area that is in a seeping environment (the seepage fraction) and the average seepage rate over this area. The repository is treated as a single 'region' with average seepage properties. The methodology used to calculate these 'repository average' properties is similar to that described in *Abstraction of Drift Seepage* (SNL 2007 [DIRS 181244], Section 6.5.1). The 'repository average' seepage properties are calculated for each climate state in the following manner.

- The infiltration scenario is sampled (10th, 30th, 50th, and 90th percentiles) based on the weighting factors shown in Table L-2.

- The percolation flux is determined for 100 discretized 'regions' for each climate state using the percolation flux distribution shown on Figure L-1 (DTN: SN0703PAEBSPCE.006_R2 [DIRS 181571]). Note that these 100 'regions' do not correspond to specific locations in the repository, but rather are regions that will experience a given percolation flux.

- The flow focusing factor is sampled from the distribution shown in Table L-5 for each of the 100 discretized 'regions' and multiplied by the corresponding percolation flux at that 'region.' This results in a localized spatially varying percolation flux distribution for 100 discretized 'regions' within the repository area.

- The uncertainty distributions for the capillary strength values are sampled (Table L-3 for capillary strength; Table L-4 for averaged values for fracture permeability).

- The spatial variability distributions for the capillary strength values are sampled at each 'node' (Table L-3 for capillary strength; Table L-4 for averaged values for fracture permeability).

- The resulting combination of local percolation flux, capillary strength, and fracture permeability are input to the intact and collapsed drift response surfaces to determine the seepage rate at each 'node' for intact and collapsed drift conditions.

- If the seepage rate for a 'node' is greater than zero, then that 'node' is considered to be seeping. The seepage fraction is simply the summation of the total number of seeping 'nodes' with each representing a fraction of 0.01.

- The seepage rate associated with each seeping 'node' is used to determine the average seepage rate using Equation L-6.

$$\overline{Q}_{Seep} = \frac{0.01 \sum_{i}^{N_{Seep}} Q_{Seep_i}}{F_{Seep}} \qquad \text{(Eq. L-6)}$$

where

$\overline{Q}_{Seep}$ = the average seepage rate (kg/yr) across the repository area experiencing seepage

Q_{Seep_i} = the seepage rate (kg/yr) for 'node' i that is experience seepage

F_{Seep} = the fraction of the repository area that is experiencing seepage.

Seepage fractions and average seepage rates are determined for each climate state for both intact and collapsed drift conditions. The effects of drift degradation are discussed in *Abstraction of Drift Seepage* (SNL 2007 [DIRS 181244], Section 6.2.2.1[a]) and the approach described there is also used in this simplified model to account for drift degradation. Rockfall volume, calculated in the simplified seismic model as discussed in Section L2.2, is used to determine both the seepage fraction and seepage rate as a function of the drift condition as follows:

- Use the intact drift seepage response surface to determine the seepage fraction and seepage rate for a rockfall volume less than 5 m^3 per meter of drift.

- Use the collapsed drift seepage response surface to determine the seepage fraction and seepage rate for a rockfall volume greater than or equal to 60 m^3 per meter of drift.

- Linear interpolate to determine the seepage fraction and seepage rate between results calculated using the collapsed and intact drift response surfaces for a rockfall volume greater than or equal to 5 m^3 per meter of drift and less than 60 m^3 per meter of drift. Increase the seepage rate by 20 percent to account for degraded drift conditions.

L2.6. IN-DRIFT ENVIRONMENT

L2.6.1 Waste Package Temperature

The *Multiscale Thermohydrologic Model* (SNL 2007 [DIRS 181383]) was used to calculate WP temperatures as a function of percolation flux, spatial location, and host rock thermal conductivity. Variability in the WP surface temperature exists due to WP location (edge effect), spatial variability in repository conditions (host rock properties and percolation flux), WP thermal output, and ventilation. The results show that the WP surface temperature is moderately sensitive to the infiltration rate, but quite sensitive to the host rock thermal conductivity. This

indicates that heat transfer within the repository and the resulting WP temperatures is dominated by conduction with thermal convection and radiation heat transfer being of lower significance.

Figure L-2 shows the commercial spent nuclear fuel (CSNF) and co-disposed (CDSP) WP temperature histories for the present-day, 10th percentile infiltration scenario, for the medium values of host rock thermal conductivity (Corroborative DTN: MO0708SIMPLIFI.000 [DIRS 182980]). The distributions of peak WP surface temperatures over the repository area for this case are shown on Figure L-3. It can be seen that the peak WP surface temperatures are approximately normally distributed across the repository area.

Figure L-4 shows the minimum and maximum temperature histories for the CSNF and CDSP WPs for low, medium, and high values of host rock thermal conductivity. Figure L-5 shows the average temperature profiles for the CSNF and CDSP WPs for low, medium, and high values of host rock thermal conductivity (Corroborative DTN: MO0708SIMPLIFI.000 [DIRS 182980]).

As discussed in Section L2.8, the general corrosion rate of the WP depends on the WP temperature through an Arrhenius relation. Over long time periods, the spatial variability in WP temperature translates to spatial variability in general corrosion penetration depths. This ultimately leads to WP failures occurring over a period of time, or temporal variability. Thus, it is necessary to capture the spatial variability in WP temperature since degradation of the WP plays an important role in the rate that radionuclides could be released from the engineered barrier system (EBS).

In order to capture spatial variability in WP temperature, this simplified model first samples the host-rock thermal conductivity with low, medium, and high each having equal probability (one-third). The range of temperatures across the repository area is then determined using the information on Figure L-4 for the 10th percentile infiltration scenario. As shown in Table L-2, this scenario is assumed to occur with a probability of over 60 percent. In addition, this infiltration scenario will result in higher WP temperatures than the other infiltration scenarios and will cause earlier WP failure because higher temperatures cause higher corrosion rates.

The temperature distribution across the repository area is assumed to vary according to a normal distribution with the minimum and maximums shown in L-2 assumed to represent the coolest and hottest 1 percent of the repository area. The WP surface temperature at each point in time across the repository horizon is then determined by interpolating over the temperature range shown on Figure L-4 using Equation L-7:

$$T_{wp}(t) = \frac{N^{-1}(\mathrm{P_A}) - z_{MIN}}{z_{MAX} - z_{MIN}} \left(T_{wp-MAX}(t) - T_{wp-MIN}(t)\right) + T_{wp-MIN}(t) \qquad \text{(Eq. L-7)}$$

where

$T_{wp,j}(t)$ = WP surface temperature at a location in the repository at time t (°C)

$T_{wp\text{-}MAX}$ = maximum WP surface temperature in the repository at time t (°C)

$T_{wp\text{-}MIN}$ = minimum WP surface temperature in the repository at time t (°C)

$N^{-1}(P_A)$ = value from the inverse of a cumulative normal distribution with a mean of 0 and a standard deviation of 1

P_A = cumulative area fraction (uniform distribution 0-1)

z_{MIN} = minimum value of a normal distribution with a mean of 0 and a standard deviation of 1 (-3.719)

z_{MAX} = maximum value of a normal distribution with a mean of 0 and a standard deviation of 1 (3.719).

As discussed in Section L.2.12, waste form degradation also depends on temperature. However, the intent of this simplified model is to evaluate repository performance under 'average' conditions and as such, the average WP temperature history is used to model waste form degradation. The average WP temperature is determined for a sampled value of the host rock thermal conductivity using Figure L-5.

L2.6.2 In-Drift Chemical Environment

The Simplified TSPA Analysis uses the CO_2 partial pressure to determine dissolved concentration limits and the total carbonate concentration used in the CSNF degradation submodel. The CO_2 partial pressure in the drift and invert is calculated in *Engineered Barrier System: Physical and Chemical Environment* (SNL 2007 [DIRS 177412]). The maximum CO_2 partial pressure was calculated for four different chemistries and degrees of rock-water reaction as a function of temperature. The results are shown on Figure L-6 (DTN: SN0701PAEBSPCE.002_R0 [DIRS 179425]) where the various lines correspond to different values of a water-rock interaction parameter that indicate the amount of feldspar dissolved in the water. The minimum value of the CO_2 partial pressure is also a function of temperature (SNL 2007 [DIRS 177412], Section 6.3.3.2.5).

The CO_2 partial pressure in the drift and the invert varies over the first few thousand years due to the thermal pulse, but thereafter tends to stabilize (SNL 2007 [DIRS 177412], Section 6.3.3.2.5). Rather than explicitly modeling the evolution of the CO_2 partial pressure over time, this simplified model assumes that the CO_2 partial pressure is equal to 10^{-2}. This is roughly equivalent to the maximum value of the CO_2 partial pressure for the various starting water chemistries and rock-water interactions at temperatures ranging from 80°C to 90°C.

Dissolved concentration limits tend to decrease with decreasing CO_2 partial pressure as shown in *Dissolved Concentration Limits of Elements with Radioactive Isotopes* (SNL 2007 [DIRS 177418]). Assuming a CO_2 partial pressure of 10^{-2} is conservative, in that it will result in larger concentrations of radionuclides in the EBS and consequently larger release rates. The degradation of CSNF, as discussed in Section L2.2, depends on the CO_2 partial pressure under acidic conditions. However, the CO_2 partial pressure is of much less significance that the specific surface area of the degrading UO_2 matrix and assuming a CO_2 partial pressure of 10^{-2} will have little effect on the degradation rate of CSNF under acidic conditions.

The O_2 partial pressure is assumed to equal 0.21 (SNL 2007 [DIRS 177412], Section 6.3.3.2.5), which further assumes that the air mass fraction in the drifts is 1 and that oxygen is not depleted through reactions with structural material in the emplacement drifts.

The pH in the invert affects the dissolved concentration limit as shown in *Dissolved Concentration Limits of Elements with Radioactive Isotopes* (SNL 2007 [DIRS 177418]). In a seeping environment with failed WPs and DSs, the invert pH is assumed to equal the in-package pH (SNL 2007 [DIRS 177412], Section 6.15.2). Otherwise, the invert pH is calculated for four different chemistries and degrees of rock-water reaction as a function of temperature and relative humidity in *Engineered Barrier System: Physical and Chemical Environment* (SNL 2007 [DIRS 177412]). The results indicate that as the relative humidity approaches 100 percent, the invert pH ranges from approximately 6 to 7 (based on the results in DTN: SN0701PAEBSPCE.001_R1 [DIRS 180523]). This simplified model thus assumes that the invert pH ranges uniformly from 6 to 7 in conditions where the DSs and WPs have not failed.

L2.7. DRIP SHIELD DEGRADATION

L2.7.1 Corrosion

Localized corrosion of the DS is excluded as a DS degradation mechanism (SNL 2007 [DIRS 179476], FEP Number 2.1.03.03.0B). DS general corrosion rate distributions are provided in *General and Localized Corrosion of the Drip Shield* (SNL 2007 [DIRS 180778]), based on weight loss and crevice corrosion specimens. DS corrosion rates were found to be both spatially variable and uncertain. However, *General and Localized Corrosion of the Drip Shield* (SNL 2007 [DIRS 180778], Section 8.1[a]) recommended that the DS corrosion rate be treated as uncertain with no variability in the TSPA-LA. Two uncertain mean corrosion rates, one for benign and one for aggressive conditions, are sampled independently and are used for the general corrosion of the DS. The distribution under aggressive conditions is applied to the top of all DSs, and the distribution for the less aggressive conditions is applied to the underside of all DSs. This simplified model uses this same approach for modeling general corrosion of the DS.

The DS general corrosion rate for aggressive conditions is represented in *General and Localized Corrosion of the Drip Shield* (SNL 2007 [DIRS 180778], Section 8.1[a]) as a student-t distribution with a mean of 46.1 nm/yr, a standard deviation of 1.19 nm/yr, and 5 degrees of freedom. This simplified analysis assumes a normal distribution with a mean of 46.1 nm/yr and a standard deviation of 1.19 nm/yr. Although these distributions are slightly different, the overall trend in DS performance will be similar.

The DS general corrosion rate for less aggressive conditions is represented in *General and Localized Corrosion of the Drip Shield* (SNL 2007 [DIRS 180778], Section 8.1[a]) as a normal distribution with a mean of 5.15 nm/yr and a standard deviation of 0.831 nm/yr. This distribution is used in this simplified model.

The corrosion rates for the DS tops and undersides are independently sampled, and the time that the DSs fail is calculated using Equation L-8. It is assumed that the entire DS surface is fully degraded.

$$t_{ds} = \frac{T_{ds}}{GC_{ds-os} + GC_{ds-us}} \qquad \text{(Eq. L-8)}$$

where

t_{ds} = the time that the DSs fail (year)

T_{ds} = DS thickness, 15 mm (BSC 2005 [DIRS 173303])

$GC_{ds\text{-}os}$ = sampled DS top surface general corrosion rate (mm/yr)

$GC_{ds\text{-}us}$ = sampled DS under side general corrosion rate (mm/yr).

The general corrosion rate of the DS frame thickness is determined by applying a factor to account for the increased general corrosion of Titanium Grade 29 (frame) as compared to Titanium Grade 7 (plates). This factor is uncertain and is shown in Table L-6 (DTN: SN0704PADSGCMT.002_R1 [DIRS 182188]).

L2.7.2 Mechanical Damage

Seismic Consequence Abstraction (SNL 2007 [DIRS 176828]) evaluated and developed approaches for modeling the effects of seismic events on the performance of the DS. It considered two modes of DS failure: rupture or tearing of the DS plates and buckling or collapse of the sides and/or top of the DS due to seismic events. Failure of the DS plates as a result of a seismic event renders the DS ineffective as a barrier to seepage. Buckling or collapse of the DS can result in the DS contacting the WP, influencing its response to seismic events. This effect on mechanical damage modeling of the WP is discussed later.

Before DS failure occurs due to either of the two failure modes discussed above, the DSs may accumulate damage from vibratory ground motion and from rockfall induced by vibratory ground motion. This is also evaluated in *Seismic Consequence Abstraction* (SNL 2007 [DIRS 176828]). Any such damage would result in an increased susceptibility to stress corrosion cracking (SCC). However, it is not expected that any water would be able to flow through such cracks and the DS would retain its effectiveness as a barrier to seepage (SNL 2007 [DIRS 179476], FEP Number 2.1.03.10.0B). Thus, this simplified model does not model the accumulation of damage to the DS surface due to seismic events.

This simplified model uses the same approach for modeling failure of the DS plates that is described in *Seismic Consequence Abstraction* (SNL 2007 [DIRS 176828], Section 6.12.2). The probability that the DS plates will fail in a seismic event or the plate fragility is shown in Table L-7 and is a function of the thickness of the plate (which degrades over time due to general corrosion), the amount of rock that has fallen into the drift, and the PGV associated with a seismic event.

When a seismic event occurs, the PGV associated with the seismic event, the current thickness of the DS plate, and the current amount of rock that has fallen into a drift are used to determine the probability that the DS plate will fail (linear interpolation). The DS plate is assumed to be failed if the random draw (Section L 2.1) associated with the seismic event is less than the calculated plate failure probability. If the DS plates fail, all DSs are assumed to no longer be a barrier to emplacement drift seepage.

This simplified model also uses the same approach for modeling failure of the DS structure due to buckling and/or collapse that is described in *Seismic Consequence Abstraction* (SNL 2007 [DIRS 176828], Section 6.12.2). The probability that the DS frame will fail in a seismic event, or due to the frame fragility, is shown in Table L-8. The frame fragility is a function of the thickness of the frame structure (which degrades over time due to general corrosion), the amount of rock that has fallen into the drift, and the PGV associated with a seismic event.

When a seismic event occurs, the PGV associated with the seismic event, the current thickness of the DS frame structure, and the current amount of rock that has fallen into a drift, are used to determine the probability that the DS plate will fail (linear interpolation). The DS frame structure is assumed to be failed if the random draw associated with the seismic event is less than the calculated plate failure probability. If the DS frame structure fails, all DSs are still assumed to be a barrier to emplacement drift seepage.

L2.8. WASTE PACKAGE DEGRADATION

L2.8.1 Corrosion

This simplified model considers two corrosion processes that can result in failure of the WPs, SCC and general corrosion. Localized corrosion (crevice corrosion and/or pitting) is not considered in this simplified model because these corrosion mechanisms are not expected to occur on the WP surface in the environment expected within the repository.

L2.8.1.1 General Corrosion

The base-case general corrosion model for the WP outer barrier is presented in *General Corrosion and Localized Corrosion of Waste Package Outer Barrier* (SNL 2007 [DIRS 178519], Section 8.2). The model is based on a temperature dependence of the corrosion process, represented by an activation energy using the natural logarithmic form of a modified Arrhenius relation as shown in Equation L-9:

$$\ln(R_T) = \ln(R_o) + C_1\left(\frac{1}{T} + \frac{1}{333.15}\right). \qquad \text{(Eq. L-9)}$$

R_T is the temperature-dependent general corrosion rate in nm/yr, T is temperature in Kelvin, and R_o and C_1 are uncertain constants. The temperature dependence term (C_1) was obtained from short-term polarization resistance data for Alloy 22 (UNS N06022) specimens tested for a range of sample configurations, metallurgical conditions, and exposure conditions. The temperature dependence term is represented as a truncated ($\pm 2\sigma$) normal distribution with a mean of 4,905°K and a standard deviation of 1,413°K (DTN: MO0703PAGENCOR.001_R4 [DIRS 182029]).

R_o is represented as a Weibull distribution shown in Equation L-10 (where p is the cumulative probability):

$$p = 1 - \exp\left[-\left(\frac{R_o}{s}\right)^b\right]. \qquad \text{(Eq. L-10)}$$

The Weibull scale and shape parameters are represented as a discrete probability distribution as shown in Table L-9. These parameters were determined from weight-loss data of 5-year exposed crevice specimens at 60°C and 90°C and were assumed to represent the distribution of long-term general corrosion rates of the WP outer barrier at 60°C (SNL 2007 [DIRS 178519], Section 8.2).

The WP outer barrier is subject to microbiologically influenced corrosion (MIC) when the relative humidity is equal to or greater than a relative humidity threshold that varies uniformly from 75 percent to 90 percent (SNL 2007 [DIRS 178519], Section 8.2). The effect of MIC on general corrosion of the WP outer barrier is treated as an enhancement factor applied to the general corrosion rate when the relative humidity threshold is exceeded. This MIC enhancement factor is represented as a uniform distribution ranging from 1 to 2 (DTN: MO0703PAGENCOR.001_R4 [DIRS 182029]).

This simplified model conservatively assumes a constant relative humidity threshold of 75 percent. Relative humidity histories (DTN: MO0506MWDPPMSV.000_R0 [DIRS 174806]) indicate that the time when the relative humidity exceeds a 75 percent threshold depends on the WP type and the host rock thermal conductivity. The time that the relative humidity exceeds a 75 percent threshold, where MIC is assumed to occur in this simplified model, is shown in Table L-10.

This simplified model assumes that the entire variance in R_o represents variability in the general corrosion process over the surface of the WP outer barrier, consistent with *General Corrosion and Localized Corrosion of Waste Package Outer Barrier* (SNL 2007 [DIRS 178519], Section 8.2). The general corrosion rate variability is applied among the modeled WPs and local areas on the surface of an individual WP. The entire variance in the temperature dependence term (C_1) is due to uncertainty, and the uncertainty is limited to ±2 standard deviations. The MIC enhancement factor is also due to uncertainty.

The simplified model calculates WP degradation due to general corrosion as discussed below. This approach captures spatial variability in general corrosion over the WP surface by discretizing the WP surface into 1,000 ‘locations’ and spatial variability in the general corrosion rate across the repository area due to spatial variability in temperature by considering 100 ‘regions’ as discussed in Section L2.6.1. The approach used in this simplified model is:

- The Weibull scale and shape parameters are sampled.
- The MIC enhancement factor is sampled.
- The MIC threshold time is determined for CSNF and CDSP WPs from Table L-10 for the sampled host rock thermal conductivity (low, medium, and high as discussed in Section L2.6.1).
- The general corrosion rate, R_o, on the WP outer surface is determined using an inversion of Equation L-10 for 1,000 ‘locations’ on the WP surface.
- The general corrosion rate, R_o, is increased by the MIC enhancement factor at each ‘location’ on the WP surface.

- The temperature dependence term, C_1, is sampled.
- The repository is discretized into 100 'regions' and the WP temperature history for each of the 100 'regions' is calculated using Equation L-7.The temperature-dependent general corrosion rate, R_T, for each 'location' on the WP outer surface is determined using Equation L-9 for each of the 100 'regions.'
- The penetration depth is calculated for each 'location' on the WP outer surface and for each 'region' using numerical integration (trapezoidal rule with finely divided steps to ensure accuracy).
- The time that each 'location' on the WP outer surface and for each 'region' is determined when the penetration depth exceeds the thickness of the WP outer barrier, 25 mm (SNL 2007 [DIRS 177407], Section 4.1.1).

This approach results in a distribution of penetration times for each of 1,000 'locations' on the WP surface for each of 100 'regions' over the repository area. The initial general corrosion WP failure distribution (fraction of WPs failed as a function of time) is determined from the earliest time that a 'location' is penetrated in each 'region.' The fractional area breached on failed WPs is determined using Equation L-11:

$$\overline{F}_{WP-Area} = \frac{\sum_{i=1}^{N} F_{WP-Area,i}}{N} \qquad \text{(Eq. L-11)}$$

where

$\overline{F}_{WP-Area}$ = the average fraction of the WP surface area failed on all failed WPs
$F_{WP-Area,i}$ = the fraction of the WP surface area failed on all failed WPs in 'region' i
N = the total number of 'regions' with failed WPs.

L2.8.1.2 Stress Corrosion Cracking

SCC of the WP outer barrier is discussed in *Stress Corrosion Cracking of Waste Package Outer Barrier and Drip Shield Materials* (SNL 2007 [DIRS 181953]). The SCC model considers the initiation and propagation of cracks in the closure weld region of the WP outer barrier due to three factors present simultaneously: material susceptibility, critical environment, and static (or sustained) tensile stress. Crack initiation was evaluated and modeled for both weld flaws and incipient cracks. Crack propagation was modeled using the slip dissolution/film rupture model for the prediction of crack growth rate.

This simplified model considers SCC of the WP outer barrier closure lid weld regions. Incipient cracks are assumed to nucleate, grow, and immediately penetrate the thickness of the weld region when general corrosion has penetrated to the depth at which the hoop stress profile exceeds the threshold stress. Analyses presented in *Analysis of Mechanisms for Early Waste Package/Drip Shield Failure* (SNL 2007 [DIRS 178765], Section 6.3.1.9) indicated that over 80 percent of the

WPs will not experience any weld flaws. Since this simplified model evaluates the 'average' evolution of the repository it does not include weld flaws as locations where SCC can occur because only a limited number of WPs will have weld flaws. In addition, weld flaws are one of the factors that can lead to early WP failure as discussed in Section L2.8.2.

The hoop stress (σ in MPa) as a function of depth (x in mm) in the closure weld regions of the Alloy 22 WP outer barrier is given by a third-order polynomial regression as shown in Equation L-12 (SNL 2007 [DIRS 181953], Equation 22):

$$\sigma(x,\theta=0) = A_0 + A_1 x + A_2 x^2 + A_3 x^3 \qquad \text{(Eq. L-12)}$$

where

σ = hoop stress as a function of depth, x, and at an angular position, θ, of 0

A_i = coefficients in third order polynomial (Table L-11).

The stress intensity factor (K_I in MPa) as a function of depth (x in mm) for the plasticity-burnished weld region was fit to a fourth-order polynomial regression as shown in Equation L-13. This regression was determined using the information for the laser peened WP outer closure weld region from *Stress Corrosion Cracking of the Drip Shield, the Waste Package Outer Barrier, and the Stainless Steel Structural Material* (SNL 2007 [DIRS 181953], Table 8-12):

$$K_I(x,\theta=0) = A_0 + A_1 x + A_2 x^2 + A_3 x^3 + A_4 x^4 \qquad \text{(Eq. L-13)}$$

where

K_I = stress intensity factor as a function of depth, x, and at an angular position, θ, of 0

A_i = coefficients in fourth order polynomial (Table L-11).

The hoop stress varies with angle (θ) around the circumference of the Alloy 22 WP outer closure lid welds (θ = 0 point arbitrarily chosen) according to Equation L-14 (SNL 2007 [DIRS 181953], Table 8-1):

$$\sigma(x,\theta) = \sigma(x,\theta=0) - 17.2369\left(1-\cos(\theta)\right). \qquad \text{(Eq. L-14)}$$

The stress intensity factor also varies with angle (θ) around the circumference of the Alloy 22 WP outer closure lid welds (θ = 0 point arbitrarily chosen) according to Equation L-15 (SNL 2007 [DIRS 181953], Table 8-1):

$$K_I(x,\theta) = K_I(x,\theta=0) \times \frac{\sigma(Thck,\theta)}{\sigma(Thck,0)} \qquad \text{(Eq. L-15)}$$

where

$K_I(x,\theta)$ = stress intensity factor as a function of depth, x, and at angular position, θ

$K_I(x,\theta=0)$ = stress intensity factor as a function of depth, x, and at angular position of 0 (shown in Equation L-13)

Thck = the thickness of the WP outer closure weld, 25 mm (SNL 2007 [DIRS 181953], Section 6.5.3.2).

The uncertainty in the stress and stress intensity factor profiles is treated through the use of a scaling factor, z, which is sampled from a normal distribution with a mean of zero and a standard deviation of 5 percent of the yield strength, with an upper-bound of 15 percent of the yield strength and a lower-bound of -15 percent of the yield strength (SNL 2007 [DIRS 181953], Table 8-1). The hoop stress as a function of depth, angle, and uncertainty is shown in Equation L-16 (SNL 2007 [DIRS 181953], Table 8-1):

$$\sigma(x,\theta,Z) = \sigma(x,\theta)\times\frac{\sigma(thck,\theta)+Z}{\sigma(thck,\theta)}. \qquad \text{(Eq. L-16)}$$

The stress intensity factor as a function of depth, angle, and uncertainty is shown in Equation L-17 (SNL 2007 [DIRS 181953], Table 8-1):

$$K_I(x,\theta,Z) = K_I(x,\theta)\times\frac{\sigma(Thck,\theta)+Z}{\sigma(Thck,\theta)} = K_I(x,\theta=0)\times\frac{\sigma(Thck,\theta)+Z}{\sigma(Thck,\theta=0)}. \qquad \text{(Eq. L-17)}$$

The threshold stress-intensity factor, $K_{I\text{-}SCC}$, is shown in Equation L-18 (SNL 2007 [DIRS 181953], Table 8-1):

$$K_{I-SCC} = \left(\frac{V_{gc}}{\overline{A}}\right)^{1/\overline{n}} \qquad \text{(Eq. L-18)}$$

where

V_{gc} = crack growth velocity, 7.23 nm/yr (DTN: MO0702PASTRESS.002_R2 [DIRS 180514]).

The parameters $\overline{A}$ and $\overline{n}$ are functions of the repassivation slope, n, and given in Equation L-19 (SNL 2007 [DIRS 181953], Table 8-1). The repassivation slope, n, is represented by a truncated normal distribution (at ± 2 standard deviations) with a mean of 1.165 and a standard deviation of 0.115 (DTN: MO0702PASTRESS.002_R2 [DIRS 180514]):

$$\overline{A}(mm/s) = 7.8\times10^{-2}\, n^{3.6}\,(4.1\times10^{-14})^{n}$$
$$\overline{n} = 4n. \qquad \text{(Eq. L-19)}$$

Cracks are assumed to nucleate when general corrosion has reduced the thickness of the WP outer barrier to a depth where the yield stress exceeds the threshold stress level. This threshold

stress is assumed in *Stress Corrosion Cracking of the Drip Shield, the Waste Package Outer Barrier, and the Stainless Steel Structural Material* (SNL 2007 [DIRS 181953], Table 8-1) to vary uniformly from 90 percent to 105 percent of the Alloy 22 yield stress, 351 MPa (DTN: MO0702PASTRESS.002_R2 [DIRS 180514]). This simplified model assumes that the threshold stress is 97.5 percent of the yield stress, the average of the range of uncertainty. Stress corrosion cracks can propagate when K_I exceeds $K_{I\text{-}SCC}$.

The depth where SCC can initiate and propagate in the WP outer closure weld is shown on Figure L-7 over the circumference of the weld region for various combinations of the repassivation slope, n, and the stress uncertainty scaling factor, 'Z', with the threshold stress at 90 percent of the yield stress (Corroborative DTN: MO0708SIMPLIFI.000 [DIRS 182980]). The solid lines show depths for mean values of 'n' at the extremes of 'Z' and at the mean values of 'Z' and the extremes of n. The dashed lines show depths for the extremes of both 'n' and 'Z'. Note that SCC does not either initiate or propagate at some locations along the circumference of the weld region for certain combinations of 'n' and 'Z' parameters. In addition, certain different combinations of 'n' and 'Z' parameters result in identical results.

The results shown on Figure L-7 indicate that the depths where SCC crack initiation and propagation can occur, range by a maximum of less than two millimeters along the circumference of the WP outer lid closure weld region. This simplified model uses an average depth where SCC crack initiation and propagation can occur as a function of the repassivation slope, n, and the stress uncertainty scaling factor, 'Z', shown in Table L-12. This average depth is computed for only those locations along the circumference of the closure weld where SCC cracks can initiate and propagate at some depth into the thickness of the closure weld region. This approach is a conservative and leads to the entire circumference of the closure weld region being susceptible to SCC at some point in time.

As stated above, incipient cracks are assumed to nucleate, grow, and immediately penetrate the thickness of the weld region when general corrosion has penetrated to the depth at which the hoop stress profile exceeds the threshold stress. The same method as discussed above is used to determine both the fraction of WPs initially failed due to SCC over time and the average fraction of 'locations' penetrated by SCC on WPs that have failed by SCC. The only difference being the penetration depth, which is determined by interpolating from Table L-12 for the sampled values of the repassivation slope, n, and the yield stress uncertainty 'Z'.

L2.8.2 Early Waste Package Failure

Analysis of Mechanisms for Early Waste Package/Drip Shield Failure (SNL 2007 [DIRS 178765], Section 6.3) identified several general types of manufacturing defects including weld flaws, base metal flaws, improper weld material, improper base metal, improper heat treatment, improper weld-flux material, poor weld-joint design, contamination, mislocated welds, missing welds, handling damage, and administrative or operational error.

Variation in the number of early failed WPs is expressed as variability deriving from a discrete Poisson distribution with an uncertain intensity parameter. The intensity parameter, or the probability that a single WP will experience early failure, is represented by a log-normal distribution. The intensity factor has a geometric mean of 4.14×0^{-5} and an error factor of 8.17

(DTN: MO0701PASHIELD.000_R2 [DIRS 180508]). This error factor translates into a geometric standard deviation of $8.17^{(1/1.645)}$. The base-10 logarithm of the intensity factor is thus represented as a normal distribution with a mean of -4.38 and a standard deviation of 0.55. This distribution is sampled and the inverse base-10 logarithm is taken to determine the intensity factor.

The realized value of the early failure intensity factor is multiplied by the number of CSNF and CDSP WPs to determine the Poisson λ for determining the number of CSNF and CDSP WP that experience early failure. The probability of having 0-5 early failed CSNF and CDSP WPs is determined using the Poisson distribution. A random number (0 to 1) is independently selected for the CSNF and CDSP WPs and compared to the early failure probability to yield the number of failed CSNF and CDSP WPs. The number of early failed CSNF and CDSP WPs is conservatively added to the total number of CSNF and CDSP WPs.

The entire WP surface is assumed to be affected by improper heat treatment and the entire surface of the WP is assumed to be lost upon failure of the WPs, because the affected area could be subjected to SCC and enhanced localized and general corrosion (SNL 2007 [DIRS 178765], Section 6.4.8). The entire surface area of the WP is assumed to be that of the CSNF WP (excluding the ends), 33.64 m^2 (DTN: SN0703PAEBSRTA.001_R3 [DIRS 183217]).

L2.8.3 Mechanical Damage

Seismic Consequence Abstraction (SNL 2007 [DIRS 176828]) evaluated and developed approaches for modeling the effects of seismic events on the performance of the WPs.

Failure of the DS changes the configuration of the EBS components. The configuration of the EBS and the mechanical response of the WPs to seismic events was defined in *Seismic Consequence Abstraction* (SNL 2007 [DIRS 176828]) for three states of the system: (1) the initial state, with an intact DS; (2) the final state, with the WPs surrounded by rubble after failure of the DS plates;, and (3) an intermediate state, where the legs of the DS have buckled, but the plates remain intact. This intermediate state can occur because the plastic load capacity of the plates is significantly greater than the plastic load capacity of the DS framework for a given reduction in thickness of the DS components from general corrosion.

While the DS is intact, the WPs are free to move and interact in response to vibratory ground motion. In this condition, end-to-end impacts between adjacent WP and impacts between the WP and its emplacement pallet may occur. The response of the WP for this initial state is assessed using the kinematic damage abstractions presented in *Seismic Consequence Abstraction* (SNL 2007 [DIRS 176828], Section 6.12.2) transportation, aging and disposal (TAD) bearing CSNF and CDSP WPs, respectively.

After the DS plates fail, rockfall can pass through the DS and surround the WP. The response for a WP was developed in *Seismic Consequence Abstraction* (SNL 2007 [DIRS 176828]) for a condition when the TAD-bearing CSNF and CDSP WPs are surrounded by rubble (i.e., the final state of the EBS).

After the DS framework buckles or collapses, the DS may be resting on top of the WP. The deformation and stresses in the Alloy 22 outer barrier of a TAD-bearing CSNF WP that is loaded by a collapsed DS was investigated with three-dimensional finite-element models (SNL 2007 [DIRS 176828], Section 6.9). Separate models represent the response of the TAD-bearing CSNF WP with intact or degraded internals.

This simplified model uses the abstractions developed in *Seismic Consequence Abstraction* (SNL 2007 [DIRS 176828], Section 6.12.2) to estimate WP damage as a result of seismic activity. WP damage is calculated using the same conceptual approach. However, it is conservatively assumed that the WP internals are degraded. This leads to higher probabilities that the WPs will fail than would be the case when the internals are intact.

Two key parameters used in this simplified WP mechanical degradation model are the residual stress threshold uncertainty (percentage of yield stress) and the thickness of the Alloy 22 WP outer barrier remaining. The residual stress threshold uncertainty is represented as a uniform distribution ranging from 90 percent to 105 percent (DTN: MO0702PASTRESS.002_R2 [DIRS 180514]).

The WP thickness remaining will vary across the WPs due to spatial variability in the repository temperature and across the WP surface due to spatial variability in general corrosion rates. However, this simplified analysis computes an average WP thickness remaining that is used on every WP.

Recall that the simplified general corrosion model presented above calculates the time that the penetration depth at each 'location' on the WP outer surface and for each of 100 'regions' exceeds the thickness of the WP outer barrier. These penetration times are used to determine an average general corrosion penetration time. The WP thickness remaining is simply calculated as the ratio of the simulation time and the average penetration time multiplied by the initial thickness of the WP outer barrier.

L2.8.3.1 Waste Package Surrounded By Rubble

As discussed in *Seismic Consequence Abstraction* (SNL 2007 [DIRS 176828], Section 6.12.2), the probability of rupture for a WP surrounded by rubble is zero for intact or degraded internals at all PGV levels and outer corrosion barrier (OCB) thicknesses that are relevant to 1,000,000 years. Table L-13 presents the probability of nonzero damaged area for the WP with degraded internals, surrounded by rubble. Note that these results are applicable to both the TAD-bearing CSNF and CDSP WPs. The PGV for the seismic event, the residual stress threshold, and the thickness of the WP outer barrier is used to determine the probability of nonzero damage area.

If the random number drawn for that seismic event is less than or equal to the probability of nonzero failure that is calculated, then the WPs are damaged by the seismic event and the damage area is calculated. All WPs are failed upon the first occurrence of damage (provided they have not already failed). The damaged area on the WP surface accumulates with each seismic event that causes damage.

The damage area for WPs surrounded by rubble developed in *Seismic Consequence Abstraction* (SNL 2007 [DIRS 176828], Section 6.12.2) is represented by a gamma distribution. However,

this simplified model assumes that the damage area is simply the mean of the gamma distribution (Table L-14) in order to model the 'average' evolution of WP when damaged by seismic events.

L2.8.3.2 Waste Package Free Movement

Seismic Consequence Abstraction (SNL 2007 [DIRS 176828], Section 6.12.2) presents an approach for determining whether TAD-bearing CSNF or CDSP WPs will rupture as a result of seismic events when they can freely move underneath the DS. This simplified model does not consider WP rupture when the WPs can move freely. Table L-15 shows the probability of TAD-bearing and CDSP WP rupture for a 17 mm thick WP outer barrier and for degraded WP internals. Table L-15 also shows the conditional probability associated with each PGV (probability that a seismic event will exceed that PGV level) and the expected number of events that would exceed that PGV level over a 1,000,000-year period. These results demonstrate that the likelihood of WP rupture over a million-year period is quite small and on the average, WPs will not rupture when they move freely underneath the DS.

Tables L-16 and L-17 present the probability of nonzero damaged area for the CSNF and CDSP WPs with intact and degraded internals that can move freely underneath the DS. Note that these results are applicable to both the TAD-bearing CSNF and CDSP WPs. The PGV for the seismic event, the residual stress threshold, and the thickness of the WP outer barrier is used to determine the probability of nonzero damage area.

If the random number drawn for that seismic event is less than or equal to the probability of nonzero failure that is calculated for intact WPs, then the WPs are damaged by the seismic event and the damage area is calculated. All WPs are failed upon the first occurrence of damage and the WP internals are assumed to be immediately degraded. Damage caused by subsequent seismic events is calculated using the probabilities of nonzero damage area in Tables L-16 and L-17 for degraded internals. The damaged area on the WP surface accumulates with each seismic event that causes damage due to free motion underneath the DS until the DS plates fail and the WPs are surrounded by rubble.

The damage area for TAD-bearing CSNF and CDSP WPs that move freely underneath the DS developed in *Seismic Consequence Abstraction* (SNL 2007 [DIRS 176828], Section 6.12.2), is represented by a gamma distribution. However, this simplified model assumes that the damage area is simply the mean of the gamma distribution, shown in Table L-18, in order to model the 'average' evolution of WP when damaged by seismic events.

L2.9. IN-PACKAGE CHEMISTRY

L2.9.1 In-Package pH

The in-package pH was evaluated in *In-Package Chemistry Abstraction* (SNL 2007 [DIRS 180506]) for both the CSNF and CDSP WPs under seeping and nonseeping (vapor influx) conditions. The in-package pH is a function of pCO_2, ionic strength. As discussed in Section L2.6.2, this simplified model assumes a pCO_2 of 0.01.

Under vapor influx and dripping conditions, the pH inside a breached CSNF WP ranges from approximately 5.5 to 7.5 for a medium ionic strength and a pCO_2 of 2.0. An order of magnitude

increase in the ionic strength yields a pH that ranges from 5.1 to 7.1 (DTN: SN0702PAIPC1CA.001_R2 [DIRS 180451]).

Under vapor influx and dripping conditions, the pH inside a breached CDSP WP and defense high-level waste (DHLW) canister ranges from approximately 5.5 to 8.2 for a medium ionic strength and a pCO_2 of 2.0. An order of magnitude increase in the ionic strength yields a pH that ranges from 5.1 to 9.0 (DTN: SN0702PAIPC1CA.001_R2 [DIRS 180451]).

Under vapor influx and dripping conditions, the pH inside a breached CDSP WP and U.S. Department of Energy (DOE) spent nuclear fuel (DSNF) canister ranges from approximately 5.5 to 7.5 for a medium ionic strength and a pCO_2 of 2.0. An order of magnitude increase in the ionic strength yields a pH that ranges from 5.1 to 7.2 (DTN: SN0702PAIPC1CA.001_R2 [DIRS 180451]).

Based on these results, this simplified model assumes the in-package chemistry ranges uniformly from 5 to 8 for both the CSNF and CDSP WPs under dripping and nondripping conditions. This sufficiently covers the range of uncertainty associated with the pH in both the CSNF and CDSP WPs for the purposes of this simplified model.

L2.9.2 In-Package Total Carbonate

The total carbonate was evaluated in *In-Package Chemistry Abstraction* (SNL 2007 [DIRS 180506], Section 8.1.3) and is a function of CO_2 partial pressure, in-package pH, and temperature as shown in Equation L-20:

$$\begin{aligned} \Sigma C &= pCO_2\left(10^{k_1} + 10^{(pH+k_1+k_2)} + 10^{(2pH+k_1+k_2+k_3)}\right) \\ Log\, k_1 &= 7\times10^{-5}T^2 - 0.0159T - 1.1023 \\ Log\, k_2 &= 5\times10^{-7}T^3 - 0.0002T^2 + 0.0132T - 6.5804 \\ Log\, k_3 &= -8\times10^{-5}T^2 + 0.0128T - 10.618 \end{aligned} \qquad \text{(Eq. L-20)}$$

where

pCO_2 = partial pressure of CO_2 in atmospheres, log[pCO_2]=-2.0 (Section L2.6.2)

pH = in-package pH

T = temperature (°C).

The degradation of the CSNF waste form depends on total carbonate as discussed in Section L2.12.1. This simplified model uses Equation L-20 to determine the total carbonate for the interior of all CSNF WPs with average CSNF WP temperature, discussed in Section L2.6.1, and the in-package pH, discussed in Section L2.9.1 as inputs.

L2.10. WASTE PACKAGE AND RADIONUCLIDE INVENTORY

The initial radionuclide and WP inventory is presented in *Initial Radionuclide Inventories* (SNL 2007 [DIRS 180472]). This simplified model includes a total of 11,629 WPs emplaced in

the repository of which 8,213 are CSNF WPs and 3,416 are CDSP WPs (DTN: MO0702PASTREAM.001_R0 [DIRS 179925]). The 413 WPs containing naval spent nuclear fuel are conservatively treated as CSNF.

The CSNF and CDSP WP inventories are further subdivided into those that reside in a seeping environment and those that do not. This subdivision is based on the seepage fraction for the long-term average climate state. Any WPs that experience early failure are assumed to reside in a seeping environment.

The radionuclide inventory per WP used in this simplified model is shown in Table L-19. Specific activities, molecular masses, half-lives, decay chains, and the manner in which each radionuclide is treated in this simplified model are also shown in Table L-19. Two additional 'species' are also included: 1,000 g/WP as a surrogate for the UO_2 matrix in CSNF WPs and 13,550 kg/WP as a surrogate for HLW glass in CDSP WPs. These are used in subsequent modeling of the degradation of the UO_2 matrix in the CSNF waste form and the HLW glass waste form.

The initial inventory values are adjusted by uncertainty multipliers shown in Table L-20 (DTN: SN0310T0505503.004_R0 [DIRS 168761]).

This simplified model accounts for radioactive decay and daughter product in-growth in the radionuclide inventory prior to exposure. A simple first-order chain decay model shown in Equation L-21 is used with subdivided timesteps to ensure accuracy. This is appropriate given the long half-lives of the radionuclides included in this simplified model. Note that this approach is conservative because it does not account for any daughter product decay during the timestep where they are formed.

$$Md_i = Md_{i-1}\, e^{-\lambda_d\, \Delta t_{sub}} + \frac{MMd}{MMp} Mp_{i-1} \left(1 - e^{-\lambda_p\, \Delta t_{sub}}\right) \qquad \text{(Eq. L-21)}$$

where

Md_i = mass of daughter radionuclide at current time sub-step i (gram per WP)

Md_{i-1} = mass of daughter radionuclide at previous time sub-step i-1 (gram per WP)

Mp_{i-1} = mass of parent radionuclide at previous time sub-step i-1 (gram per WP)

λ_p = decay constant of parent radionuclide (yr^{-1})

λ_d = decay constant of daughter radionuclide (yr^{-1})

MMp = molecular mass of parent radionuclide (g)

MMd = molecular mass of daughter radionuclide (g)

Δt = time sub-step size (yr).

L2.11. MASS EXPOSURE RATES

Radionuclides cannot be released from the EBS if they remain bound within the waste forms (or un-exposed). A radionuclide is considered to be exposed when it is made available for subsequent transport through the EBS. The rate that radionuclides are exposed depends on where they reside within the waste form. Radionuclides are contained in the waste form matrix for the CSNF, HLW, and DSNF waste forms. A fraction of the radionuclides reside in the fuel-clad gap and in grain boundary regions in CSNF and are assumed to be exposed instantaneously upon failure of the WP. In addition, it is conservatively assumed that the DSNF waste form degrades immediately upon WP failure, resulting in instantaneous exposure of the radionuclides. The approach for calculating mass exposure rates used in this simplified analysis is essentially identical to the approach used in the GoldSim software (GoldSim Technology Group 2007 [DIRS 183214], Appendix E).

The radionuclide exposure rate for those radionuclides in the CSNF fuel-clad gap and grain boundary region and those contained in the DSNF waste form is shown in Equation L-22:

$$e_{i,j}(t) = N_{wp} \bullet I_j(t) \bullet f_{wp}(t) \qquad \text{(Eq. L-22)}$$

where

$e_{i,j}(t)$ = the instantaneous exposure rate of radionuclide j at time t (g/yr)
N_{wp} = the number of WPs
I_j = the inventory of radionuclide j at time t (gram per WP)
$f_{wp}(t)$ = the WP fractional failure rate at time t (yr^{-1}).

The radionuclide exposure rate for those radionuclides bound in the CSNF and HLW glass matrix is shown in Equation L-23:

$$e_{b,j}(t) = N_{wp} \bullet M_s(t) \bullet k_s(t) \bullet I_j(t)$$
$$\frac{dM_s}{dt} = h(t) - M_s(t) \bullet k_s(t) \qquad \text{(Eq. L-23)}$$

where

$e_{b,j}(t)$ = the bound radionuclide exposure rate of radionuclide j at time t (g/yr)
N_{wp} = the number of WPs
$M_s(t)$ = the fraction of un-protected, but un-degraded matrix (unitless)
$k_s(t)$ = the fractional degradation rate of the waste matrix (yr^{-1})
$h(t)$ = the rate that the matrix becomes un-protected (yr^{-1})
I_j = the inventory of radionuclide j at time t (gram per WP).

The rate that the matrix becomes un-protected, h(t), depends on the number of barriers between the matrix and the repository environment. Both the CSNF and DHLW waste forms have additional barriers besides the Alloy 22 WP outer barrier. These barriers include the stainless steel WP inner barrier, cladding for CSNF, and canister for DHLW. However, no performance credit is ascribed to any of these barriers in relation to mass exposure in this simplified model and the rate that the matrix becomes unprotected, h(t), is simply the rate that the WPs fail, $f_{wp}(t)$.

If $f_{wp}(t)$ and $k_s(t)$ are constant, the equation for the fraction of un-protected, but un-degraded matrix is shown in Equation L-24 (GoldSim Technology Group 2007 [DIRS 183214], Appendix E):

$$M_s(t) = \frac{h}{k_s}\left(1 - e^{-k_s t}\right) + M_s(0)e^{-k_s t}. \quad \text{(Eq. L-24)}$$

However, both $f_{wp}(t)$ and $k_s(t)$ vary over time but are assumed to be constant over a timestep. The fraction of mass un-protected, but un-degraded matrix is solved numerically using Equation L-25 (GoldSim Technology Group 2007 [DIRS 183214], Appendix E):

$$M_s(t) = \frac{h(t-\Delta t)}{k_s(t-\Delta t)}\left(1 - e^{-k_s \Delta t}\right) + M_s(t-\Delta t)e^{-k_s \Delta t}. \quad \text{(Eq. L-25)}$$

L2.12. WASTE FORM DEGRADATION

L2.12.1 Commercial Spent Nuclear Fuel Waste Form Degradation

The CSNF waste form degradation model is developed in *CSNF Waste Form Degradation: Summary Abstraction* (BSC 2004 [DIRS 169987]). As discussed above, this model assumes instantaneous release of the fraction of radionuclides residing in either the fuel-clad gap or in the grain boundaries and a response surface for the degradation of the spent UO_2 matrix.

The release of the gap and grain-boundary inventories of cesium, iodine, and technetium is modeled as an instantaneous release of the fraction (f_i) of the total inventory of each of these elements estimated to be in the gap and grain-boundary regions. The instantaneous fractional releases for ^{135}Cs, ^{129}I, and ^{99}Tc are modeled as triangular distributions with the apex of the triangular probability distribution function located at the average release fractions shown in Table L-21 and spanning the range shown in the last row of this table for each element (DTN: MO0404ANLSF001.001_R0 [DIRS 169007]).

The CSNF waste form degradation model is shown in Equation L-26 (BSC 2004 [DIRS 169987], Section 8.1):

$$Log[k_{s-CSNF}] = Log(A) + a_0 + a_1 \bullet \frac{1}{T} + a_2 \bullet \Sigma C + a_3 \bullet pO_2 + a_4 \bullet pH \quad \text{(Eq. L-26)}$$

where

$k_{s\text{-}CSNF}$	=	fractional degradation rate of the CSNF UO_2 matrix (d^{-1})
A	=	fuel effective specific surface area (m^2/d)
T	=	temperature (K)
ΣC	=	negative base 10 log of total carbonate (molal)
pO_2	=	negative base 10 log of oxygen pressure (atmospheres)
a_0, a_1, a_2, a_3, a_4	=	regression coefficients.

This model is used for both alkaline and acidic conditions with different regression coefficients. The expected values for each of these coefficients is shown in Table L-22 (DTN: MO0404ANLSF001.001_R0 [DIRS 169007]).

Uncertainties in the regression coefficients shown in Table L-22 are related through a Cholesky factorization method. Tables L-23 and L-24 show the covariance matrices for alkaline and acidic conditions, respectively. Note that coefficients a_1 and a_3 are identical for both alkaline and acidic conditions, and their values are determined using the covariance matrix shown in Table L-23.

The sampled value of the regression coefficients is determined using Equation L-27:

$$[a_n] = [CHO] \bullet [U] + [a_n^{expected}] \quad \text{(Eq. L-27)}$$

where

$[a_n]$	=	vector of regression coefficient (of length n)
$[U]$	=	vector of uncertainty coefficients (n values sampled from a normal distribution with a mean of 0 and a standard deviation of 1)
$[CHO]$	=	Cholesky factorization matrix (Tables L-23 and L-24)
$a_n^{expected}$	=	expected value of the regression coefficients (Table L-22).

Regression coefficients are sampled for each realization through the use of the covariance matrix. Fractional degradation rates are computed for both alkaline and acidic conditions and the maximum of the two is used for the CSNF waste form fractional degradation rate.

Figure L-8 (Corroborative DTN: MO0708SIMPLIFI.000 [DIRS 182980]) shows the CSNF waste form fractional degradation rate as a function of pH and temperature for the expected value of the coefficients in the CSNF degradation model shown in Table L-22. It can be seen that the CSNF waste form fully degrades in less than 1,000 years under expected repository conditions.

L2.12.2 Defense High-Level Waste Form Degradation

The DHLW glass waste form degradation model is developed in *Defense HLW Glass Degradation Model* (BSC 2004 [DIRS 169988]). This model is a simple model with the fractional degradation rate shown in Equation L-28 (BSC 2004 [DIRS 169988], Section 8.1):

$$k_{s-DHLW} = S \bullet f_{\exp} \bullet R_{alt} \quad \text{(Eq. L-28)}$$

where

$k_{s\text{-}DLHW}$ = fractional degradation rate of DHLW glass (yr^{-1})
S = specific surface area (m^2/g)
f_{exp} = glass exposure factor
R_{alt} = glass alteration rate ($g/m^2/yr$).

The glass specific surface area, S, is constant at 2.7E-3 m^2/kg, and the glass exposure factor is a triangular distribution (minimum = 4, most probable value = 4, maximum = 17) (DTN: MO0502ANLGAMR1.016_R0 [DIRS 172830]). The glass alteration rate is shown in Equation L-29 (BSC 2004 [DIRS 169988], Section 8.1):

$$R_{alt} = k_g \times 10^{\eta \bullet pH} \times \exp\left(\frac{-E_a}{RT}\right) \quad \text{(Eq. L-29)}$$

where

R_{alt} = glass alteration rate ($g/m^2/yr$)
k_g = forward glass dissolution rate ($g/m^2/yr$)
η = order of the reaction with respect to H^+
pH = in-package pH
E_a = activation energy for rate limiting step (kJ/mol)
R = gas constant, 8.314E-3 (kJ/mol/K)
T = temperature (K).

Separate sets of parameters are used for alkaline or acidic conditions. These parameters are provided in Table L-25 (DTN: MO0502ANLGAMR1.016_R0 [DIRS 172830]). Fractional degradation rates are calculated as a function of pH and temperature using both the alkaline and acidic parameters and the maximum is used as the fractional DHLW degradation rate.

Figure L-9 (Corroborative DTN: MO0708SIMPLIFI.000 [DIRS 182980]) shows the DHLW waste form fractional degradation rate as a function of pH and temperature for the expected value of the coefficients in the DHLW degradation model shown in Table L-25. It can be seen that the DHLW waste form degrades more slowly than the CSNF waste form.

L2.13. ENGINEERED BARRIER SYSTEM FLOW

The *EBS Radionuclide Abstraction* (SNL 2007 [DIRS 177407], Sections 6.3.2 and 6.3.3) describes the approach used in the TSPA-LA for determining the amount of water that flows through the engineered barriers.

This simplified model assumes that no water flows through either failed WPs or through the invert in regions of the repository that do not experience seepage. In those regions experiencing seepage, no flowing water is assumed to contact the surface of the WP when the DSs have not failed due to general corrosion. The DSs may experience SCC. However, it is not expected that any water would be able to flow through such cracks and the DS would retain its effectiveness as a barrier to seepage. Water is assumed to be diverted around the intact DSs and flow through the invert at a flow rate equal to the seepage rate. Water is assumed to contact the WP surface at a rate equal to the seepage rate when the DS fails due to general corrosion or due to plate failure due to a seismic event.

The WPs may experience SCC in the weld region and possibly due to seismic events. However, it is not expected that any water would be able to flow through such cracks and the WPs would retain their effectiveness as a barrier to seepage even if SCC occurs.

The fraction of drift seepage that enters a WP having general corrosion breaches underneath a failed DS is shown in Equation L-30 (SNL 2007 [DIRS 177407], Section 6.3.3.2.5):

$$F_{WP} = \min\left[\frac{N_P \frac{L_P}{2}}{L_{WP}} f'_{WP}, 1\right] \qquad \text{(Eq. L-30)}$$

where

F_{WP} = the fraction of drift seepage that enters a WP through general corrosion breaches

N_P = the number of patch penetrations on a failed WP

L_P = the length of a WP patch

L_{WP} = the total axial length of a WP

f'_{WP} = uncertainty factor for the fraction of rivulet flow that enters a breach, uniform distribution, 0-2.41 (DTN: SN0703PAEBSRTA.001_R3 [DIRS 183217]).

The approach for computing the fraction of seepage that flows through the WPs using Equation L-30 discretizes the surface of the WP into a number of patches over the WP surface in order to utilize computations from *WAPDEG Analysis of Waste Package and Drip Shield Degradation* (SNL 2007 [DIRS 177407]).

The number of patches failed can be expressed as the product of the fraction of the WP surface that is breached due to general corrosion and the total number of patches assumed in the discretization of the WP surface. The TSPA-LA Model discretizes the WP surface into approximately 1,400 patches each with an area of 23,150 mm^2 (Section 6.3.5.1.2). This gives a patch length, L_P, equal to 152.15 mm. The total axial length of a TAD-bearing WP, L_{WP}, is 5.691 m (DTN: SN0703PAEBSRTA.001_R3 [DIRS 183217]).

Figure L-10 shows fraction of seepage that would flow through a WP as a function of the fractional area of the WP surface penetrated by general corrosion and the uncertainty factor for rivulet flow, f'_{WP} (shown as percentiles of the uniform distribution). It can be seen that this approach results in a relatively small fraction of the WP surface needing to be breached by general corrosion to allow all of the drift seepage entering the WP. Based on these results, this simplified model assumes that all seepage that contacts the WP surface can flow through the WP upon initial failure by general corrosion.

L2.14. DISSOLVED CONCENTRATION LIMITS

Dissolved concentration limits (solubility limits) were determined in *Dissolved Concentration Limits of Radioactive Elements* (SNL 2007 [DIRS 177418]) as a function of geochemical conditions. The functional form for the dissolved concentration limits is shown in Equation L-31:

$$Log[SL] = S(pH, pCO_2) + \varepsilon_1 + Log[\varepsilon_2 \times N(pH)] \quad \text{(Eq. L-31)}$$

where

- $Log[SL]$ = the base-10 logarithm of the dissolved concentration limit, including uncertainty (solubility limits in mg/L)
- $S(pH,pCO_2)$ = the base-10 logarithm of the dissolved concentration limit as a function of pH and pCO_2
- ε_1 = uncertainty in the base-10 logarithm of the dissolved concentration limit due to uncertainties in the thermodynamic properties of both the controlling solid and significant dissolved species
- ε_2 = term for uncertainty in the base-10 logarithm of the dissolved concentration limit due to uncertainties in the fluoride concentration
- $N(pH)$ = multiplication term (function of pH) for uncertainty in the base-10 logarithm of the dissolved concentration limit due to uncertainties in the fluoride concentration.

As discussed in Section L.2.6.2, the pCO_2 is assumed to be constant at 0.01 and the pH in the EBS can vary from 5.0 to 8.0. The base-10 logarithm of the dissolved concentration limits as a function of pH at a pCO_2 of -2 are shown in Table L-24. These values are used in this simplified model. The dissolved concentration limit for U is assumed to be controlled by schoepite for pH<=6.75 and by Na-boltwoodite/$Na_4UO_2(CO_3)_3$ for pH>=7.75. The average in between the two is assumed to be the dissolved concentration limit. The dissolved concentration limits, not

accounting for uncertainty, used in this simplified model are shown on Figure L-11. The dissolved concentration limits shown in Table L-26 and on Figure L-11 show that uncertainty in the pH translates to a broad variation in the dissolved concentration limit, covering approximately two orders of magnitude over the pH range of 5 to 8.

The uncertainty terms are functions of the waste form type and the manner in which the WPs are breached (corrosion, seismic mechanical damage, or igneous intrusion). The dissolved concentration limit uncertainty terms used in this simplified model are shown in Table L-27. The ε_2 term for the CSNF and CDSP WPs is represented by a very skewed triangular distribution with minimums and best estimates of zero for all WP failure modes (DTN: MO0702PADISCON.001_R0 [DIRS 179358]). In addition, the N term, which is multiplied by the ε_2 term, has a maximum of 1 and minimums as low as 10^{-3} (depending on the pH) (DTN: MO0702PADISCON.001_R0 [DIRS 179358]). Given the skewness of the ε_2 triangular distribution, relatively low distribution maximums, and N values typically much less than 1, the contribution of fluoride uncertainty to the total uncertainty in the dissolved concentration limit will be small. Thus, this simplified model does not consider uncertainty in the fluoride concentration and the dissolved concentration limit is determined using Equation L-32 and the values in Tables L-26 and L-27.

$$Log[SL] = S(pH, pCO_2) + \varepsilon_1 \qquad \text{(Eq. L-32)}$$

Infinite solubility is assumed for carbon, chlorine, cesium, iodine, selenium, and technetium (SNL 2007 [DIRS 177418], Sections 6.14 to 6.17).

L2.15. RADIONUCLIDE TRANSPORT THROUGH THE ENGINEERED BARRIER SYSTEM

This simplified approach models the transport of dissolved radionuclides through the EBS via advective and diffusive transport mechanisms. The diffusive and advective conductance depends on the failure state of the EBS components (DS and WP) and the seepage environment (seeping or nonseeping). Colloid-facilitated radionuclide transport is not considered in this simplified model because past TSPA model results have demonstrated that colloid-facilitated radionuclide transport is not a significant contributor to overall repository performance.

The TSPA-LA Model incorporates radionuclide transport through the EBS by using a series of mixing cells to model one-dimensional transport via advective and diffusive processes. The governing equation is shown in Equation L-33 (GoldSim Technology Group 2007 [DIRS 183214], Appendix B):

$$\frac{dm}{dt} = -m\lambda + m_p\lambda_p \frac{MM}{MM_p} + \dot{m}_{in} - \dot{m}_{out} + S \qquad \text{(Eq. L-33)}$$

where

m = radionuclide mass in a cell

m_p = parent radionuclide mass in a cell

λ = radionuclide decay constant (yr^{-1})

λ_p = parent radionuclide decay constant (yr^{-1})

MM = molecular mass of radionuclide (g)

MM_p = molecular mass of parent radionuclide (g)

$\dot{m}_{in}$ = radionuclide mass flux into the cell (g/yr)

$\dot{m}_{out}$ = radionuclide mass flux out of cell (g/yr)

S = rate of direct radionuclide mass input from an external source, such as waste form degradation (g/yr).

The radionuclide mass flux into and out of a cell can be via advection, diffusion, or both. The advective mass flux from a cell is shown in Equation L-34. The advective 'direction' is always in the direction of the advective flow rate:

$$\dot{m}_{adv} = C\, q_{adv} \quad \text{(Eq. L-34)}$$

where

$\dot{m}_{adv}$ = the advective radionuclide mass flux out of a cell (g/yr)

C = the dissolved radionuclide concentration in the cell (g/m^3)

q_{adv} = the advective flow rate out of the cell (m^3/yr).

The diffusive mass flux between two cells is shown in Equation L-35. The diffusive 'direction' depends on the concentration gradient between adjacent cells:

$$\dot{m}_{dif,i\to j} = D\left(C_i - C_j\right) \quad \text{(Eq. L-35)}$$

where

$\dot{m}_{dif,i\to j}$ = the diffusive radionuclide mass flux between cells i and j (g/yr)

D = the diffusive conductance between cells i and j (m^3/yr)

C = the dissolved radionuclide concentration in cells i and j (g/m^3).

The diffusive conductance is shown in Equation L-36:

$$D = \frac{A_d}{\frac{L_i}{Deff_i} + \frac{L_j}{Deff_j}} \quad \text{(Eq. L-36)}$$

where

A_d = the diffusive area between cells i and j (m^2)

L = the diffusive length in cells i and j (m)

$Deff$ = the effective diffusion coefficient in cells i and j (m^2/yr).

The dissolved radionuclide concentration may be constrained by the dissolved concentration limit (solubility limit). For those radionuclides that are not constrained by a dissolved concentration limit, the radionuclide concentration in a cell is given by the radionuclide mass in the cell divided by the fluid volume. For those radionuclides that are constrained by a dissolved concentration limit, the radionuclide concentration in the cell is the minimum of either the radionuclide mass in the cell divided by the fluid volume or the dissolved concentration limit. This is shown in Equation L-37:

$$\begin{aligned} &\text{No Solubility Constraint} \quad C = \frac{M}{V} \\ &\text{Solubility Constraint} \quad C = \min\left(\frac{M}{V}, S_L\right) \end{aligned} \qquad \text{(Eq. L-37)}$$

where

C = the dissolved radionuclide concentration in a cell (g/m^3)

M = the radionuclide mass in the cell (g)

V = the fluid volume in the cell (m^3)

S_L = the dissolved concentration limit (g/m^3).

The EBS radionuclide transport model used in the TSPA-LA is detailed in *EBS Radionuclide Transport Abstraction* (SNL 2007 [DIRS 177407]). The TSPA-LA discretizes the repository into six regions to account for spatial variability in the repository environment. Within each region there are four networks of cells that represent the CSNF and CDSP WPs in seeping and nonseeping environments. A cell network is shown schematically on Figure L-12. Diffusive links are present in all cell networks whereas advective links are present only in those networks representing seeping environments. A total of 24 cell networks is established. Applying the above equations to each cell, results in a series of coupled differential equations that must be solved numerically at each timestep to determine the radionuclide mass in each cell.

This simplified model represents repository average conditions. A much simpler network of cells is used as shown on Figure L-13. There are two cell networks for each of the CSNF and CDSP WPs; one for those WPs that experience seepage and one for those WPs that do not experience seepage. CSNF and CDSP WPs that experience early failure are assumed to always experience seepage.

In the nonseeping environment, radionuclide transport is via diffusion only. In the seeping environment, radionuclide transport is via diffusion and advection.

In addition, the governing series of differential equation is not solved explicitly at each timestep. Rather, an approximate solution is used as outlined below. This approximation is applied to each cell progressing from the waste form cell to the corrosion product cell to the invert cell. Radionuclide sorption onto degraded materials within the EBS is conservatively not considered in this simplified model.

- Radionuclide mass is added to the cell from either degradation of the waste form or from an 'up-stream' cell.
- A fraction of the radionuclide mass within a cell in the no-seeping network is moved to the corresponding cell in the seeping network as a result of changes in the seepage fraction that occur when the climate state changes.
- The radionuclide mass is updated over the length of the timestep due to radioactive decay and daughter product in-growth. The technique used to update the radionuclide inventory per WP discussed above is used.
- The dissolved radionuclide concentration is determined in each cell using Equation L-37.
- The diffusive conductance (Equation L-36) and, for the seeping environment, the advective flow rate is determined. The total conductance is then determined.
- The total conductance and the dissolved radionuclide concentration in the cell is used to calculate the mass of each radionuclide that is passed to the 'down-stream' cell. If the radionuclide mass calculated to be passed to the 'down-stream' cell exceeds the radionuclide mass in the cell, then the radionuclide mass to be passed is set equal to the radionuclide mass in the cell.
- 'Back diffusion' is not allowed when the concentration of a 'down-stream' cell exceeds that of the 'up-stream' cell.

This approximate approach is essentially an explicit-in-time solution of Equation L-33.

L2.15.1 Corrosion Product Mass and Pore Volume in Waste Form and Corrosion Product Mixing Cells

The mixing cells contain corrosion product and water in the corrosion product void space from the degradation of (SNL 2007 [DIRS 177407], Section 6.5.3.4):

- CSNF waste form cell: basket tubes and absorber plates
- CDSP waste form cell: five DHLW canisters and one DSNF canister
- CSNF corrosion product cell: guide assembly, TAD canister, and inner vessel
- CDSP corrosion product cell: divider plate, inner brackets, support tube, and inner vessel.

This simplified analysis calculates the average mass of corrosion product in failed WPs using the same approach described in *EBS Radionuclide Transport Abstraction* (SNL 2007 [DIRS 177407], Section 6.5.3.4). The corrosion of both carbon and stainless steel is considered. Four corrosion products are also modeled; goethite, ferrihydrite (HFO), chromium oxides, and nickel oxides. The total mass of each corrosion product in each cell is determined using Equation L-38 (SNL 2007 [DIRS 177407], Equation 8-4):

$$m_{CPm,CS,n}(t) = \begin{cases} \left(\frac{\bar{t}}{t_{LCS,n}}\right) f_{CS} f_{GHFO} \omega_{CS,m} \frac{M_{CPm}}{\alpha_{CPm} M_m} m_{s,n}, & \bar{t} \le t_{LCS,n} \\ f_{CS} f_{GHFO} \omega_{CS,m} \frac{M_{CPm}}{\alpha_{CPm} M_m} m_{s,n}, & \bar{t} > t_{LCS,n} \end{cases}$$

$$m_{CPm,SS,n}(t) = \begin{cases} \left(\frac{\bar{t}}{t_{LSS,n}}\right)(1 - f_{CS}) f_{GHFO} \omega_{SS,m} \frac{M_{CPm}}{\alpha_{CPm} M_m} m_{s,n}, & \bar{t} \le t_{LSS,n} \\ (1 - f_{CS}) f_{GHFO} \omega_{SS,m} \frac{M_{CPm}}{\alpha_{CPm} M_m} m_{s,n}, & \bar{t} > t_{LSS,n} \end{cases} \quad \text{(Eq. L-38)}$$

where

$m_{CP,n}$ = total mass of corrosion products in cell ‘n’ (n is either CSNF waste form, CDSP waste form, CSNF corrosion product, or CDSP corrosion product cells) [kg]

$m_{CPm,CS,n}$ = mass of corrosion product m in cell ‘n’ from corrosion of carbon steel [kg]

$m_{CPm,SS,n}$ = mass of corrosion product m in cell ‘n’ from corrosion of stainless steel [kg]

$\bar{t}$ = average WP failure time [yr]

$t_{LCS,n}$ = lifetime of carbon steel in cell ‘n’ [yr]

$t_{LSS,n}$ = lifetime of stainless steel in cell ‘n’ [yr]

f_{CS} = fraction of carbon steel in steel mass [dimensionless]

$\omega_{CS,m}$ = mass fraction of metal *m* in carbon steel [dimensionless]

$\omega_{SS,m}$ = mass fraction of metal *m* in stainless steel [dimensionless]

M_m = atomic weight of metal *m* [kg mol^{-1}]

M_{CPm} = molecular weight of corrosion products from corrosion of metal *m* [kg mol^{-1}]

$\alpha_{CP,m}$ = stoichiometric coefficient for conversion of metal *m* to corrosion products from corrosion of metal *m* [mol *m* mol^{-1} *CPm*]

$m_{s,n}$ = total mass of steel in cell ‘n’ [kg].

The mass of corrosion products in breached WPs is calculated using the average WP failure time, shown as Equation L-39 (Section 6.3.7.2.3). The average WP failure time for those WPs that fail early (initially) is simply the time since repository closure:

$$\bar{t} = \frac{\left(N_{WP\ Failed}^{new} \times \frac{1}{2}\Delta t\right) + \left(N_{WP\ Failed}^{prev} \times (\bar{t}^{\,prev} + \Delta t)\right)}{N_{WP\ Failed}^{new} + N_{WP\ Failed}^{prev}} \qquad \text{(Eq. L-39)}$$

where

$\bar{t}$ = average WP failure time [yr]

$N_{WPFailed}^{New}$ = the number of new failures in the current timestep

$N_{WPFailed}^{prev}$ = the number of total failures in the previous timestep

Δt = the timestep length [yr].

The lifetime of carbon steel in cell ‘n’ is shown in Equation L-40 (SNL 2007 [DIRS 177407], Equation 8-4):

$$t_{LCS,n} = \frac{1000\, t_{max,CS,n}}{2 r_{CS}}$$

$$t_{LSS,n} = \frac{1000\, t_{max,SS,n}}{2 r_{SS}} \qquad \text{(Eq. L-40)}$$

where

r_{CS} = rate of corrosion of carbon steel [μm yr^{-1}]

r_{SS} = rate of corrosion of stainless steel [μm yr^{-1}]

$t_{max,CS,n}$ = maximum thickness of carbon steel in cell ‘n’ [m]

$t_{max,SS,n}$ = maximum thickness of stainless steel in cell ‘n’ [m].

The carbon steel corrosion rate, r_{CS}, is represented as a truncated log-normal distribution (μ = 78.5 μm yr^{-1}; σ = 25.0 μm yr^{-1}; minimum = 25.0 μm yr^{-1}; maximum =1,35.0 μm yr^{-1}) and the stainless steel corrosion rate, r_{SS}, is represented as a truncated log-normal distribution (μ = 0.267 μm yr^{-1}, σ = 0.209 μm yr^{-1}, minimum = 0.01 μm yr^{-1}, and maximum = 0.51 μm yr^{-1}) (DTN: SN0703PAEBSRTA.001_R3 [DIRS 183217]).

The parameter f_{GHFO} is shown in Equation L-41 (SNL 2007 [DIRS 177407], Equation 8-4):

$$f_{GHFO} = \begin{cases} \omega_G, & \text{for goethite} \\ (1-\omega_G), & \text{for HFO} \\ 1.0, & \text{for NiO and } Cr_2O_3 \end{cases} \quad \text{(Eq. L-41)}$$

where

ω_{Gn} = mass fraction of goethite in iron corrosion products, uniform distribution (0.45 - 0.80) (DTN: SN0703PAEBSRTA.001_R3 [DIRS 183217]).

The pore volume in the corrosion product is calculated for each cell using Equation L-42:

$$\begin{aligned} PV_{CP,n} &= \frac{\phi_{CP}}{1-\phi_{CP}} V_{CP,n} \\ &= \frac{\phi_{CP}}{1-\phi_{CP}} \sum_{CPm} \left(m_{CPm,CS,n} + m_{CPm,SS,n} \right) / \rho_{CPm} \end{aligned} \quad \text{(Eq. L-42)}$$

where

$PV_{CP,n}$ = pore volume of the corrosion product in cell 'n' (m^3)

$V_{CP,n}$ = volume of the corrosion product in cell 'n' (m^3)

ϕ_{CP} = porosity of corrosion product, 0.4 (DTN: SN0703PAEBSRTA.001_R3 [DIRS 183217])

ρ_{CPm} = density of corrosion product m (kg/m^3).

The parameters used to calculate the mass of each corrosion product and the total volume of water in the corrosion product for each cell are shown in Tables L-28 through L-30 (DTN: SN0703PAEBSRTA.001_R3 [DIRS 183217]).

L2.15.2 Commercial Spent Nuclear Fuel Waste Form Cell Parameters

The CSNF waste form cell contains the rind from reacted CSNF rods and corrosion product from degradation of the Stainless Steel Type 316 basket tubes and Borated Stainless Steel Type 304B4 absorber plates (SNL 2007 [DIRS 177407], Section 6.5.2.1.1). The volume of water in the CSNF waste form cell is the sum of the pore volume of the degraded UO_2 matrix and the pore volume of the corrosion product as shown in Equation L-43. This assumes that both the degraded UO_2 matrix and the corrosion product are fully saturated. The pore volume of the corrosion product is calculated using the approach described above:

$$PV_{CSNF-WF} = \phi_{rind} V_{rind} + PV_{CP,CSNF-WF} \quad \text{(Eq. L-43)}$$

where

$PV_{CSNF\text{-}WF}$ = pore volume of the CSNF waste form mixing cell (m^3)

$V_{rind\text{-}CSNF}$ = volume of reacted CSNF rind (m^3)

$PV_{CP,CSNF\text{-}WF}$ = pore volume of corrosion product in CSNF waste form (m^3)

ϕ_{rind} = porosity of the CSNF schoepite rind, uniform distribution: 0.05 to 0.30 (DTN: MO0411SPACLDDG.003_R1 [DIRS 180755]).

Models for the corrosion of the CSNF UO_2 matrix, and the subsequent rind volume, are described in *Cladding Degradation Summary for LA* (SNL 2007 [DIRS 180616]). The volume of the reacted CSNF rind is shown in Equation L-44 (SNL 2007 [DIRS 180616], Equation 6-7):

$$V_{rind-CSNF} = V_i \cdot VM \cdot F_{cor} \quad \text{(Eq. L-44)}$$

where

V_i = initial volume of CSNF UO_2 pellets per WP (m^2)

VM = volume increase due to UO_2 alteration to schoepite

F_{cor} = fraction of UO_2 altered to schoepite.

The initial volume of CSNF UO_2 pellets per WP is shown in Equation L-45 (SNL 2007 [DIRS 180616], Equation 6-4):

$$V_I = N_R \cdot L_R \cdot \pi/4 \cdot D_R^2 \quad \text{(Eq. L-45)}$$

where

L_R = fuel rod length, 3.66 m (DTN: MO0411SPACLDDG.003_R1 [DIRS 180755])

D_R = diameter of the fuel pellets, 0.819 cm (DTN: MO0411SPACLDDG.003_R1 [DIRS 180755])

N_R = total number of fuel rods failed in a WP, 5,544 (DTN: MO0411SPACLDDG.003_R1 [DIRS 180755]).

The volume increase due to the UO_2 alteration to schoepite is shown in Equation L-46 (SNL 2007 [DIRS 180616], Equation 6-3):

$$VM = \frac{MW_{schoepite}}{MW_{UO_2}} \frac{\rho_{UO_2}}{(1-\phi_{schoepite})\rho_{schoepite}} \quad \text{(Eq. L-46)}$$

where

$MW_{schoepite}$ = the molecular weight of schoepite, 322.1 g (DTN: MO0411SPACLDDG.003_R1 [DIRS 180755])

MW_{UO2} = the molecular weight of UO_2, 270 g (DTN: MO0411SPACLDDG.003_R1 [DIRS 180755])

$\rho_{schoepite}$ = the density of schoepite, 4.83 g/cm^3 (DTN: MO0411SPACLDDG.003_R1 [DIRS 180755])

ρ_{UO2} = the density of UO_2, 10.97 g/cm^3 (DTN: MO0411SPACLDDG.003_R1 [DIRS 180755])

$\phi_{schoepite}$ = the porosity of schoepite, uniform distribution: 0.05 to 0.30 (DTN: MO0411SPACLDDG.003_R1 [DIRS 180755]).

The fraction of UO_2 altered to schoepite is determined as an average over the total number of WPs that have failed in each region according to Equation L-47. This simplified model ascribes no barrier capability to the clad and the number of failed CSNF rods per WP equals the number of fuel rods in a WP:

$$F_{cor,j} = \frac{\frac{\Sigma M_{r,j}}{NF_{wp,j}}}{M_t} \qquad \text{(Eq. L-47)}$$

where

$F_{cor,j}$ = fraction of UO_2 altered to schoepite in region j (seeping or nonseeping)

$\Sigma M_{r,j}$ = total mass of UO_2 released from the waste form in region j

$NF_{wp,j}$ = number of failed CSNF WPs in region j

M_t = total mass of UO_2 per WP.

The total mass of UO_2 per WP, M_t, is set as a surrogate at 10^3 grams in the CSNF inventory as a nonradioactive species. The cumulative release is tracked over time and the numerator of Equation L-47 coverts this to an average mass of UO_2 (surrogate) released per failed fuel rod. The denominator is the total mass of UO_2 (surrogate) in a fuel rod.

The diffusion path length is equal to the inner radius of the TAD canister, 0.819 m (DTN: SN0703PAEBSRTA.001_R3 [DIRS 183217]). The diffusive area is equal to the surface area of a cylinder with a radius of half the TAD canister inner radius, and a length equal to the length of the fuel basket tubes (excluding the ends), 12.5 m^2 (DTN: SN0703PAEBSRTA.001_R3 [DIRS 183217]).

The effective diffusion coefficient in the CSNF rind is shown in Equation L-48 (SNL 2007 [DIRS 177407], Table 8.2-1):

$$\phi_{eff}\, S_w\, D_{CSNF,j} = \phi_{eff}^{1.3}\, S_w^{2}\, D_{0,j} \qquad \text{(Eq. L-48)}$$

where

$D_{CSNF,j}$ = effective diffusion coefficient for radionuclide j in CSNF waste form cell (m^2/s)

$D_{0,,j}$ = free water diffusion coefficient for radionuclide j (m^2/s)

ϕ_{eff} = effective porosity of CSNF waste form cell

S_w = water saturation, 1 (SNL 2007 [DIRS 177407], Table 8.2-1).

The effective porosity of the CSNF waste form cell is shown in Equation L-49:

$$\phi_{CSNF-WF} = \frac{PV_{CSNF-WF}}{V_{rind-CSNF} + V_{CP,CSNF-WF}} \quad \text{(Eq. L-49)}$$

where

$PV_{CSNF\text{-}WF}$ = pore volume of the CSNF waste form mixing cell (m^3)

$V_{rind\text{-}CSNF}$ = volume of reacted CSNF rind in the waste form mixing cell (m^3)

$V_{CP,CSNF\text{-}WF}$ = volume of corrosion product in the CSNF waste form mixing cell (m^3).

The free diffusion coefficients for the species considered in this simplified model are shown in Table L-31. This simplified model first calculates an overall effective diffusion coefficient using the self-diffusion coefficient of water, 2.299×10^{-9} m^2/s. The diffusion coefficient for each radionuclide is then adjusted using the ratio of the free water diffusion coefficients shown in Table L-31 and self-diffusion coefficient of water.

L2.15.3 CDSP Waste Form Cell Parameters

The CDSP waste form cell contains the degraded DHLW glass and corrosion product from the degradation of the DHLW and DSNF canisters. This is a simpler representation of the CDSP waste form than is modeled in *EBS Radionuclide Transport Abstraction* (SNL 2007 [DIRS 177407]), where the DHLW and DSNF are each represented as a waste form cell.

The volume of water in the CDSP waste form cell is the sum of the pore volume of the degraded DHLW glass and the pore volume of the corrosion as shown in Equation L-50. This assumes that both the degraded DHLW glass and the corrosion product are fully saturated. The pore volume of the degraded DSNF is not included in the total pore volume. The pore volume of the corrosion product is calculated using the approach described above.

$$PV_{CDSP-WF} = PV_{glass} + PV_{CP,CDSP-WF} \quad \text{(Eq. L-50)}$$

where

$PV_{CDSP\text{-}WF}$ = pore volume of the CDSP waste form mixing cell (m^3)

PV_{glass} = volume of reacted DHLW glass (m^3)

$PV_{CP,CDSP\text{-}WF}$ = pore volume of corrosion product in CDSP waste form (m^3).

Models for the corrosion of the DHLW glass matrix, and the subsequent rind volume, are described in *Defense HLW Glass Degradation Model* (BSC 2004 [DIRS 169988]). The total volume and pore volume in the glass alteration layer is calculated using Equation L-51 (BSC 2005 [DIRS 169988], Section 8.1, Equations 54 and 55):

$$V_{glass} = 3.7 \times 10^{-4} \Sigma M_t$$
$$PV_{glass} = 6.3 \times 10^{-5} \Sigma M_t \quad \text{(Eq. L-51)}$$

where

V_{glass} = volume of the DHLW glass alteration layer (m^3)

PV_{glass} = pore volume of the DHLW glass alteration layer (m^3)

ΣM_t = total mass of altered DHLW glass (kg).

The total mass of altered DHLW glass is determined as an average over the total number of WPs that have failed in a region according to Equation L-52:

$$\Sigma M_{t,j} = \frac{\Sigma M_{ga,j}}{NF_{wp,j} \cdot N_{can}} \quad \text{(Eq. L-52)}$$

where

$\Sigma M_{t,j}$ = total mass of altered DHLW glass in region j (seeping or nonseeping environment) (kg)

$\Sigma M_{ga,j}$ = total mass of glass altered in region j

$NF_{wp,j}$ = number of failed CDSP WPs in region j

N_{can} = number of DHLW canisters per WP, 5 (DTN: SN0703PAEBSRTA.001_R3 [DIRS 183217]).

The initial mass of glass per canister, M_{gi}, is set as a surrogate at 2,710 kg in the DHLW inventory as a nonradioactive species. The cumulative release, $\Sigma M_{ga,j}$, is tracked over time for each region and Equation L-52 converts this to an average mass of glass altered per canister in the failed WPs.

The diffusion path length is equal to the radius of the inner vessel of the 5-DHLW/DOE Long WP, 0.941 m (DTN: MO0411SPACLDDG.003_R1 [DIRS 180755]). The diffusive area is equal to the surface area of a cylinder with a radius equal to half the radius of the inner vessel of

the 5-DHLW/DOE Long WP and a length of the inner vessel of that WP, 13.7 m^2 (DTN: SN0703PAEBSRTA.001_R3 [DIRS 183217]).

The diffusion coefficient in the altered glass is shown in Equation L-53 (SNL 2007 [DIRS 177407], Table 8.2-1):

$$\phi_{eff} S_w D_{HLW,j} = \phi_{eff}^{1.3} S_w^2 D_{0,j} \quad \text{(Eq. L-53)}$$

where

$D_{HLW,j}$ = effective diffusion coefficient for radionuclide j in the CDSP waste form (m^2/s)
$D_{0,j}$ = free water diffusion coefficient for radionuclide j (Table L-29) (m^2/s)
ϕ_{eff} = effective porosity of CDSP waste form cell
S_w = water saturation, 1 (SNL 2007 [DIRS 177407], Table 8.2-1).

The effective porosity of the CDSP waste form cell is shown in Equation L-54:

$$\phi_{CDSP-WF} = \frac{PV_{CDSP-WF}}{V_{glass} + V_{CP,CDSP-WF}} \quad \text{(Eq. L-54)}$$

where

$PV_{CDSP\text{-}WF}$ = pore volume of the CDSP waste form mixing cell (m^3)
V_{glass} = volume of reacted DHLW glass in the waste form mixing cell (m^3)
$V_{CP,CDSP\text{-}WF}$ = volume of corrosion product in the CDSP waste form mixing cell (m^3).

L2.15.4 Corrosion Product Cell Parameters

The volume of water in the CSNF and CDSP WP corrosion product cells, is the total pore volume of the degraded WP internals. This assumes that the corrosion products are fully saturated. The pore volume of the corrosion product is calculated using the approach described above.

The diffusive path length in the CSNF corrosion product cell excluding the outer barrier is the combined thickness of TAD and the inner vessel, 0.0914 m (DTN: SN0703PAEBSRTA.001_R3 [DIRS 183217]). The diffusive path length through the outer barrier of the CSNF corrosion product cell is the thickness of the WP outer barrier, 0.0302 m (DTN: SN0703PAEBSRTA.001_R3 [DIRS 183217]). This simplified model combines these into a total diffusion path length of 0.1216 m.

The diffusive area for the path through the outer barrier of the CSNF WP cell is the smaller of either the total area of all WP breaches or the surface area of a cylinder at the midpoint between the inner vessel outer surface and the outer surface of the CSNF WP outer barrier, 33.1 m^2 (DTN: SN0703PAEBSRTA.001_R3 [DIRS 183217]).

The diffusive path length in the CDSP corrosion product cell excluding the outer barrier is the thickness of inner vessel, 0.0508 m (DTN: MO0411SPACLDDG.003_R1 [DIRS 180755]). The diffusive path length through the CDSP outer barrier is given by the thickness of the WP outer barrier, 0.0302 m (DTN: SN0703PAEBSRTA.001_R3 [DIRS 183217]). This simplified model combines these into a total diffusion path length of 0.081 m.

The diffusive area for the path through the outer barrier of the CDSP WP is the smaller of either the total area of all WP breaches or the surface area of a cylinder at the midpoint between the inner vessel outer surface and the outer surface of the CSNF WP outer barrier, 33.1 m^2 (DTN: SN0703PAEBSRTA.001_R3 [DIRS 183217]).

The diffusive area for general corrosion breaches equals the product of the fraction of the WP that has failed due to general corrosion determined using Equation L-11 and the total area of the WP outer surface (33.1 m^2). The diffusive area for stress corrosion cracks in the outer weld region is determined using Equation L-55:

$$A_{D-SCC\ Weld} = F_{SCC\ Weld} N_{SCC\ Cracks} A_{SCC\ Crack} \quad \text{(Eq. L-55)}$$

where

$A_{D\text{-}SCC\ Weld}$ = diffusive area through SCC cracks in the closure weld region of the WP (m^2)

$F_{SCC\ Weld}$ = fractional area of the closure weld region that has experienced SCC penetration (calculated using Equation L-11)

$N_{SCC\ Cracks}$ = total number of SCC cracks that can ultimately penetrate the closure weld region

$A_{SCC\ Crack}$ = area of a single SCC crack opening (m^2).

The total number of SCC cracks that could ultimately penetrate the outer closure weld region, $N_{SCC\ Cracks}$, is determined from *WAPDEG Analysis of Waste Package and Drip Shield Degradation* (BSC 2004 [DIRS 169996], Section 6.3.2.1) and is equal to 192. The area of a single SCC crack opening, $A_{SCC\ Crack}$, is 7.682 mm^2 (DTN: SN0703PAEBSRTA.001_R3 [DIRS 183217]).

Determining the area of the WP outer barrier damaged due to seismic events is discussed in Section L2.8.3. The crack density in this area is represented as a uniform distribution with the bounds defined by Equation L-56 (SNL 2007 [DIRS 181953], Section 6.7.2):

$$\rho_{SEIS-SCC,Min} = \frac{\sqrt{3}}{2T_{WPOB}}$$
$$\rho_{SEIS-SCC,Max} = \frac{2}{\sqrt{3}T_{WPOB}} \quad \text{(Eq. L-56)}$$

where

$\rho_{SEIS\text{-}SCC,Min}$ = minimum SCC crack density (crack/m^2)

$\rho_{SEIS\text{-}SCC,Max}$ = maximum SCC crack density (crack/m^2)

T_{WPOB} = thickness of WP outer barrier (m).

The area of SCC cracks caused by seismic events is shown in Equation L-57 (SNL 2007 [DIRS 181953], Section 6.7.2):

$$A_{SEIS-SCC} = \frac{(2\pi T_{WPOB}^2)\sigma_{YS}}{E} \quad \text{(Eq. L-57)}$$

where

$A_{SEIS\text{-}SCC}$ = area of seismically induced SCC crack (m^2)

T_{WPOB} = thickness of WP outer barrier (m)

σ_{YS} = Alloy 22 yield stress, 403 MPa (DTN: MO0702PASTRESS.002_R2 [DIRS 180514])

E = Young's Modulus of Alloy 22, 206 GPa (DTN: MO0702PASTRESS.002_R2 [DIRS 180514]).

The diffusion coefficient in the corrosion product is shown in Equation L-58 (SNL 2007 [DIRS 177407], Table 8.2-1):

$$\phi_{CP}\, S_w\, D_{CP,j} = \phi_{CP}^{1.3}\, S_w^{2}\, D_{0,j} \quad \text{(Eq. L-58)}$$

where

$D_{CP,j}$ = effective diffusion coefficient for radionuclide j in corrosion product (cm^2/s)

$D_{0,j}$ = free water diffusion coefficient for radionuclide j (Table L-29) (m^2/s)

ϕ_{CP} = porosity of corrosion product, 0.4 (DTN: SN0703PAEBSRTA.001_R3 [DIRS 183217])

S_w = water saturation in rind, 1 (SNL 2007 [DIRS 177407], Table 8.2-1).

L2.15.5 Invert Cell Parameters

The invert is modeled assuming it is comprised of crushed tuff. The mass of crushed tuff in the invert is calculated as the product of the invert volume, density of crushed tuff, and one-minus the invert porosity. The invert volume is equal to the length of the DS, 5.805 m; invert width, 4.7 m; and average thickness of the invert, 0.934 m (DTN: SN0703PAEBSRTA.001_R3 [DIRS 183217]). This results in an invert volume of 25.48 m^3. The invert porosity is 0.224 (DTN: SN0703PAEBSRTA.001_R3 [DIRS 183217]). The water volume in the invert is the

product of the total invert volume and the invert porosity, assuming that the invert is fully saturated. This gives an invert water volume of 3.1 m^3.

The invert diffusive area is assumed to equal the product of the invert length and width, 22.09 m^2. The diffusive path length in the invert is assumed to equal the average thickness of the invert, 0.934 m^2. The diffusion coefficient in the invert is shown in Equation L-59 (SNL 2007 [DIRS 177407], Table 8.2-7):

$$\phi_{Invert} S_w D_{Invert,j} = \phi_{Invert}^{1.863} S_w^{1.863} D_{0,j} 10^U \quad \text{(Eq. L-59)}$$

where

$D_{Invert,j}$ = effective diffusion coefficient for radionuclide j in the invert (cm^2/s)

$D_{0,j}$ = free water diffusion coefficient for radionuclide j (Table L-29) (m^2/s)

ϕ_{Invert} = porosity of corrosion product, 0.224 (DTN: SN0703PAEBSRTA.001_R3 [DIRS 183217])

S_w = water saturation in invert, assumed to be 1.

U = invert diffusion uncertainty factor, normal distribution with a mean of 0.033 and a standard deviation of 0.218

L2.16. RADIONUCLIDE TRANSPORT THROUGH THE NATURAL BARRIER SYSTEM

Modeling radionuclide transport in the UZ and SZ requires the use of complex three-dimensional models to accurately reflect the controlling processes and spatial variability in hydrologic properties. In order to model radionuclide transport it is first necessary to determine the rate and direction that groundwater flows in both the UZ and SZ. This is accomplished through the use of a dual permeability continuum approach in the UZ that is documented in *UZ Flow Models and Submodels* (SNL 2007 [DIRS 184614]) and an effective continuum approach in the SZ that is documented in *Saturated Zone Site-Scale Flow Model* (SNL 2007 [DIRS 177391]).

Several processes related to radionuclide transport within the natural system below the repository prevent or substantially reduce the movement of radionuclides from the repository to the accessible environment. These processes include matrix diffusion, radionuclide sorption, dispersion, and radionuclide decay along the transport pathway. The natural system below the repository alone can effectively isolate short lived and/or strongly-sorbing radionuclides from the environment. This barrier also reduces the movement of radionuclides that are long lived and non- or moderately-sorbing to the accessible environment.

Radionuclide transport modeling in the UZ is presented in *Radionuclide Transport Models Under Ambient Conditions* (SNL 2007 [DIRS 177396]) and *Particle Tracking Model and Abstraction of Transport Processes* (SNL 2008 [DIRS 184748]). Radionuclide transport modeling in the SZ is presented in *Site Scale Saturated Zone Transport* (SNL 2007 [DIRS 177392]) and *Saturated Zone Flow and Transport Model Abstraction* (SNL 2007 [DIRS 183750]).

L2.16.1 Radionuclide Transport in the Unsaturated Zone

The percentage of percolation flux in the rock matrix, fractures, and fault regions for the sixteen UZ flow fields (four infiltration scenarios; four climate states) considered in the TSPA-LA (SNL 2007 [DIRS 184614], Tables 6.6-2 and 6.6-3) indicates that a significant amount of the UZ percolation flux, both at the repository horizon and at the water table, flows in the fractures or in faults. The amount of flow in the fractures and faults is larger for higher infiltration rates and wetter climate states. Radionuclide breakthrough curves for Tc (nonsorbing), Np (moderately sorbing), and Pu (strongly sorbing) indicate that a significant fraction of these radionuclides is transported in fractures and faults from the repository horizon to the water table. This leads to the early arrival portion of the breakthrough curves. The fraction of radionuclides that is transported either partially or completely within the rock matrix leads to the later arrival portion of the breakthrough curves.

Based on these results, it can be concluded that a large fraction of any radionuclides being transported in the fractures or fault regions will traverse a hydrologic unit in the UZ within a single timestep used in this simplified model. It is therefore not necessary to reflect the breakthrough curve over the timestep for those radionuclides being transported in the fractures of a hydrologic unit in this simplified model. Rather, it is necessary to only determine the total amount of radionuclide mass that would traverse a unit during a single timestep. Radionuclide transport through the rock matrix is much slower with breakthrough occurring over many timesteps. It is necessary to reflect the breakthrough curve for those radionuclides transported in the rock matrix.

A simplified approach is used to model radionuclide transport in the UZ. The purpose of this simplified approach is to reflect the general behavior of the breakthrough curve, rather than the detailed behavior of groundwater flow and radionuclide transport within the UZ.

The UZ is represented by two ‘regions’ and three layers. The three layers represent the Topopah Spring, Calico Hills, and Prow Pass units, and the two ‘regions’ represent the area of the repository horizon that is and is not underlain by zeolitic rock. Average hydrologic properties are determined from the calibrated property sets contained in *Calibrated UZ Properties* (SNL 2007 [DIRS 179545]).

The EBS model presented above treats the repository as a single areal ‘region’ with discretization to account for seeping conditions and different waste forms only. A fraction of the entire mass flux out of the EBS is assumed to be released over the portion of the repository horizon underlain by zeolitic rock with the remaining fraction released over the portion of the repository not underlain by zeolitic rock. The interpreted extent of the vitric region in the various hydrologic units under the repository is given in *Development of Numerical Grids for UZ Flow and Transport* Modeling (BSC 2004 [DIRS 169855], Figures 6-7 and 6-8). It is assumed, based on these interpretations, that 70 percent of the area underlying the repository has zeolitic rock in the lower Topopah Spring and Calico Hills hydrologic units. Thus, 70 percent of the EBS releases are assumed to occur over the portion of the repository horizon underlain by zeolitic rock, with the remaining 30 percent assumed to be released over the portion of the repository not underlain by zeolitic rock.

The fraction of percolation flux flowing in the fractures and in the matrix is determined for each of the three layers by comparing the percolation flux to the saturated hydraulic conductivity using Equation L-60:

$$\begin{aligned} &\text{IF} \quad \phi > K_{sat} \quad \text{THEN} \quad F_{matrix} = \frac{K_{sat}}{\phi};\ F_{fracture} = \left(1 - \frac{K_{sat}}{\phi}\right) \\ &\text{ELSE} \qquad\qquad\qquad\qquad F_{matrix} = 1; \qquad F_{fracture} = 0 \end{aligned} \qquad \text{(Eq. L-60)}$$

where

F_{matrix} = fraction of percolation flux flowing in the rock matrix

$F_{fracture}$ = fraction of percolation flux flowing in the rock fractures

ϕ = percolation flux (m/yr)

K_{sat} = matrix saturated hydraulic conductivity (m/yr).

The fraction of radionuclides transported in the matrix and the fractures of each layer are also determined using Equation L-60. The total release (matrix and fracture) from each layer is determined at each timestep and apportioned to the matrix and fracture 'columns' in the next layer. For example, a fraction of radionuclides exiting the fractures of one layer would be transported in the matrix of the next layer.

Interaction between radionuclides transported in the fractures and matrix, such as by matrix diffusion, is not considered in this simplified representation. This is a conservative approach since including matrix diffusion would result in radionuclide breakthrough being delayed. The approach being utilized herein (no fracture-matrix interaction) is conservative.

Radionuclides being transported in the fractures are assumed to migrate through a layer in a single timestep. Radionuclide transport in the matrix is modeled using a semi-analytic solution to the one-dimensional transport equation with radionuclide decay shown in Equation L-61 (Zheng and Bennett 1995 [DIRS 154702]). This simplified model does not include colloid facilitated transport in the UZ because past TSPA analysis results have shown that radionuclides transported on colloids do not contribute significantly to overall repository performance.

$$M(x,t) = \frac{x}{2\sqrt{\pi D'_x}} \sum_{i=1}^{NP} \Delta M_i \int_0^{t-t_i} \frac{1}{\xi^{\frac{3}{2}}} \exp\left[-\lambda\xi - \frac{(x - v'\xi)^2}{4D'_x \xi}\right] d\xi \qquad \text{(Eq. L-61)}$$

$$D'_x = \frac{\alpha_L v}{R}; \quad v' = \frac{v}{R}; \quad R = 1 + \rho K_d; \quad v = \frac{\phi}{\theta}$$

where

$M(x,t)$ = cumulative mass that has reached position x at time t (g)

ΔM_i = the radionuclide mass released into a layer over timestep i (g)

λ = decay constant (yr^{-1})

v = Groundwater velocity (m/yr)

α_L = longitudinal dispersivity (m)

R = retardation coefficient (unitless)

ρ = rock density (g/m^3)

K_d = distribution coefficient (m^3/g)

ϕ = Groundwater flux (m/yr)

θ = rock porosity (unitless)

NP = number of discrete steps (simulation time divided by the timestep size).

Equation L-61 is used to compute the total radionuclide mass that has been transported through the rock matrix to the bottom of each layer at each timestep where x is equal to the thickness of the layer. The integral is solved numerically using the trapezoidal rule with the overall timestep divided into five substeps to improve numerical accuracy. This numerical integration technique is appropriate for this simplified model because the breakthrough curves vary gradually over the timestep utilized. The numerical solution to Equation L-61 utilizing the trapezoidal numerical integration rule is given as Equation L-62:

$$M(T_{L,Unit,M},t_i)=\frac{T_L}{2\sqrt{\pi D'_x}}\frac{\Delta t}{2}\sum_{j=1}^{NP=t_i/\Delta t}\Delta M_{Unit,M}(t_i)\sum_{k=1}^{t_i-t_j/\Delta t}\left(f(\lambda,D'_x,t_{k-1})+f(\lambda,D'_x,t_k)\right)$$

$$f(\lambda,D'_x,t_k)=\frac{1}{t_k^{3/2}}\exp(-\lambda t_k-\frac{(T_L-v't_k)^2}{4D'_x t_k});\quad f(\lambda,D'_x,t_0)=0 \qquad \text{(Eq. L-62)}$$

$$t_k=k\Delta t$$

where

$M(T_{L,Unit,M},t_i)$ = cumulative mass that has exited the matrix at the bottom of a UZ layer at timestep t_i (g)

$\Delta M_{Unit,M}(t_i)$ = the mass that enters the matrix at the top of the UZ layer time over the timestep length (yr)

T_L = thickness of UZ layer (m)

Δt = timestep length (yr).

The mass that enters the top of each UZ layer in the matrix, $\Delta M_{Unit,M}(t_i)$, and the fractures, $\Delta M_{Unit,F}(t_i)$, is shown in Equation L-63:

Topopah Spring Zeolitic

$$\Delta M_{TSW-Z,M}(t_i) = F_{zeolitic}\ F_{TSW-Z,matrix}\ \Delta M_{EBS}(t_i) \quad Matrix$$
$$\Delta M_{TSW-Z,F}(t_i) = F_{zeolitic}\ F_{TSW-Z,fracture}\ \Delta M_{EBS}(t_i) \quad Fractures$$

Topopah Spring Vitric

$$\Delta M_{TSW-V,M}(t_i) = \left(1-F_{zeolitic}\right) F_{TSW-V,matrix}\ \Delta M_{EBS}(t_i) \quad Matrix$$
$$\Delta M_{TSW-V,F}(t_i) = \left(1-F_{zeolitic}\right) F_{TSW-V,fracture}\ \Delta M_{EBS}(t_i) \quad Fractures$$

Calico Hills Zeolitic

$$\Delta M_{CH-Z,M}(t_i) = F_{CH-Z,matrix}\ \Delta M(T_{L,TSW-Z},t_i) \quad Matrix$$
$$\Delta M_{CH-Z,F}(t_i) = F_{CH-Z,fracture}\ \Delta M(T_{L,TSW-Z},t_i) \quad Fractures$$

Calico Hills Vitric

$$\Delta M_{CH-V,M}(t_i) = F_{CH-V,matrix}\ \Delta M(T_{L,TSW-V},t_i) \quad Matrix$$
$$\Delta M_{CH-V,F}(t_i) = F_{CH-V,fracture}\ \Delta M(T_{L,TSW-V},t_i) \quad Fractures$$

Prow Pass

$$\Delta M_{PP,M}(t_i) = F_{PP,matrix}\left(\Delta M(T_{L,CH-Z},t_i) + \Delta M(T_{L,CH-V},t_i)\right) \quad Matrix \qquad \text{(Eq. L-63)}$$
$$\Delta M_{PP,F}(t_i) = F_{PP,fracture}\left(\Delta M(T_{L,CH-Z},t_i) + \Delta M(T_{L,CH-V},t_i)\right) \quad Fractures$$

where

- $\Delta M_{Unit,,M/F}(t_i)$ = the mass entering the top of the unit in the matrix/fractures at timestep i (g)
- $\Delta M_{EBS}(t_i)$ = the total mass exiting the EBS at timestep i (g)
- $\Delta M(T_{L,Unit},t_i)$ = the mass exiting the bottom of the unit in the matrix and fractures at timestep i (g)
- $F_{zeolitic}$ = fraction of repository underlain by zeolitic rock (0.70 [see above])
- $F_{Unit,matrix.fractures}$ = fraction of percolation flux flowing in the matrix/fractures of the unit (Equation L-59).

Radionuclide decay and daughter product in growth are modeled in the UZ matrix units by tracking the cumulative mass that exits the matrix for a parent radionuclide assuming no radioactive decay. It is assumed that the difference between the cumulative breakthrough of the parent without and with radioactive decay equals the mass of daughter product that built up during transit through that layer. This approach does not account for decay of the daughter radionuclide within the layer where it is formed. This approach is conservative as it leads to larger amounts of daughter product mass as compared to methods that allow for decay within the

layers. Thus, the radionuclide mass exiting the matrix at the bottom of each layer over a timestep, $\Delta M_{Unit,m}(T_L,t_i)$, is shown in Equation L-64:

No Parent

$$\Delta M(T_{L,Unit,m},t_i) = M(T_{L,Unit,m},t_i) - M(T_{L,Unit,m},t_{i-1})$$

Parent (Eq. L-64)

$$\Delta M(T_{L,Unit,m},t_i) = \left(M(T_{L,Unit,m},t_i) - M(T_{L,Unit,m},t_{i-1})\right) + \left[\left(MP_0(T_{L,Unit,m},t_i) - MP(T_{L,Unit,m},t_i)\right) - \left(MP_0(T_{L,Unit,m},t_{i-1}) - MP(T_{L,Unit,m},t_{i-1})\right)\right]$$

where

$MP(T_{L,Unit,m},t_i)$ = cumulative mass of parent radionuclide that has exited the matrix at the bottom of a UZ layer at timestep t_i (g)

$MP_0(T_{L,Unit,m},t_i)$ = cumulative mass of parent radionuclide that has exited the matrix at the bottom of a UZ layer at timestep t_i with no decay (g).

The total mass exiting the bottom of a unit is shown in Equation L-65 as the sum of the total mass exiting the matrix and fracture continua of each unit. Recall, radionuclide transport in the fractures is assumed to occur over one timestep and the mass exiting the fractures of a unit is simply equal to the mass entering the fractures. Note that daughter in-growth is not considered in the fracture continua given the relatively rapid transit times assumed.

$$\Delta M(T_{L,Unit},t_i) = \Delta M(T_{L,Unit,M},t_i) + \Delta M(T_{L,Unit,F},t_i) \quad \text{(Eq. L-65)}$$

where

$\Delta M(T_{L,Unit},t_i)$ = the mass exiting the bottom of the unit in the matrix and fractures at timestep i (g)

$\Delta M(T_{L,Unit,M},t_i)$ = the mass exiting the bottom of the unit in the matrix at timestep i (g)

$\Delta M(T_{L,Unit,F},t_i)$ = the mass exiting the bottom of the unit in the fractures at timestep i (g).

The average thickness for each layer was determined using unit contact information from *Development of Numerical Grids for UZ Flow and Transport Modeling* (BSC 20074 [DIRS 169855], Attachment II, Table II-1). The average thickness of the three layers used in this simplified model is shown in Table L-32 and was determined using the boreholes and contact information shown in Table L-33.

The average absolute matrix permeability in each layer is determined using Equation L-66:

$$\bar{k} = \frac{\sum_{i=1}^{NL} T_i}{\sum_{i=1}^{NL} \frac{T_i}{k_i}} \quad \text{(Eq. L-66)}$$

where

$\bar{k}$ = the average absolute matrix permeability in the layer (m^2)

T_i = the thickness of unit i in the layer (m)

k_i = the absolute matrix permeability of unit i in the layer (m^2).

The average relative permeability is determined using Equation L-67 (SNL 2007 [DIRS 184614], Appendix A, Equation A-9):

$$\bar{k}_r = \bar{k}\, S_E^{\frac{1}{2}} \left[1 - \left(1 - S_E^{\frac{1}{m}} \right)^m \right]^2 \quad \text{(Eq. L-67)}$$

where

$\bar{k}_r$ = the average relative matrix permeability in the layer (m^2)

$\bar{k}$ = the average absolute matrix permeability in the layer (m^2)

S_E = the effective matrix saturation (unitless)

m = Van Genuchten matrix parameter.

The effective saturation, S_E, is determined using Equation L-68:

$$S_E = \frac{S_M - S_R}{1 - S_R} \quad \text{(Eq. L-68)}$$

where

S_M = matrix saturation (unitless)

S_R = Residual matrix saturation (unitless).

The residual saturation, S_R, for each layer was determined from uncalibrated matrix properties provided in *UZ Flow Models and Submodels* (SNL 2007 [DIRS 184614], Section 4.1.2.1) using Equation L-69 and are shown in Table L-34.

$$\overline{S}_R = \frac{\sum_{i=1}^{NL} T_i S_{R,i}}{\sum_{i=1}^{NL} T_i} \quad \text{(Eq. L-69)}$$

where

$\overline{S}_R$ = the average residual saturation in the layer (m^2)

T_i = the thickness of unit i in the layer

$S_{R,i}$ = the residual saturation of unit i in the layer (m^2).

The van Genuchten matrix parameter, m, for each layer, was determined from calibrated matrix properties using Equation L-70 and is shown in Table L-35.

$$\overline{m} = \frac{\sum_{i=1}^{NL} T_i m_i}{\sum_{i=1}^{NL} T_i} \quad \text{(Eq. L-70)}$$

where

$\overline{m}$ = the average matrix van Genuchten parameter in the layer (m^2)

T_i = the thickness of unit i in the layer

m_i = the van Genuchten parameter m of unit i in the layer (m^2).

The matrix hydraulic conductivity is determined using Equation L-71:

$$K = \overline{k}_r \frac{\gamma}{\mu} \quad \text{(Eq. L-71)}$$

where

$\overline{k}_r$ = the average relative matrix permeability in the layer (m^2)

γ = the specific weight of water (9807 N/m^3)

μ = the dynamic viscosity of water (8.9×10^{-4} Pa·s).

The absolute permeability and Van Genuchten matrix parameter for each unit were obtained from *Calibrated UZ Properties* (SNL 2007 [DIRS 179545]), and the matrix saturation was estimated for each model layer from results shown in *UZ Flow Models and Submodels* (SNL 2007 [DIRS 184614]). These properties were used to calculate the effective saturation for each layer, the average layer relative permeability, and the layer average saturated hydraulic conductivities, which are shown in Table L-35.

The average porosity in each layer is determined using Equation L-72. The porosity of each unit was obtained from *Calibrated UZ Properties* (SNL 2007 [DIRS 179545]), and is shown in Table L-36.

$$\bar{\theta} = \frac{\sum_{i=1}^{NL} T_i \theta_i}{\sum_{i=1}^{NL} T_i} \qquad \text{(Eq. L-72)}$$

where

$\bar{\theta}$ = the average matrix porosity in the layer (m^2)

T_i = the thickness of unit i in the layer

θ_i = the matrix porosity of unit i in the layer (m^2).

Table L-37 shows the matrix and fracture percolation flux for each layer considered in this simplified model. The matrix and fracture percolation flux for each layer was determined using the average percolation flux for each climate state and infiltration scenario provided in Table L-2. The percolation flux in the matrix and fractures for each layer was then calculated using Equation L-60 and the layer average hydraulic conductivities provided in Table L-35 for each infiltration scenario.

Table L-38 shows the groundwater velocity in each layer and Table L-39 shows the time for flowing groundwater to traverse each layer. It can be seen from Table L-36 that the time to traverse a layer is much faster when groundwater is flowing in fractures as compared to when flowing in the matrix. Except for the present-day climate, low infiltration case, fracture travel times are significantly less than 500 years and are as small as tens of years or less. Thus, it is appropriate, and conservative, to assume that any radionuclides that are transported within the fractures immediately traverse a layer to the top of the underlying layer (or the interface with the SZ).

As discussed in *Radionuclide Transport Models Under Ambient Conditions* (SNL 2007 [DIRS 177396], Section 6.1.2.2), past analyses of UZ flow assumed that longitudinal dispersivity, α_L, values for both the fractures and matrix of all units had a mean of 20 meters and a standard deviation of 5 meters. This simplified model thus assumes that the longitudinal dispersivity, α_L, is normally distributed with a mean of 20 meters and a standard deviation of 5 meters.

The average density in each layer is determined using Equation L-73. The density of each unit was obtained from *Particle Tracking Model and Abstraction of Transport Processes* (SNL 2008 [DIRS 184748]) and is shown in Table L-40.

$$\overline{\rho} = \frac{\sum_{i=1}^{NL} T_i \rho_i}{\sum_{i=1}^{NL} T_i} \qquad \text{(Eq. L-73)}$$

where

$\overline{\rho}$ = the average rock density in the layer (m^2)

T_i = the thickness of unit i in the layer

ρ_i = the rock density of unit i in the layer (m^2).

The distribution coefficients used for each layer used in this simplified model were obtained from *Particle Tracking Model and Abstraction of Transport Processes* (SNL 2008 [DIRS 184748]) and are shown in Table L-41.

L2.16.2 Radionuclide Transport in the Saturated Zone

Radionuclide transport in the SZ is also modeled using the semi-analytic solution to the one-dimensional transport equation with radionuclide decay that is used to model radionuclide transport in the UZ, shown in Equation L-61. The same numerical solution technique is utilized. This simplified model does not include colloid facilitated transport in the SZ because past TSPA analysis results have shown that radionuclides transported on colloids do not contribute significantly to overall repository performance.

The SZ is divided into three segments: (1) fractured-volcanic rock from underneath the repository to 5 km down gradient, (2) fractured-volcanic rock from 5 km to 13 km down gradient to the alluvium contact, and (3) alluvium to the 18 km compliance location. Radionuclides exiting the UZ enter the first segment.

If the groundwater transport time through a segment is less than the simulation timestep size, it is assumed that the radionuclides are immediately transported through that segment. If the groundwater transport time through a segment is greater than the simulation timestep, Equation L-74 is used to compute the total radionuclide mass that has been transported through the each segment of the SZ at each timestep. The integral is solved numerically using the trapezoidal rule. Given that radionuclide travel times in the SZ may be more rapid than those in the UZ matrix, the overall timestep is divided into 500 substeps for numerical accuracy.

$$M(T_{L,SZ-SEG}, t_i) = \frac{T_L}{2\sqrt{\pi D'_x}} \frac{\Delta t}{2} \sum_{j=1}^{NP=t_i/\Delta t} \Delta M_{SZ-SEG}(t_i) \sum_{k=1}^{t_i - t_j/\Delta t} \left(f(\lambda, D'_x, t_{k-1}) + f(\lambda, D'_x, t_k) \right)$$

$$f(\lambda, D'_x, t_k) = \frac{1}{t_k^{3/2}} \exp\left(-\lambda t_k - \frac{(T_L - v' t_k)^2}{4 D'_x t_k}\right); \quad f(\lambda, D'_x, t_0) = 0 \qquad \text{(Eq. L-74)}$$

$$t_k = k\Delta t$$

where

$M(T_{L,SZ\text{-}SEG},t_i)$ = cumulative mass that has exited the SZ segment at timestep t_i (g)

$\Delta M_{SZ\text{-}SEGt,M}(t_i)$ = the mass that enters the SZ segment time over the timestep length (yr)

T_L = length of SZ segment (m)

Δt = timestep length (yr).

The mass that enters each SZ segment, $\Delta M_{SZ\text{-}SEG}(t_i)$, is shown in Equation L-75:

$$\begin{gathered}\text{SZ Segment 1}\\ \Delta M_{SZ-SEG1,M}(t_i)=\Delta M(T_{L,PP},t_i)\\ \text{SZ Segment 2}\\ \Delta M_{SZ-SEG2,M}(t_i)=\Delta M(T_{L,SZ-SEG1},t_i)\\ \text{SZ Segment 3}\\ \Delta M_{SZ-SEG3,M}(t_i)=\Delta M(T_{L,SZ-SEG2},t_i)\end{gathered} \qquad \text{(Eq. L-75)}$$

where

$\Delta M_{SZ\text{-}SEG}(t_i)$ = the mass entering the SZ segment at timestep i (g)

$\Delta M(T_{L,PP},t_i)$ = the mass exiting the bottom of the Prow Pass unit in the matrix and fractures at timestep i (g)

$\Delta M(T_{L,SZ\text{-}SEG},t_i)$ = the mass exiting the SZ segment at timestep i (g).

Radionuclide decay and daughter product in growth are modeled in the SZ segments by tracking the cumulative mass that exits the matrix for a parent radionuclide assuming no radioactive decay. It is assumed that the difference between the cumulative breakthrough of the parent without and with radioactive decay equals the mass of daughter product that built up during transit through that layer. This approach does not account for decay of the daughter radionuclide within the layer where it is formed. This approach is conservative as it leads to larger amounts of daughter product mass as compared to methods that allow for decay within the layers. Thus, the radionuclide mass exiting each SZ segment over a timestep, $\Delta M_{SZ\text{-}SEG}(T_L,t_i)$, is shown in Equation L-76:

$$\begin{gathered}\text{No Parent}\\ \Delta M(T_{L,SZ-SEG},t_i)=M(T_{L,SZ-SEG},t_i)-M(T_{L,SZ-SEG},t_{i-1})\\ \text{Parent}\\ \Delta M(T_{L,SZ-SEG},t_i)=\left(M(T_{L,SZ-SEG},t_i)-M(T_{L,SZ-SEG},t_{i-1})\right)+\\ \left[\left(MP_0(T_{L,SZ-SEG},t_i)-MP(T_{L,SZ-SEG},t_i)\right)-\left(MP_0(T_{L,SZ-SEG},t_{i-1})-MP(T_{L,SZ-SEG},t_{i-1})\right)\right]\end{gathered} \qquad \text{(Eq. L-76)}$$

where

$MP(T_{L,SZ\text{-}SEG}, t_i)$ = cumulative mass of parent radionuclide that has exited the SZ segment at timestep t_i (g)

$MP_0(T_{L,SZ\text{-}SEG}, t_i)$ = cumulative mass of parent radionuclide that has exited the SZ segment at timestep t_i with no decay (g).

The length of each segment is taken from the pipe length segments used in the one dimensional model developed in *Saturated Zone Flow and Transport Model Abstraction* (SNL 2007 [DIRS 183750], Section 6.5.1.2, Table 6-7). The pipe length segments used in the one dimensional model were determined for four source regions underneath the repository as a function of uncertainty in the horizontal anisotropy and in the contact between volcanic and alluvium units. The first pipe length segment is set at five kilometers.

The lengths of the second and third segments were determined by averaging the minimum and maximum values for each source region for a horizontal anisotropy of 5.0 (near the median of the uncertainty distribution). The length of the second segment is assumed to vary uniformly between 11 and 14 kilometers. The length of the third segment is assumed to vary uniformly between 2 and 5 kilometers, negatively correlated to the length of the second segment. For example, if the length of the second segment is 11 kilometers (the minimum), the length of the third segment is 5 kilometers (the maximum).

The specific discharge used in the one dimensional model developed in *Saturated Zone Flow and Transport Model Abstraction* (SNL 2007 [DIRS 183750], Section 6.5.1.2, Table 6-6) is also a function of uncertainty in the horizontal anisotropy as shown in Table L-42. The uncertainty distribution for the horizontal anisotropy is shown in Table L-43 (DTN: SN0302T0502203.001_R0 [DIRS 163563]). Additional uncertainty is applied to the average specific discharge through the use of a multiplication factor shown in Table L-44 (DTN: SN0702PASZFTMA.002_R1 [DIRS 183471]). The specific discharge values shown in Table L-44 are for the present-day climate state.

Saturated Zone Flow and Transport Model Abstraction (SNL 2007 [DIRS 183750], Section 6.5) applies an additional factor of 3.9 to the groundwater discharge for the glacial-transition climate state (DTN: SN0702PASZFTMA.002_R1 [DIRS 183471]). This factor is applied to all climate states in this simplified model. Applying this factor to the present-day and monsoon climate states is conservative because it leads to higher groundwater velocities. Application of this factor to the time period beyond 10,000 years is consistent with the approach being taken in the TSPA-LA.

The porosity in the fractured volcanic segments is assumed to be equal to the flowing interval porosity given in Table L-45 (SNL 2007 [DIRS 183750], Section 6.5.1.2, Table 6-8). The porosity of the alluvium is 0.30 (DTN: SN0702PASZFTMA.002_R1 [DIRS 183471]).

The logarithm of the longitudinal dispersivity is represented as a normal distribution with a mean of 2.0 and a standard deviation of 0.75 (DTN: MO0003SZFWTEEP.000_R0 [DIRS 148744]).

The average density of the fractured volcanic rock is 1,880 kg/m^3 (DTN: SN0702PASZFTMA.002_R1 [DIRS 183471]). The average density of the alluvium is 1,910 kg/m^3 (DTN: SN0310T0502103.009_R0 [DIRS 168763]).

The distribution coefficients used in this simplified model are shown in Table L-46.

L2.17. BIOSPHERE

The dose to the reasonably exposed maximally individual is calculated in this simplified model using Equation L-77:

$$D_T(t_i) = \sum_{j=1}^{NR} D_j(t_i)$$
$$D_j(t_i) = BDCF_j \frac{\dot{m}_{SZ,j}(t_i)}{Q_{well}} \quad \text{(Eq. L-77)}$$

where

$D_{T,}(t_i)$ = total dose from NR radionuclides included in the simulation at timestep t_i (mrem/yr)

$D_{j,}(t_i)$ = dose from radionuclide j at timestep t_i (mrem/yr)

$BDCF_j$ = biosphere dose conversion factor for radionuclide j (mrem/yr per g/m^3)

$\dot{m}_{SZ,j}(t_i)$ = mass flux of radionuclide j crossing the 18 km boundary over timestep t_i (g/m^3)

Q_{well} = volumetric flow rate from the receptor wells, the representative volume of 3,000 acre-ft/yr).

The mass flux that crosses the 18 km boundary is determined from the cumulative mass that exits SZ segment three discussed above. As discussed above, radionuclide decay and daughter product in growth are modeled in the SZ segments by tracking the cumulative mass that exits the matrix for a parent radionuclide assuming no radioactive decay. It is assumed that the difference between the cumulative breakthrough of the parent through SZ segment three without and with radioactive decay equals the mass of daughter product that built up during transit through that layer. Thus, the mass flux exiting SZ segment three is shown in Equation L-78:

No Parent

$$\dot{m}_{SZ}(t_i) = \left(M(T_{L,SZ-SEG3}, t_i) - M(T_{L,SZ-SEG3}, t_{i-1})\right)/\Delta t$$

Parent

$$\dot{m}_{SZ}(t_i) = \left(M(T_{L,SZ-SEG3}, t_i) - M(T_{L,SZ-SEG3}, t_{i-1})\right)/\Delta t + \left[\left(MP_0(T_{L,SZ-SEG3}, t_i) - MP(T_{L,SZ-SEG3}, t_i)\right) - \left(MP_0(T_{L,SZ-SEG3}, t_{i-1}) - MP(T_{L,SZ-SEG3}, t_{i-1})\right)\right]/\Delta t$$

(Eq. L-78)

where

$M(T_{L,SZ\text{-}SEG3}, t_i)$ = cumulative mass of radionuclide that has exited SZ segment three at timestep t_i (g)

$MP(T_{L,SZ\text{-}SEG3}, t_i)$ = cumulative mass of parent radionuclide that has exited SZ segment three at timestep t_i (g)

$MP_0(T_{L,SZ\text{-}SEG3}, t_i)$ = cumulative mass of parent radionuclide that has exited SZ segment three at timestep t_i with no decay (g).

The development of all-pathway biosphere dose conversion factors (BDCFs) is presented in *Biosphere Model Report* (SNL 2007 [DIRS 177399]). This simplified model uses the groundwater BDCFs for the present-day climate state, consistent with the approach taken in the TSPA-LA (Section 6.3.11.3). The BDCF probability distributions used in this simplified model are shown in Table L-47 (DTN: MO0702PAGBDCFS.001_R0 [DIRS 179327]). This simplified model assumes that:

- Ra^{226} and Pb^{210} are in radioactive equilibrium with Th^{230} at the receptor location
- Th^{228} and Ra^{228} are in radioactive equilibrium with Th^{232} at the receptor location
- Ac^{227} is in radioactive equilibrium with Pa^{231} at the receptor location.

L2.18. IGNEOUS INTRUSION MODELING CASE

This simplified model includes a simplified approach for evaluating the consequences of the igneous intrusion modeling case. In modeling cases where this is considered, it is assumed that a single igneous intrusion event occurs randomly over the duration of the simulation. The entire simplified model presented above is utilized with the following exceptions:

- WP and DS degradation due to general corrosion, SCC, and seismic induced mechanical damage is not considered.

- All WPs and DSs are assumed to fail completely when the intrusive event occurs.

- Collapsed drift seepage conditions are assumed to occur when the intrusive event occurs.

The simplified model then calculates a dose conditional on the occurrence of an igneous intrusion scenario. The probability-weighted dose is then calculated by multiplying the resultant conditional dose by the total probability of a single event occurring over the duration of the simulation. The mean frequency is 1.7×10^{-8} yr^{-1} (DTN: LA0307BY831811.001_R0 [DIRS 164713]), and in over 1,000,000 years the expected probability of a single event occurring is 0.017. The probability of two events is approximately 10^{-4} over 1,000,000 years.

L3. SIMULATIONS AND RESULTS

L3.1. SIMULATION METHODOLOGY AND APPROACH

The Simplified TSPA presented above was developed as a stand-alone computer program written in FORTRAN 90 and compiled/linked using Compaq Visual FORTRAN Professional Edition

Version 6.6.0 as unqualified software for execution on a personal computer using a Microsoft Windows operating system. The source code, input files, and output files for each modeling case are in corroborative DTN: MO0708SIMPLIFI.000 [DIRS 182980].

The Simplified TSPA was used to simulate four modeling cases that were analyzed using the TSPA-LA Model. These are:

- **Waste Package Early Failure Modeling Case**—This case evaluated repository performance considering only those WPs that experience early failure. In this case, no failure of the WPs is considered to occur due to general corrosion, SCC, or seismic mechanical damage. The number of early failures is determined using the approach described in Section L.2.8.2.

- **Nominal Modeling Case**—This case considered degradation of the WPs and DSs from corrosion processes only. Early WP failure was not considered in this case. Mechanical damage of the DS and WP was not considered in this case. Seismic induced rockfall and its subsequent effects on seepage were also not considered.

- **Seismic Ground Motion Modeling Case**—This modeling case considered degradation of the WPs and DSs from corrosion processes. The effects of ground motion were also considered, including mechanical damage to the WPs and DSs, and induced rockfall. Aleatory and epistemic uncertainties were both sampled randomly in each realization. Seismic events of varying magnitude were assumed to occur randomly following a Poisson process (Section L.2.1). The subsequent effects on rockfall, DS damage, and WP damage were then calculated.

- **Igneous Intrusion Modeling Case**—This case considered the degradation of the engineered barriers as a result of an intruding magma dike. Degradation of the WPs and DSs due to corrosion processes, seismic mechanical damage, and early WP failure were not considered. Aleatory and epistemic uncertainties were both randomly sampled in each realization. As discussed in Section L.2.18, a single igneous intrusion was assumed to occur randomly over the simulation period resulting in the failure of all DSs and WPs.

L3.2. SIMPLIFIED TSPA RESULTS

Further descriptions of the modeling cases simulated with this simplified model and the results can be found in Section 7.7.2.

Table L-1. Bounded Hazard Curve for Horizontal Peak Ground Velocity at the Emplacement Drifts

λ (1/yr)	PGV (m/s)
4.29 × 10-4	0.219
1.000 × 10-4	0.4019
3.826 × 10-5	0.6
1.919 × 10-5	0.8
9.955 × 10-6	1.05
6.682 × 10-6	1.2
3.812 × 10-6	1.4
2.136 × 10-6	1.6
1.288 × 10-6	1.8
8.755 × 10-7	2.0
6.399 × 10-7	2.2
4.518 × 10-7	2.44
3.504 × 10-7	2.6
2.507 × 10-7	2.8
1.731 × 10-7	3.0
1.137 × 10-7	3.2
7.168 × 10-8	3.4
4.362 × 10-8	3.6
2.508 × 10-8	3.8
1.319 × 10-8	4.0
5.967 × 10-9	4.20

Source: DTN: MO0501BPVELEMP.001_R0 [DIRS 172682].

Table L-2. Average Percolation Rate over the Repository Area

Infiltration Uncertainty Scenario (Percentile)	Climate State				Weighting Factor[b]
	Present-Day[a]	Monsoon[a]	Glacial Transition[a]	Post-10,000 Year[a]	
10th	2.73	6.14	8.66	15.82	0.6191
30th	7.34	12.01	18.07	24.79	0.1568
50th	11.16	13.81	22.12	31.49	0.1645
90th	25.10	68.78	42.34	45.87	0.0596

Sources: [a] DTN: SN0703PAEBSPCE.006_R2 [DIRS 181571]
[b] DTN: LB0701PAWFINFM.001_R0 [DIRS 179283].

Table L-3. Spatial Variability and Uncertainty Distributions for 1/α for Methods A, B, C, and D

***1*/α (Lithophysal Units)**		***1*/α (Nonlithophysal Units)**	
Spatial Variability Distribution	**Uncertainty Distribution**	**Spatial Variability Distribution**	**Uncertainty Distribution**
Uniform Distribution with Mean 591 Pa Lower Bound is 402 Pa Upper Bound is 780 Pa	Triangular Distribution with Mean 0 Lower Bound is - 105 Pa Upper Bound is + 105 Pa	Uniform Distribution with Mean 591 Pa Lower Bound is 402 Pa Upper Bound is 780 Pa	Triangular Distribution with Mean 0 Lower Bound is - 105 Pa Upper Bound is + 105 Pa

Source: DTN: LB0407AMRU0120.001_R0 [DIRS 173280].

Table L-4. Spatial Variability and Uncertainty Distributions Fracture Permeability (log (k [m2]))

Fracture Log (*k* [m^2]) (Lithophysal Units)		**Fracture Log (*k* [m^2]) (Nonlithophysal Units)**	
Spatial Variability Distribution	**Uncertainty Distribution**	**Spatial Variability Distribution**	**Uncertainty Distribution**
Log Normal Distribution with Mean - 11.5	Triangular Distribution with Mean 0	Log Normal Distribution with Mean - 12.2	Triangular Distribution with Mean 0
Standard Deviation 0.47	Lower Bound is - 0.92	Standard Deviation 0.34	Lower Bound is - 0.68
	Upper Bound is + 0.92		Upper Bound is + 0.68
Source: DTN: LB0407AMRU0120.001_R0 [DIRS 173280].			

Average Fracture Log (k [m^2]) (Lithophysal Units)	
Spatial Variability Distribution	**Uncertainty Distribution**
Log Normal Distribution with Mean - 11.6	Triangular Distribution with Mean 0
Standard Deviation 0.45	Lower/Upper Bounds are - 0.88/0.88

Table L-5. Flow Focusing Factor

Flow Focusing Factor	Cumulative Probability (%)
0.116	0
0.116	0.06
0.25	12.09
0.50	31.56
0.75	47.55
1.00	60.49
1.25	70.79
1.50	78.85
1.75	85.00
2.00	89.59
2.25	92.90
2.50	95.20
2.75	96.72
3.00	97.68
3.25	98.24
3.50	98.56
3.75	98.76
4.00	98.92
4.25	99.10
4.50	99.34
5.016	100.00

$y = -0.3137 x^4 + 5.4998 x^3 - 35.66 x^2 + 102.3 x - 11.434$

y = flow focusing factor

x = cumulative probability

valid for $0.116 < x < 0.5016$ and $0 \leq y \leq 1$

Source: SNL 2007 [DIRS 181244], Section 6.7.1.1.

Table L-6. Drip Shield General Corrosion Rate Ratio for Titanium Grade 29 Frame Material

Discrete Probability	Cumulative Probability	Ti-29/Ti-7 General Corrosion Rate Ratio
0.50000	0.50000	1.0000
0.11111	0.61111	1.1131
0.05556	0.66667	1.2522
0.02778	0.69445	1.3914
0.05556	0.75000	1.6697
0.11111	0.86111	2.0871
0.08333	0.94445	3.3393
0.02778	0.97222	4.1741
0.02778	1.00000	6.6786

Source: DTN: SN0704PADSGCMT.002_R1 [DIRS 182188].

Table L-7. Probability of Failure for the Drip Shield Plates

	Thickness of the Drip Shield Plate (mm)				
	0	2	5	10	15
PGV (m/s)	**Probability of Failure for 0% Rockfall Load (FDj = 0.0)**				
All Values	1	0	0	0	0
PGV (m/s)	**Probability of Failure for 10% Rockfall Load (FDj = 0.10)**				
0.2	1	0	0	0	0
0.4	1	0	0	0	0
1.05	1	0	0	0	0
2.44	1	0.006	0	0	0
4.07	1	0.036	0	0	0
PGV (m/s)	**Probability of Failure for 50% Rockfall Load (FDj = 0.50)**				
0.2	1	0	0	0	0
0.4	1	0.005	0	0	0
1.05	1	0.083	0.002	0	0
2.44	1	0.377	0.047	0.004	0
4.07	1	0.637	0.182	0.028	0.007
PGV (m/s)	**Probability of Failure for 100% Rockfall Load (FDj = 1.0)**				
0.2	1	0.027	0	0	0
0.4	1	0.093	0	0	0
1.05	1	0.390	0.030	0.001	0
2.44	1	0.765	0.268	0.047	0.013
4.07	1	0.912	0.557	0.186	0.073

Source: DTN: MO0703PASDSTAT.001_R3 [DIRS 183148].

NOTES: 1. Probabilities below 0.001 have been rounded down to 0.

2. Linear interpolate for given values of PGV, rock fall load, and drip shield thickness.

Table L-8. Probability of Failure for the Drip Shield Framework

	Reduction in Thickness of Framework Components (mm)				
	15	13	10	5	0
PGV (m/s)	**Probability of Failure for 0% Rockfall Load (FDj = 0.0)**				
All Values	1	0	0	0	0
PGV (m/s)	**Probability of Failure for 10% Rockfall Load (FDj = 0.10)**				
0.2	1	0	0	0	0
0.4	1	0	0	0	0
1.05	1	0.007	0	0	0
2.44	1	0.107	0.001	0	0
4.07	1	0.311	0.011	0	0
PGV (m/s)	**Probability of Failure for 50% Rockfall Load (FDj = 0.50)**				
0.2	1	0.048	0	0	0
0.4	1	0.192	0	0	0
1.05	1	0.635	0.025	0	0
2.44	1	0.929	0.230	0.029	0.006
4.07	1	0.985	0.502	0.127	0.039
PGV (m/s)	**Probability of Failure for 100% Rockfall Load (FDj = 1.0)**				
0.2	1	0.716	0.001	0	0
0.4	1	0.867	0.016	0	0
1.05	1	0.981	0.210	0.018	0.003
2.44	1	0.999	0.649	0.191	0.063
4.07	1	1.000	0.867	0.449	0.219

Source: DTN: MO0703PASDSTAT.001_R3 [DIRS 183148].

NOTES: 1. Probabilities below 0.001 have been rounded down to 0.

2. Linear interpolate for given values of PGV, rock fall load, and drip shield thickness.

Table L-9. Weibull Parameters for Alloy 22 Waste Package Outer Barrier General Corrosion

Probability	Weibull Scale Parameter, s (nm/yr)	Weibull Shape Parameter, b (unitless)
0.05	6.628	1.38
0.90	8.134	1.476
0.05	9.774	1.578

Source: DTN: MO0703PAGENCOR.001_R4 [DIRS 182029]

Table L-10. Time that Relative Humidity Exceeds 75 percent Threshold

Host Rock Thermal Conductivity	CSNF Waste Packages	CDSP Waste Packages
Low	950 years	700 years
Medium	850 years	500 years
High	600 years	400 years

Source: Determined from average bin WP relative humidity histories in DTN: MO0506MWDPPMSV.000_R0 [DIRS 174806].

Table L-11. Stress and Stress Intensity Factor Coefficients

Coefficient	Hoop Stress Outer Closure Lid Laser Peened[a]	K_I Outer Closure Lid Laser Peened[b]
A0	-519.127	-8.9124
A1	231.675	-9.4255
A2	-17.377	2.9749
A3	0.388	-0.1925
A4		0.0041

Source: [a] DTN: MO0702PASTRESS.002_R2 [DIRS 180514]
[b] Fitted from data in DTN: MO0702PASTRESS.002_R2 [DIRS 180514].

Table L-12. Average Depth Where SCC Cracks Can Initiate and Propagate

			Yield Stress Uncertainty (Z)												
			-15.0 %	**-12.5 %**	**-10.0 %**	**-7.5 %**	**-5.0 %**	**-2.5 %**	**0.0 %**	**2.5 %**	**5.0 %**	**7.5 %**	**10.0 %**	**12.5 %**	**15.0 %**
Repassivation Slope, n	-2 Standard Deviation	0.935	8.59	8.26	7.90	7.41	7.05	6.76	**6.52**	6.31	6.13	5.97	5.83	5.72	5.65
	5th percentile	0.976	8.59	8.26	7.90	7.41	7.05	6.76	**6.52**	6.31	6.13	5.97	5.84	5.74	5.68
	10th percentile	1.018	8.59	8.26	7.90	7.41	7.05	6.76	**6.52**	6.31	6.13	5.97	5.86	5.78	5.73
	15th percentile	1.046	8.59	8.26	7.90	7.41	7.05	6.76	**6.52**	6.31	6.13	5.98	5.88	5.81	5.78
	-1 Standard Deviation	1.050	8.59	8.26	7.90	7.41	7.05	6.76	**6.52**	6.31	6.13	5.98	5.88	5.81	5.78
	20th percentile	1.068	8.59	8.26	7.90	7.41	7.05	6.76	**6.52**	6.31	6.13	5.99	8.90	5.84	5.82
	30th percentile	1.105	8.59	8.26	7.90	7.41	7.05	6.76	**6.52**	6.31	6.14	6.03	5.95	5.92	5.90
	40th percentile	1.136	8.59	8.26	7.90	7.41	7.05	6.76	**6.52**	6.31	6.17	6.07	6.02	6.00	5.98
	Mean	1.165	**8.59**	**8.26**	**7.90**	**7.41**	**7.05**	**6.76**	**6.52**	**6.33**	**6.21**	**6.13**	**6.10**	**6.08**	**6.06**
	60th percentile	1.194	8.59	8.26	7.90	7.41	7.05	6.76	**6.52**	6.36	6.26	6.21	6.19	6.17	6.14
	70th percentile	1.225	8.59	8.26	7.90	7.41	7.05	6.76	**6.55**	6.42	6.35	6.32	6.29	6.26	6.24
	80th percentile	1.262	8.59	8.26	7.90	7.41	7.05	6.78	**6.62**	6.52	6.49	6.45	6.42	6.39	6.36
	1 Standard Deviation	1.280	8.59	8.26	7.90	7.41	7.05	6.81	**6.66**	6.80	6.53	6.53	6.49	6.46	6.43
	85th percentile	1.284	8.59	8.26	7.90	7.41	7.05	6.82	**6.67**	6.61	6.57	6.54	6.50	6.47	6.44
	90th percentile	1.312	8.59	8.26	7.90	7.41	7.08	6.88	**6.78**	6.73	6.69	6.65	6.61	6.52	6.55
	95th percentile	1.354	8.59	8.26	7.90	7.43	7.17	7.04	**6.98**	6.93	6.88	6.83	6.79	6.75	6.71
	2 Standard Deviation	1.395	8.59	8.26	7.92	7.53	7.32	7.25	**7.19**	7.13	7.08	7.03	6.98	7.02	6.89

Table L-13. Probability of Nonzero Damage for the Waste Package Surrounded by Rubble

	Residual Stress Threshold (% of Yield Strength)		
PGV Level (m/s)	**90%**	**100%**	**105%**
23-mm-Thick OCB with Degraded Internals			
0.40	0	0	0
1.05	0	0	0
2.44	0	0	0
4.07	0.294	0.118	0.059
17-mm-Thick OCB with Degraded Internals			
0.40	0	0	0
1.05	0	0	0
2.44	0.118	0	0
4.07	0.412	0.176	0.118

Source: DTN: MO0703PASDSTAT.001_R3 [DIRS 183148].

NOTES: 1. Linear interpolation for PGV and residual stress threshold.
2. If the thickness of the Alloy 22 outer barrier ≥ 23 mm, use the 23 mm thickness probabilities.
3. If the thickness is < 23 mm, calculate the probability using (interpolate for thickness between 17 mm and 23 mm, extrapolate for thickness less than 17 mm): $PD_{17\text{-}mm} + (PD_{23\text{-}mm} - PD_{17\text{-}mm})(t - 17\text{-mm})/(6\text{-mm})$.

Table L-14. Conditional Damaged Areas on the Waste Package Surrounded by Rubble

Waste Package Outer Barrier Thickness (mm)	State of Internals	Damage Area (m^2)
23	Degraded	$(0.0153492)(RST_i)^2 - 3.1814*RST_i + 165.834$
17	Degraded	$(0.0083948)(RST_i)^2 - 1.7755*RST_i + 94.0116$

Source: DTN: MO0703PASDSTAT.001_R3 [DIRS 183148].

NOTES: 1. Linear interpolation for PGV and residual stress threshold.
2. If the thickness of the Alloy 22 outer barrier ≥ 23 mm, use the 23 mm thickness probabilities.
3. If the thickness is < 23 mm, calculate the damage area using (interpolate for thickness between 17 mm and 23 mm, extrapolate for thickness less than 17 mm):

$DA_{17\text{-}mm} + (DA_{23\text{-}mm} - DA_{17\text{-}mm})(t - 17\text{-mm})/(6\text{-mm})$.

Table L-15. Probability of TAD-Bearing and CDSP Waste Package Rupture (17-mm-Thick Waste Package Outer Barrier, Degraded Internals)

PGV Level (m/s)	Conditional Probability of Exceedance[2]	Average Number of Events Expected over 1,000,000 Years having Larger PGV[3]	TAD-Bearing Waste Package[1]		CDSP Waste Package[1]	
			Probability of Incipient Rupture	Probability of Rupture	Probability of Incipient Rupture	Probability of Rupture
0.40	3.77×10^{-1}	~100	0	0	0	0
1.05	3.71×10^{-2}	~10	0.007	0	0	0
2.44	1.68×10^{-3}	~0.45	0.040	0	0.030	0
4.07	4.90×10^{-5}	~0.013	0.127	0.188	0.124	0.120

NOTES: 1. TAD-bearing WP information is derived from DTN: MO0703PASDSTAT.001_R3 [DIRS 183148].

2. Exceedance frequency for a given PGV from Table L-1 (λ) divided by the mean exceedance frequency (2.6909×10^{-4} yr^{-1}).

3. Conditional probability of exceedance x mean exceedance frequency (2.6909×10^{-4} yr^{-1}) x 1,000,000 years.

Table L-16. Probability of Nonzero Damage for the TAD-bearing Waste Package, Free Movement Underneath the Drip Shield

	Residual Stress Threshold (%)		
	90	**100**	**105**
***PGV* (m/s)**	**Probability of Nonzero Damage for 23-mm-Thick OCB with Intact Internals**		
0.2	0	0	0
0.4	0	0	0
1.05	0	0	0
2.44	0	0	0
4.07	0.118	0	0
***PGV* (m/s)**	**Probability of Nonzero Damage for 23-mm-Thick OCB with Degraded Internals**		
0.266	0	0	0
0.349	0.085	0	0
0.4	0.137	0.059	0
1.05	0.804	0.804	0.784
2.44	1	1	1
4.07	1	1	1
***PGV* (m/s)**	**Probability of Nonzero Damage for 17-mm-Thick OCB with Degraded Internals**		
0.280	0	0	0
0.351	0.081	0	0
0.4	0.137	0.059	0
1.05	0.882	0.843	0.804
2.44	1	1	1
4.07	1	1	1

Source: DTN: MO0703PASDSTAT.001_R3 [DIRS 183148].

NOTES: 1. Linear interpolation for PGV and residual stress threshold.

2. If the thickness of the Alloy 22 outer barrier ≥ 23 mm, use the 23 mm thickness probabilities.

3. If the thickness is < 23 mm, calculate the probability using (interpolate for thickness between 17 mm and 23 mm, extrapolate for thickness less than 17 mm): $PD_{17\text{-}mm} + (PD_{23\text{-}mm} - PD_{17\text{-}mm})$(t - 17-mm)/(6-mm).

Table L-17. Probability of Nonzero Damage for the CDSP Waste Package, Free Movement Underneath the Drip Shield

	Residual Stress Threshold (%)		
	90	100	105
***PGV* (m/s)**	**Probability of Nonzero Damage for 23-mm-Thick OCB with Intact Internals**		
0.364	0	0	0
0.4	0.029	0	0
1.05	0.559	0	0
2.44	0.941	0.147	0
4.07	1	0.412	0
***PGV* (m/s)**	**Probability of Nonzero Damage for 23-mm-Thick OCB with Degraded Internals**		
0.238	0	0	0
0.285	0	0	0
0.364	0.060	0.060	0
0.4	0.088	0.088	0.029
1.05	0.588	0.588	0.559
2.44	0.941	0.941	0.941
4.07	1	1	1
***PGV* (m/s)**	**Probability of Nonzero Damage for 17-mm-Thick OCB with Degraded Internals**		
0.219	0	0	0
0.338	0.097	0	0
0.4	0.147	0.059	0
1.05	0.676	0.676	0.382
2.44	0.941	0.941	0.882
4.07	1	1	1

Source: DTN: MO0703PASDSTAT.001_R3 [DIRS 183148].

NOTES: 1. Linear interpolation for PGV and residual stress threshold.

2. If the thickness of the Alloy 22 outer barrier ≥ 23 mm, use the 23 mm thickness probabilities.

3. If the thickness is < 23 mm, calculate the probability using (interpolate for thickness between 17 mm and 23 mm, extrapolate for thickness less than 17 mm): $PD_{17\text{-}mm} + (PD_{23\text{-}mm} - PD_{17\text{-}mm})(t - 17\text{-mm})/(6\text{-mm})$.

Table L-18. Conditional Damage Area on TAD-bearing and CDSP Waste Packages When Damaged Due to Free Motion Underneath the Drip Shield

	Waste Package Outer Barrier Thickness (mm)	State of Internals	Damage Area (m^2)
TAD-Bearing Waste Packages		Intact	0.00408
	23	Degraded	$(0.1096 - 0.00664*(RSTi - 100))PGV^2 + (0.1722 - 0.01701*(RSTi - 100))PGV + 0.0828 - 0.00661*(RSTi - 100)$
	17	Degraded	$(0.1394 - 0.00838*(RSTi - 100))PGV^2 + (0.1649 - 0.02224*(RSTi - 100))PGV + 0.0766 - 0.00628*(RSTi - 100)$
CDSP Waste Packages		Intact	If $(RST \leq 100)$ $- 0.0033*(RSTi - 100)PGV^2 - 0.00567*(RSTi - 100)PGV - 0.0004*(RSTi - 100))+0.0061$ Else $-0.0012(RST-105)$
	23	Degraded	$(0.0637 - 0.0016*(RSTi - 100))PGV^2 + (0.2274 - 0.0277*(RSTi - 100))PGV + (-0.0144 + 0.0029*(RSTi - 100))$
	17	Degraded	$(0.0670 - 0.0011*(RSTi - 100))PGV^2 + (0.1879 - 0.0376*(RSTi - 100))PGV + (-0.0187 + 0.0034*(RSTi - 100))$

Source: DTN: MO0703PASDSTAT.001_R3 [DIRS 183148].

NOTES: 1. Linear interpolation for PGV and residual stress threshold.

2. If the thickness of the Alloy 22 outer barrier ≥ 23 mm, use the 23 mm thickness probabilities.

3. If the thickness is < 23 mm, calculate the damage area using (interpolate for thickness between 17 mm and 23 mm, extrapolate for thickness less than 17 mm):

$DA_{17\text{-}mm} + (DA2_{3\text{-}mm} - DA_{17\text{-}mm})$(t - 17-mm)/(6-mm).

Table L-19. Initial Radionuclide Inventory and Treatment

Radio-nuclide	Specific Activity (Ci/g)	Initial Inventory[1] CSNF w/MOX Added (g/WP)	DSNF (g/WP)	HLW w/LABS Added (g/WP)	Molecular Mass (g/mol)	Decay Constant (yr^{-1})	Half Life (yr)[1]	Treatment in Simplified Analyses[2]
^{227}Ac	7.23E+01	2.47E-06	1.22E-03	1.91E-04	227	3.18E-02	2.18E+01	Inventory fully decays, secular equilibrium with ^{231}Pa at well
^{241}Am	3.43E+00	8.20E+03	2.18E+02	6.53E+01	241	1.60E-03	4.33E+02	Inventory fully decays to ^{237}Np
^{243}Am	2.00E-01	1.29E+03	6.73E+00	5.75E-01	243	9.40E-05	7.37E+03	Inventory fully decays to ^{239}Pu
^{14}C	4.47E+00	1.38E+00	1.81E+00	0.00E+00	14	1.21E-04	5.72E+03	
^{36}Cl	3.30E-02	3.23E+00	4.23E+00	0.00E+00	36	2.30E-06	3.01E+05	
^{245}Cm	1.72E-01	1.89E+01	9.25E-02	5.43E-02	245	8.15E-05	8.50E+03	Inventory fully decays to ^{241}Pu
^{135}Cs	1.15E-03	4.43E+03	9.74E+01	1.27E+02	135	3.01E-07	2.30E+06	
^{137}Cs	8.68E+01	6.06E+03	9.72E+01	3.02E+02	137	2.31E-02	3.01E+01	Inventory fully decays
^{129}I	1.77E-04	1.76E+03	3.56E+01	7.27E+01	129	4.41E-08	1.57E+07	
^{237}Np	7.05E-04	4.59E+03	8.14E+01	1.00E+02	237	3.24E-07	2.14E+06	Parent of ^{233}U
^{231}Pa	4.72E-02	9.17E-03	2.14E+00	1.53E+00	231	2.11E-05	3.28E+04	Secular Equilibrium with ^{227}Ac at well
^{210}Pb	7.63E+01	1.13E-12	3.35E-07	3.40E-10	210	3.11E-02	2.23E+01	Inventory fully decays, secular equilibrium with ^{230}Th at well
^{238}Pu	1.71E+01	1.54E+03	1.25E+01	4.25E+01	238	7.90E-03	8.77E+01	Inventory fully decays to ^{234}U
^{239}Pu	6.21E-02	4.42E+04	2.21E+03	4.04E+03	239	2.88E-05	2.41E+04	Parent of ^{235}U
^{240}Pu	2.27E-01	2.13E+04	4.35E+02	3.56E+02	240	1.06E-04	6.56E+03	Parent of ^{236}U
^{241}Pu	1.03E+02	3.08E+03	2.92E+01	1.38E+01	241	4.81E-02	1.44E+01	Inventory fully decays to ^{237}Np
^{242}Pu	3.94E-03	5.45E+03	3.02E+01	9.98E+00	242	1.85E-06	3.75E+05	Parent of ^{238}U
^{226}Ra	9.89E-01	8.79E-11	4.57E-05	2.42E-05	226	4.33E-04	1.60E+03	Inventory fully decays, secular equilibrium with ^{230}Th at well
^{228}Ra	2.72E+02	5.89E-17	1.51E-05	6.00E-06	228	1.20E-01	5.76E+00	Inventory fully decays
^{79}Se	1.56E-02	4.24E+01	6.82E+00	7.01E+00	79	2.39E-06	2.90E+05	
^{126}Sn	1.23E-02	4.75E+02	9.40E+00	1.70E+01	126	3.01E-06	2.30E+05	
^{90}Sr	1.38E+02	2.53E+03	5.22E+01	1.74E+02	90	2.41E-02	2.88E+01	Inventory fully decays
^{99}Tc	1.70E-02	7.65E+03	1.58E+02	1.01E+03	99	3.25E-06	2.13E+05	
^{229}Th	2.14E-01	2.68E-09	3.24E-01	3.30E-03	229	9.50E-05	7.30E+03	
^{230}Th	2.06E-02	1.52E-01	1.18E-01	8.12E-04	230	9.19E-06	7.54E+04	Secular equilibrium with ^{226}Ra at well

Table L-19. Initial Radionuclide Inventory and Treatment (Continued)

Radio-nuclide	Specific Activity (Ci/g)	Initial Inventory[1] CSNF w/MOX Added (g/WP)	Initial Inventory[1] DSNF (g/WP)	Initial Inventory[1] HLW w/LABS Added (g/WP)	Molecular Mass (g/mol)	Decay Constant (yr^{-1})	Half Life (yr)[1]	Treatment in Simplified Analyses[2]
^{232}Th	1.10E-07	1.15E-06	2.17E+04	2.98E+04	232	4.95E-11	1.40E+10	
^{232}U	2.21E+01	1.02E-02	1.28E+00	4.08E-04	232	9.93E-03	6.98E+01	Inventory fully decays
^{233}U	9.63E-03	5.76E-02	5.38E+02	1.94E+01	233	4.35E-06	1.59E+05	Parent of ^{229}Th
^{234}U	6.21E-03	1.75E+03	4.73E+02	2.75E+01	234	2.82E-06	2.46E+05	Parent of ^{230}Th
^{235}U	2.16E-06	6.27E+04	2.51E+04	1.67E+03	235	9.85E-10	7.04E+08	Parent of ^{231}Pa
^{236}U	6.47E-05	3.85E+04	1.25E+03	5.99E+01	236	2.96E-08	2.34E+07	Parent of ^{232}Th
^{238}U	3.36E-07	7.90E+06	6.84E+05	2.38E+05	238	1.55E-10	4.47E+09	Parent of ^{234}U

Sources: 1. DTN: MO0702PASTREAM.001_R0 [DIRS 179925].
2. Decay series from *Initial Radionuclide Inventories* (SNL 2007 [DIRS 180472], Table 4-14).

Table L-20. Uncertainty Multipliers for Grams per Waste Package for Each Waste Type

	CSNF	Defense Spent Nuclear Fuel	HLW
Isotope	All except ^{238}U	All except ^{238}U	All
Distribution	Uniform	Triangular	Triangular
Minimum	0.85	0.45	0.70
Most Likely	N/A	0.62	1
Maximum	1.40	2.90	1.5

Source: DTN: SN0310T0505503.004_R0 [DIRS 168761].

Table L-21. Gap and Grain Boundary Fractions for CSNF Waste Forms

	Cs^{135}	I^{129}	Tc^{99}
Average Release Fraction (%)	3.63	11.24	0.1
Range (%)	0.39 – 11.06	2.04 – 26.75	0.01 – 0.26

Source: DTN: MO0404ANLSF001.001_R0 [DIRS 169007].

Table L-22. Coefficients in CSNF Degradation Rate Model

Coefficient	Acidic Conditions	Alkaline Conditions
Log(A)	Triangular Distribution (minimum = -7.3, expected value = -6.7, maximum = -5.4)	
a_0	4.705	6.6
a_1	-1093.826	-1093.823
a_2	-0.102	0
a_3	-0.388	-0.338
a_4	0	-0.34

Source: DTN: MO0404ANLSF001.001_R0 [DIRS 169007].

NOTE: The values for the regression coefficient are expected values.

Table L-23. CSNF Waste Form Degradation Covariance Matrix for Alkaline Conditions

	a_0	a_1	a_2	a_3
a_0	0.60095	0	0	0
a_1	-181.156	45.68717	0	0
a_2	-0.00834	-0.03852	0.02586	0
a_3	-0.00831	-0.0226	-0.03754	0.02659

Source: DTN: MO0404ANLSF001.001_R0 [DIRS 169007].

Table L-24. CSNF Waste Form Degradation Covariance Matrix for Acidic Conditions

	a_0	a_4
a_0	0.4475	0
a_4	-0.10475	0.03495

Source: DTN: MO0404ANLSF001.001_R0 [DIRS 169007].

Table L-25. DHLW Glass Degradation Parameters

Parameter	Alkaline Conditions	Acidic Conditions
k_g, forward glass dissolution rate ($g/m^2/day$)	Triangular Distribution	Triangular Distribution
	Minimum = 2.82×10^{1}	Minimum = 8.41×10^{3}
	Most Probable = 2.82×10^{1}	Most Probable = 8.41×10^{3}
	Maximum = 3.47×10^{4}	Maximum = 1.15×10^{7}
η, order of the reaction with respect to H+	0.49	-0.49
E_a, activation energy for rate limiting step (kJ/mol)	69	31

Source: DTN: MO0502ANLGAMR1.016_R0 [DIRS 172830].

Table L-26. Dissolved Concentration Limits (without Uncertainty)

pH	Base-10 Logarithm of the Dissolved Concentration Limit (mg/L)								
	NpO_2	Np_2O_5	Pa	Pu	Th	Sn	U (Schoepite)	U (Na-boltwoodite and $Na_4UO_2(CO_3)_3$	U[1]
4.00	2.05E+00	3.29E+00	3.29E+00	7.12E-01	1.14E+00	-2.39E+00	2.86E+00		2.86E+00
4.25	1.80E+00	3.03E+00	3.03E+00	4.12E-01	9.41E-01	-2.39E+00	2.33E+00		2.33E+00
4.50	1.55E+00	2.77E+00	2.77E+00	1.35E-01	7.42E-01	-2.39E+00	1.91E+00		1.91E+00
4.75	1.29E+00	2.52E+00	2.52E+00	-1.22E-01	3.82E-01	-2.39E+00	1.59E+00		1.59E+00
5.00	1.04E+00	2.26E+00	2.26E+00	-3.60E-01	-2.94E-01	-2.38E+00	1.31E+00		1.31E+00
5.25	7.94E-01	2.01E+00	2.01E+00	-5.75E-01	-1.20E+00	-2.38E+00	1.02E+00		1.02E+00
5.50	5.44E-01	1.76E+00	1.76E+00	-7.62E-01	-1.99E+00	-2.38E+00	7.55E-01		7.55E-01
5.75	2.94E-01	1.51E+00	1.51E+00	-9.17E-01	-2.13E+00	-2.38E+00	6.11E-01		6.11E-01
6.00	4.36E-02	1.26E+00	1.26E+00	-1.03E+00	-1.94E+00	-2.37E+00	6.30E-01		6.30E-01
6.25	-2.06E-01	1.01E+00	1.01E+00	-1.12E+00	-1.70E+00	-2.37E+00	7.66E-01		7.66E-01
6.50	-4.54E-01	7.62E-01	7.62E-01	-1.17E+00	-1.46E+00	-2.35E+00	9.70E-01		9.70E-01
6.75	-6.98E-01	5.17E-01	5.17E-01	-1.21E+00	-1.22E+00	-2.33E+00	1.22E+00	2.00E+00	1.61E+00
7.00	-9.24E-01	2.84E-01	2.84E-01	-1.23E+00	-9.69E-01	-2.29E+00	1.51E+00	1.82E+00	1.67E+00
7.25	-1.09E+00	8.83E-02	8.30E-02	-1.24E+00	-7.16E-01	-2.22E+00	1.89E+00	1.51E+00	1.70E+00
7.50	-1.09E+00	-1.94E-02	-1.94E-02	-1.24E+00	-4.60E-01	-2.12E+00	2.54E+00	1.55E+00	2.05E+00
7.75	-8.33E-01	8.77E-03	8.77E-03	-1.23E+00	-2.02E-01	-1.99E+00		1.98E+00	1.98E+00
8.00	-3.51E-01	1.71E-01	1.71E-01	-1.17E+00	5.91E-02	-1.82E+00		2.76E+00	2.76E+00
8.25	3.96E-01	4.49E-01	4.49E-01	-8.71E-01	3.23E-01	-1.62E+00		4.78E+00	4.78E+00
8.50	4.41E-01	1.00E+00	1.00E+00	1.11E+00	5.96E-01	-1.39E+00		4.78E+00	4.78E+00

Source: DTN: MO0702PADISCON.001_R0 [DIRS 179358]: column NpO_2 (Table 2); column Np_2O_5 (Table 3); column Pa (Table 9); column Pu (Table 1); column Th (Table 7); column Sn (Table 16); column U (Table 5); column U (Na-boltwoodite and $Na_4UO_2(CO_3)_3$ (Table 6).

NOTE: Dissolved concentration limit for U is controlled by schoepite for pH<=6.75 and by Na-boltwoodite, and $Na_4UO_2(CO_3)_3$ for pH>=7.75. In between, the average between the two is assumed to be the dissolved concentration limit.

Table L-27. Dissolved Concentration Limit Uncertainty Terms

Element	ε[1]	
	μ	σ
NpO_2	0	0.6
Np_2O_5	0	0.8
Pa	-4.42[1]	-0.05[1]
Pu	0	1
Th	0	0.7
U	0	0.5
Sn	0	0.45

Source: DTN: MO0702PADISCON.001_R0 [DIRS 179358].

NOTE: [1]Uniform Distribution (min., max.).

Table L-28. Mixing Cell Steel Parameters Used in Calculation of Corrosion Product Mass and Volume of Water

		Waste Form Cell				Corrosion Product Cell			
Waste Form		m_s Mass of Steel (kg)	f_{CS} Fraction of Carbon Steel	$t_{max,CS}$ Maximum Thickness of Carbon Steel (mm)	$t_{max,SS}$ Maximum Thickness of Stainless Steel (mm)	m_s Mass of Steel (kg)	f_{CS} Fraction of Carbon Steel	$t_{max,CS}$ Maximum Thickness of Carbon Steel (mm)	$t_{max,SS}$ Maximum Thickness of Stainless Steel (mm)
CSNF		9,980	0	0	11.11	24,600	0	0	11.11
CDSP	DHLW	3,800	0	0	10.5	18,900	0.31	31.75	50.8
	DSNF	1,270	0.24	6.35	9.525				

Source: DTN: SN0703PAEBSRTA.001_R3 [DIRS 183217].

Table L-29. Metal Mass Fractions and Atomic Weights Used in Calculation of Corrosion Product Mass and Volume of Water

Metal	$\omega_{CS,m}$ Mass Fraction of Metal in Carbon Steel	$\omega_{SS,m}$ Mass Fraction of Metal in Stainless Steel	M_m Atomic Weight of Metal (kg/mol)
Fe	0.98	0.65	0.055847
Ni	0	0.12	0.05869
Cr	0	0.17	0.051996

Source: DTN: SN0703PAEBSRTA.001_R3 [DIRS 183217].

Table L-30. Properties of Corrosion Product Used in Calculation of Corrosion Product Mass and Volume of Water

Corrosion Product	$M_{CP,m}$ Molecular Weight of Corrosion Product (kg/mol)	$\alpha_{CP,m}$ Stoichiometric Coefficient	$\rho_{CP,m}$ Density of Corrosion Product (kg/m^3)
Goethite	0.088852	1 mol goethite/mol Fe	4,260
HFO	0.088852	1 mol HFO/mol Fe	3,960
NiO	0.074692	1 mol NiO/mol Ni	5,220
Cr_2O_3	0.151990	2 mol Cr_2O_3/mol Cr	6,720

Source: DTN: SN0703PAEBSRTA.001_R3 [DIRS 183217].

Table L-31. Free Water Diffusion Coefficients

Species	Free Water Diffusion Coefficient (m^2/s)
C	1.18×10^{-9}
Cs	2.06×10^{-9}
I	2.05×10^{-9}
Np	6.18×10^{-10}
Pa	6.04×10^{-10}
Pu	1.30×10^{-9}
Tc	1.95×10^{-9}
Th	5.97×10^{-10}
U	6.64×10^{-10}
Se	1.04×10^{-9}
Cl	2.03×10^{-9}
Sn	1.55×10^{-9}

Source: DTN: SN0703PAEBSRTA.001_R3 [DIRS 183217].

Table L-32. Calculation of Average Unsaturated Zone Layer Thickness

Unit	Average Thickness (m)	Simplified Model Layer	
		Layer Configuration	Thickness (m)
tsw31	2.0		
tsw32	42.5		
tsw33	78.6		
tsw34	34.7		
tsw35	102.4	TSW Layer = 1/2 tsw35+ tsw36+tsw37+ tsw38+tsw39	120
tsw36	31.3		
tsw37	15.7		
tsw38	15.5		
tsw39	6.7		
ch1	15.7	CH Layer = ch1+ch2+ch3+ ch4+ch5+ch6	111
ch2	19.3		
ch3	19.3		
ch4	19.3		
ch5	19.3		
ch6	18.0		
pp4	9.7	PP Layer = pp1+pp2+pp3+ pp4	81
pp3	19.1		
pp2	17.4		
pp1	34.5		
Total Depth (meters)			312

Source: BSC 2004 [DIRS 169855], Attachment II, Table II-1.

Table L-33. Layer Contact and Thickness from the GFM2000 Contact Information

Unit	USW H-4		USW H-5		USW G-1		USW G-4		USW H-1	
	GFM2000 Contact (m)[a]	Thick-ness (m)	GFM2000 Contact (m)[a]	Thick-ness (m)	GFM2000 Contact (m)[a]	Thick-ness (m)	GFM2000 Contact (m)[a]	Thick-ness (m)	GFM2000 Contact (m)[a]	Thick-ness (m)
tsw31	1,172.261	2.0	1,307.783	2.0	1,244.388	2.0	1,197.259	2.0	1,202.741	2.0
tsw32	1,170.261	36.1	1,305.783	40.0	1,242.388	49.2	1,195.259	47.2	1,200.741	51.3
tsw33	1,134.161	61.0	1,265.736	87.7	1,193.215	84.0	1,148.069	83.4	1,149.401	86.3
tsw34	1,073.201	38.7	1,178.021	30.5	1,109.192	31.0	1,064.668	30.5	1,063.142	33.2
tsw35	1,034.491	86.6	1,147.494	110.3	1,078.217	117.1	1,034.197	107.8	1,029.919	130.1
tsw36	947.928	40.2	1,037.192	26.9	961.1646	18.0	926.425	38.4	899.7696	17.5
tsw37	907.6944	20.1	1,010.321	13.4	943.1175	9.0	888.0687	19.2	882.2944	8.7
tsw38	887.576	7.3	996.8859	23.5	934.094	17.0	868.8906	8.8	873.5568	18.1
tsw39	880.2624	11.6	973.4256	4.0	917.0564	5.5	860.0588	2.5	855.4212	5.1
ch1	868.68	21.3	969.4739	10.1	911.5274	19.5	857.5441	17.0	850.331	5.7
ch2	847.344	19.4	959.3875	13.3	892.0233	23.5	840.5243	22.6	844.6008	22.6
ch3	827.913	19.4	946.072	13.3	868.4737	23.6	817.9547	22.6	821.9694	22.6
ch4	808.482	19.4	932.7565	13.3	844.8841	23.6	795.3852	22.6	799.338	22.6
ch5	789.051	19.4	919.441	13.3	821.3145	23.6	772.8157	22.6	776.7066	22.6
ch6	769.62	16.8	906.1255	19.8	797.7448	19.0	750.2462	17.4	754.072	18.0
pp4	752.865	10.7	886.3395	6.8	778.724	19.3	732.8007	2.2	736.092	5.5
pp3	742.188	11.7	879.5576	35.9	759.4007	5.2				
pp2			843.6558	13.7						
pp1			829.9347	54.3						
Water Table	730.5		775.6		754.2		730.6		730.6	

Table L-33. Layer Contact and Thickness from the GFM2000 Contact Information (Continued)

Unit	USW SD-9		USW SD-12		USW UZ-1/14		USW WT-2	
	GFM2000 Contact (m)[a]	Thick-ness (m)	GFM2000 Contact (m)[a]	Thick-ness (m)	GFM2000 Contact (m)[a]	Thick-ness (m)	GFM2000 Contact (m)[a]	Thick-ness (m)
tsw31	1,221.181	2.0	1,224.839	2.0	1,263.237	2.0	1,216.156	2.0
tsw32	1,219.181	53.3	1,222.839	32.1	1,261.237	43.7	1,214.156	29.4
tsw33	1,165.86	85.3	1,190.732	69.3	1,217.538	86.2	1,184.726	64.0
tsw34	1,080.516	35.3	1,121.421	37.5	1,131.36	34.4	1,120.757	41.3
tsw35	1,045.22	102.5	1,083.899	84.9	1,096.919	95.4	1,079.452	87.2
tsw36	942.7464	35.8	998.982	43.2	1,001.555	28.2	992.2496	33.7
tsw37	906.9832	17.9	955.7817	21.6	973.3775	14.1	958.5879	16.8
tsw38	889.1013	18.4	934.1815	9.1	959.2885	23.8	941.7571	13.5
tsw39	870.6917	2.2	925.068	9.0	935.5172	7.6	928.2658	12.4
ch1	868.4666	16.5	916.0764	22.6	927.9533	11.7	915.8546	17.0
ch2	851.9465	21.7	893.5212	14.3	916.2651	21.0	898.901	15.4
ch3	830.2676	21.7	879.1956	14.3	895.2167	21.0	883.5388	15.4
ch4	808.5887	21.7	864.87	14.3	874.1683	21.0	868.1765	15.4
ch5	786.9098	21.7	850.5444	14.3	853.1199	21.0	852.8143	15.4
ch6	765.2309	17.2	836.2188	14.9	832.0715	17.2	837.452	22.1
pp4	748.0706	14.6	821.3141	8.7	814.8519	19.8		0.0
pp3	733.4402	2.3	812.5968	33.5	795.0506	10.8	815.3688	34.1
pp2			779.0688	23.8	784.2032	5.2	781.2358	26.9
pp1			755.2944	25.3			754.3675	23.8
Water Table	731.1		730		779		730.6	

Source: BSC 2004 [DIRS 169855], Attachment II, Table II-1.

Table L-34. Layer Average Residual Saturation

Layer	Unit	Thickness (m)	Residual Saturation[1]	Average Residual Saturation[2]
TSW	tsw35	102.4	0.12	0.1
	tsw36	31.3	0.20	
	tsw37	15.7	0.20	
	tsw38	15.5	0.42	
	tsw39	6.7	0.36	
CH	Zeolitic		0.3	0.3
	Vitric		0.1	0.1
PP	pp4	9.7	0.29	0.1
	pp3	19.1	0.08	
	pp2	17.4	0.10	
	pp1	34.5	0.30	

Source: [1] Calibrated Unsaturated Zone Properties [DIRS 179545], Table 4-2.

[2] Average residual saturation calculated using Equation L-68 for TSW and PP layers.

Table L-35. Unsaturated Zone Layer Average Properties for Determination of Matrix Hydraulic Conductivity

10th Percentile Infiltration Scenario, Repository Underlain by Vitric Units tsw39 and Ch1-6											
Model Layer	Unit	Average Thick-ness (m)	Matrix Permeability (m^2)[a]	Van Genuchten m[a]	Layer Average Matrix Permeability (m^2)	Layer Average Van Genuchten m	Average Saturation[e]	Residual Saturation	Effective Saturation	Layer Average Matrix Relative Permeability (m^2)	Layer Average Matrix Hydraulic Conductivity (mm/yr)
TSW	tsw35	51.2	1.09E-17	0.216	5.09E-18	0.32	0.95	0.1	0.94	9.39E-19	3.27E-01
	tsw36	31.3	3.16E-18	0.442							
	tsw37	15.7	3.16E-18	0.442							
	tsw38	15.5	3.79E-18	0.286							
	tsw39	6.7	1.49E-13	0.293							
CH	ch1	15.7	2.21E-12	0.24	1.08E-12	0.17	0.7	0.1	0.67	2.13E-16	7.42E+01
	ch2	19.3	1.55E-12	0.158							
	ch3	19.3	1.55E-12	0.158							
	ch4	19.3	1.55E-12	0.158							
	ch5	19.3	1.55E-12	0.158							
	ch6	18.0	3.92E-13	0.147							
PP	pp4	9.7	3.01E-17	0.474	7.90E-17	0.34	0.8	0.1	0.78	2.62E-18	9.12E-01
	pp3	19.1	9.24E-14	0.407							
	pp2	17.4	1.68E-15	0.309							
	pp1	34.5	5.01E-17	0.272							

Table L-35. Unsaturated Zone Layer Average Properties for Determination of Matrix Hydraulic Conductivity (Continued)

30th Percentile Infiltration Scenario, Repository Underlain by Vitric Units tsw39 and Ch1-6											
Model Layer	**Unit**	**Average Thick-ness (m)**	**Matrix Permeability (m^2)[b]**	**Van Genuchten m[b]**	**Layer Average Matrix Permeability (m^2)**	**Layer Average Van Genuchten m**	**Average Saturation[e]**	**Residual Saturation**	**Effective Saturation**	**Layer Average Matrix Relative Permeability (m^2)**	**Layer Average Matrix Hydraulic Conductivity (mm/yr)**
TSW	tsw35	51.2	1.11E-17	0.216	5.81E-18	0.32	0.95	0.1	0.94	1.07E-18	3.73E-01
	tsw36	31.3	3.16E-18	0.442							
	tsw37	15.7	3.16E-18	0.442							
	tsw38	15.5	1.27E-17	0.286							
	tsw39	6.7	2.23E-13	0.293							
CH	ch1	15.7	2.59E-12	0.24	1.51E-12	0.17	0.7	0.1	0.67	2.98E-16	1.04E+02
	ch2	19.3	6.77E-11	0.158							
	ch3	19.3	6.77E-11	0.158							
	ch4	19.3	6.77E-11	0.158							
	ch5	19.3	6.77E-11	0.158							
	ch6	18.0	2.71E-13	0.147							
PP	pp4	9.7	3.51E-17	0.474	4.95E-17	0.34	0.8	0.1	0.78	1.65E-18	5.72E-01
	pp3	19.1	1.02E-13	0.407							
	pp2	17.4	1.69E-15	0.309							
	pp1	34.5	2.57E-17	0.272							

Table L-35. Unsaturated Zone Layer Average Properties for Determination of Matrix Hydraulic Conductivity (Continued)

50th Percentile Infiltration Scenario, Repository Underlain byVitric Units tsw39 and Ch1-6											
Model Layer	**Unit**	**Average Thick-ness (m)**	**Matrix Permeability (m^2)[c]**	**Van Genuchten m[c]**	**Layer Average Matrix Permeability (m^2)**	**Layer Average Van Genuchten m**	**Average Saturation[e]**	**Residual Saturation**	**Effective Saturation**	**Layer Average Matrix Relative Permeability (m^2)**	**Layer Average Matrix Hydraulic Conductivity (mm/yr)**
TSW	tsw35	51.2	1.94E-17	0.216	8.65E-18	0.32	0.95	0.1	0.94	1.60E-18	5.55E-01
	tsw36	31.3	4.45E-18	0.442							
	tsw37	15.7	4.45E-18	0.442							
	tsw38	15.5	2.16E-17	0.286							
	tsw39	6.7	2.24E-13	0.293							
CH	ch1	15.7	3.16E-12	0.24	2.47E-12	0.17	0.7	0.1	0.67	4.89E-16	1.70E+02
	ch2	19.3	1.58E-11	0.158							
	ch3	19.3	1.58E-11	0.158							
	ch4	19.3	1.58E-11	0.158							
	ch5	19.3	1.58E-11	0.158							
	ch6	18.0	5.14E-13	0.147							
PP	pp4	9.7	1.89E-17	0.474	4.31E-17	0.34	0.8	0.1	0.78	1.43E-18	4.98E-01
	pp3	19.1	1.79E-13	0.407							
	pp2	17.4	1.00E-15	0.309							
	pp1	34.5	2.57E-17	0.272							

Table L-35. Unsaturated Zone Layer Average Properties for Determination of Matrix Hydraulic Conductivity (Continued)

90th Percentile Infiltration Scenario, Repository Underlain by Vitric Units tsw39 and Ch1-6											
Model Layer	**Unit**	**Average Thick-ness (m)**	**Matrix Permeability (m^2)[d]**	**Van Genuchten m[d]**	**Layer Average Matrix Permeability (m^2)**	**Layer Average Van Genuchten m**	**Average Saturation[e]**	**Residual Saturation**	**Effective Saturation**	**Layer Average Matrix Relative Permeability (m^2)**	**Layer Average Matrix Hydraulic Conductivity (mm/yr)**
TSW	tsw35	51.2	7.54E-17	0.216	1.65E-17	0.32	0.95	0.1	0.94	3.05E-18	1.06E+00
	tsw36	31.3	7.50E-18	0.442							
	tsw37	15.7	7.50E-18	0.442							
	tsw38	15.5	4.40E-17	0.286							
	tsw39	6.7	2.24E-13	0.293							
CH	ch1	15.7	2.51E-12	0.240	1.80E-12	0.17	0.7	0.1	0.67	3.56E-16	1.24E+02
	ch2	19.3	3.16E-11	0.158							
	ch3	19.3	3.16E-11	0.158							
	ch4	19.3	3.16E-11	0.158							
	ch5	19.3	3.16E-11	0.158							
	ch6	18.0	3.40E-13	0.147							
PP	pp4	9.7	1.00E-17	0.474	4.78E-17	0.34	0.8	0.1	0.78	1.59E-18	5.52E-01
	pp3	19.1	1.71E-13	0.407							
	pp2	17.4	6.31E-16	0.309							
	pp1	34.5	5.01E-17	0.272							

Table L-35. Unsaturated Zone Layer Average Properties for Determination of Matrix Hydraulic Conductivity (Continued)

10th Percentile Infiltration Scenario, Repository Underlain by Zeolitic Units tsw39 and Ch1-6											
Model Layer	Unit	Average Thick-ness (m)	Matrix Permeability (m^2)[a]	Van Genuchten m[a]	Layer Average Matrix Permeability (m^2)	Layer Average Van Genuchten m	Average Saturation[e]	Residual Saturation	Effective Saturation	Layer Average Matrix Relative Permeability (m^2)	Layer Average Matrix Hydraulic Conductivity (mm/yr)
TSW	tsw35	51.2	1.09E-17	0.216	5.05E-18	0.30	0.95	0.1	0.94	8.48E-19	2.95E-01
	tsw36	31.3	3.16E-18	0.442							
	tsw37	15.7	3.16E-18	0.442							
	tsw38	15.5	3.79E-18	0.286							
	tsw39	6.7	3.50E-17	0.059							
CH	ch1	15.7	3.50E-17	0.349	2.98E-18	0.31	0.7	0.3	0.57	6.52E-21	2.27E-03
	ch2	19.3	5.20E-18	0.257							
	ch3	19.3	5.20E-18	0.257							
	ch4	19.3	5.20E-18	0.257							
	ch5	19.3	5.20E-18	0.257							
	ch6	18.0	8.20E-19	0.499							
PP	pp4	9.7	3.01E-17	0.474	7.90E-17	0.34	0.8	0.1	0.78	2.62E-18	9.12E-01
	pp3	19.1	9.24E-14	0.407							
	pp2	17.4	1.68E-15	0.309							
	pp1	34.5	5.01E-17	0.272							

Table L-35. Unsaturated Zone Layer Average Properties for Determination of Matrix Hydraulic Conductivity (Continued)

30th Percentile Infiltration Scenario, Repository Underlain by Zeolitic Units tsw39 and Ch1-6											
Model Layer	Unit	Average Thick-ness (m)	Matrix Permeability (m^2)[b]	Van Genuchten m[b]	Layer Average Matrix Permeability (m^2)	Layer Average Van Genuchten m	Average Saturation[e]	Residual Saturation	Effective Saturation	Layer Average Matrix Relative Permeability (m^2)	Layer Average Matrix Hydraulic Conductivity (mm/yr)
TSW	tsw35	51.2	1.11E-17	0.216	5.76E-18	0.30	0.95	0.1	0.94	9.68E-19	3.37E-01
	tsw36	31.3	3.16E-18	0.442							
	tsw37	15.7	3.16E-18	0.442							
	tsw38	15.5	1.27E-17	0.286							
	tsw39	6.7	3.50E-17	0.059							
CH	ch1	15.7	3.50E-17	0.349	2.98E-18	0.31	0.7	0.3	0.57	6.52E-21	2.27E-03
	ch2	19.3	5.20E-18	0.257							
	ch3	19.3	5.20E-18	0.257							
	ch4	19.3	5.20E-18	0.257							
	ch5	19.3	5.20E-18	0.257							
	ch6	18.0	8.20E-19	0.499							
PP	pp4	9.7	3.51E-17	0.474	4.95E-17	0.34	0.8	0.1	0.78	1.65E-18	5.72E-01
	pp3	19.1	1.02E-13	0.407							
	pp2	17.4	1.69E-15	0.309							
	pp1	34.5	2.57E-17	0.272							

Table L-35. Unsaturated Zone Layer Average Properties for Determination of Matrix Hydraulic Conductivity (Continued)

50th Percentile Infiltration Scenario, Repository Underlain by Zeolitic Units tsw39 and Ch1-6											
Model Layer	Unit	Average Thick-ness (m)	Matrix Permeability (m^2)[c]	Van Genuchten m[c]	Layer Average Matrix Permeability (m^2)	Layer Average Van Genuchten m	Average Saturation[e]	Residual Saturation	Effective Saturation	Layer Average Matrix Relative Permeability (m^2)	Layer Average Matrix Hydraulic Conductivity (mm/yr)
TSW	tsw35	51.2	1.94E-17	0.216	8.53E-18	0.30	0.95	0.1	0.94	1.43E-18	4.99E-01
	tsw36	31.3	4.45E-18	0.442							
	tsw37	15.7	4.45E-18	0.442							
	tsw38	15.5	2.16E-17	0.286							
	tsw39	6.7	3.50E-17	0.059							
CH	ch1	15.7	3.50E-17	0.349	2.98E-18	0.31	0.7	0.3	0.57	6.52E-21	2.27E-03
	ch2	19.3	5.20E-18	0.257							
	ch3	19.3	5.20E-18	0.257							
	ch4	19.3	5.20E-18	0.257							
	ch5	19.3	5.20E-18	0.257							
	ch6	18.0	8.20E-19	0.499							
PP	pp4	9.7	1.89E-17	0.474	4.31E-17	0.34	0.8	0.1	0.78	1.43E-18	4.98E-01
	pp3	19.1	1.79E-13	0.407							
	pp2	17.4	1.00E-15	0.309							
	pp1	34.5	2.57E-17	0.272							

Table L-35. Unsaturated Zone Layer Average Properties for Determination of Matrix Hydraulic Conductivity (Continued)

90th Percentile Infiltration Scenario, Repository Underlain by Zeolitic Units tsw39 and Ch1-6											
Model Layer	**Unit**	**Average Thick-ness (m)**	**Matrix Permeability (m^2)[d]**	**Van Genuchten m[d]**	**Layer Average Matrix Permeability (m^2)**	**Layer Average Van Genuchten m**	**Average Saturation[e]**	**Residual Saturation**	**Effective Saturation**	**Layer Average Matrix Relative Permeability (m^2)**	**Layer Average Matrix Hydraulic Conductivity (mm/yr)**
TSW	tsw35	51.2	7.54E-17	0.216	1.61E-17	0.30	0.95	0.1	0.94	2.70E-18	9.40E-01
	tsw36	31.3	7.50E-18	0.442							
	tsw37	15.7	7.50E-18	0.442							
	tsw38	15.5	4.40E-17	0.286							
	tsw39	6.7	3.50E-17	0.059							
CH	ch1	15.7	3.50E-17	0.349	5.91E-18	0.20	0.7	0.3	0.57	6.79E-22	2.36E-04
	ch2	19.3	5.20E-18	0.240							
	ch3	19.3	5.20E-18	0.158							
	ch4	19.3	5.20E-18	0.158							
	ch5	19.3	5.20E-18	0.158							
	ch6	18.0	5.20E-18	0.158							
PP	pp4	9.7	1.00E-17	0.474	4.78E-17	0.34	0.8	0.1	0.78	1.59E-18	5.52E-01
	pp3	19.1	1.71E-13	0.407							
	pp2	17.4	6.31E-16	0.309							
	pp1	34.5	5.01E-17	0.272							

Sources: [a] DTN:LB0610UZDSCP10.001_R0 [DIRS 180502]
[b] DTN:LB0610UZDSCP30.001_R0 [DIRS 179180]
[c] DTN:LB0611UZDSCP50.001_R0 [DIRS 183948]
[d] DTN:LB0612UZD SCP90.001_R0 [DIRS 183949]
[e] Estimated from Calibrated UZ Properties, ANL-NBS-HS-000058 [DIRS 179545], Figures 6-1, 6-3, 6-5, and 6-9.

Table L-36. Unsaturated Zone Layer Average Matrix and Fracture Porosity

Model Layer	Unit	Thickness (m)	Matrix Porosity (Vitric tsw39 and Ch)[a]	Matrix Porosity (Zeolitic tsw39 and Ch)[a]	Fracture Porosity[b]	Layer Average Matrix Porosity (Vitric tsw39 and Ch)	Layer Average Matrix Porosity (Zeolitic tsw39 and Ch)	Layer Average Fracture Porosity
TSW	tsw35	102.42	1.31E-01	1.31E-01	9.60E-03	0.12	0.12	0.010
	tsw36	31.31	1.03E-01	1.03E-01	1.30E-02			
	tsw37	15.655	1.03E-01	1.03E-01	1.30E-02			
	tsw38	15.507	4.30E-02	4.30E-02	1.10E-02			
	tsw39	6.6511	2.29E-01	2.75E-01	4.30E-03			
CH	ch1	15.71	3.31E-01	2.85E-01	6.10E-04	0.34	0.31	0.001
	ch2	19.324	3.46E-01	3.22E-01	7.70E-04			
	ch3	19.328	3.46E-01	3.22E-01	7.70E-04			
	ch4	19.326	3.46E-01	3.22E-01	7.70E-04			
	ch5	19.326	3.46E-01	3.22E-01	7.70E-04			
	ch6	18.039	3.31E-01	2.71E-01	7.70E-04			
PP	pp4	9.736	3.21E-01	3.21E-01	3.70E-04	0.29	0.29	0.001
	pp3	19.091	3.18E-01	3.18E-01	9.70E-04			
	pp2	17.392	2.21E-01	2.21E-01	9.70E-04			
	pp1	34.466	2.97E-01	2.97E-01	3.70E-04			

Sources: [a]BSC 2004 [DIRS 169857], Table 4-2; DTN: LB0207REVUZPRP.002_R0 [DIRS 159672]
[b]BSC 2004 [DIRS 169857], Table 4-3; DTN: LB0205REVUZPRP.001_R0 [DIRS 159525] and DTN: LB0207REVUZPRP.001_R0 [DIRS 159526].

Table L-37. Unsaturated Zone Layer Fracture and Matrix Percolation Flux (mm/yr)

10th Percentile Infiltration Scenario									
Layer	Ksat	Present-Day		Monsoon		Glacial-Transition		Post-10,000 Year	
		Matrix Flux (mm/yr)	Fracture Flux (mm/yr)	Matrix Flux (mm/yr)	Fracture Flux (mm/yr)	Matrix Flux (mm/yr)	Fracture Flux (mm/yr)	Matrix Flux (mm/yr)	Fracture Flux (mm/yr)
TSW-Vitric	2.58E-01	0.33	2.40	0.33	5.81	0.33	8.33	0.33	15.49
TSW-Zeolitic	1.57E-01	0.29	2.44	0.29	5.85	0.29	8.37	0.29	15.53
CH-Vitric	6.29E+01	2.73	0.00	6.14	0.00	8.66	0.00	15.82	0.00
CH-Zeolitic	1.57E-03	0.00	2.73	0.00	6.14	0.00	8.66	0.00	15.82
PP	7.78E-01	0.91	1.82	0.91	5.23	0.91	7.75	0.91	14.91
30th Percentile Infiltration Scenario									
Layer	Ksat	Present-Day		Monsoon		Glacial-Transition		Post 10,000 Year	
		Matrix Flux (mm/yr)	Fracture Flux (mm/yr)	Matrix Flux (mm/yr)	Fracture Flux (mm/yr)	Matrix Flux (mm/yr)	Fracture Flux (mm/yr)	Matrix Flux (mm/yr)	Fracture Flux (mm/yr)
TSW-Vitric	2.94E-01	0.37	6.97	0.37	11.64	0.37	17.70	0.37	24.42
TSW-Zeolitic	1.80E-01	0.34	7.00	0.34	11.67	0.34	17.73	0.34	24.45
CH-Vitric	8.78E+01	7.34	0.00	12.01	0.00	18.07	0.00	24.79	0.00
CH-Zeolitic	1.57E-03	0.00	7.34	0.00	12.01	0.00	18.07	0.00	24.79
PP	4.88E-01	0.57	6.77	0.57	11.44	0.57	17.50	0.57	24.22
50th Percentile Infiltration Scenario									
Layer	Ksat	Present-Day		Monsoon		Glacial-Transition		Post 10,000 Year	
		Matrix Flux (mm/yr)	Fracture Flux (mm/yr)	Matrix Flux (mm/yr)	Fracture Flux (mm/yr)	Matrix Flux (mm/yr)	Fracture Flux (mm/yr)	Matrix Flux (mm/yr)	Fracture Flux (mm/yr)
TSW-Vitric	4.38E-01	0.56	10.60	0.56	13.25	0.56	21.56	0.56	30.93
TSW-Zeolitic	2.66E-01	0.50	10.66	0.50	13.31	0.50	21.62	0.50	30.99
CH-Vitric	1.44E+02	11.16	0.00	13.81	0.00	22.12	0.00	31.49	0.00
CH-Zeolitic	1.57E-03	0.00	11.16	0.00	13.81	0.00	22.12	0.00	31.49
PP	4.24E-01	0.50	10.66	0.50	13.31	0.50	21.62	0.50	30.99
90th Percentile Infiltration Scenario									
Layer	Ksat	Present-Day		Monsoon		Glacial-Transition		Post 10,000 Year	
		Matrix Flux (mm/yr)	Fracture Flux (mm/yr)	Matrix Flux (mm/yr)	Fracture Flux (mm/yr)	Matrix Flux (mm/yr)	Fracture Flux (mm/yr)	Matrix Flux (mm/yr)	Fracture Flux (mm/yr)
TSW-Vitric	8.35E-01	1.06	24.04	1.06	67.72	1.06	41.28	1.06	44.81
TSW-Zeolitic	5.02E-01	0.94	24.16	0.94	67.84	0.94	41.40	0.94	44.93
CH-Vitric	1.05E+02	25.10	0.00	68.78	0.00	42.34	0.00	45.87	0.00
CH-Zeolitic	1.20E-04	0.00	25.10	0.00	68.78	0.00	42.34	0.00	45.87
PP	4.71E-01	0.55	24.55	0.55	68.23	0.55	41.79	0.55	45.32

Table L-38. Unsaturated Zone Fracture and Matrix Groundwater Velocity

10th Percentile Infiltration Scenario										
Layer	Layer Average Matrix Porosity	Layer Average Fracture Porosity	Present-Day		Monsoon		Glacial-Transition		Post-10,000 Year	
			Matrix Velocity (mm/yr)	Fracture Velocity (mm/yr)	Matrix Velocity (mm/yr)	Fracture Velocity (mm/yr)	Matrix Velocity (mm/yr)	Fracture Velocity (mm/yr)	Matrix Velocity (mm/yr)	Fracture Velocity (mm/yr)
TSW-Vitric	0.12	9.95E-03	2.74E+00	2.42E+02	2.74E+00	5.84E+02	2.74E+00	8.37E+02	2.74E+00	1.56E+03
TSW-Zeolitic	0.12	9.95E-03	2.44E+00	2.45E+02	2.44E+00	5.87E+02	2.44E+00	8.41E+02	2.44E+00	1.56E+03
CH-Vitric	0.34	7.42E-04	8.00E+00		1.80E+01		2.54E+01		4.63E+01	
CH-Zeolitic	0.31	7.42E-04		3.68E+03		8.27E+03		1.17E+04		2.13E+04
PP	0.29	5.14E-04	3.16E+00	3.54E+03	3.16E+00	1.02E+04	3.16E+00	1.51E+04	3.16E+00	2.90E+04
30th Percentile Infiltration Scenario										
Layer	Layer Average Matrix Porosity	Layer Average Fracture Porosity	Present-Day		Monsoon		Glacial-Transition		Post-10,000 Year	
			Matrix Velocity (mm/yr)	Fracture Velocity (mm/yr)	Matrix Velocity (mm/yr)	Fracture Velocity (mm/yr)	Matrix Velocity (mm/yr)	Fracture Velocity (mm/yr)	Matrix Velocity (mm/yr)	Fracture Velocity (mm/yr)
TSW-Vitric	0.12	9.95E-03	3.13E+00	7.00E+02	3.13E+00	1.17E+03	3.13E+00	1.78E+03	3.13E+00	2.45E+03
TSW-Zeolitic	0.12	9.95E-03	2.78E+00	7.04E+02	2.78E+00	1.17E+03	2.78E+00	1.78E+03	2.78E+00	2.46E+03
CH-Vitric	0.34	7.42E-04	2.15E+01		3.52E+01		5.29E+01		7.26E+01	
CH-Zeolitic	0.31	7.42E-04		9.89E+03		1.62E+04		2.43E+04		3.34E+04
PP	0.29	5.14E-04	1.98E+00	1.32E+04	1.98E+00	2.23E+04	1.98E+00	3.41E+04	1.98E+00	4.71E+04

Table L-38. Unsaturated Zone Fracture and Matrix Groundwater Velocity (Continued)

50th Percentile Infiltration Scenario										
Layer	Layer Average Matrix Porosity	Layer Average Fracture Porosity	Present-Day		Monsoon		Glacial-Transition		Post-10,000 Year	
			Matrix Velocity (mm/yr)	Fracture Velocity (mm/yr)	Matrix Velocity (mm/yr)	Fracture Velocity (mm/yr)	Matrix Velocity (mm/yr)	Fracture Velocity (mm/yr)	Matrix Velocity (mm/yr)	Fracture Velocity (mm/yr)
TSW-Vitric	0.12	9.95E-03	4.66E+00	1.07E+03	4.66E+00	1.33E+03	4.66E+00	2.17E+03	4.66E+00	3.11E+03
TSW-Zeolitic	0.12	9.95E-03	4.12E+00	1.07E+03	4.12E+00	1.34E+03	4.12E+00	2.17E+03	4.12E+00	3.11E+03
CH-Vitric	0.34	7.42E-04	3.27E+01		4.04E+01		6.48E+01		9.22E+01	
CH-Zeolitic	0.31	7.42E-04		1.50E+04		1.86E+04		2.98E+04		4.24E+04
PP	0.29	5.14E-04	1.73E+00	2.08E+04	1.73E+00	2.59E+04	1.73E+00	4.21E+04	1.73E+00	6.03E+04
90th Percentile Infiltration Scenario										
Layer	Layer Average Matrix Porosity	Layer Average Fracture Porosity	Present-Day		Monsoon		Glacial-Transition		Post-10,000 Year	
			Matrix Velocity (mm/yr)	Fracture Velocity (mm/yr)	Matrix Velocity (mm/yr)	Fracture Velocity (mm/yr)	Matrix Velocity (mm/yr)	Fracture Velocity (mm/yr)	Matrix Velocity (mm/yr)	Fracture Velocity (mm/yr)
TSW-Vitric	0.12	9.95E-03	8.89E+00	2.42E+03	8.89E+00	6.81E+03	8.89E+00	4.15E+03	8.89E+00	4.50E+03
TSW-Zeolitic	0.12	9.95E-03	7.77E+00	2.43E+03	7.77E+00	6.82E+03	7.77E+00	4.16E+03	7.77E+00	4.51E+03
CH-Vitric	0.34	7.42E-04	7.35E+01		2.01E+02		1.24E+02		1.34E+02	
CH-Zeolitic	0.31	7.42E-04		3.38E+04		9.26E+04		5.70E+04		6.18E+04
PP	0.29	5.14E-04	1.91E+00	4.78E+04	1.91E+00	1.33E+05	1.91E+00	8.14E+04	1.91E+00	8.82E+04

Table L-39. Unsaturated Zone Layer Groundwater Travel Times (yr)

Layer	Average Layer Thick-ness (m)	Present-Day		Monsoon		Glacial-Transition		Post-10,000 Year	
		Matrix Travel Time (yr)	Fracture Travel Time (yr)	Matrix Travel Time (yr)	Fracture Travel Time (yr)	Matrix Travel Time (yr)	Fracture Travel Time (yr)	Matrix Travel Time (yr)	Fracture Travel Time (yr)
10th Percentile Infiltration Scenario									
TSW-Vitric	120	43,902	498	43,902	206	43,902	144	43,902	77
TSW-Zeolitic	120	49,343	492	49,343	205	49,343	143	49,343	77
CH-Vitric	111	13,889		6,176		4,379		2,397	
CH-Zeolitic	111		30		13		10		5
PP	81	25,511	23	25,511	8	25,511	5	25,511	3
30th Percentile Infiltration Scenario									
TSW-Vitric	120	38,416	172	38,416	103	38,416	68	38,416	49
TSW-Zeolitic	120	43,227	171	43,227	103	43,227	68	43,227	49
CH-Vitric	111	5,166		3,157		2,098		1,530	
CH-Zeolitic	111		11		7		5		3
PP	81	40,662	6	40,662	4	40,662	2	40,662	2
50th Percentile Infiltration Scenario									
TSW-Vitric	120	25,822	113	25,822	90	25,822	56	25,822	39
TSW-Zeolitic	120	29,184	112	29,184	90	29,184	55	29,184	39
CH-Vitric	111	3,398		2,746		1,714		1,204	
CH-Zeolitic	111		7		6		4		3
PP	81	46,773	4	46,773	3	46,773	2	46,773	1
90th Percentile Infiltration Scenario									
TSW-Vitric	120	13,538	50	13,538	18	13,538	29	13,538	27
TSW-Zeolitic	120	15,488	50	15,488	18	15,488	29	15,488	27
CH-Vitric	111	1,511		551		896		827	
CH-Zeolitic	111		3		1		2		2
PP	81	42,167	2	42,167	1	42,167	1	42,167	1

Table L-40. Unsaturated Zone Layer Average Rock Density

Layer	Unit	Thickness (m)	Density (kg/m^3)[a]	Layer Average Matrix Density (Vitric tsw39 and Ch)
TSW	tsw35	102.4	1.98E+03	2067.8
	tsw36	31.3	2.21E+03	
	tsw37	15.7	2.21E+03	
	tsw38	15.5	2.17E+03	
	tsw39	6.7	2.17E+03	
CH	ch1	15.7	1.48E+03	1510.6
	ch2	19.3	1.52E+03	
	ch3	19.3	1.52E+03	
	ch4	19.3	1.52E+03	
	ch5	19.3	1.52E+03	
	ch6	18.0	1.52E+03	
PP	pp4	9.7	1.48E+03	1554.9
	pp3	19.1	1.48E+03	
	pp2	17.4	1.83E+03	
	pp1	34.5	1.48E+03	

Source: [a]SNL 2008 [DIRS 184748], Table 6-6.

Table L-41. Unsaturated Zone Layer Distribution Coefficients

Species	Layer	Type of Uncertainty Distribution	Coefficients Describing Distribution (Kd: mL/g)
U	TSW	Cumulative	(Kd value, probability) (0, 0) (0.2, 0.5) (3.0, 1.0)
	CHV	Cumulative	(Kd value, probability) (0, 0) (0.2, 0.5) (3.0, 1.0)
	CHZ	Cumulative	(Kd value, probability) (0, 0) (0.5, 0.5) (30.0, 1.0)
	PP	Cumulative	(Kd value, probability) (0, 0) (0.2, 0.5) (3.0, 1.0)
Np	TSW	Cumulative	(Kd value, probability) (0, 0) (1.0, 0.5) (3.0, 1.0)
	CHV	Cumulative	(Kd value, probability) (0, 0) (1.0, 0.5) (3.0, 1.0)
	CHZ	Cumulative	(Kd value, probability) (0, 0) (0.5, 0.5) (6.0, 1.0)
	PP	Cumulative	(Kd value, probability) (0, 0) (1.0, 0.5) (3.0, 1.0)
Pu	TSW	Cumulative	(Kd value, probability) (10.0, 0) (100.0, 0.5) (200.0, 1.0)
	CHV	Cumulative	(Kd value, probability) (10.0, 0) (100.0, 0.5) (200.0, 1.0)
	CHZ	Cumulative	(Kd value, probability) (10.0, 0) (100.0, 0.5) (200.0, 1.0)
	PP	Cumulative	(Kd value, probability) (10.0, 0) (100.0, 0.5) (200.0, 1.0)
Pa	TSW	Truncated Normal	Range = 1,000 - 10,000, μ = 5500 σ = 1500
	CHV	Truncated Normal	Range = 1,000 - 10,000, μ = 5500 σ = 1500
	CHZ	Truncated Normal	Range = 1,000 - 10,000, μ = 5500 σ = 1500
	PP	Truncated Normal	Range = 1,000 - 10,000, μ = 5500 σ = 1500
Cs	TSW	Cumulative	(Kd value, probability) (0.0, 0) (2.0, 0.5) (100.0, 1.0)
	CHV	Cumulative	(Kd value, probability) (0.0, 0) (2.0, 0.5) (100.0, 1.0)
	CHZ	Cumulative	(Kd value, probability) (425.0, 0) (5,000.0, 0.5) (20,000.0, 1.0)
	PP	Cumulative	(Kd value, probability) (0.0, 0) (2.0, 0.5) (100.0, 1.0)
Sr	TSW	Uniform	Range = 0 - 50
	CHV	Uniform	Range = 0 - 50
	CHZ	Uniform	Range = 50 - 2,000
	PP	Uniform	Range = 0 - 50
Th	TSW	Uniform	Range = 1,000 - 10,000
	CHV	Uniform	Range = 1,000 - 10,000
	CHZ	Uniform	Range = 1,000 - 30,000
	PP	Uniform	Range = 1,000 - 10,000
Se[1]	TSW	Truncated Normal	Range = 0 - 25, μ = 8.6 σ = 7.9
	CHV	Truncated Normal	Range = 0 - 25, μ = 8.6 σ = 7.9
	CHZ	Truncated Normal	Range = 1 - 35, μ = 14.3 σ = 7.9
	PP	Truncated Normal	Range = 0 - 25, μ = 8.6 σ = 7.9
Sn[1]	TSW	Log Uniform	Range = 100 - 5,000
	CHV	Log Uniform	Range = 100 - 5,000
	CHZ	Log Uniform	Range = 100 - 5,000
	PP	Log Uniform	Range = 100 - 5,000

Sources: DTN: LA0408AM831341.001_R0 [DIRS 171584] except for those noted by [1], then DTN: LB0701PAKDSESN.001_R0 [DIRS 179299].

Table L-42. Average Specific Discharge in Flow Path Segments

HAVO	Average Specific Discharge (m/year)		
	0-5 km	5-13 km	13-18 km
0.05	0.354	0.408	2.56
1.00	0.459	0.486	0.769
5.00	0.409	0.544	5.98
20.00	0.555	0.500	5.93

Source: DTN: SN0702PASZFTMA.002_R1 [DIRS 183471].

Table L-43. Saturated Zone Horizontal Anisotropy

Horizontal Anisotropy	Cumulative Probability
0.05	0
0.2	0.0042
0.4	0.0168
0.6	0.0379
0.8	0.0674
1.0	0.1
5.0	0.6
8.0	0.744
11.0	0.856
14.0	0.936
17.0	0.984
20.0	1

Source: DTN: SN0302T0502203.001_R0 [DIRS 163563].

Table L-44. Saturated Zone Specific Discharge Multiplier

Log-10 of Specific Discharge Multiplier	Cumulative Probability
-0.951	0
-0.506	0.05
-0.394	0.1
-0.208	0.25
0.208	0.75
0.394	0.9
0.506	0.95
0.951	1

Source: Modified from *Saturated Zone Flow and Transport Model Abstraction* (SNL 2007 [DIRS 183750], Tables 6-7[a] and 6-8). The following updated or new parameters are from Table 6-7[a]: GWSPD, FISVO, FPLANW, Kd_Pu_Col, Kd_Cs_Col, Kd_Sn_Col, Kd_Sn_Vo, Kd_Sn_Al, Kd_Se_Vo, Kd_Sn_Al, and Correlation matrix for K_d sampling in the SZ. Parameters NVF26 and NVF11 are new names for Parameters NVF19 and NVF7 in Table 6-8. Only the names are changed. The rest of the parameters are from Table 6-8.

Table L-45. Saturated Zone Flowing Interval Porosity

Log-10 of Flowing Interval Porosity	Cumulative Probability
-5	0
-4	0.05
-3	0.5
-2	0.8
-1	1

Source: DTN: SN0310T0502103.009_R0 [DIRS 168763].

Table L-46. Saturated Zone Distribution Coefficients in mL/g

Species	Unit	Distribution Type and Parameters	
Np[a]	Fractured Volcanic	Cumulative	
		Value	Probability
		0.00	0.00
		0.99	0.05
		1.83	0.90
		6.00	1.00
	Alluvium	Cumulative	
		Value	Probability
		1.80	0.00
		4.00	0.05
		8.70	0.95
		13.00	1.00
Sn[b]	Fractured Volcanic	Log-Uniform	
		Min.	10^2
		Max.	10^5
	Alluvium	Log-Uniform	
		Min.	10^2
		Max.	10^5
U[a]	Fractured Volcanic	Cumulative	
		Value	Probability
		0.00	0.00
		5.39	0.05
		8.16	0.95
		20.00	1.00
	Alluvium	Cumulative	
		Value	Probability
		1.70	0.00
		2.90	0.05
		6.30	0.95
		8.90	1.00

Species	Unit	Distribution Type and Parameters	
Cs[a]	Fractured Volcanic	Cumulative	
		Value	Probability
		100.00	0.00
		3,000.59	0.05
		6,782.92	1.00
	Alluvium	Truncated Normal	
		μ	728
		σ	464
		Min.	100
		Max.	1,000
Pa[c]	Fractured Volcanic	Truncated Normal	
		μ	5,500
		σ	1,500
		Min.	1,000
		Max.	10,000
	Alluvium	Truncated Normal	
		μ	5,500
		σ	1,500
		Min.	1,000
		Max.	10,000
Th[c]	Fractured Volcanic	Truncated Normal	
		μ	5,500
		σ	1,500
		Min.	-3σ
		Max.	$+3\sigma$
	Alluvium	Truncated Normal	
		μ	5,500
		σ	1,500
		Min.	-3σ
		Max.	$+3\sigma$

Table L-46. Saturated Zone Distribution Coefficients in mL/g (Continued)

Species	Unit	Distribution Type and Parameters		Species	Unit	Distribution Type and Parameters	
Pu[d]	Fractured Volcanic	Cumulative		Se[b]	Fractured Volcanic	Truncated Normal	
		Value	Probability			μ	14
		10.00	0.00			σ	11
		89.90	0.25			Min.	1
		129.87	0.95			Max.	50
		300.00	1.00		Alluvium	Truncated Normal	
	Alluvium	Normal[b]				μ	14
		μ	100			σ	11
		σ	15			Min.	1
						Max.	50

Sources: [a]DTN: SN0310T0502103.009_R0 [DIRS 168763]
[b]DTN: LA702AM150304.001_R5 [DIRS 184763]
[c]*Site-Scale Saturated Zone Transport* (SNL 2007 [DIRS 177392], Table A-4.
[d]DTN: SN0310T0502103.009_R0 [DIRS 168763] - Beta distribution in source; used mean and standard deviation in normal

Table L-47. Groundwater Biosphere Dose Conversion Factors for the Present-Day Climate

Cumulative Probability	Biosphere Dose Conversion Factor (Sv/yr per Bq/m^3)							
	Ac-227	C-14	Cl-36	Cs-135	I-129	Np-237	Pa-231	Pb-210
0%	4.08E-07	7.18E-10	1.28E-09	3.10E-09	8.59E-08	1.06E-07	6.58E-07	1.63E-06
5%	6.23E-07	8.30E-10	1.88E-09	4.97E-09	9.37E-08	1.43E-07	1.20E-06	1.82E-06
10%	7.07E-07	8.78E-10	2.14E-09	5.80E-09	9.69E-08	1.66E-07	1.38E-06	1.90E-06
15%	7.93E-07	9.33E-10	2.41E-09	6.68E-09	1.00E-07	1.81E-07	1.50E-06	1.95E-06
20%	8.59E-07	9.96E-10	2.65E-09	7.38E-09	1.02E-07	1.92E-07	1.63E-06	2.00E-06
25%	9.27E-07	1.04E-09	2.96E-09	7.99E-09	1.04E-07	2.05E-07	1.73E-06	2.06E-06
30%	9.78E-07	1.09E-09	3.22E-09	8.72E-09	1.07E-07	2.17E-07	1.85E-06	2.12E-06
35%	1.03E-06	1.16E-09	3.61E-09	9.35E-09	1.09E-07	2.26E-07	1.96E-06	2.17E-06
40%	1.09E-06	1.22E-09	4.03E-09	1.02E-08	1.11E-07	2.37E-07	2.04E-06	2.23E-06
45%	1.15E-06	1.28E-09	4.42E-09	1.10E-08	1.14E-07	2.49E-07	2.14E-06	2.29E-06
50%	1.21E-06	1.36E-09	4.86E-09	1.17E-08	1.17E-07	2.58E-07	2.26E-06	2.38E-06
55%	1.27E-06	1.44E-09	5.72E-09	1.26E-08	1.20E-07	2.69E-07	2.36E-06	2.49E-06
60%	1.32E-06	1.54E-09	6.31E-09	1.36E-08	1.24E-07	2.80E-07	2.45E-06	2.56E-06
65%	1.40E-06	1.68E-09	6.99E-09	1.45E-08	1.28E-07	2.93E-07	2.58E-06	2.67E-06
70%	1.47E-06	1.86E-09	7.74E-09	1.58E-08	1.33E-07	3.06E-07	2.71E-06	2.82E-06
75%	1.57E-06	2.04E-09	8.63E-09	1.73E-08	1.37E-07	3.22E-07	2.88E-06	2.99E-06
80%	1.68E-06	2.36E-09	1.02E-08	1.93E-08	1.43E-07	3.43E-07	3.09E-06	3.16E-06
85%	1.82E-06	2.71E-09	1.19E-08	2.24E-08	1.53E-07	3.73E-07	3.35E-06	3.46E-06
90%	2.07E-06	3.28E-09	1.54E-08	2.69E-08	1.66E-07	4.07E-07	3.78E-06	4.01E-06
95%	2.30E-06	5.11E-09	2.29E-08	3.46E-08	1.90E-07	4.52E-07	4.44E-06	5.22E-06
100%	4.32E-06	2.56E-08	3.00E-07	8.48E-08	1.13E-06	8.05E-07	8.56E-06	1.30E-05

Cumulative Probability	Biosphere Dose Conversion Factor (Sv/yr per Bq/m^3)							
	Pu-239	Pu-240	Pu-242	Ra-226	Ra-228	Se-79	Sn-126	Tc-99
0%	3.49E-07	3.47E-07	3.31E-07	8.79E-07	6.14E-07	3.62E-09	8.92E-08	5.28E-10
5%	5.20E-07	5.19E-07	4.94E-07	1.46E-06	7.12E-07	5.02E-09	1.57E-07	6.01E-10
10%	5.85E-07	5.84E-07	5.56E-07	1.67E-06	7.43E-07	5.68E-09	1.89E-07	6.29E-10
15%	6.35E-07	6.35E-07	6.03E-07	1.85E-06	7.66E-07	6.19E-09	2.15E-07	6.53E-10
20%	6.70E-07	6.69E-07	6.36E-07	2.08E-06	7.83E-07	6.64E-09	2.35E-07	6.77E-10
25%	7.06E-07	7.05E-07	6.71E-07	2.23E-06	8.01E-07	7.14E-09	2.58E-07	6.99E-10
30%	7.43E-07	7.41E-07	7.06E-07	2.41E-06	8.23E-07	7.65E-09	2.75E-07	7.26E-10
35%	7.82E-07	7.81E-07	7.43E-07	2.59E-06	8.38E-07	8.31E-09	2.93E-07	7.57E-10
40%	8.29E-07	8.25E-07	7.88E-07	2.76E-06	8.53E-07	8.89E-09	3.17E-07	7.82E-10
45%	8.62E-07	8.61E-07	8.18E-07	2.98E-06	8.67E-07	9.66E-09	3.44E-07	8.15E-10
50%	9.01E-07	8.99E-07	8.57E-07	3.21E-06	8.80E-07	1.02E-08	3.74E-07	8.51E-10
55%	9.38E-07	9.34E-07	8.92E-07	3.46E-06	9.02E-07	1.12E-08	4.07E-07	8.85E-10
60%	9.75E-07	9.72E-07	9.26E-07	3.74E-06	9.24E-07	1.24E-08	4.36E-07	9.29E-10
65%	1.02E-06	1.02E-06	9.69E-07	4.02E-06	9.42E-07	1.37E-08	4.70E-07	9.82E-10
70%	1.08E-06	1.07E-06	1.03E-06	4.35E-06	9.60E-07	1.58E-08	5.08E-07	1.05E-09
75%	1.14E-06	1.14E-06	1.08E-06	4.75E-06	9.86E-07	1.89E-08	5.50E-07	1.13E-09
80%	1.19E-06	1.19E-06	1.13E-06	5.23E-06	1.01E-06	2.27E-08	6.20E-07	1.24E-09

Table L-47. Groundwater Biosphere Dose Conversion Factors for the Present-Day Climate (Continued)

Cumulative Probability	Biosphere Dose Conversion Factor (Sv/yr per Bq/m^3)							
	Pu-239	Pu-240	Pu-242	Ra-226	Ra-228	Se-79	Sn-126	Tc-99
85%	1.27E-06	1.27E-06	1.21E-06	5.85E-06	1.05E-06	2.92E-08	6.84E-07	1.42E-09
90%	1.38E-06	1.38E-06	1.31E-06	6.57E-06	1.09E-06	4.11E-08	7.61E-07	1.79E-09
95%	1.61E-06	1.61E-06	1.53E-06	7.64E-06	1.16E-06	6.75E-08	8.76E-07	2.41E-09
100%	2.93E-06	2.90E-06	2.79E-06	1.75E-05	1.53E-06	1.51E-06	1.68E-06	2.85E-08

Cumulative Probability	Biosphere Dose Conversion Factor (Sv/yr per Bq/m^3)								
	Th-228	Th-229	Th-230	Th-232	U-233	U-234	U-235	U-236	U-238
0%	1.38E-07	7.43E-07	2.74E-07	5.05E-07	4.13E-08	3.96E-08	3.91E-08	3.75E-08	3.85E-08
5%	1.95E-07	1.32E-06	5.30E-07	8.97E-07	5.14E-08	4.90E-08	4.93E-08	4.61E-08	4.70E-08
10%	2.16E-07	1.49E-06	6.13E-07	1.05E-06	5.58E-08	5.30E-08	5.44E-08	5.00E-08	5.11E-08
15%	2.33E-07	1.64E-06	6.76E-07	1.16E-06	6.00E-08	5.66E-08	6.01E-08	5.33E-08	5.49E-08
20%	2.44E-07	1.75E-06	7.33E-07	1.24E-06	6.41E-08	6.02E-08	6.40E-08	5.66E-08	5.82E-08
25%	2.55E-07	1.88E-06	7.88E-07	1.31E-06	6.68E-08	6.27E-08	6.67E-08	5.88E-08	6.04E-08
30%	2.64E-07	2.00E-06	8.29E-07	1.39E-06	6.97E-08	6.57E-08	7.03E-08	6.17E-08	6.26E-08
35%	2.75E-07	2.09E-06	8.70E-07	1.48E-06	7.23E-08	6.77E-08	7.47E-08	6.35E-08	6.51E-08
40%	2.87E-07	2.19E-06	9.20E-07	1.56E-06	7.50E-08	7.03E-08	7.78E-08	6.60E-08	6.75E-08
45%	2.96E-07	2.28E-06	9.62E-07	1.64E-06	7.79E-08	7.26E-08	8.16E-08	6.81E-08	6.99E-08
50%	3.06E-07	2.37E-06	1.01E-06	1.73E-06	8.09E-08	7.45E-08	8.53E-08	7.00E-08	7.24E-08
55%	3.19E-07	2.48E-06	1.04E-06	1.84E-06	8.46E-08	7.79E-08	8.93E-08	7.31E-08	7.50E-08
60%	3.27E-07	2.61E-06	1.10E-06	1.92E-06	8.87E-08	8.21E-08	9.41E-08	7.68E-08	7.85E-08
65%	3.39E-07	2.73E-06	1.15E-06	2.02E-06	9.31E-08	8.55E-08	9.98E-08	8.01E-08	8.21E-08
70%	3.50E-07	2.89E-06	1.23E-06	2.12E-06	9.87E-08	8.93E-08	1.06E-07	8.36E-08	8.71E-08
75%	3.63E-07	3.05E-06	1.30E-06	2.24E-06	1.05E-07	9.52E-08	1.15E-07	8.89E-08	9.14E-08
80%	3.80E-07	3.28E-06	1.38E-06	2.41E-06	1.12E-07	1.01E-07	1.22E-07	9.39E-08	9.73E-08
85%	3.94E-07	3.52E-06	1.50E-06	2.62E-06	1.21E-07	1.08E-07	1.32E-07	1.01E-07	1.04E-07
90%	4.15E-07	3.94E-06	1.64E-06	2.83E-06	1.33E-07	1.17E-07	1.43E-07	1.09E-07	1.11E-07
95%	4.70E-07	4.58E-06	1.91E-06	3.22E-06	1.52E-07	1.35E-07	1.65E-07	1.25E-07	1.29E-07
100%	8.02E-07	8.05E-06	3.27E-06	5.26E-06	3.13E-07	2.20E-07	2.97E-07	2.02E-07	2.07E-07

Source: DTN: MO0702PAGBDCFS.001_R0 [DIRS 179327].

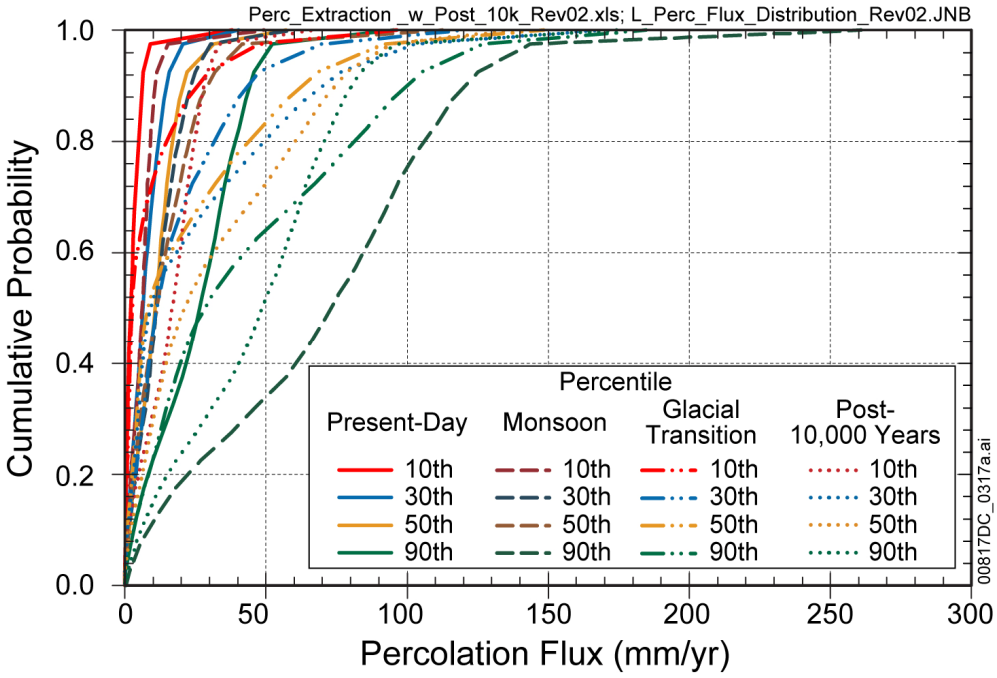

Source: DTN: SN0703PAEBSPCE.006_R2 [DIRS 181571].

Figure L-1. Percolation Flux over the Repository Area

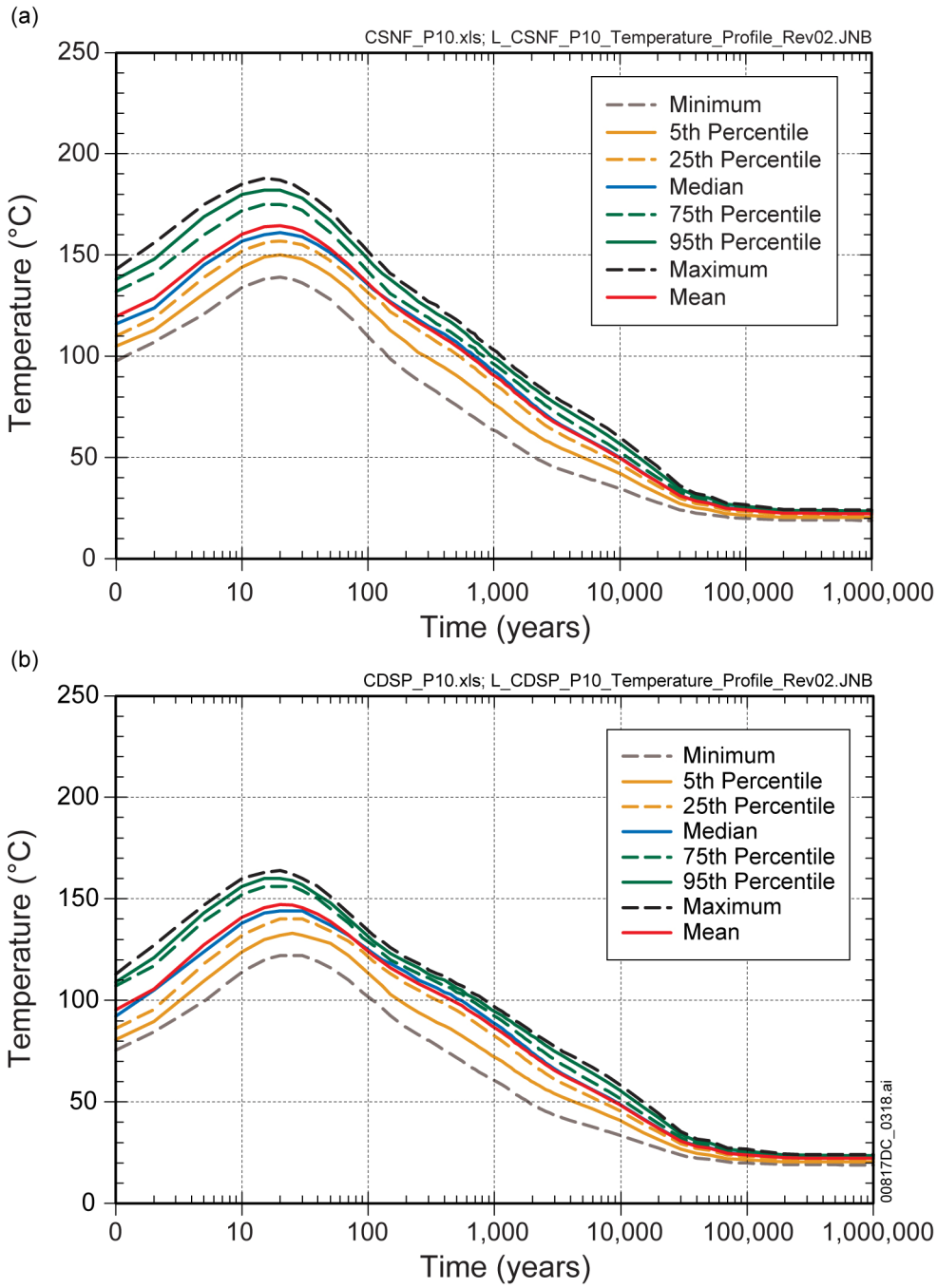

Source: Corroborative DTN: MO0708SIMPLIFI.000 [DIRS 182980].

Figure L-2. CSNF and Defense HLW Waste Package Surface Temperatures, 10th Percentile Infiltration Scenario, Medium Thermal Conductivity

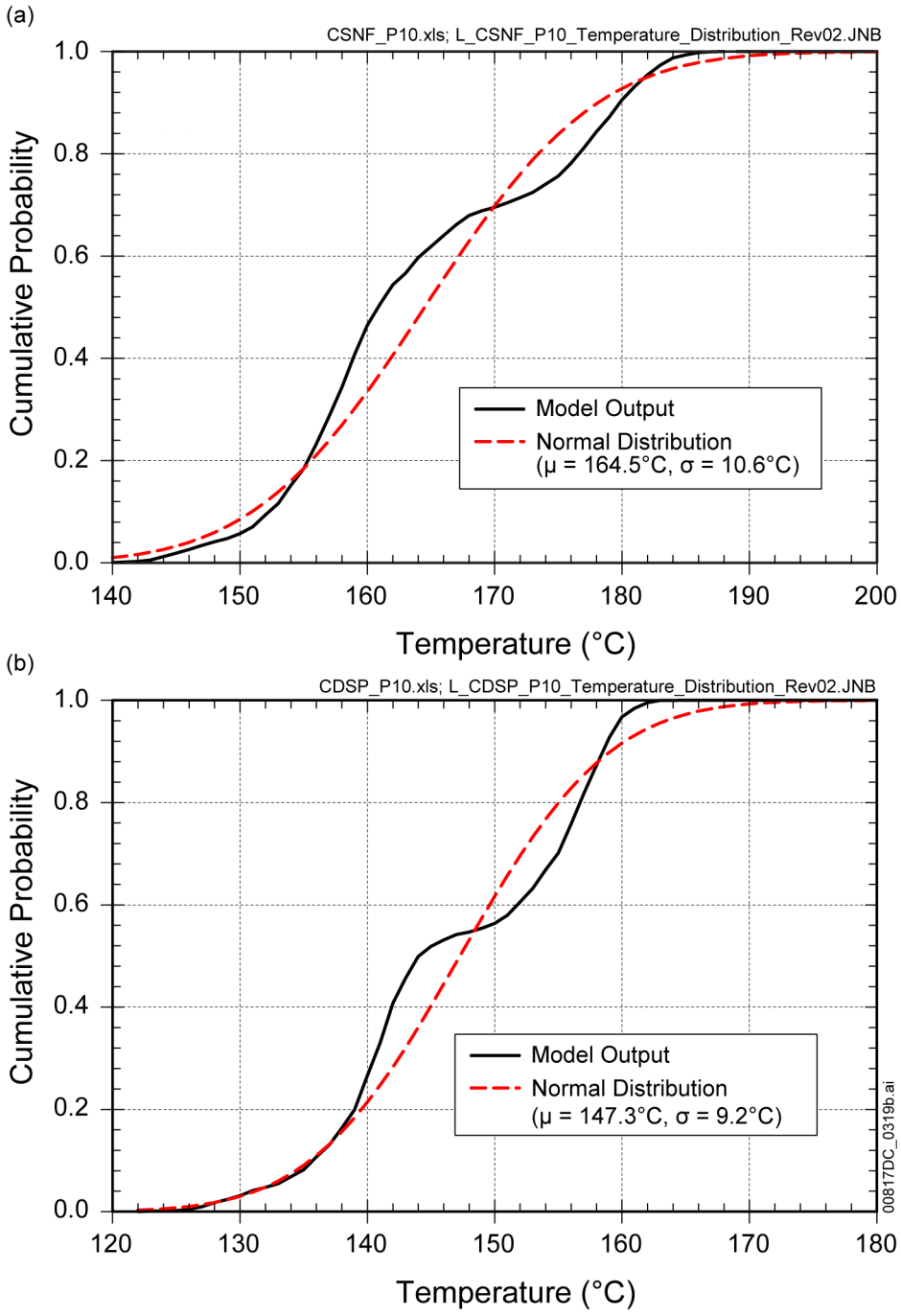

Source: Corroborative DTN: MO0708SIMPLIFI.000 [DIRS 182980].

Figure L-3. CSNF and Defense HLW Peak Waste Package Surface Temperature Distribution, 10th Percentile Infiltration Scenario, Medium Thermal Conductivity

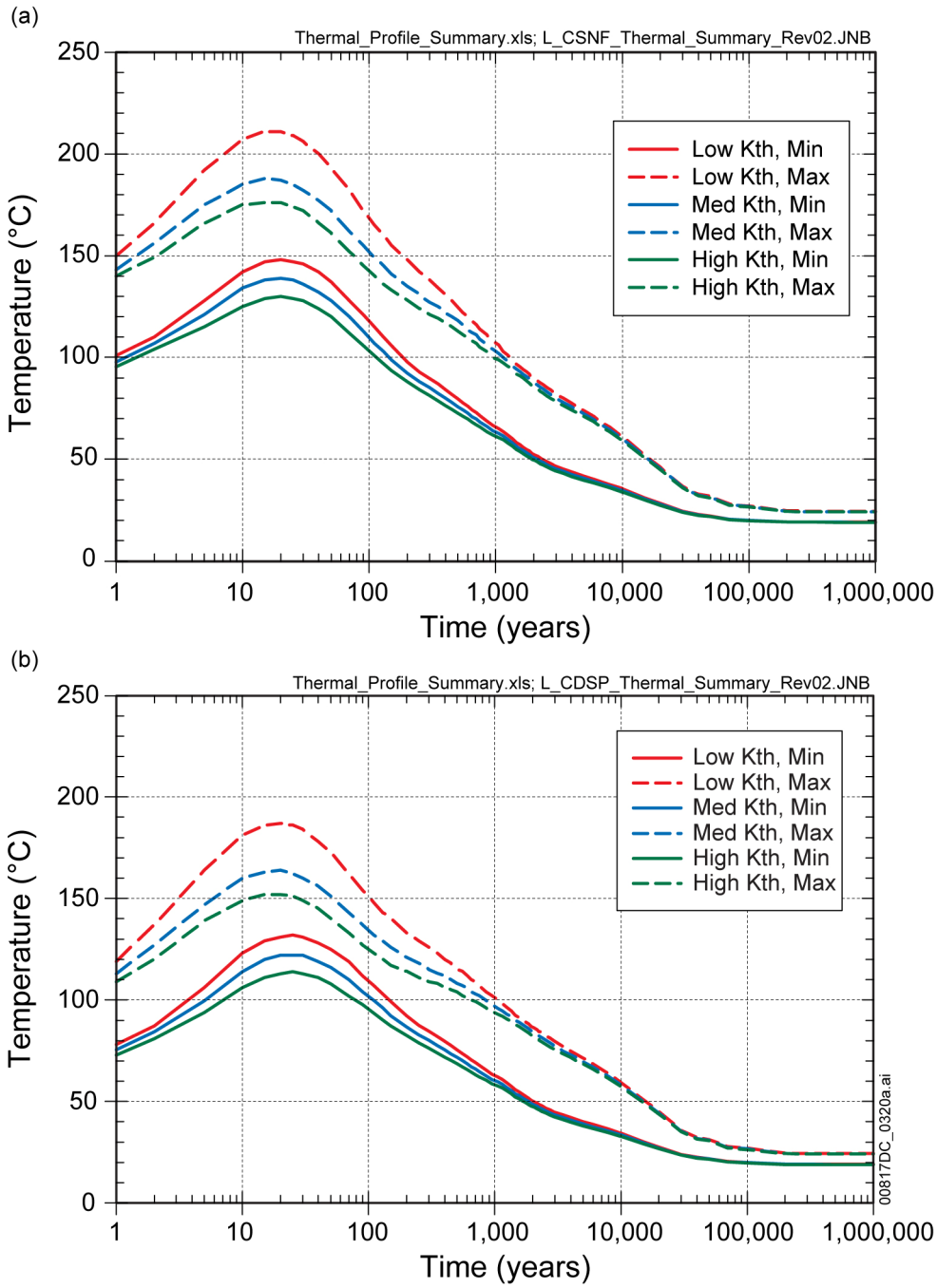

Source: Corroborative DTN: MO0708SIMPLIFI.000 [DIRS 182980].

Figure L-4. CSNF and Defense HLW Waste Package Surface Temperature Range, 10th Percentile Infiltration Scenario

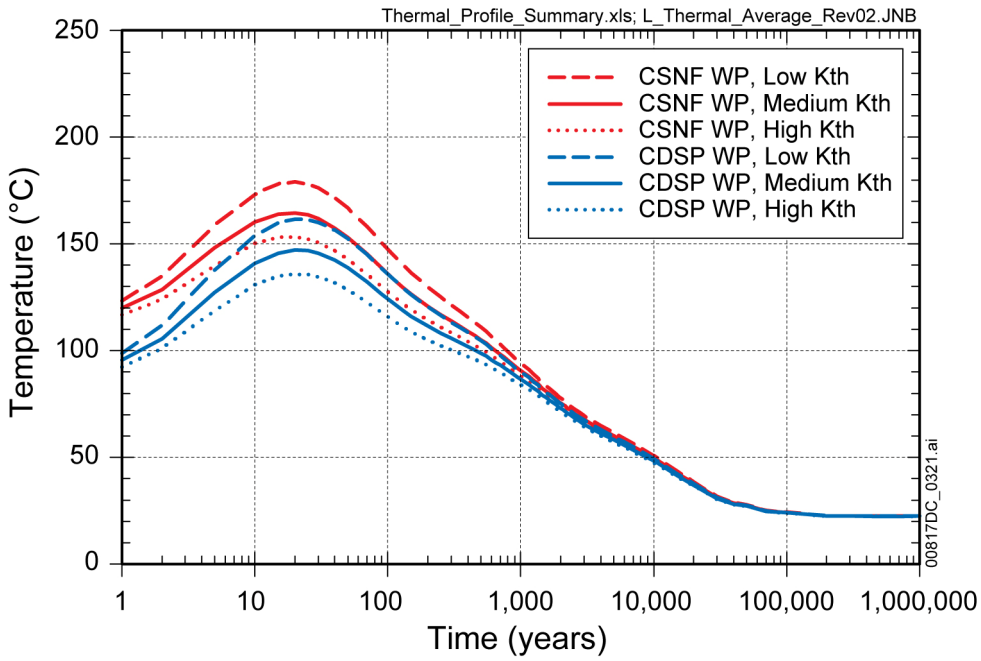

Source: Corroborative DTN: MO0708SIMPLIFI.000 [DIRS 182980].

Figure L-5. Average CSNF and Defense HLW Peak Waste Package Surface Temperature, 10th Percentile Infiltration Scenario

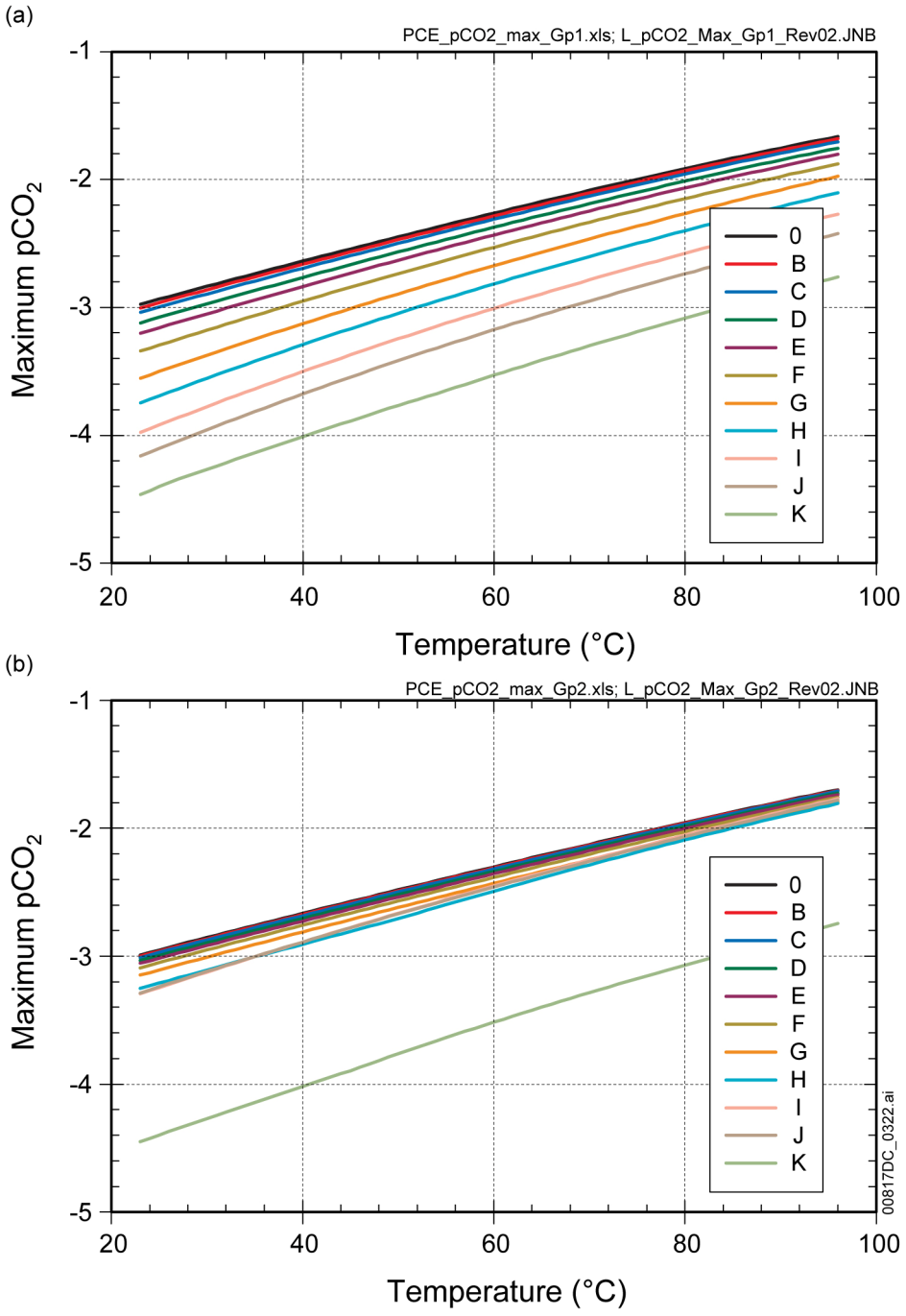

Source: DTN: SN0701PAEBSPCE.002_R0 [DIRS 179425].

NOTES: The lines represent different values of a water-rock interaction parameter.

Figure L-6. Maximum CO_2 Partial Pressure: (a) Group 1 Starting Water, (b) Group 2 Starting Water, (c) Group 3 Starting Water, and (d) Group 4 Starting Water

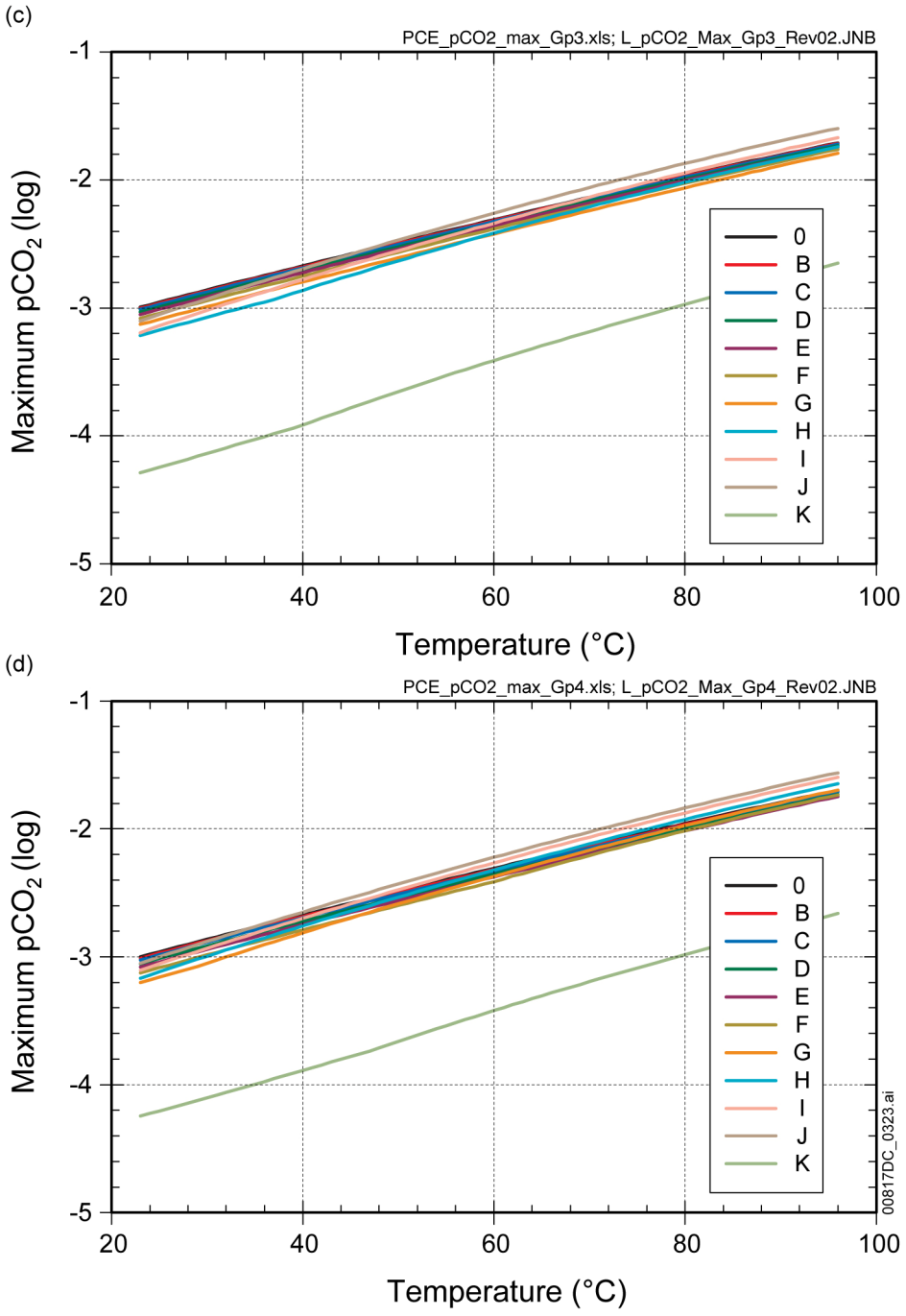

Source: DTN: SN0701PAEBSPCE.002_R0 [DIRS 179425].

NOTES: The lines represent different values of a water-rock interaction parameter.

Figure L-6. Maximum CO_2 Partial Pressure: (a) Group 1 Starting Water, (b) Group 2 Starting Water, (c) Group 3 Starting Water, and (d) Group 4 Starting Water (Continued)

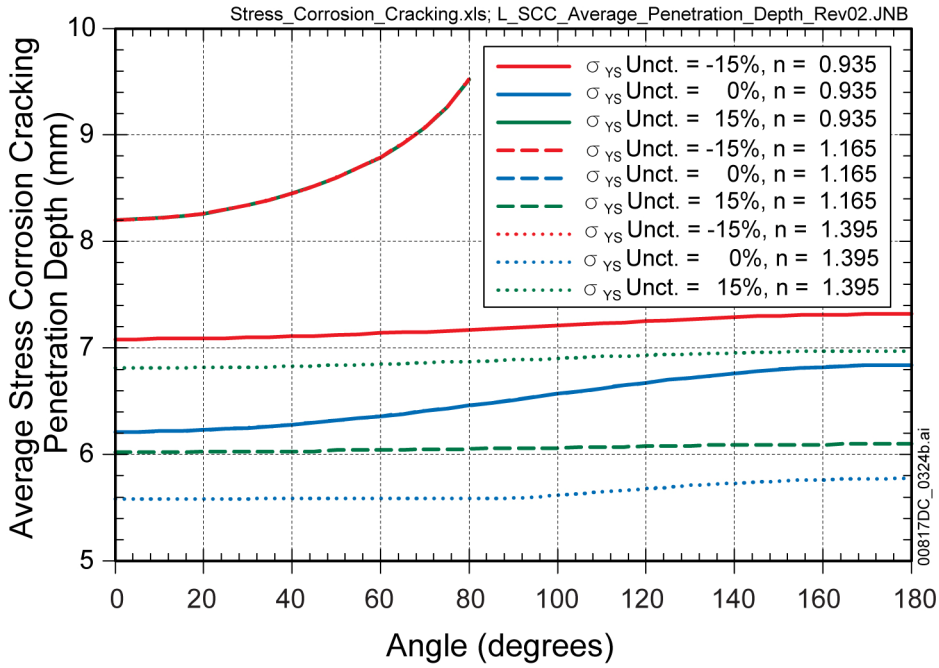

Source: Corroborative DTN: MO0708SIMPLIFI.000 [DIRS 182980].

Figure L-7. Depth Where Stress Corrosion Cracks Can Initiate and Propagate Along the Circumference of the Waste Package Outer Lid Closure Weld Region

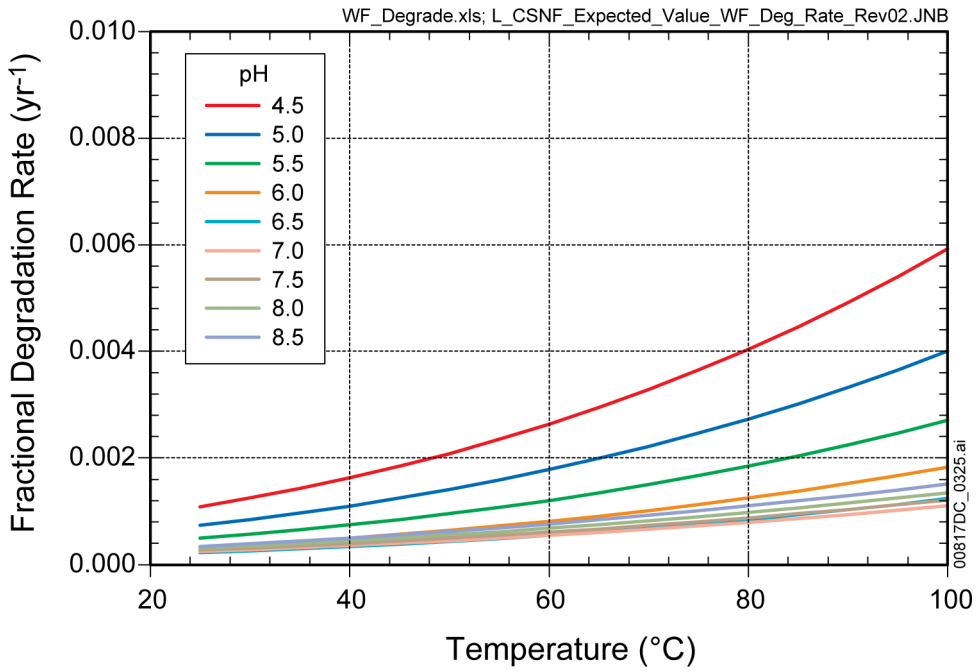

Source: Corroborative DTN: MO0708SIMPLIFI.000 [DIRS 182980].

Figure L-8. CSNF Waste Form Degradation for Expected Value Coefficients with Varying pH

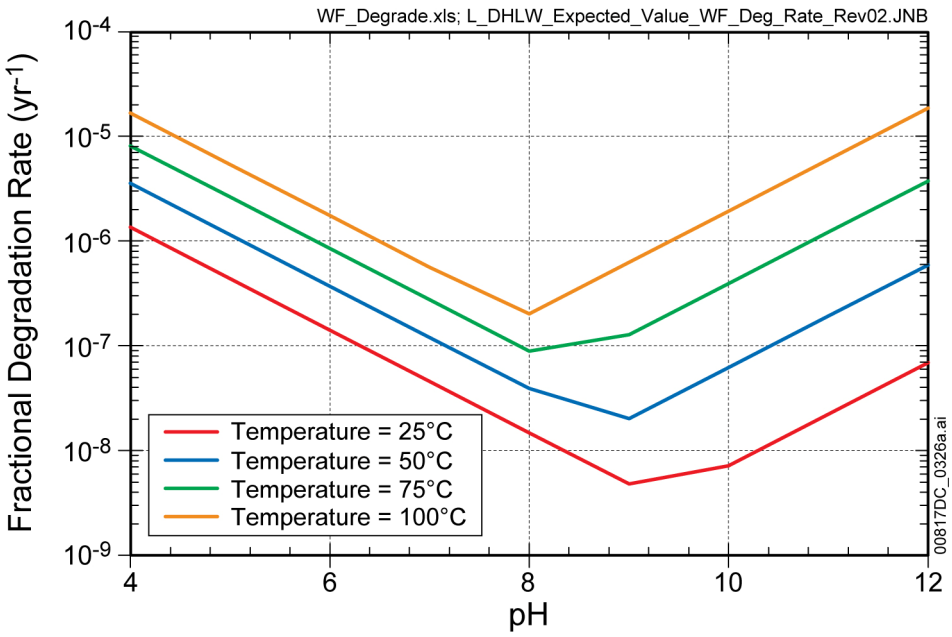

Source: Corroborative DTN: MO0708SIMPLIFI.000 [DIRS 182980].

Figure L-9. Defense HLW Waste Form Degradation for Expected Value Coefficients at Different Temperatures

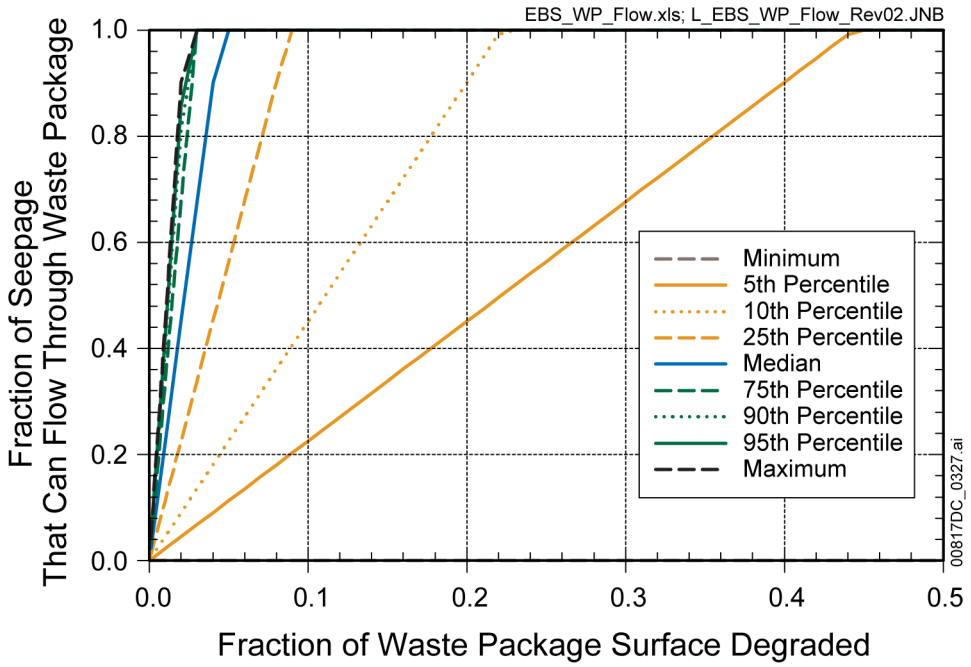

Source: Corroborative DTN: MO0708SIMPLIFI.000 [DIRS 182980].

Figure L-10. Fraction of Seepage that Can Enter a Waste Package with General Corrosion Breaches

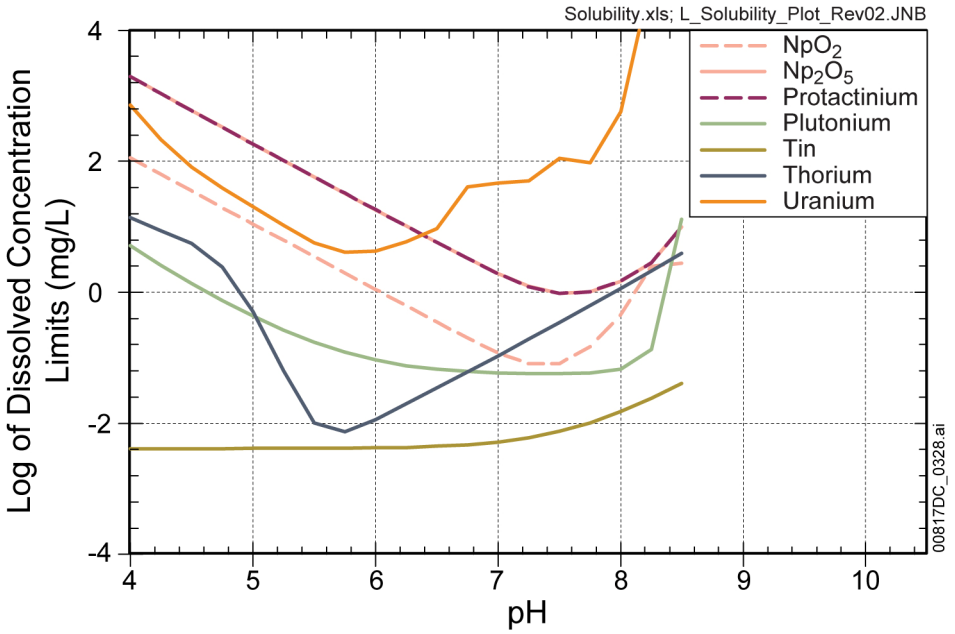

Source: Corroborative DTN: MO0708SIMPLIFI.000 [DIRS 182980].

Figure L-11. Dissolved Concentration Limits

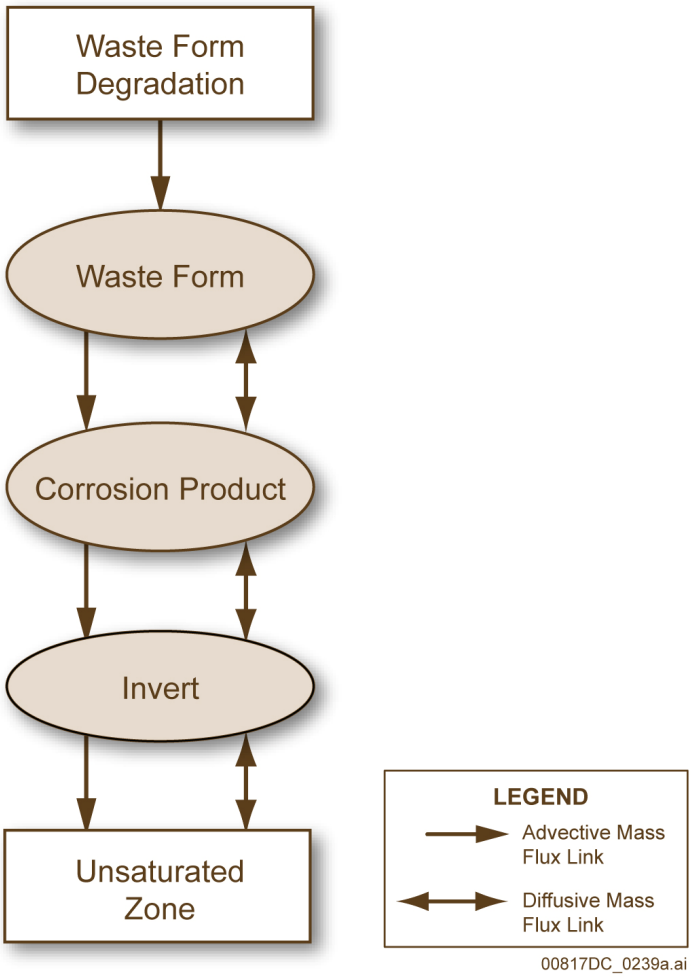

Figure L-12. General Schematic Diagram of a Single EBS Radionuclide Transport Network in Simplified TSPA

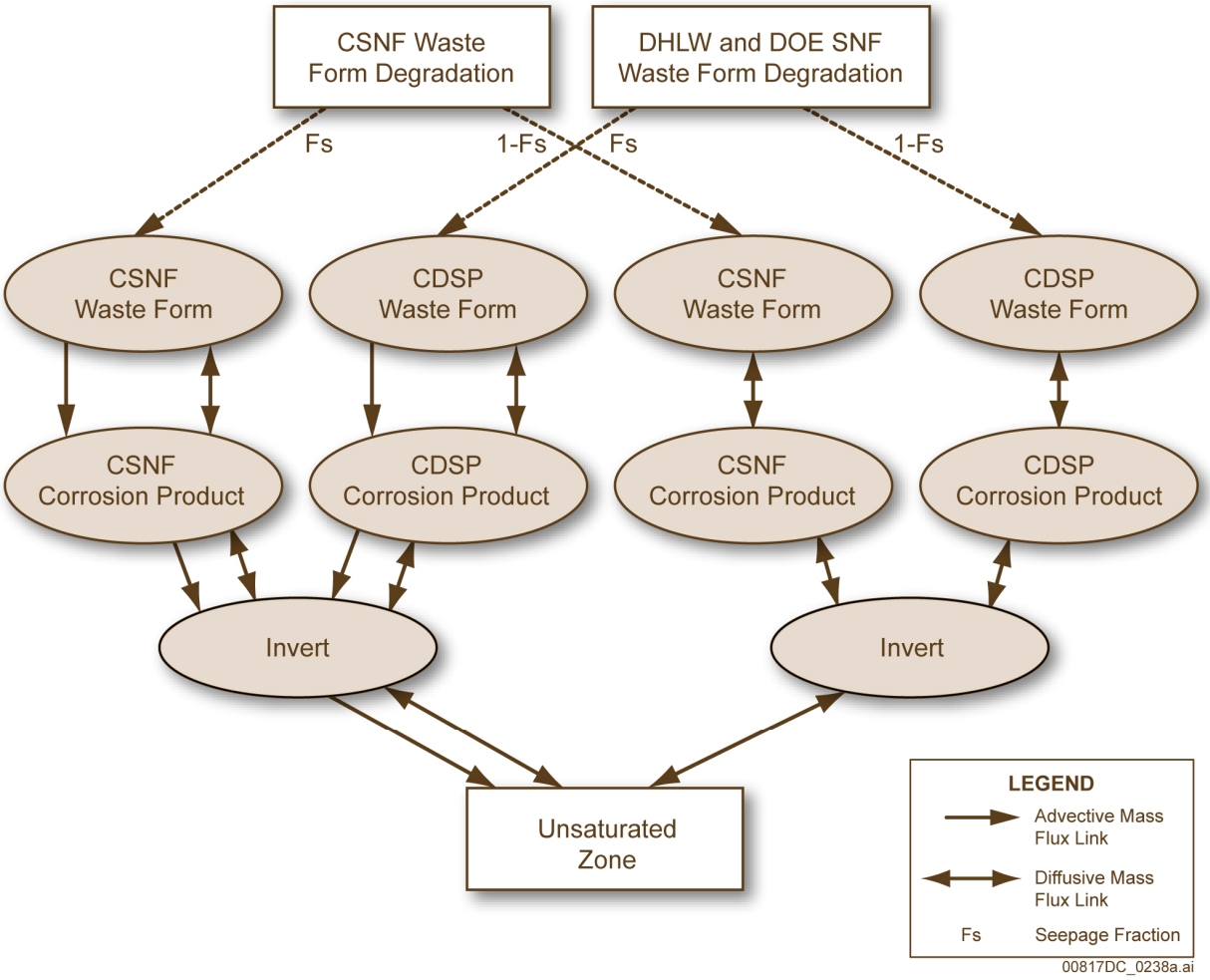

Figure L-13. General Schematic Diagram of a Single EBS Radionuclide Transport Network Used in the Simplified TSPA

APPENDIX M
COMPARISON WITH ELECTRIC POWER RESEARCH INSTITUTE MODEL

M1. INTRODUCTION

This appendix presents a comparison of the Total System Performance Assessment for the License Application (TSPA-LA) Model and the TSPA of the proposed high-level waste repository at Yucca Mountain conducted by the Electric Power Research Institute (EPRI). The purpose of the comparison of the Yucca Mountain TSPA conducted by EPRI with the TSPA-LA Model is to provide a potential unique independent means of TSPA-LA Model validation. The EPRI TSPA Analysis was developed by an independent organization, based on independently developed methodology and its own total systems performance code, the Integrated Multiple Assumptions and Release Code (IMARC). Input into IMARC is generally derived from the model and/or analyses reports developed for the TSPA-LA. Because the input to the EPRI TSPA Analysis corresponds to an earlier version of the TSPA model, an exact comparison between the results from the EPRI TSPA Analysis and the TSPA-LA Model is not possible. Nevertheless, the overall features of the dose curves can be compared and, together with evaluating the apparent differences, provide a validation of the general methodology and strategy used in the TSPA-LA Model.

M1.1 APPROACH

The approach for the comparison includes discussion of the rationale and objectives of EPRI's TSPA efforts and review of the development and status of EPRI's TSPA IMARC, which serves as the basis for the comparison with the TSPA-LA Model that is implemented in GoldSim. The focus of the comparison is on the Nominal Scenario Class for which specific model parameters of both models are examined in greater detail. EPRI has been conducting independent assessments of the total system performance of the candidate radioactive waste repository at Yucca Mountain, Nevada, since 1989 (Kozak and Kessler 2005 [DIRS 178580]). The objective of the EPRI's TSPA Analysis is to provide an independent third-party assessment of key technical and scientific issues associated with the proposed geologic repository at Yucca Mountain and to ensure that adequate information exists to support resolution of those issues that have the potential to significantly impact any Yucca Mountain regulatory activities.

M1.2 IMARC OVERVIEW

The development of EPRI's TSPA IMARC has followed the evolution of Yucca Mountain regulations, disposal system design, and conceptual understanding of the proposed repository. IMARC is intended to permit an independent probabilistic evaluation of the performance of the proposed Yucca Mountain Repository. The EPRI TSPA approach is guided by the principal U.S. Nuclear Regulatory Commission (NRC) regulations, which are consistent with a reasonable expectation philosophy as opposed to a most conservative philosophy.

The IMARC solves the equations for transport of radionuclides in groundwater for an abstracted concept of the behavior of Yucca Mountain. The overall conceptual approach of the IMARC and the basic elements of the analysis method are similar to the TSPA-LA approach depicted on Figure 6.1.5-9. The differences between the implementation in IMARC and that in the TSPA-LA Model are in the details of the implementation and the specifics of the assumptions, models, parameters, and couplings used.

The different scenarios thus far considered in the IMARC TSPA include:

- Nominal scenario
- Igneous scenario, distinguishing an igneous intrusive and an igneous extrusive scenario
- Seismic scenario.

The evolution of the IMARC and associated evaluation of the proposed Yucca Mountain Repository has been reported in a series of EPRI reports. The most recent comprehensive description of the IMARC, designated as Version 8, has been reported in a final report dated May 2005 (Kozak and Kessler 2005 [DIRS 178580]). More recent updates and implementations in the IMARC Version 9 were reported in November 2005 (Apted and Ross 2005 [DIRS 182229]). The most recent documentations include various analyses related to Yucca Mountain, such as a progress report on *Effects of Seismicity and Rockfall on Long-Term Performance of the Yucca Mountain Repository* (Apted and Kessler 2005 [DIRS 182228]), a final report in November 2006 on the effects of multiple seismic events (Apted 2006 [DIRS 182227]), and a December 2006 progress report (Apted et al., 2006 [DIRS 182231]). Accordingly, the EPRI TSPA does not account for the most recent updates of analysis and/or model reports, which are incorporated in the TSPA-LA Model.

M2. TSPA CONCEPTUAL MODEL DESIGN

The overall conceptual approach of the EPRI TSPA Analysis and the model components implemented in the IMARC follows the TSPA-LA approach and model components for the Nominal Scenario Class depicted on Figure 6.1.5-9.

M2.1 FEATURES, EVENTS, AND PROCESSES AND SCENARIO DEVELOPMENT

For the nominal and igneous scenarios, EPRI lists the following features, events, and processes (FEPs) that correspond to the *System Performance Assessment-License Application Features, Events, and Processes* (BSC 2005 [DIRS 173800], Section 3.1 and Appendix E):

- Present-day climate and future climate variation affecting rainfall and human behavior (variation in use of surface and groundwater and agricultural practices).

- Rainfall and temperatures for the different climate states affect infiltration into the upper saturated zone (SZ).

- Lateral redistribution of infiltrating groundwater due to heterogeneous fracture and matrix properties in the upper part of the unsaturated zone (UZ).

- The amount of water percolating into the drifts is a function of the lateral distribution of infiltrating groundwater above the drifts, capillary effects at the drift walls, or, for the igneous scenario, the hydrologic characteristic of the cooled magma.

- Some of the groundwater seeping into the drift may drip onto the drip shields (DSs), which prevents water from dripping onto the underlying waste packages (WPs); if the DSs fail, water will drip onto the underlying WPs.

- DS failure mechanisms considered include improper emplacement, seismic rockfall processes, and general corrosion and hydride embrittlement.
- WPs prevent humid air and groundwater from penetrating into the WP and from releasing gaseous, dissolved, or colloidal radionuclides. If WPs fail, water may condensate from either humid air or dripping groundwater.
- WP failure mechanisms considered include seismic, rockfall, and various corrosion processes. For the igneous intrusion scenario, a high temperature effect on failure is considered.
- Cladding surrounding the spent fuel, which prevents water from contacting the waste form, can fail by various mechanisms, including initial failures at emplacement, creep, localized corrosion, and hydride embrittlement.
- Seepage entering the failed WP and cladding may absorb radionuclides released from the waste form. The release of radionuclides is controlled by waste-form degradation, seepage rates, solubility limits, and diffusion.
- The released radionuclides are transported from the failed WPs through the lower area of the drift and into the lower UZ, which is governed largely by fracture/matrix interaction and radionuclide sorption.
- The radionuclides are then transported through the SZ to a far-field point 18 km downstream, where it is assumed to be taken up by the reasonably maximally exposed individual (RMEI). According to RMEI behavior, assumptions stipulated by the applicable regulations determine the committed radiological dose to the RMEI.
- For the igneous intrusion scenario, the repository functions according to the nominal scenario but includes the additional FEPs associated with igneous intrusion events (Apted and Kessler 2005 [DIRS 182327], Section 8).
- Magma intrudes via a basaltic dike and enters the drift at a slow rate, which does not affect the mechanical integrity of the DS away from the dike.
- The hot magma contacts WPs and spent fuel, cools, and solidifies rapidly.
- Indirect thermal and chemical effects may be propagated along the drift farther than the magma itself intrudes.
- The magma, and any radionuclide released into it from failed WPs, is not released via an intrusive pathway but remains available for release to groundwater.
- The far-field groundwater flow system returns to its undisturbed condition after a localized (tens of meters) and brief disruption (tens of years).
- The near-field rock surrounding the intrusion zone requires on the order of 1,000 years to resaturate before groundwater can begin flowing into the drift.

For the igneous extrusive scenario, EPRI concluded that it is very unlikely that WPs will be breached by the magma during the active eruption period or that radioactive material will be released from the repository as a result of a volcanic event (EPRI 2004 [DIRS 171915]). As a result, the igneous extrusive scenario was not implemented in the IMARC model.

The FEPs associated with multiple seismic events that could affect the repository performance include (Apted 2006 [DIRS 182227]):

- Vibratory ground motion damaging the engineered barrier system (EBS) components
- Seismically induced collapse of open drifts damaging the EBS
- Potential stress corrosion cracking (SCC) due to static load from accumulated drift collapse rock.

The potential effects of fault displacement induced by seismic events are considered to be mitigatable through drift construction and appropriate WP emplacement practice and are not considered in the EPRI TSPA Analysis (Apted and Kessler 2005 [DIRS 182228]).

M2.2 TREATMENT OF UNCERTAINTY

IMARC uses the logic tree analysis methodology for quantifying the impacts of model and parameter uncertainty in the TSPA calculations. Logic tree analysis is particularly useful for uncertainty propagation when parameter and/or model uncertainty is described using a limited number of probable states (e.g., high, medium, low values) and their likelihoods (Kozak and Kessler 2005 [DIRS 178580], Figure 2-3). Logic trees (also known as probability trees) combine individual scenarios resulting from uncertain discrete events and/or parameter states. As such, they may be recognized as a special case of decision trees containing only chance nodes but no decision nodes.

The logic tree is ordered such that independent effects are placed to the upstream (left) side, and dependent effects are organized to the downstream (right) side. Each branch is assigned a probability, conditional on the values of the previous branches leading to that node. All possibilities must be considered in building the logic tree such that probabilities for branches originating from each node sum to one.

Consider a simple groundwater contaminant transport modeling problem involving two uncertain inputs—source concentration (s) and groundwater velocity (v). Uncertainty in the source node is represented by two values, s1 and s2, with probabilities P1 and P2, respectively. Uncertainty in the velocity node is also represented by two values, v1 and v2. These values have conditional probabilities ranging from P3 to P6, depending on which branch of the source node they are attached. Each path from the root to an end branch (or terminal node) of the tree represents a feasible scenario. The four feasible scenarios for this system can be enumerated as: (s1,v1), (s1,v2), (s2,v1), and (s2,v2). The probability of each scenario is the product of conditional probabilities of the branches along that path.

The logic tree thus organizes various parameter (model) combinations and their probabilities. Given this information, the computation of the consequence for each of the discrete

combinations is a straightforward task. The results can be organized in terms of a table or graph of sorted discrete outcomes versus the corresponding summed probabilities. Such a risk profile is equivalent to a cumulative distribution of model output generated via Monte Carlo simulation by GoldSim.

M2.3 MODEL STRUCTURE AND IMPLEMENTATION

The IMARC solves for transport of radionuclides in groundwater for an abstracted concept of the behavior of the Yucca Mountain Repository. The different model components represented in the TSPA-LA (Figure 6.1.3-1) are incorporated into the EPRI TSPA Analysis as look-up tables, failure distribution curves, and numerical submodels. IMARC includes three major numerical submodels describing: (1) near-field radionuclide release and transport, (2) UZ flow and transport beneath the repository, and (3) SZ flow and transport.

The UZ above the repository is represented by look-up tables providing the fraction of the repository with active groundwater flow where the groundwater flux is controlled by net infiltration rates into the upper UZ which, in turn, depends on the climate state. EPRI considers three climate states represented by step changes in infiltration rates (EPRI 2002 [DIRS 158069]). Uncertainties in the amount of net infiltration that depend on rainfall and temperature for the different climate states are included in a look-up table of low, moderate, and high net infiltration.

Degradation of WPs and DSs is represented by failure distribution curves, which were generated by Monte Carlo simulations of models describing various failure mechanisms, implemented in EPRI's TSPA code (EPRI 2002 [DIRS 158069]) and in its successor EBSCOM code (Apted and Kessler 2005 [DIRS 182228]). Input to these Monte Carlo simulations included uncertainty distributions of model parameters describing different degradation mechanisms for DSs, WPs, and cladding.

A near-field model comprises all the components inside the drift, which includes the DS, WP, cladding, waste form, pedestal, and invert. The release of radionuclides from the near field is computed using the COMPASS (Compartment Model for Partially Saturated Repository Source Terms) code (Kozak and Kessler 2005 [DIRS 178580]). Releases from the repository are only assumed to occur after the thermal pulse has significantly dissipated. Thermal effects are neglected in the model for the nominal scenario, because it is assumed that there will be little to no liquid water present to facilitate radionuclide mobilization and movement until temperatures have decreased to near the boiling point of water. For the igneous intrusion scenario, thermal effects on the failure mechanisms of DSs, WPs, and cladding and on in-drift groundwater flow behavior are taken into account.

The hydrologic behavior of the near field is represented by two zones, representing dripping and non-dripping conditions, for which different cumulative probability curves of failure versus time are computed for DSs, WPs, and cladding. Additional inputs to the near-field model include: seepage rates into drifts, as a function of time and climate conditions; near-field transport parameters, including dimensions, sorption coefficients, and solubility limits; densities; and porosities in the near-field materials; and diffusion/advection distances to the nearest flowing fracture.

The combined computed radionuclide release rates from both dripping and non-dripping zones are used as boundary conditions for the UZ.

The UZ is represented by the second numerical submodel embedded within the IMARC. The submodel simulates flow and transport through the natural barriers of the UZ beneath the repository horizon. Flow and transport through the UZ is treated as one-dimensional, down vertically, into different geologic horizons. At the base of the UZ, the flux of radionuclides exiting the UZ is used as a time series input to the SZ code.

The SZ is represented by the third numerical submodel embedded within the IMARC. This submodel simulates flow and transport through the natural barriers of the SZ. The SZ code has a specified upstream flow rate, and a uniform infiltration rate is added to the upper surface of the computation region such that the groundwater flow velocity increases along the transport path length.

The SZ model consists of two segments: (1) the first representing fractured tuff extending from beneath the repository to 15 km downgradient, and (2) the second, representing the alluvium extending from 15 km downgradient to the location of the RMEI 18 km downgradient.

The UZ and SZ models communicate with the remainder of IMARC by the transfer of radionuclides from the near field and to the biosphere. All other parameters needed for the UZ and SZ models are unique to this part of the code making them, to a large extent, stand-alone calculations.

The resulting fluxes of radionuclide in the groundwater at 18 km are assumed to enter the biosphere via groundwater used by the RMEI. These radionuclide fluxes in the groundwater are adjusted to concentrations based on the residential water usage of 3,000 acre-feet per year (3.7×10^6 m^3/yr) according to the requirements of 10 CFR 63.332(a)(3) [DIRS 180319]. These concentrations are then multiplied by the radionuclide-specific biosphere dose conversion factor (BDCF) for the RMEI to produce the dose to the RMEI for individual radionuclides at a given time of output concentration. These individual radionuclide doses are then summed to produce the total dose to the RMEI as a function of time.

M2.4 OVERALL COMPARISON OF EPRI TSPA ANALYSIS AND TSPA-LA MODEL

Overall, the EPRI TSPA Analysis accounts for the same model components and considers the same FEPs as the TSPA-LA Model. The EPRI model implementation is a more simplified abstraction of the relevant processes and uncertainty in model parameters. EPRI uses the logic tree approach and cumulative distributions of failure curves of different EBS components. Even though these distributions were derived from Monte Carlo simulations, uncertainty parameters were not sampled in the EPRI model but, instead, used mean parameter values as input in IMARC.

The main differences in model components include:

- The EPRI Analysis considers a single infiltration domain distinguishing wet and dry conditions, compared to five infiltration bins having different infiltration rates and UZ properties in the TSPA-LA Model.

- EPRI only considers the inventory of spent nuclear fuel (SNF) in commercial spent nuclear fuel (CSNF) packages compared to the TSPA-LA Model, which includes U.S. Department of Energy spent nuclear fuel (DSNF) and high-level radioactive waste (HLW) in DSNF WPs.

- EPRI accounts for the gradual cladding failure following WP failure, whereby the TSPA-LA takes no cladding credit.

- The radionuclide inventory used in the EPRI TSPA Analysis is based on that given in *Initial Radionuclides Inventories* (SNL 2007 [DIRS 180472], Table 7-1), which is superseded by SNL 2007 [DIRS 180472], Table 7-1[a], and considers only 12 radionuclides; whereas the TSPA-LA Model considers 26 radionuclides, including ^{135}Cs and ^{79}Se.

M3. TSPA NOMINAL SCENARIO COMPARISON

M3.1 UNSATURATED FLOW

In the EPRI TSPA Analysis, groundwater flow in the UZ above the repository is represented in a simplified manner by a set of lumped parameters describing:

- Time history of infiltration rate
- Flow focusing factor
- Fraction of the repository that is wet.

All three parameters are represented in the logic tree as uncertain parameters, described in Section M2.2. EPRI considers three climate states corresponding to step changes in infiltration rates (EPRI 2002 [DIRS 158069]):

- Greenhouse period (0 to 1,000 years)
- Interglacial period (1,000 to 2,000 years) similar to present-day climate
- Full glacial period (2,000 to one million years).

Uncertainties in the amount of net infiltration that depend on rainfall and temperature for the different climate states are included in a look-up table of low, moderate, and high net infiltration. In the logic tree, the low infiltration rate is assigned a branch probability of 0.05, the moderate 0.9, and the high 0.05. For each climate state, values of low, moderate, and high net infiltration rate were averaged across the entire repository shown in Table M-1. In the most recent IMARC Version 9, the infiltration rates for the period after 10,000 years were based on an infiltration range of 19 to 64 mm/yr with a mean of 32 mm/yr as specified in NRC Proposed Rule 10 CFR 63.342(c)(2) [DIRS 178394]).

The IMARC implementation of the SZ also considers infiltration beyond the footprint of the repository along the 18 km distance to the location of the RMEI. However, the infiltration rate over the water table of the SZ beyond the repository does not vary with climate states but is fixed to a constant rate. Similarly, the groundwater flow rate in the SZ upstream of the repository is fixed to a steady-state value, resulting in steady-state flow conditions and constant water table

depth. This prescribed infiltration at the water table of the SZ along the flow path results in continuous dilution of radionuclide release from the UZ beneath the repository.

In the TSPA-LA Model, the UZ flow above the repository is simulated by the Site-Scale UZ Flow Process Model described in Section 6.1.4.1. This process model simulated three-dimensional, dual permeability, steady-state flow conditions and generated 16 three-dimensional flow fields for 10th percentile, 30th percentile, 50th percentile, and 90th percentile infiltration boundary condition scenarios and four different climate states within each infiltration scenario. Four climate states are used in the TSPA LA Model: (1) present-day climate for the first 550 years after repository closure; 600 years after emplacement; (2) monsoon climate for the period 550 to 1,950 years after repository closure; (3) glacial-transition climate for the period 1,950 to 10,000 years after repository closure; and (4) post-10,000-years climate, for the period 10,000 to the modeling time frame of 1,000,000 years after repository closure (Section 1, Regulatory Framework).

The 16 flow fields and UZ hydrologic properties generated by the Site-Scale UZ Flow Process Model are used by the Multiscale Thermohydrologic Model (MSTHM) process model (SNL 2007 [DIRS 181383]) for the development of EBS environment thermo-hydrologic (TH) conditions and are accessed directly by the UZ Transport Submodel (SNL 2008 [DIRS 184748], Sections 6 and 8). The four infiltration scenarios are sampled in the TSPA-LA Model once per realization based on the probability weighting factors, shown in Table M-2. Overall infiltration rates for the different climate states used in the EPRI TSPA Analysis (Table M-1) compare reasonably well with the weighted mean infiltration rates used in TSPA-LA Model (Table M-2).

In the IMARC model, heterogeneity within the fractured tuff is described by the flow focusing factor, which is also represented in the logic tree as an uncertain parameter. For the branch of focused flow, the infiltration rate is increased by a factor of four over 25 percent of the area of the repository, but is set to zero for the remaining 75 percent of the repository. The probability for the branch with focused flow is 0.135 and for the branch without focused flow is 0.865.

Estimates of seepage rates into the drifts and seepage fractions used in the EPRI TSPA were based on TSPA-SR analyses, described by uncertain parameters representing a base-case seepage and a high seepage rate, with probabilities of 0.96 and 0.04, respectively (Table M-3a) (Kozak and Kessler 2005 [DIRS 178580], Table 3-2). A comparison of the seepage rates relative to infiltration rates shown in Table M-3a with those used in the TSPA-LA Model summarized in Table M-3b indicates that the seepage rates used in the EPRI TSPA are higher than those in the TSPA-LA Model (Figure 7.7.3-1(a)). A comparison of the seepage fraction given in Table M-3a with those given in the TSPA-LA analysis (Table M-3b) indicates that the seepage fractions used in the EPRI TSPA Analysis are lower than those in the TSPA-LA Model for the corresponding infiltration rate (Figure 7.7.3-1(b)), The 96% probability base-seepage case and 4% probability high-seepage case in the EPRI TSPA Analysis indicate seepage conditions only at infiltration rates greater than 60 mm/yr and 2.4 mm/yr, respectively (Table M-3a). The TSPA-LA Model indicates seepage conditions for the 10% percentile infiltration scenario at infiltration rates of 3.7 mm/yr (Table M-3b). Even though the seepage rates in the EPRI TSPA Analysis are higher, the lower seepage fractions contribute to the lower estimated dose calculated by the EPRI TSPA Analysis as compared to the dose calculated by the TSPA-LA Model.

M3.2 ENGINEERED BARRIER SYSTEM ENVIRONMENT

The EPRI TSPA Analysis neglects thermal effects on water flow, release, and migration of radionuclides for the nominal scenario. It is assumed that there is little to no liquid water present to facilitate radionuclide mobilization and migration until temperatures have decreased to near the local boiling point of water. However, failure distributions generated for each of the three main EBS components (i.e., DS, WP, and cladding) do take into account thermal history within the drift and drift stability due to thermal stresses, described in Section M3.3.

In the TSPA-LA Model, the EBS TH Environment Submodel implements the EBS TH abstraction, which is provided by the MSTHM described in detail in Section 6.1.4.2. The MSTHM subdivides the repository footprint into subdomains and computes temperatures and relative humidity for the WP and associated DS, average drift wall temperature, average invert temperature, average invert saturation, and average invert flux in each subdomain. These TH responses are used as input to the Drift Seepage and Drift Condensation submodels, the WP and DS Degradation model components, the EBS Chemical Environment model, the EBS Flow Submodel, the Waste Form Degradation and Mobilization model component, and the EBS Transport Submodel.

M3.3 WASTE PACKAGE AND DRIP SHIELD DEGRADATION

Waste form degradation and mobilization is computed as part of the near-field radionuclide release and transport submodel EBSCOM in the IMARC. The EBSCOM code uses Monte Carlo simulations to take into account uncertainty and variability of various input parameters in the abstracted corrosion models. These models are used to compute failure curves of various engineered barrier components, which include the DS, WP shell, WP outer closure lid weld, and WP middle closure lid weld. In addition to temperature evolution, the chemical environment associated with the different seepage water bins that was updated and described in *Engineered Barrier System*: *Physical and Chemical Environmental Model* (SNL 2007 [DIRS 177412]) is the principal parameter for the various corrosion processes. The different corrosion processes include:

For DS:

- Initial failure due to undetected manufacturing defect or emplacement error
- General corrosion (main failure mechanism)
- Hydrogen-induced cracking (low probability).

For the WP in the nominal scenario:

- Initial failure due to undetected manufacturing defect
- General corrosion and microbially influenced corrosion (MIC) (main failure mechanism
- Localized corrosion (low probability)
- SCC (for the outer and middle WP closure lids).

In addition to the conditions for the nominal scenario, different versions of the EBSCOM code incorporate the additional effects of seismic events and igneous events, respectively.

The TSPA-LA Model considers five degradation processes, which include: general corrosion, MIC, SCC, early failure, and localized corrosion, which correspond largely to those listed above for the EPRI TSPA Analysis. The implementation of the abstracted degradation modes are described in Section 6.3.5. The TSPA-LA Model uses the WAPDEG software to model general corrosion, MIC, and SCC. Early failure of WPs is directly implemented in GoldSim, accounting for manufacturing and material defects, including defects due to improper heat treatment that augment corrosion processes and result in early failures. WP degradation considers general corrosion, microbially enhanced corrosion, and SCC. In addition, localized corrosion is implemented within the TSPA-LA Model using a submodel (Figure 6.3.5-2), which is only considered for WP degradation. For DS degradation only general corrosion is considered. Overall, TSPA-LA and EPRI consider the same degradation processes, except for localized corrosion that was considered low probability in the EPRI TSPA. Early WP failure in the TSPA-LA Model was defined by a Poisson distribution, which gave a failure distribution and the number of realizations having at least one WP failure, whereby early failure mechanisms applicable for DSs were determined to have no consequence on DS performance and were therefore excluded in TSPA-LA (Section 6.3.5.1.2). In the EPRI TSPA Analysis, early failure of both the DS and WP is considered.

In the EPRI TSPA Analysis, the computed failure distributions curves for the nominal scenario for the DS and for the WP are shown on Figure 4-5 in EPRI (Apted and Ross 2005 [DIRS 182229]). In comparison, the mean WP failure curve for the TSPA-LA nominal scenario (Figure 7.7.3-2) indicates a later failure onset but a steeper curve, where 6,256 WPs failed after one million years.

M3.4 WASTE FORM DEGRADATION AND MOBILIZATION

Waste form degradation and mobilization is computed as part of the near-field radionuclide release and transport submodel COMPASS in IMARC, which includes the Engineered Barrier System Flow and Transport, described in Section M3.5 (Table 7.7.3-1). The COMPASS Near-Field Model consists of different components and solves mass transfer across these compartments, which includes: waste, corrosion product, pallet/basalt, invert, near-field rock matrix and fracture, and farfield rock (Kozak and Kessler 2005 [DIRS 178580], Figure 5-1). In addition, the COMPASS model considers diversion of seepage water entering the drift and flowing into the invert, thereby bypassing the waste.

The waste that contains the radionuclide inventory degrades after water contact following WP and cladding failure. Radionuclides dissolve into water congruently with the waste form degradation rate. Uncertainty in waste form degradation rates is accounted for in the logic tree analysis, using alteration times of 1,000 years; 3,000 years; and 5,000 years and associated probabilities (Kozak and Kessler 2005 [DIRS 178580], Figure 2-3). The EPRI TSPA accounts for gradual cladding failure whereby the fraction of radionuclides in the gap and grain-boundaries of the spent fuel dissolve instantaneously into water.

For specific radionuclides bound in the waste form, the release of radionuclides in water is constrained by solubility limits. The ranges in solubility limits used in TSPA-LA and in the EPRI TSPA Analysis are summarized in Table M-4. In the EPRI TSPA Analysis, the uncertainty in the solubility limits represented by low, moderate, and high values is linked to the

probabilities for the alteration times of the waste form degradation (Kozak and Kessler 2005 [DIRS 178580], Figure 2-3).

The EPRI TSPA Analysis only considers CSNF WPs and the associated inventory, whereby the inventory is based on that given in *Initial Radionuclides Inventories* (SNL 2007 [DIRS 180472], Table 7-1). Furthermore, the EPRI TSPA considers only 12 radionuclides, which were identified to have a significant contribution to total dose. The inventory used in the EPRI TSPA Analysis, in comparison with that used in the current TSPA-LA Model (Table M-5), indicates that the total inventory per WP compares well with that for CSNF in the TSPA-LA Model. The inventory for DSNF and HLW, in a WP that is not considered in the EPRI TSPA, amounts to about 12.5 percent of the inventory in a CSNF WP. The EPRI TSPA accounts for 8,160 CSNF WPs, whereas the TSPA-LA Model considered 8,203 CSNF WPs and 3,413 CDSP WPs containing DSNF and HLW.

The implementation of waste form degradation and mobilization in the TSPA-LA Model is described in detail in Section 6.3.7. The Waste Form Degradation and Mobilization Model Component of the TSPA-LA Model evaluates cladding failure and calculates the rate of degradation for CSNF, DSNF, and HLW forms. Given the radionuclide inventory of the different wastes, the submodel calculates solubilities of radioactive elements (given the solubility limits) and colloidal concentrations of radionuclides in a failed WP and the invert, accounting for the in-package chemistry and drift geochemical environment. The computed solubilities and colloidal concentrations of radionuclides serve as inputs to the EBS Transport Submodel.

M3.5 ENGINEERED BARRIER SYSTEM FLOW AND TRANSPORT

In the COMPASS model, radionuclides released from the waste form are transported by diffusion and advection through the corrosion product, pallet/basalt, invert, and near-field rock fractures and rock matrix (diffusion only) to the far-field rock (Kozak and Kessler 2005 [DIRS 178580], Figure 5-1). The compartments are assumed to be partially saturated, forming a continuous water pathway, and water flows through the near-field fractures only in wet conditions. For wet conditions (release dominated by advective transport), a saturation of 0.01 is assumed inside the WP and the near-field rock fracture saturation is set to 0.05. For dry conditions (release only by diffusion, no advective transport), a saturation of 0.001 is assumed inside the WP and the minimum saturation in the fractures is set to 0.002. The COMPASS model did not consider colloid-facilitated transport of certain radionuclides. The EPRI's assessment of the potential for colloid-facilitated transport indicated that "colloids will not be present at high enough concentrations to be significant," "colloid suspensions will not be stable over necessary time and space scales," and that "colloids will be appreciably filtered, both in the near-field and in the SZ."

The computed radionuclide release rates from the far-field rock is then used as the boundary condition for the UZ submodel, simulating radionuclide transport in the UZ below the repository.

In the TSPA-LA, the EBS is represented by a series of domains, representing the waste form, the corrosion products, the invert, and the EBS-UZ interface, which is described in detail in Section 6.3.8. Radionuclide transport through each domain occurs by advection and diffusion. Diffusion is the primary transport mechanism when the water flow into the WP is negligibly

small. Advection is the primary mechanism when there is appreciable flow through the WP. In general, the treatment of transport through the EBS is similar between the EPRI TSPA Analysis and TSPA-LA Model. However, the TSPA-LA EBS flow and transport model is more complex in incorporating DSNF and HLW, diffusive and advective transport through corrosion cracks and patches, respectively, in the WP, and considering the transport of reversibly and irreversibly sorbed radionuclides on ironhydroxide colloids and waste-form colloids.

M3.6 UNSATURATED ZONE TRANSPORT

In the EPRI TSPA, flow and transport in the UZ below the repository is simulated by the UZ-code represented by several one-dimensional vertical columns approximating spatial variations of repository releases and different lengths corresponding to spatial and temporal variations in the water table. The vertical discretization distinguishes the main UZ layers below the repository, which include: Tsw-35, TSv-5, CHnv-5, and CHnz-6.

The model accounts for variations in saturations associated with variations in permeability, capillary pressure, porosity, and fracture spacing for both fractures and matrix in each geologic layer. Unsaturated flow and transport of radionuclides is downward only. The one-dimensional columns account for coupled matrix-fracture interaction, representing either a single-porosity, single-permeability, or double-porosity/double-permeability medium. Radionuclide transport accounts for dispersion, decay, diffusion, and sorption, which is parameterized for the different layers and columns. Uncertainty in sorption in the UZ is represented in the logic tree approach as retardation (Kozak and Kessler 2005 [DIRS 178580], Figure 2-3), which also includes sorption in the SZ. In the EPRI TSPA Analysis, sorption coefficients are defined for specific radionuclides for volcanic rocks in the UZ and SZ and for the alluvium in the SZ. Only for neptunium is uncertainty in sorption coefficients considered for individual layers, which is represented as low, median, and high values in the logic-tree analysis.

The UZ Transport Submodel of the TSPA-LA Model computes the transport from the EBS through the UZ to the SZ, which is simulated by the Finite Element Heat and Mass (Model) (FEHM) external code, which is linked to GoldSim. The details of the UZ Transport Submodel are described in Section 6.3.9. Input to FEHM is given by transport parameters and associated uncertainties as well as by the rate of radionuclide mass release from the waste emplacement drifts. Processes affecting transport of dissolved or colloidal-bound radionuclides through the UZ include advection, diffusion, sorption, hydrodynamic dispersion, and radioactive decay and ingrowth. Colloids are transported through the UZ primarily in the fractures due to size exclusion, and diffusion into the rock matrix is limited owing to low values of diffusion coefficients.

The main mechanisms for retardation of radionuclides are through sorption. A comparison of the Kd values used in the EPRI TSPA Analysis and in the TSPA-LA Model is given in Table M-6. Median Kd values for plutonium and thorium are lower in the EPRI TSPA compared to the median values in the TSPA-LA Model, whereas the Kd value for neptunium and uranium are greater.

M3.7 SATURATED ZONE TRANSPORT

The SZ submodel in the EPRI TSPA Analysis (SZ code) consists of two segments representing the fractured tuff (15 km downgradient) and the subsequent alluvial segment (5 km), which extends 2 km beyond the location of the RMEI. The SZ was initially implemented using a three-dimensional rectangular model geometry for simulating linear mass transport in a steady-state groundwater flow field. For transport simulations, the model considers steady-state groundwater flow in the fracture only. A more simplified two-dimensional, vertically integrated aquifer model produced similar results and was ultimately used as the SZ submodel in the TSPA Model.

Boundary conditions for the transport simulation include prescribed mass fluxes from the UZ model along the footprint of the repository, and infiltration (head-dependent flux boundary condition) is prescribed along the entire water table. Similar to the UZ model, transport is affected by fracture flow and sorption in the tuff and in the alluvium. Uncertainty in the Kd values in the SZ is included in the logic-tree analysis that is combined with the UZ Kds (Kozak and Kessler 2005 [DIRS 178580], Figure 2-3).

For the TSPA-LA Model, the SZ transport was abstracted from an external three-dimensional SZ model to calculate flow and transport of individual radionuclides through the SZ to the regulatory boundary 18 km downgradient from the repository. A detailed description of the model abstraction is given in Section 6.3.10. The results of the three-dimensional transport model were put in the form of unit-source radionuclide breakthrough curves, which are combined with time-varying radionuclide sources from the UZ to compute the radionuclide transport to the regulatory boundary. In addition, a one-dimensional SZ Transport Submodel is implemented in the TSPA-LA Model to calculate radionuclide daughter products. Similar to the UZ zone, sorption is the main mechanism for retardation of radionuclides in the SZ. A comparison of the sorption coefficients between those used in the EPRI TSPA Analysis and those used in TSPA-LA is presented in Table M-7. In general, median Kd values are similar in the EPRI TSPA and TSPA-LA Model for both fractured volcanic rocks and alluvium.

M3.8 BIOSPHERE

The conversion of radionuclide concentration to dose is through the BDCFs for the RMEI living approximately 18 km downstream of the repository. For this, a representative volume of 3,000 acre-feet for consumption by the RMEI is assumed. The BDCFs used in the EPRI TSPA Analysis and those used in the TSPA-LA are compared in Table M-8. Overall, the EPRI BDCFs are higher than those used in the TSPA-LA, which would result in higher doses in the EPRI TSPA for the same concentration.

M3.9 MEAN ANNUAL DOSE COMPARISON – NOMINAL CASE

The computed mean radionuclide doses for the EPRI nominal scenario are shown on Figure 5-10 in Apted and Ross (2005 [DIRS 182229]). In comparison, the results of the computed mean doses for the TSPA-LA combined Nominal and Waste Package Early Failure Modeling Cases are shown on Figure 7.7.3-3. The results indicate a similar pattern for the nominal scenario characterized by a significant increase in dose after 100,000 years. The early failure dose is

represented by the dose increase after about 1,000 years in the TSPA-LA Model (Figure 7.7.3-3), which is somewhat delayed in the EPRI TSPA Analysis (Apted and Ross 2005 [DIRS 182229], Figure 5-10). Overall, the mean annual dose in the EPRI TSPA is about 2.E-2 mrem/yr compared to about 4.E-1 mrem/yr in the TSPA-LA Model at one million years. The main contributor to total dose at late time is ^{129}I in both cases.

The differences between the EPRI TSPA Analysis and the TSPA-LA Model dose results can be accounted for by differences in:

- Seepage fraction and seepage rates through the repository
- Early failure representation and failure curves of the EBS components
- Inventory, both in terms of waste type and individual radionuclides
- Solubility limits and sorption characteristics in the UZ and SZ.

Seepage rates used in the EPRI TSPA are higher than the corresponding rates used in the TSPA-LA Model (Figure 7.7.3-1(a)). The seepage rates in the EPRI TSPA are based on previous analysis and/or model report results. The lower seepage fraction values for the EPRI TSPA Analysis (Figure 7.7.3-1(b)) results in a lower number of packages being subjected to seepage conditions. This causes a delay in radionuclide release from the EBS and a corresponding lower estimate of total dose compared to the dose calculated by the TSPA-LA Model.

The EPRI TSPA Analysis only accounts for CSNF waste and considers failure of DSs, WPs, and cladding, whereas the TSPA-LA Model accounts for CSNF, DSNF, and HLW, but does not take credit for cladding of CSNF WPs. Consequently, the overall dose release in the EPRI TSPA Analysis is delayed both during the early failure scenario and for the nominal scenario. The WP failure curves in the EPRI TSPA Analysis indicate that only about 5,300 CSNF WPs failed after one million years, whereas the TSPA-LA Model results indicate that on average about 6,256 WPs failed after one-million years, even though the onset of WP failure for the nominal scenario is later (Figure 7.7.3-2) compared to that in the EPRI TSPA Analysis (Apted and Ross 2005 [DIRS 182229], Figure 4-5).

The total CSNF radionuclide inventory used in the EPRI TSPA Analysis is about 10 percent less than the combined inventory for all CSNF and CDSP WPs (Table M-4). During early failure, C-14 is shown to contribute significantly to total dose in the TSPA-LA Model, which is not considered in the EPRI TSPA. At late time, the dominant radionuclides contributing to total dose include ^{129}I, ^{99}Tc, ^{135}Cs, and ^{79}Se in the TSPA-LA Model. The dominant radionuclides in the EPRI TSPA Analysis include ^{129}I followed by ^{237}Np, ^{233}U, and ^{229}Th. However, the EPRI does not consider ^{135}Cs and ^{79}Se.

Solubility limits used in the EPRI TSPA Analysis are significantly lower for neptunium, plutonium, and thorium compared to the range assigned in the TSPA-LA Model. On the other hand, sorption characteristics used in the EPRI TSPA Analysis for the UZ are significantly lower for uranium and plutonium compared to those in the TSPA-LA Model. However, this does not affect ^{129}I, ^{99}Tc, and ^{135}Cs, which represent the main contributors to total dose in the TSPA-LA Model.

In general, the main features of the dose release curves for the nominal scenario compare reasonably well with the TSPA-LA Model. The differences can be related mostly to differences in seepage and in different implementation of the inventory and EBS failure characteristics. This is primarily due to the fact that the EPRI TSPA did not use the most recent analysis and/or model report results.

Table M-1. Net Infiltration Rates (mm/yr) used in the Integrated Multiple Assumptions and Release Code Event Tree Branches for Infiltration

	Scenario			
	Low	**Med**	**High**	**Weighted Avg. Infiltration (mm/yr)**
Greenhouse	1.1	11	19	10.905
Interglacial	1.1	7.2	13.81	7.2255
Full Glacial Maximum	6.8	20	22.12	19.446
Weighting Factor	0.05	0.9	0.05	
Post-10,000 yr	19	32	64	32.95

Source: Kozak and Kessler 2005 [DIRS 178580], Table 3-1.

Table M-2. Infiltration Rates (mm/yr) used in TSPA-LA

	Flux Map Percentile				Weighted Avg. Infiltration (mm/yr)
	10th percentile	30th percentile	50th percentile	90th percentile	
Present-Day	3.7	9.4	13.4	31.4	7.84033
Monsoon	7.2	14.8	17.8	85.1	14.77822
Glacial-Transition	10.8	23.8	32.5	63.4	19.54301
Post-10,000 Year	19.8	36.3	47.1	56.8	29.08325
Weighting Factor	0.6191	0.1568	0.1645	0.0596	

Sources: *Abstraction of Drift Seepage* (SNL 2007 [DIRS 181244], Table 6-5[a]) and DTN: LB0701PAWFINFM.001_R0 [DIRS 179283].

Table M-3a. Seepage Fraction and Flow Rate as a Function of Infiltration Rate

	Base-Seepage Case (Probability 0.96)		High-Seepage Case (Probability 0.04)	
Infiltration Rate* (mm/yr)	**Fraction**	**Flow Rate (m^3/yr)**	**Fraction**	**Flow Rate (m^3/y)**
2.4	0	0	0	0
5	0	0	0.083	0.086
14.6	0	0	0.083	0.401
60	0	0	0.31	0.701
73.2	0.054	0.365	0.376	0.788
213	0.054	4.24	0.452	4.24

Source: Kozak and Kessler 2005 [DIRS 178580].

*The infiltration rate immediately above the repository horizon.

Table M-3b. Summary Statistics for Probabilistic Seepage Evaluation (Intact Drifts)

Summary Statistics for Probabilistic Seepage Evaluation (Intact Drifts)				
	10 Percentile Infiltration Scenario			
	Seepage Rate (kg/yr/WP)	Seepage Rate (m^3/yr/WP)*	Seepage Fraction (%)	Infiltration Rate (mm/yr)**
Present Day	1.2	0.0012	7.6	3.7
Monsoon	4.6	0.0046	13.4	7.2
Glacial Transition	14.4	0.0144	17.0	10.8
	30 Percentile Infiltration Scenario			
	Seepage Rate (kg/yr/WP)	Seepage Rate (m^3/yr/WP)*	Seepage Fraction (%)	Infiltration Rate (mm/yr)**
Present Day	8.1	0.0081	16.7	9.4
Monsoon	20.5	0.0205	22.8	14.8
Glacial Transition	54.0	0.0540	29.5	23.8
	50 Percentile Infiltration Scenario			
	Seepage Rate (kg/yr/WP)	Seepage Rate (m^3/yr/WP)*	Seepage Fraction (%)	Infiltration Rate (mm/yr)**
Present Day	16.5	0.0165	21.6	13.4
Monsoon	30.4	0.0304	25.4	17.8
Glacial Transition	98.4	0.0984	33.9	32.5
	90 Percentile Infiltration Scenario			
	Seepage Rate (kg/yr/WP)	Seepage Rate (m^3/yr/WP)*	Seepage Fraction (%)	Infiltration Rate (mm/yr)**
Present Day	82.9	0.0829	34.9	31.4
Monsoon	470.8	0.4708	52.6	85.1
Glacial Transition	297.1	0.2971	46.1	63.4
	Post-10,000-Year Period			
	Seepage Rate (kg/yr/WP)	Seepage Rate (m^3/yr/WP)*	Seepage Fraction (%)	Infiltration Rate (mm/yr)**
Flow Field 1	35.2	0.0352	27.3	19.8
Flow Field 2	119.8	0.1198	35.5	36.3
Flow Field 3	178.3	0.1783	40.9	47.1
Flow Field 4	237.2	0.2372	45.2	56.8

Source: Modified from SNL 2007 [DIRS 181244], Table 6-6[a]

* SeepageRate(m^3/yr/WP) is calculated by dividing the SeepageRate(kg/yr/WP) by 1,000 kg/m^3, which is the assumed water density.

** Source: SNL 2007 [DIRS 181244], Tables 6-5[a]

Table M-4. Comparison of Solubility Limits used in TSPA-LA and EPRI

	Base-10 Logarithm of the Dissolved Concentration Limit (mg/L)						
	TSPA-LA[1]				EPRI[2]		
	Min.	Max.	Min. Range	Max. Range	median	min	max
NpO_2	-1.090	2.050	-2.890	3.850	-2.998	-4.002	-2.002
Np_2O_5	-0.019	3.290	-2.419	5.690			
Pa	-0.019	3.290	-4.440	3.239	-0.159		
Pu	-1.240	1.110	-4.240	4.110	-2.703	-4.701	-0.701
Th	-2.130	1.140	-4.230	3.240	-3.163	-4.701	-1.701
Sn	-2.390	-1.390	-3.740	-0.040			
U	0.611	2.860	-0.889	4.360	0.830	0.639486	1.690
U	1.510	4.780	0.010	6.280			
U1	0.611	4.780	-0.889	6.280			
I	No solubility limit				5.003		
Tc	No solubility limit				5.037		

Sources: [1] Modified from DTN: MO0702PADISCON.001_R0 [DIRS 179358], Table L-25.
[2] Modified from Kozak and Kessler 2005 [DIRS 178580], Table 5-2.

Table M-5. Inventory used in EPRI Model (Based on SNL 2007) and in TSPA-LA Model

Inventory used in EPRI Model[1]				Inventory used in TSPA-LA Model[2]			
	CSNF	CSNF			CSNF	DSNF	HLW
Element	mol/WP	grams/WP		Element	grams/WP	grams/WP	grams/WP
Ac-227	1.1013E-08	2.5000E-06		Ac-227	2.470E-06	1.219E-03	1.907E-04
Am-241	3.4357E+01	8.2800E+03		Am-241	8.180E+03	2.183E+02	3.749E+01
Am-243	5.1852E+00	1.2600E+03		Am-243	1.245E+03	6.733E+00	5.748E-01
C-14	9.7857E-02	1.3700E+00		C-14	1.353E+00	1.808E+00	0.000E+00
Cl-36	9.0833E-02	3.2700E+00		Cl-36	3.231E+00	4.235E+00	0.000E+00
Cm-245	7.2245E-02	1.7700E+01		Cm-245	1.749E+01	9.251E-02	5.425E-02
Cs-135	3.2667E+01	4.4100E+03		Cs-135	4.357E+03	9.739E+01	1.271E+02
Cs-137	4.3577E+01	5.9700E+03		Cs-137	5.898E+03	9.718E+01	3.021E+02
I-129	***1.3566E+01***	***1.7500E+03***		I-129	1.729E+03	3.564E+01	7.268E+01
Np-237	***1.9536E+01***	***4.6300E+03***		Np-237	4.574E+03	8.144E+01	9.948E+01
Pa-231	4.0173E-05	9.2800E-03		Pa-231	9.168E-03	2.143E+00	1.529E+00
Pb-210	0.0000E+00	0.0000E+00		Pb-210	0.000E+00	3.351E-07	3.399E-10
Pu-238	6.4706E+00	1.5400E+03		Pu-238	1.521E+03	1.249E+01	3.906E+01
Pu-239	***1.8285E+02***	***4.3701E+04***		Pu-239	4.317E+04	2.214E+03	5.582E+02
Pu-240	***8.6667E+01***	***2.0800E+04***		Pu-240	2.055E+04	4.346E+02	4.615E+01
Pu-241	1.1162E+01	2.6900E+03		Pu-241	2.658E+03	2.925E+01	1.216E+00
Pu-242	2.2066E+01	5.3400E+03		Pu-242	5.276E+03	3.016E+01	3.887E+00
Ra-226	0.0000E+00	0.0000E+00		Ra-226	0.000E+00	4.570E-05	2.423E-05
Ra-228	0.0000E+00	0.0000E+00		Ra-228	0.000E+00	1.513E-05	5.997E-06
Se-79	5.3671E-01	4.2400E+01		Se-79	4.189E+01	6.824E+00	7.010E+00
Sn-126	3.7222E+00	4.6900E+02		Sn-126	4.633E+02	9.404E+00	1.704E+01
Sr-90	2.8000E+01	2.5200E+03		Sr-90	2.490E+03	5.220E+01	1.741E+02
Tc-99	***7.7172E+01***	***7.6400E+03***		Tc-99	7.548E+03	1.584E+02	1.013E+03
Th-229	***0.0000E+00***	***0.0000E+00***		Th-229	0.000E+00	3.239E-01	3.298E-03
Th-230	***6.6957E-04***	***1.5400E-01***		Th-230	1.521E-01	1.178E-01	8.115E-04
Th-232	0.0000E+00	0.0000E+00		Th-232	0.000E+00	2.173E+04	2.975E+04
U-232	4.4397E-05	1.0300E-02		U-232	1.018E-02	1.280E+00	4.081E-04
U-233	***2.5021E-04***	***5.8299E-02***		U-233	5.760E-02	5.382E+02	1.944E+01
U-234	***7.5641E+00***	***1.7700E+03***		U-234	1.749E+03	4.732E+02	2.330E+01
U-235	***2.6979E+02***	***6.3401E+04***		U-235	6.264E+04	2.508E+04	1.409E+03
U-236	***1.6483E+02***	***3.8900E+04***		U-236	3.843E+04	1.249E+03	5.987E+01
U-238	***3.3277E+04***	***7.9199E+06***		U-238	7.824E+06	6.845E+05	2.367E+05
Total EPRI		***8.1025E+06***		Total	8.0370E+06	7.3702E+05	2.7050E+05
Total/WP	3.4287E+04	8.1351E+06					
No. of Waste Packages:		**8160**		No. of Waste Packages:	8213		3416
(bold: radionuclides used in EPRI model)							
Total/Repository		6.612E+7			6.601E+7		3442E+9

Sources: [1] SNL 2007 [DIRS 180472], Table 7-1 (EPRI) and Table 7-1[a] (TSPA-LA Model).

[2] DTN: MO0702PASTREAM.001_R0 [DIRS 179925].

[3] Radionuclide inventory given [mol/WP] in Apted et. al., 2006 [DIRS 182231] Table 5-29.

Table M-6. Unsaturated Zone Layer Distribution Coefficients

	EPRI[1]	TSPA-LA[2]
	Median Kd	Median Kd
Radionuclide	[mL/g]	[mL/g]
I	0	0
Tc	0	0
C	0	0
Np	1.5	0.5 - 1.0
U	1	0.2 – 0.5
Am	400	5,500
Pa	500	5,500
Cs	4	2 – 5,000
Se	2	8.6 - 14.3
Pu	50	70 - 100
Sr	18	25 – 1,025
Th	2,500	5,500 – 15,500

Sources: [1] Modified from Apted and Ross 2005 [DIRS 182229], Table 5-4.
[2] Modified Table 6.3.9-2: DTN: LA0408AM831341.001_R0 [DIRS 171584] and DTN: LB0701PAKDSESN.001_R0 [DIRS 179299].

Table M-7. Saturated Zone Layer Distribution Coefficients

	EPRI Median Kd[1]		TSPA-LA Median Kd[2]	
	Volcanics	Alluvium	Volcanics	Alluvium
	[mL/g]	[mL/g]	[mL/g]	[mL/g]
Np	1.50E+00	3.30E+00	1.43E+00	6.35E+00
U	5.00E+00	2.20E+00	6.78E+00	4.60E+00
Th	2.50E+03	2.50E+03	5.50E+03	5.50E+03
Pu	7.50E+01	7.50E+00	1.04E+02	1.00E+02

Sources: [1] Modified from Apted and Ross 2005 [DIRS 182229],Table 5-5.
[2] Modified from Table L-46, Source: DTN: SN0310T0502103.009_R0 [DIRS 168763] and LA0702AM150304.001_R5 [DIRS 184763].

Table M-8. BDCFs used in EPRI Model

	EPRI-BDCF[1]	TSPA-LA: Mean BDCF[2]
Radionuclide	Sv/yr per Bq/m^3	Sv/yr per Bq/m^3
TC-99	3.3724E-09	1.68E-09
I-129	1.1505E-06	1.48E-07
Np-237	1.7793E-06	2.79E-07
U-233	6.9646E-07	9.20E-08
TH-229	3.0884E-05	2.62E-06
PU-239	6.1914E-06	9.74E-07
U-235	3.9934E-07	9.59E-08
U-238	3.7177E-07	7.94E-08
U-234	3.8870E-07	8.27E-08
Th-230	5.3621E-05	1.10E-06
PU-240	5.4570E-06	9.71E-07
U-236	3.1861E-07	7.73E-08

Source: [1] Modified from Apted and Kessler 2005 [DIRS 182228], Table 5-7.
[2] Modified from Table L-42, Source: DTN: MO0702PAGBDCFS.001_R0 [DIRS 179327].

INTENTIONALLY LEFT BLANK

APPENDIX N
DERIVATION OF IMPLEMENTING EQUATIONS FOR WASTE PACKAGE PARSING AND AVERAGE DAMAGE AREA

N1. DERIVATION OF IMPLEMENTING EQUATIONS FOR WASTE PACKAGE PARSING AND AVERAGE DAMAGE AREA

In the Total System Performance Assessment for the License Application (TSPA-LA) Model, the failure properties of a group of waste packages (WPs) are assigned to the entire group of failed WPs. If the group of WPs contains WPs failing by different mechanisms, average failure properties are applied for all of the failed WPs in the group. In general, averaging WP failure properties can lead to unintended model responses, such as overestimating the opening area on a failed WP. Therefore, to mitigate unintended model responses introduced by averaging WP failure properties for WPs with very different properties, it is desirable to define the WP groups based on WP failure properties. This appendix describes the calculations implemented in the TSPA-LA Model that divide the entire set of WPs into smaller WP groups.

WP damage mechanisms and dripping conditions are the two characteristics that define the WP groups implemented in the TSPA-LA Model. As discussed in Section 6.1.5, the TSPA-LA Model divides that total number of emplaced WPs into five percolation subregions and two fuel types. For modeling purposes, each of these 10 WP groups, is then further divided into three smaller groups based on WP damage mechanism and dripping conditions. Therefore, the TSPA-LA Model includes calculations for 30 different WP groups each time the model is exercised.

The implementing equations defining the WP groups are discussed first for the Nominal Scenario Class. Following the discussion of the Nominal Scenario Class, the adjustments necessary to accommodate the other scenario classes are described.

N2. NOMINAL SCENARIO CLASS

This section of the text describes the derivation for the number of WPs in each WP group and the average WP damage area for a WP group, modeled in the Nominal Scenario Class. In the Nominal Scenario Class there are two major mechanisms for WP damage:

1. Stress corrosion cracking (SCC) coupled with general corrosion
2. Localized corrosion coupled with general corrosion

Early failure of the WP, seismic-induced WP damage, and igneous intrusion WP damage are excluded from the Nominal Scenario Class, but are captured in separate modeling cases.

WP failure and damage area resulting from the first damage mechanism listed above, SCC coupled with general corrosion, is calculated as a function of time using the software code WAPDEG V4.07 (STN: 10000-4.07-00 [DIRS 161240] and STN: 10000-4.07-01 [DIRS 181064]). WAPDEG V4.07 calculates the fraction of the WPs that are failed by either SCC or general corrosion. WAPDEG V4.07 also calculates the average number of SCCs on a failed WP and the average number of general corrosion patches on a failed WP. Coupled with the area of each opening and the total surface area of the WP, the dynamically linked libraries (DLL) output can be used to calculate the fraction of the WP surface area damaged by SCC and/or general corrosion.

WP failure resulting from the second damage mechanism listed above, localized corrosion coupled with general corrosion, is calculated as a function of time using the TSPA-LA Localized Corrosion Initiation Submodel, a separate GoldSim analysis that is described in Section 6.3.5.2.3. WP damage area from localized corrosion is implemented in the TSPA-LA Model as a fixed damage area once localized corrosion failure occurs. The TSPA-LA Localized Corrosion Initiation Submodel calculates the fraction of WPs that are failed by localized corrosion coupled with general corrosion as a function of time. The results are stored as external files and read into the TSPA-LA Model using the software code PassTable1D_LA V2.0 (STN: 11142-2.0-00 [DIRS 181051]). Two different localized corrosion mechanisms, termed LC1 and LC2, are considered in the equations derived below. As derived below, the WP damage area from each localized corrosion mechanism does not need to be the same amount. The TSPA-LA Model only considers crown seepage localized corrosion from one mechanism, but the capability to consider a second mechanism is retained in the model. These two mechanisms could represent crown seepage localized corrosion resulting separately from early and late failed drip shields (DS). Because the damage area from each localized corrosion mechanism is treated as a fixed value, the mechanism for localized corrosion damage is not relevant to the equations derived below.

In order to derive general equations that can be used to determine the average properties of the WP group, certain simplifications are modeled.

1. The WP surface area damage by localized corrosion is instantly damaged when a localized corrosion penetration occurs on a WP. The damage area per WP is a fixed value for each localized corrosion mechanism considered.

2. SCC and general corrosion failures develop independently from localized corrosion on different areas of the WP. Furthermore, an area that is previously damaged by localized corrosion or SCC/general corrosion is not also subject to SCC/general corrosion or localized corrosion until the entire WP surface area is damaged. This simplification allows WP damage area due to multiple damage mechanisms to be additive on a WP. Thus, if localized corrosion occurs on one patch and general corrosion occurs on one patch, the two patch openings will not be at the same location on the WP. This simplification maximizes the opening area on a WP.

Considering the discussion presented above, there are seven types of damage areas that are possible in the TSPA-LA Model from these two sources. Figure N-1 graphically depicts the definition of these seven areas. The seven areas, as identified on Figure N-1, are:

A. SCC and general corrosion damage without any localized corrosion damage
B. SCC and general corrosion damage with LC2 damage and without LC1 damage
C. SCC and general corrosion damage with LC1 damage and without LC2 damage
D. SCC and general corrosion damage with both LC1 and LC2 damage
E. LC1 and LC2 damage without SCC or general corrosion damage
F. LC2 damage without LC1 damage or SCC and general corrosion damage
G. LC1 damage without LC2 damage or SCC and general corrosion damage.

Furthermore, if all WPs eventually fail by the SCC and general corrosion mechanism, then damage types E, F, and G become null sets.

It should be noted that the derivations of the functions defined below are valid for any damage mode and should not be limited to SCC/general corrosion and localized corrosion conditions.

The following variables are identified as inputs in the calculations that are coupled together to assess WP damage area on a group of failed WPs for the Nominal Scenario Class. These input values and time histories are considered in the derivation of the damage area equation for each of the seven damage types discussed above. Additional definitions are presented in the derivation discussion.

$f_{fail,WAPDEG}(t)$ The fraction of the total number of WPs that are failed by SCC or general corrosion processes as a function of time.

$f_{dam,SCC,WAPDEG}(t)$ The average fraction of the WP surface area damaged by SCC as a function of time on a WP failed by SCC or general corrosion.

$f_{dam,patch,WAPDEG}(t)$ The average fraction of the WP surface area damaged by general corrosion patches as a function of time on a WP failed by SCC or general corrosion.

$f_{fail,LC1}(t)$ The fraction of the total number of WPs that are failed by localized corrosion mechanism #1 as a function of time.

$f_{dam,LC1}(t)$ The average fraction of the WP surface area damaged by localized corrosion patches as a function of time on a WP that is failed by localized corrosion mechanism #1.

$f_{fail,LC2}(t)$ The fraction of the total number of WPs that are failed by localized corrosion mechanism #2 as a function of time.

$f_{dam,LC2}(t)$ The average fraction of the WP surface area damaged by localized corrosion patches as a function of time on a WP that is failed by localized corrosion mechanism #2.

f^{tmax} The fraction of damage or failure evaluated at the end of the simulated duration.

$f^{C,tmax}$ The complement to the fraction of damage or failure evaluated at the end of the simulated duration.

N_{Total} The total number of WPs distributed between the seven groups including WPs that do not fail by any damage mechanism in the simulated duration

For consideration in the TSPA-LA Model, WP damage areas will be derived for seven WP damage mechanisms, or combinations of damage mechanisms. Failure fractions for each of the seven damage mechanisms are identified as f_A, f_B, f_C, f_D, f_E, f_F, and f_G, where the subscript is consistent with the regions described below and depicted on Figure N-1. These calculations

become part of the WP parsing calculations in the TSPA-LA Model. These calculations are used to determine the size of each WP group in the Nominal Scenario Class. For classification purposes, the fraction of the total WPs assigned to each of the seven WP failure groups is determined by the damage state of the WPs at the simulated duration. Thus, all WPs assigned to WP Group D have an end state combining SCC coupled with general corrosion damage, LC1 damage, and LC2 damage.

Applying the principals of inclusion and exclusion, at the end of the simulated duration, the fraction of WPs that are damaged by SCC/general corrosion only, without localized corrosion from damage mechanisms #1 or #2 is:

$$f_A = f_{fail,WAPDEG}^{t\max} \cap f_{fail,LC1}^{C,t\max} \cap f_{fail,LC2}^{C,t\max} \quad \text{(Eq. N-1)}$$

where $f_{fail,LC1}^{C,t\max}$ and $f_{fail,LC2}^{C,t\max}$ define the complement to the fraction of WPs that are failed by localized corrosion mechanism #1 and localized corrosion mechanism #2, respectively. The complement fractions define the fraction of WPs that are not failed by the mechanism indicated.

At the end of the simulated duration, the fraction of WPs that are damaged by SCC/general corrosion and also have damage from LC2 but not any damage from LC1 is:

$$f_B = f_{fail,WAPDEG}^{t\max} \cap f_{fail,LC1}^{C,t\max} \cap f_{fail,LC2}^{t\max}. \quad \text{(Eq. N-2)}$$

At the end of the simulated duration, the fraction of WPs that are damaged by SCC/general corrosion and also have damage from LC1 but not any damage from LC2 is:

$$f_C = f_{fail,WAPDEG}^{t\max} \cap f_{fail,LC1}^{t\max} \cap f_{fail,LC2}^{C,t\max}. \quad \text{(Eq. N-3)}$$

At the end of the simulated duration, the fraction of WPs that are damaged by SCC/general corrosion and also have damage from LC1 and LC2 is:

$$f_D = f_{fail,WAPDEG}^{t\max} \cap f_{fail,LC1}^{t\max} \cap f_{fail,LC2}^{t\max}. \quad \text{(Eq. N-4)}$$

At the end of the simulated duration, the fraction of WPs that are damaged by LC1 and LC2, but have no SCC/general corrosion damage is:

$$f_E = f_{fail,WAPDEG}^{C,t\max} \cap f_{fail,LC1}^{t\max} \cap f_{fail,LC2}^{t\max} \quad \text{(Eq. N-5)}$$

where $f_{fail,WAPDEG}^{C,t\max}$ defines the compliment to the fraction of WPs that are failed SCC and/or general corrosion.

At the end of the simulated duration, the fraction of WPs that are damaged by LC2 only is:

$$f_F = f_{fail,WAPDEG}^{C,t\max} \cap f_{fail,LC1}^{C,t\max} \cap f_{fail,LC2}^{t\max} \quad \text{(Eq. N-6)}$$

At the end of the simulated duration, the fraction of WPs that are damaged by LC1 only is:

$$f_G = f_{fail,WAPDEG}^{C,t\max} \cap f_{fail,LC1}^{t\max} \cap f_{fail,LC2}^{C,t\max} \quad \text{(Eq. N-7)}$$

Using the simplification that the SCC, general corrosion, and localized corrosion damage are independent events, the fraction of WPs failing by the intersection of two or more mechanisms is equal to the product of the individual failure fractions ($f_i \cap f_j = f_i f_j$). Furthermore, the definition of a complement is

$$f_i^C = 1 - f_i \quad \text{(Eq. N-8)}$$

Therefore, the above equations can be rewritten as

$$f_A = f_{fail,WAPDEG}^{t\max} \times (1 - f_{fail,LC1}^{t\max}) \times (1 - f_{fail,LC2}^{t\max}) \quad \text{(Eq. N-9)}$$

$$f_B = f_{fail,WAPDEG}^{t\max} \times (1 - f_{fail,LC1}^{t\max}) \times f_{fail,LC2}^{t\max} \quad \text{(Eq. N-10)}$$

$$f_C = f_{fail,WAPDEG}^{t\max} \times f_{fail,LC1}^{t\max} \times (1 - f_{fail,LC2}^{t\max}) \quad \text{(Eq. N-11)}$$

$$f_D = f_{fail,WAPDEG}^{t\max} \times f_{fail,LC2}^{t\max} \times f_{fail,LC1}^{t\max} \quad \text{(Eq. N-12)}$$

$$f_E = (1 - f_{fail,WAPDEG}^{t\max}) \times f_{fail,LC2}^{t\max} \times f_{fail,LC1}^{t\max} \quad \text{(Eq. N-13)}$$

$$f_F = (1 - f_{fail,WAPDEG}^{t\max}) \times (1 - f_{fail,LC1}^{t\max}) \times f_{fail,LC2}^{t\max} \quad \text{(Eq. N-14)}$$

$$f_G = (1 - f_{fail,WAPDEG}^{t\max}) \times f_{fail,LC1}^{t\max} \times (1 - f_{fail,LC2}^{t\max}) \quad \text{(Eq. N-15)}$$

The number of WPs damaged by each of the seven mechanisms at the end of the simulated duration is equal to the product of the failure fraction and the total number of WPs to be modeled, N_{Total}. If a WP does not fail by one of these modes in the simulated duration, then it is not considered in the average damage calculations. For this reason, it is necessary to normalize the WP failure fractions so that the equations only represent the WPs that will be damaged by the applicable mechanism in the simulated duration. Normalizing the failure fractions is done by dividing the time-dependent failure fraction by its final value.

Once the number of WPs in each of the seven WP groups is determined, the average fraction of WP surface area damaged on the failed WPs in each group is then determined.

For Group A, the average damage fraction on the failed WPs is calculated by the WAPDEG DLL:

$$f_{dam,A}(t) = f_{dam,WAPDEG}(t) = \mathrm{f_{dam,SCC,WAPDEG}(t) + f_{dam,patch,WAPDEG}(t).} \quad \text{(Eq. N-16)}$$

For Groups F and G, the average damage fraction on the failed WPs is equal to the fixed values:

$$f_{dam,F}(t) = f_{dam,LC2} \quad \text{(Eq. N-17)}$$

$$f_{dam,G}(t) = f_{dam,LC1}. \quad \text{(Eq. N-18)}$$

When determining the average damage area for a WP that will fail by a combination of two or more mechanisms, the damage area for the group needs to be applied as an average to the entire group. Given that SCC and general corrosion damage may not occur at the same time as localized corrosion, but given that eventually both will occur for the group, the average area needs to consider the timing at which the damage occurs. For simplification, LC1 and/or LC2 damage to a WP occurs instantly once LC1 and/or LC2 failures have occurred. In the equations derived below, the total surface area damaged by one mechanism or a combination of mechanisms cannot exceed the total WP surface area; therefore, damage fractions are limited to the value 1.

For Group B, which has damage due to SCC/general corrosion and LC2 combined, the average damage area for the group considers the total damage area from the damage mechanisms and then divides the total damage area by the number of failed WPs in the group. The parts are:

B1. WPs with SCC/general corrosion only damage prior to LC2 damage
B2. WPs with LC2 damage only prior to SCC/general corrosion damage
B3. WPs with both LC2 damage and SCC/general corrosion damage.

The failure fractions defined previously are the time-dependent failure fractions of all WPs that are failed by a specified mechanism. Because Group B only contains WPs that will fail by SCC/general corrosion and LC2 combined, the failure fractions applied in these equations should only consider those WPs that will fail by both mechanisms and thus each failure fraction must have a final value of one. Therefore, the SCC/general corrosion and LC2 failure fractions are both normalized by the final failure fraction.

$$f^{norm}_{fail,WAPDEG}(t) = \frac{f_{fail,WAPDEG}(t)}{f^{t\max}_{fail,WAPDEG}} \quad \text{(Eq. N-19)}$$

$$f^{norm}_{fail,LC2}(t) = \frac{f_{fail,LC2}(t)}{f^{t\max}_{fail,LC2}}. \quad \text{(Eq. N-20)}$$

Eventually WPs in Group B with SCC/general corrosion only damage prior to LC2 damage (B1) and WPs with LC2 damage only prior to SCC/general corrosion damage (B2) will eventually become WPs with both LC2 damage and SCC/general corrosion damage (B3). However, as time elapses, the number of B1 WPs, B2 WPs, and B3 WPs changes according to the time histories of the applicable failure fractions. Prior to this time, the average damage on a B1 WP is the SCC/general corrosion damage fraction, but the average Group B damage fraction is the weighted average of B1, B2, and B3 damage fractions. When calculating the average damage area to all Group B WPs, the damage area contribution from B1 WPs to the Group B total as a

function of time is the product of the fraction of WP surface area damaged by SCC/general corrosion and the fraction of WPs in Group B with only SCC/general corrosion damage.

$$f_{dam,B1}(t) = f_{dam,WAPDEG}(t) \times f^{norm}_{fail,WAPDEG}(t) \times (1 - f^{norm}_{fail,LC2}(t)) \quad \text{(Eq. N-21)}$$

The damage area contribution from B2 WPs to the Group B total as a function of time is the product of the fraction of WP surface area damaged by LC2 and the fraction of WPs in Group B with only LC2 damage.

$$f_{dam,B2}(t) = f_{dam,LC2} \times f^{norm}_{fail,LC2}(t) \times (1 - f^{norm}_{fail,WAPDEG}(t)) \quad \text{(Eq. N-22)}$$

The damage area contribution from B3 WPs to the Group B total as a function of time is the product of the fraction of WP surface area damaged by SCC/general corrosion and LC2 and the fraction of WPs in Group B with both SCC/corrosion and LC2 damage.

$$f_{dam,B3}(t) = \min[1, f_{dam,LC2} + f_{dam,WAPDEG}(t)] \times f^{norm}_{fail,LC2}(t) \times f^{norm}_{fail,WAPDEG}(t) \quad \text{(Eq. N-23)}$$

The average damage for Group B WPs is then the sum of the products of the number of WP in each subgroup and the damage area for the subgroup divided by the total number of Group B WPs that are failed as a function of time. Expressed as fractions, the equation simplifies to:

$$f_{dam,B}(t) = \min\left(1, \frac{[f_{dam,LC2} \times f^{norm}_{fail,LC2}(t) + f_{dam,WAPDEG}(t) \times f^{norm}_{fail,WAPDEG}(t)]}{f^{norm}_{fail,LC2}(t) + f^{norm}_{fail,WAPDEG}(t) - f^{norm}_{fail,LC2}(t) \times f^{norm}_{fail,WAPDEG}(t)}\right) \quad \text{(Eq. N-24)}$$

Analogous equations can be derived for the Group C WPs but the equations will be the same as those in Equations N-19 through N-24, replacing LC2 fractions with LC1 equivalents. Likewise, analogous equations can be derived for the Group E WPs but the equations will be the same as those in Equations N-19 through N-24, replacing SCC/general corrosion fractions and with LC1 equivalents.

For Group D, which at the end of the simulation has damage due to SCC/general corrosion and LC1 and LC2 combined, the average damage area for the group as a function of time considers the total damage area from the damage mechanisms and then divides the total damage area by the number of failed WPs in the group. The parts are:

D1. WPs with SCC/general corrosion only damage prior to LC1 and LC2 damage
D2. WPs with LC1 damage only prior to SCC/general corrosion and LC2 damage
D3. WPs with LC1 and SCC/general corrosion damage only prior to LC2 damage
D4. WPs with LC1 and LC2 damage only prior to SCC/general corrosion damage
D5. WPs with LC2 damage only prior to SCC/general corrosion and LC1 damage
D6. WPs with LC2 and SCC/general corrosion damage only prior to LC1 damage
D7. WPs with SCC/general corrosion and LC1 and LC2 damage.

Because Group D only contains WPs that will fail by SCC/general corrosion and localized corrosion combined and the failure fractions are defined for all WPs, the failure fractions are normalized by the value at the end of the simulation. The SCC/general corrosion and localized

corrosion failure fractions are normalized. Equations N-19, N-20, and N-25 are the normalization equations.

$$f_{fail,LC1}^{norm}(t) = \frac{f_{fail,LC1}(t)}{f_{fail,LC1}^{t\max}} \quad \text{(Eq. N-25)}$$

The damage contribution from D1 WPs to Group D total as a function of time is the product of the fraction of WP surface area damaged by SCC/general corrosion and the fraction of WPs in Group D with only SCC/general corrosion damage.

$$f_{dam,D1}(t) = f_{dam,WAPDEG}(t) \times f_{fail,WAPDEG}^{norm}(t) \times [(1 - f_{fail,LC1}^{norm}(t)) \times (1 - f_{fail,LC2}^{norm}(t))] \quad \text{(Eq. N-26)}$$

The damage contribution from D2 WPs to Group D total as a function of time is the product of the fraction of WP surface area damaged by LC1 and the fraction of WPs in Group D with only LC1 damage.

$$f_{dam,D2}(t) = f_{dam,LC1} \times f_{fail,LC1}^{norm}(t) \times [(1 - f_{fail,WAPDEG}^{norm}(t)) \times (1 - f_{fail,LC2}^{norm}(t))] \quad \text{(Eq. N-27)}$$

The damage contribution from D3 WPs to Group D total as a function of time is the product of the fraction of WP surface area damaged by LC1 and SCC/general corrosion and the fraction of WPs in Group D with only LC1 and SCC/general corrosion damage.

$$f_{dam,D3}(t) = \min[1, f_{dam,WAPDEG}(t) + f_{dam,LC1}] \times f_{fail,LC1}^{norm}(t) \times f_{fail,WAPDEG}^{norm}(t) \times (1 - f_{fail,LC2}^{norm}(t)) \quad \text{(Eq. N-28)}$$

The damage contribution from D4 WPs to Group D total as a function of time is the product of the fraction of WP surface area damaged by LC1 and LC2 and the fraction of WPs in Group D with only LC1 and LC2 damage.

$$f_{dam,D4}(t) = \min[1, f_{dam,LC1}(t) + f_{dam,LC2}] \times f_{fail,LC1}^{norm}(t) \times f_{fail,LC2}^{norm}(t) \times (1 - f_{fail,WAPDEG}^{norm}(t)) \quad \text{(Eq. N-29)}$$

The damage contribution from D5 WPs to Group D total as a function of time is calculated using Equation N-27 with the LC1 and LC2 inputs reversed.

The damage contribution from D6 WPs to Group D total as a function of time is calculated using Equation N-28 with the LC1 and LC2 inputs reversed.

The damage contribution from D7 WPs to Group D total as a function of time is the product of the fraction of WP surface area damaged by LC1, LC2, and SCC/general corrosion and the fraction of WPs in Group D with LC1, LC2, and SCC/general corrosion damage.

$$f_{dam,D7}(t) = \min[1, f_{dam,LC1} + f_{dam,LC2} + f_{dam,WAPDEG}(t)] \times f^{norm}_{fail,LC1}(t) \times f^{norm}_{fail,LC2}(t) \times f^{norm}_{fail,WAPDEG}(t) \quad \text{(Eq. N-30)}$$

The average damage for Group D WPs is then

$$f_{dam,D}(t) = \min\left(1, \frac{\begin{array}{l}[f_{dam,D1}(t) + f_{dam,D2}(t) + f_{dam,D3}(t) + f_{dam,D4}(t) + \\ f_{dam,D5}(t) + f_{dam,D6}(t) + f_{dam,D7}(t)]\end{array}}{\begin{array}{l}f^{norm}_{fail,LC1}(t) + f^{norm}_{fail,LC2}(t) + f^{norm}_{fail,WAPDEG}(t) - \\ f^{norm}_{fail,LC2}(t) \times f^{norm}_{fail,WAPDEG}(t) - \\ f^{norm}_{fail,LC1}(t) \times f^{norm}_{fail,WAPDEG}(t) - f^{norm}_{fail,LC1}(t) \times f^{norm}_{fail,LC2}(t) + \\ f^{norm}_{fail,LC1}(t) \times f^{norm}_{fail,LC2}(t) \times f^{norm}_{fail,WAPDEG}(t)\end{array}}\right) \quad \text{(Eq. N-31)}$$

N3. WP PARSING

For the Nominal Scenario Class, the emplaced number of WP are first binned by fuel type and percolation subregion (see Section 6.3.2) before assigning WPs to one of the seven groups described above. There are two fuel types and five percolation subregions for a total of 10 WP subgroups. These 10 subgroups are then further divided into three groups each for a total of 30 WP groups. Equations N-1 through N-31 are applicable to each of the 10 subgroups. A subset of these equations applies to the smaller set of three WP groups within each of the 10 subgroups. The first of these three groups contains the subset of WPs that are not exposed to drift seepage. According to the Drift Seepage Abstraction (see Section 6.3.3), a certain fraction of WPs within each percolation subregion are in locations that are not susceptible to drift seepage. Because the WPs in this group are not susceptible to localized corrosion, the failed WPs in this group belong to Group A described above. The second of these three groups contains the subset of WPs that are subject to drift seepage, but are not susceptible to localized corrosion as a result of exposure to corrosive seepage water. These WPs are the subset of WPs in a dripping location that do not have the environmental conditions (e.g., pH, temperature, DS failure, etc.) that initiate localized corrosion when the WP is exposed to the seepage water. Like the non-seeping group, the WPs in this group are not susceptible to localized corrosion and the failed WPs in this group also belong to Group A described above. The third group contains the subset of WPs that are subject to drift seepage and are also susceptible to localized corrosion following exposure to seepage water. Because the WPs in this group are susceptible to localized corrosion, the failed WPs in this group belong to groups B through G described above.

To determine the number of WPs that populate each of the 30 WP groups, the group of WPs that comprise the first and second subsets are the WPs in Group A. These WPs have no localized corrosion. For the first group, the non-seeping group, the number of WPs of each fuel type in each percolation subregion is the product of the number of WPs of each fuel type in each percolation subregion assigned to Group A and the fraction of WPs that are not exposed to drift seepage. The number of WPs in the second group, the seeping group without localized corrosion, is the balance of the Group A WPs and is the product of the number of WPs of each fuel type in each percolation subregion, the number of WPs in Group A, and the fraction of WPs that are exposed to drift seepage. For the third group, the seeping group with localized corrosion, the number of WPs of each fuel type in each percolation subregion is the number of WPs of each fuel type in each percolation subregion assigned to Groups B through G ($=N_{TOTAL}*(f_B+f_C+f_D+f_E+f_F+f_G)$, where N_{TOTAL} is the number of WPs of a specified fuel type in a specified percolation subregion).

Within the TSPA-LA Model, for WPs modeled in the third WP group, those WPs that incur localized corrosion damage by either localized corrosion mechanism, an average damage area is determined for the WP group. The average damage area is the sum of the products of the fraction of damage on each WP of type B, C, D, E, F, or G, above, and the fraction of WPs failed that belong to each WP type B, C, D, E, F, or G, above divided by the sum of the fraction of WPs failed that belong to each WP type B, C, D, E, F, or G

$$f_{dam}^{avg,LC}(t) = \frac{\sum_{i=B}^{G} f_{dam,i}(t) \times f_{fail,i}(t)}{\sum_{i=B}^{G} f_{fail,i}(t)} \quad \text{(Eq. N-32)}$$

Where $f_{fail,i}(t)$ defines the fraction of WP belonging to each of the six applicable groups that are failed as a function of time. These fractions are calculated using a time-dependent form of Equation N-10 through Equation N-15. The time-dependent form replaces the value at the end of the simulation, f^{tmax}, with the equivalent value for the current time.

N4. DISRUPTIVE EVENTS

When seismic or igneous event(s) are considered, Equations N-1 though N-32 need to be updated to reflect the additional damage caused by the event(s). In the Igneous Intrusion Modeling Case of the Igneous Scenario Class, all of the WPs in a group will be subjected to the same igneous damage area because the igneous intrusion events cause all of the WPs to fail at the time of the event, and the amount of damage to the WP is the entire WP surface area (Section 6.5.1). Thus, when computing an average damage area for each WP group, the amount of damage to a WP from the igneous intrusion event is additive to any prior damage caused by nominal processes. Similarly, in the Seismic Scenario Class, all WPs in a group will be subjected to the same seismic damage area because the events cause all WPs to fail at the time of the event and the amount of seismic damage is calculated as an average damage for all failed WPs. Thus, when computing an average damage area for each WP group, the amount of damage to a WP from each seismic event is additive to any prior damage caused by nominal processes or seismic events.

For the Igneous Intrusion Modeling Case of the Igneous Scenario Class, all of the WPs are impacted and the damage area becomes unity for all modeled WPs (Section 6.5.1). Therefore, there is no need to consider WP damage area averaging for this case. Prior to the igneous intrusion event, the average WP damage area is calculated under nominal repository conditions.

When seismic consequences are considered, the equations for the average WP damage fraction need to be updated to reflect additional damage caused by the seismic event. For the Seismic Scenario Class, the equations derived below are applicable to both modeling cases of the Seismic Scenario Class presented in Sections 6.6.1 and 6.6.2. The mechanism of damage, vibratory ground motion, or fault displacement, is irrelevant to the derivation of the equations provided that the appropriate failure fraction and damage fractions are applied. In addition, when considering the average of a group of WPs, the average damage area may not increase by the amount of the seismic damage because WPs that are already fully failed will not be subjected to additional damage and thus the contribution of damage from these WPs will not increase following an event.

The revised equations considering the consequences of a seismic event are presented below.

Adding in seismic consequences affects all Group A, F, and G WPs similarly. If the fraction of seismic failed WPs is $f_{fail,seismic}(t)$ and the amount of seismic damage is $f_{dam,seismic}(t)$, then Equation N-16 is modified as follows:

$$f_{dam,A}(t) = \min[1, f_{dam,WAPDEG}(t) + f_{dam,seismic}(t)] \quad \text{(Eq. N-33)}$$

Since all WPs are failed following the seismic event, but localized corrosion failures may not be completed by the time of the seismic event, there may be seismic-damaged WPs with and without localized corrosion. The average damage area considers the fraction of WPs that have localized corrosion damage and Equations N-17 and N-18 are modified as follows:

$$f_{dam,F}(t) = f^{norm}_{fail,LC2}(t) \times \min[1, f_{dam,seismic}(t) + f_{dam,LC2}] + (1 - f^{norm}_{fail,LC2}(t)) \times f_{dam,seismic}(t) \quad \text{(Eq. N-34)}$$

$$f_{dam,G}(t) = if^{norm}_{fail,LC1}(t) \times \min[1, f_{dam,seismic}(t) + f_{dam,LC1}] + (1 - f^{norm}_{fail,LC1}(t)) \times f_{dam,seismic}(t) \quad \text{(Eq. N-35)}$$

With the added constraint that the seismic and SCC/general corrosion damage cannot exceed total surface area of the failed WPs, Equation N-21 can then be rewritten as:

$$f_{dam,seismic,B1}(t) = \min[1, f_{dam,seismic}(t) + f_{dam,WAPDEG}(t)] \times f^{norm}_{fail,WAPDEG}(t) \times (1 - f^{norm}_{fail,LC2}(t)) \quad \text{(Eq. N-36)}$$

Similarly, with the added constraint that the seismic and localized corrosion damage cannot exceed total surface area of the failed WPs, the Equation N-22 can then be rewritten as:

$$f_{dam,seismic,B2}(t) = \min[1, f_{dam,seismic}(t) + f_{dam,LC2}] \times f^{norm}_{fail,LC2}(t) \times (1 - f^{norm}_{fail,WAPDEG}(t)) \quad \text{(Eq. N-37)}$$

It follows then that, with the added constraint that the seismic and SCC/general corrosion and localized corrosion damage cannot exceed total surface area of the failed WPs, the Equation N-23 can then be rewritten as:

$$f_{dam,B3}(t) = \min[1, f_{dam,seismic}(t) + f_{dam,LC2} + f_{dam,WAPDEG}(t)] \times f^{norm}_{fail,LC2}(t) \times f^{norm}_{fail,WAPDEG}(t) \quad \text{(Eq. N-38)}$$

The localized corrosion failure fractions do not need to be adjusted to accommodate the seismic consequence. Localized corrosion continues to propagate at the calculated rate and additional WP damage should be considered at the same rate. Therefore, Equation N-24 does not need to be modified to include seismic consequences. Because the seismic event fails all WPs of the same fuel type simultaneously, (see Sections 6.6.1 and 6.6.2), the denominator in Equation N-24 becomes unity at the time of the seismic event and the result will be based on the damage area for all WPs in the group at the time of the event. Under seismic conditions that cause the failure fraction output by the WAPDEG DLL to become unity at the time of the event, Equation N-37 becomes zero at the time of the event and the damage area calculated by Equation N-24 becomes the sum of the seismic damage and SCC/general corrosion damage weighted by the fraction of non-localized corrosion damaged WPs and the seismic damage and SCC/general corrosion damage and localized corrosion damage weighted by the fraction of localized corrosion damaged WPs,

$$f_{dam,B}(t) = \min\begin{pmatrix} 1, \{\min[1, f_{dam,seismic}(t) + f_{dam,WAPDEG}(t)] \times (1 - f^{norm}_{fail,LC2}(t)) + \\ \min[1, f_{dam,seismic}(t) + f_{dam,LC2} + f_{dam,WAPDEG}(t)] \times f^{norm}_{fail,LC2}(t)\} \end{pmatrix} \quad \text{(Eq. N-39)}$$

Analogous equations can be derived for the Group C WPs but the equations will be the same as those in Equations N-36 through N-39, replacing LC2 fractions with LC1 equivalents. Similarly, analogous equations can be derived for the Group E WPs but the equations will be the same as those in Equations N-36 through N-39, replacing SCC/general corrosion fractions with LC1 equivalents.

Similar to the discussion presented for Group B WPs, Group D equations are modified to account for seismic activity by adding seismic damage fractions to the damage area calculation in each of the seven Group D calculations (Equations N-26 through N-30) to yield the following modified forms:

$$f_{dam,D1}(t) = \min[1, f_{dam,seismic}(t) + f_{dam,WAPDEG}(t)] \times f^{norm}_{fail,WAPDEG}(t) \times [1 - f^{norm}_{fail,LC2}(t) - f^{norm}_{fail,LC1}(t) + f^{norm}_{fail,LC2}(t) \times f^{norm}_{fail,LC1}(t)] \quad \text{(Eq. N-40)}$$

$$f_{dam,D2}(t) = \min[1, f_{dam,seismic}(t) + f_{dam,LC1}] \times f^{norm}_{fail,LC1}(t) \times [1 - f^{norm}_{fail,WAPDEG}(t) - f^{norm}_{fail,LC2}(t) + f^{norm}_{fail,WAPDEG}(t) \times f^{norm}_{fail,LC2}(t)] \quad \text{(Eq. N-41)}$$

$$f_{dam,D3}(t) = \min[1, f_{dam,seismic}(t) + f_{dam,WAPDEG}(t) + f_{dam,LC1}] \times f^{norm}_{fail,LC1}(t) \times f^{norm}_{fail,WAPDEG}(t) \times (1 - f^{norm}_{fail,LC2}(t)) \quad \text{(Eq. N-42)}$$

$$f_{dam,D4}(t) = \min[1, f_{dam,seismic}(t) + f_{dam,LC1}(t) + f_{dam,LC2}] \times f^{norm}_{fail,LC1}(t) \times f^{norm}_{fail,LC2}(t) \times (1 - f^{norm}_{fail,WAPDEG}(t)) \quad \text{(Eq. N-43)}$$

$$f_{dam,D5}(t) = \min[1, f_{dam,seismic}(t) + f_{dam,LC2}] \times f^{norm}_{fail,LC2}(t) \times [1 - f^{norm}_{fail,WAPDEG}(t) - f^{norm}_{fail,LC1}(t) + f^{norm}_{fail,WAPDEG}(t) \times f^{norm}_{fail,LC1}(t)] \quad \text{(Eq. N-44)}$$

$$f_{dam,D6}(t) = \min[1, f_{dam,seismic}(t) + f_{dam,WAPDEG}(t) + f_{dam,LC2}] \times f^{norm}_{fail,LC2}(t) \times f^{norm}_{fail,WAPDEG}(t) \times (1 - f^{norm}_{fail,LC1}(t)) \quad \text{(Eq. N-45)}$$

$$f_{dam,D7}(t) = \min[1, f_{dam,seismic}(t) + f_{dam,LC1} + f_{dam,LC2} + f_{dam,WAPDEG}(t)] \times f^{norm}_{fail,LC1}(t) \times f^{norm}_{fail,LC2}(t) \times f^{norm}_{fail,WAPDEG}(t) \quad \text{(Eq. N-46)}$$

Because the failure fraction output by the WAPDEG DLL becomes unity at the time of the seismic event, the denominator in Equation N-31 becomes unity at the time of the seismic event and the calculated average will be based on the damage area for all WPs in the group at the time of the event. Under seismic conditions that cause the WP failure fraction to become unity at the time of the event, Equations N-41, N-43, and N-44 become zero at the time of the event and the damage area calculated by Equation N-31 becomes the sum of the seismic damage and SCC/general corrosion damage weighted by the fraction of non-localized corrosion damaged WPs and the seismic damage and SCC/general corrosion damage and localized corrosion damage weighted by the fraction of SCC/general corrosion and localized corrosion damaged WPs for each localized corrosion mechanism.

$$\begin{aligned} f_{dam,D}(t) = & \\ & \min[1, f_{dam,seismic}(t) + f_{dam,WAPDEG}(t)] \times (1 - f^{norm}_{fail,LC2}(t))(1 - f^{norm}_{fail,LC1}(t)) + \\ & \min[1, f_{dam,seismic}(t) + f_{dam,WAPDEG}(t) + f_{dam,LC1}] \times f^{norm}_{fail,LC1}(t) \times (1 - f^{norm}_{fail,LC2}(t)) + \\ & \min[1, f_{dam,seismic}(t) + f_{dam,WAPDEG}(t) + f_{dam,LC2}] \times f^{norm}_{fail,LC2}(t) \times (1 - f^{norm}_{fail,LC1}(t)) + \\ & \min[1, f_{dam,seismic}(t) + f_{dam,LC1} + f_{dam,LC2} + f_{dam,WAPDEG}(t)] \times f^{norm}_{fail,LC1}(t) \times f^{norm}_{fail,LC2}(t) \end{aligned} \quad \text{(Eq. N-47)}$$

Seismic event damage is additive to the WP damage caused by localized corrosion in WP groups E, F, and G.

To account for WPs damaged by the seismic event before other damage mechanisms cause damage, the average damage must be set equal to the seismic damage fraction if the damage by SCC/general corrosion and /or localized corrosion is not incurred before the seismic event.

The calculations described above are necessary to determine the average patch damage on the failed WPs. The seismic crack damage is added to SCC damage when the two occur simultaneously and is tracked separately.

Similar to the Nominal Scenario Class, for WPs modeled in the third WP group, those WPs that incur localized corrosion damage by either localized corrosion mechanism, an average damage area is determined for the WP group. The average damage area is the sum of the products of the fraction of damage on each WP of type B, C, D, E, F, or G, above, and the fraction of WPs failed that belong to each WP type B, C, D, E, F, or G, above divided by the sum of the fraction of WPs failed that belong to each WP type B, C, D, E, F, or G (Equation N-32).

For the Seismic Fault Displacement Modeling Case, which includes fault failed WPs with and without localized corrosion, the average damage will be the average calculated by Equation N-32 weighted by the fraction of failed WPs with localized corrosion damage plus the fraction of damage on WPs that do not get localized corrosion damage times the fraction of fault damaged WPs that do not get localized corrosion.

$$f_{dam}^{avg,seismic-FD}(t) =$$
$$\min[1, f_{dam,seismic}(t) + f_{dam}^{avg,LC}(t)] \times (f_{fail,LC1}(t) + f_{fail,LC2}(t) - f_{fail,LC1}(t) \times f_{fail,LC2}(t)) \quad \text{(Eq. N-48)}$$
$$+ f_{dam,seismic}(t) \times (1 - (f_{fail,LC1}(t) + f_{fail,LC2}(t) - f_{fail,LC1}(t) \times f_{fail,LC2}(t)))$$

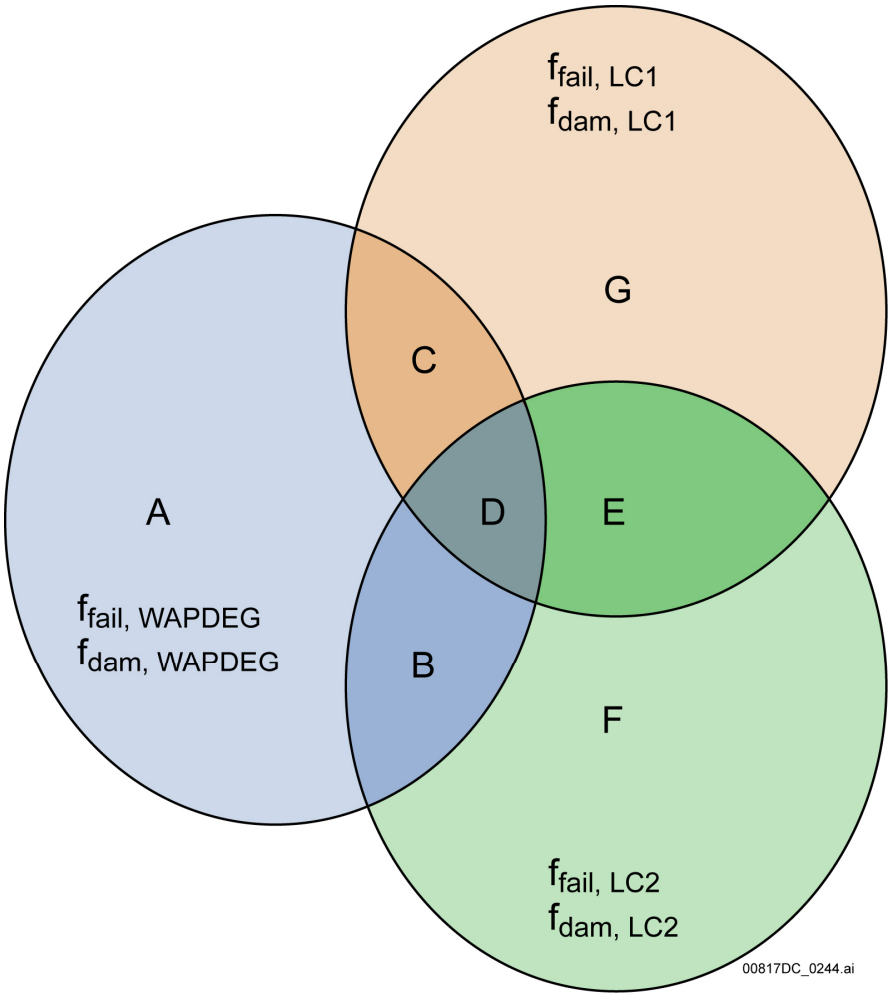

Figure N-1. Venn diagram of overlapping damage modes

INTENTIONALLY LEFT BLANK

APPENDIX O
LOCALIZED CORROSION INITIATION UNCERTAINTY ANALYSIS

O1. INTRODUCTION

This appendix presents the Localized Corrosion Initiation Uncertainty Analysis, which implements the Localized Corrosion Initiation Submodel described in Section 6.3.5.2. The original Localized Corrosion Initiation Model is developed in *General Corrosion and Localized Corrosion of Waste Package Outer Barrier* (SNL 2007 [DIRS 178519], Sections 6.4.4, 6.4.4.3.1, and 6.4.4.5). The effects of localized corrosion are not directly included and calculated in the TSPA-LA Model. The results of the Localized Corrosion Initiation Uncertainty Analysis are used to support screening arguments that localized corrosion initiation can occur only with a low probability and only at a few locations in the repository.

The Localized Corrosion Initiation Uncertainty Analysis uses only a subset of the TSPA-LA Model. Specifically, it is an Engineered Barrier System (EBS) only model in which the unsaturated zone (UZ), saturated zone (SZ), biosphere, and results portions of the TSPA-LA Model have been removed. Also, the EBS has been simplified so that only seepage, thermal hydrology, drift-wall condensation, and chemistry are calculated. The epistemic sampling is identical to the TSPA-LA Model. Also, the aleatory submodels, including the seismic model, are identical. However, the Localized Corrosion Initiation Uncertainty Analysis does not use the representative package for each percolation subregion, but instead it calculates conditions at each of the 3,264 thermal-hydrologic (TH) nodes in the repository. This gives the spatial variability that is necessary to evaluate whether localized corrosion initiates throughout the repository.

The uncertainty analysis in this appendix calculates the chemical conditions on the waste package (WP) surface to determine if the conditions for localized corrosion initiation can exist. If the drip shield (DS) is intact, localized corrosion initiation cannot occur because seepage does not contact the WP surface. However, if the DS is breached or if the DS is assumed to not perform as intended, then the chemistry on the WP surface may allow localized corrosion to initiate. This Localized Corrosion Initiation Uncertainty Analysis assumes that the DS is failed and does not keep seepage water from contacting the WP. The results and conclusions of this analysis can then be used qualitatively in the TSPA-LA Model for any cases in which the DS does not perform as intended.

As will be discussed in more detail later, the conditions for localized corrosion initiation do not exist anywhere in the repository beyond 12,000 years after closure because temperatures decrease and chemical conditions become less aggressive. The average fraction of WPs on which localized corrosion may potentially initiate peaks at about 0.08 in the first few hundred years after closure when the repository is hot, and highly evaporative conditions exist on the WP surface. After 5,000 years, the fraction decreases to below 10^{-3}. Because the probability of localized corrosion initiation is small, the effect on dose would also be low.

O2. MODEL ABSTRACTION

As discussed in Section 6.3.5.2, the Localized Corrosion Initiation Submodel stipulates that localized corrosion of the WP outer surface initiates when the open-circuit potential, or corrosion potential (E_{corr}), is equal to or greater than the critical threshold potential ($E_{critical}$); that is, when $\Delta E = E_{critical} - E_{corr} \leq 0$. This Localized Corrosion Initiation Uncertainty Analysis uses $\Delta E \leq 0$ as the condition necessary for localized corrosion to initiate. For the TSPA-LA Model, the Localized Corrosion Initiation Abstraction uses the crevice repassivation potential (E_{rcrev}) as the critical potential. The crevice repassivation potential for crevice corrosion on the WP outer surface is defined in terms of WP surface temperature and chemical conditions as follows:

$$E_{critical} = E_{rcrev} = a_o + a_1 T + a_2 \ln\left[Cl^-\right] + a_3 \frac{\left[NO_3^-\right]}{\left[Cl^-\right]} + a_4 T\left[Cl^-\right] + \varepsilon_{rcrev} \qquad \text{(Eq. O-1)}$$

where a_o, a_1, a_2, a_3, and a_4 are regression constants, T is the WP outer barrier surface temperature (°C), $[NO_3^-]$ is the nitrate ion molality (moles/kg water), and $[Cl^-]$ is the chloride ion molality (moles/kg water). The error term, ε_{rcrev}, represents data variance not explained by the fitting procedure and is modeled by a normal distribution with a mean of 0 mV versus the saturated silver chloride electrode and a standard deviation (SD) of 45.055 mV versus saturated silver chloride electrode. The Localized Corrosion Initiation Abstraction stipulates that the calculated value of E_{rcrev} be constrained to the ±2 SD prediction intervals of the unconstrained model.

The long-term steady-state corrosion potential, E_{corr}, for the WP outer surface is expressed as:

$$E_{corr} = c_o + c_1 T + c_2 pH + c_3 \frac{\left[NO_3^-\right]}{\left[Cl^-\right]} + c_4 T \frac{\left[NO_3^-\right]}{\left[Cl^-\right]} + c_5 pH \frac{\left[NO_3^-\right]}{\left[Cl^-\right]} + c_6 pH \ln[Cl^-] + \varepsilon_{corr} \text{ (Eq. O-2)}$$

where c_o, c_1, c_2, c_3, c_4, c_5, and c_6 are coefficients of the parameters, pH is the calculated Pitzer pH, and the other parameters are as previously defined. The error term, ε_{corr}, is a term representing data variance not explained by the fitting procedure and has a normal distribution with a mean of zero mV versus saturated silver chloride electrode, and an SD of 85.265 mV versus saturated silver chloride electrode. The units of the coefficients should be consistent with E_{corr} having units of mV. The calculated value of E_{rcrev} should also be constrained to the ±2 SD prediction intervals of the unconstrained model.

The thermal hydrology, seepage, and chemistry submodels used in the Localized Corrosion Initiation Uncertainty Analysis differ from those in the TSPA-LA Model in that they are applied at the individual WP level. Seepage and drift wall condensation are important because localized corrosion initiation requires seepage or condensation to bring corrosive chemicals to the WP surface. The seepage calculation in the Localized Corrosion Initiation Uncertainty Analysis is similar to the TSPA-LA Model. The main difference is that the seepage calculation is implemented directly in the Localized Corrosion Initiation GoldSim model instead of as a linked external program. Also, rather than calculating the average seepage rate and seepage fraction for the percolation subregion, the seepage calculation in this Localized Corrosion Initiation Uncertainty Analysis determines the seepage rate at each WP location. The seepage calculation

includes the same seismic effects as the TSPA-LA Model. The drift-wall condensation is calculated as part of the analysis. Driftwall condensation is independent of seepage and can also bring water and chemicals to the surface of the WP. Drift wall condensation is especially important for co-disposed (CDSP) WPs during Stage 2 when all CDSP WPs are assumed to have drift-wall condensation.

The Localized Corrosion Initiation Uncertainty Analysis uses a similar chemistry submodel (Section 6.3.4.3.2) as the TSPA-LA Model, accessing the same 396 chemical composition look-up tables. However, rather than calculating the *pH* and ionic strength in the invert, the chemistry submodel calculates the *pH*, $[Cl^-]$, and $[NO_3^-]$ on the WP surface

The thermal-hydrology submodel is similar to the TSPA-LA Model (Section 6.3.2) and determines the temperature and relative humidity on the WP surface. The effects on the temperature and relative humidity from rubble are included as in the TSPA-LA Model. The main difference is in how the individual locations in the repository are modeled. The repository is divided into percolation subregions, or bins with a total of 3,264 multi-scale thermal hydrology nodes in all of the bins. Bin 1 has 163 nodes, bin 2 has 817 nodes, bin 3 has 1,300 nodes, bin 4 has 820 nodes, and bin 5 has 164 nodes. These nodes do not correspond exactly to the actual WP locations. The TSPA-LA Model represents each bin with a representative WP (Section 6.3.2). Unlike in the TSPA-LA Model, this Localized Corrosion Initiation Uncertainty Analysis represents the uncertainty in the thermal hydrology submodel by modeling two CDSP WPs and six commercial spent nuclear fuel (CSNF) WPs at each of the 3,264 nodes.

In summary, the Localized Corrosion Initiation Submodel samples the epistemic parameters for the 300 realizations just like the TSPA-LA Model. At each node within each bin for every realization, a specific CSNF WP and CDSP WP is chosen from the thermal-hydrology files. The model determines the thermal conditions and the relative humidity conditions for the WPs. Then, at every timestep, the model determines the chemical conditions on the WP surface. The model determines whether or not seepage is occurring on the WP, assuming that the DS does not keep water off of the WP. Finally, the model outputs the total number of nodes in each bin with $\Delta E \leq 0$ as a function of time. This total number of nodes is further post-processed to determine the fraction of nodes within each bin that have conditions favorable for the initiation of localized corrosion. Ultimately, the results of this Localized Corrosion Initiation Uncertainty Analysis are used in qualitative arguments in the TSPA-LA.

O3. RESULTS

The Localized Corrosion Initiation Uncertainty Analysis calculates the ΔE at each WP location in the repository for 300 epistemic realizations. The DS is assumed to allow water to contact the WP surface. The main result of the Localized Corrosion Initiation Uncertainty Analysis shown on Figure O-1 is the fraction of nodes for each WP type in each bin that have $\Delta E \leq 0$, indicating localized corrosion could initiate on the WP surface. Each figure shows 300 curves, one for each of 300 realizations of the epistemic parameters. Each curve displays the fraction of locations within the percolation bin at which localized corrosion could potentially occur, if a WP of the appropriate type were present at these locations. Statistics (mean, median, and 95th and 5th percentiles) are shown for the distribution of these 300 curves. In addition, one realization (Realization 142) is identified for further analysis. The curves for each realization end at the last

time at which localized corrosion could occur at any location. The plots of statistics end at the time when no realization has localized corrosion at any location. All of the plots end at 12,000-years, indicating conditions for WP localized corrosion initiation do not occur in the repository beyond 12,000 years.

In general, bins 3, 4, and 5 have higher fractions of localized corrosion because they have more locations with seepage. The climate changes at 2,000 years and 10,000 years are evident as small kinks in the mean curves. These kinks are due to more WPs having seepage in the glacial transition climate and the post-10,000-year climate. Before about 1,000 years, the CDSP WPs have a higher fraction of locations with potential localized corrosion initiation. This is due solely to the Stage 2 drift-wall condensation at every CDSP WP location. After Stage 2 ends at around 1,000-years, drift seepage dominates over drift-wall condensation and CSNF WPs have a higher incidence of localized corrosion initiation mainly because CSNF WPs have higher temperatures than CDSP WPs. Also, shown on Figure O-1 is the dominant effect of the single epistemic realization number 142, which is the only realization to have any nodes with localized corrosion after a few thousand years.

Figure O-2 shows the average fraction of WPs that could potentially experience localized corrosion, computed by multiplying each of the mean curves on Figure O-1 by its respective bin fraction (0.05, 0.25, 0.40, 0.25, and 0.05) and its WP type fraction (3416/11629 for CDSP WP and 8213/11629 for CSNF WP). There are more CSNF WPs and they are hotter so they have a higher incidence of potential localized corrosion than CDSP WPs. Thus, CSNF WPs comprise a larger fraction of the total number of WPs that could experience localized corrosion. The repository total curve shows the mean fraction of WPs with potential for localized corrosion for the entire repository.

As mentioned previously, only realization 142 has conditions favorable for localized corrosion initiation persisting beyond a few thousand years. This persistence is due to the combination of uncertain parameters in this realization. The coefficients in Equation O-1 and Equation O-2 are correlated within each equation, but the uncertainty terms and the coefficients are not correlated between the two equations. This allows for sampling large negative values for a_o and ε_{rcrev}, and large positive values for c_o and ε_{corr}. Also, the algorithm for applying uncertainty in the chemistry model essentially fixes the $[Cl^-]/[NO_3^-]$ ratio as an epistemic parameter (Section 6.3.4.3.2). These two features of this analysis imply that seven of the epistemic uncertain parameters essentially combine to give a constant value for each realization.

$$\text{Constant value} = \left(a_o + a_3 \frac{\left[NO_3^-\right]}{\left[Cl^-\right]} + \varepsilon_{rcrev} \right) - \left(c_o + c_3 \frac{\left[NO_3^-\right]}{\left[Cl^-\right]} + \varepsilon_{corr} \right) \qquad \text{(Eq. O-3)}$$

The combined value of the uncertain parameters in Equation O-3 for realization 142 is -936 mV, which is the tenth lowest of the 300 realizations. This large negative value means that the other conditions must change dramatically for the ΔE to become positive. Specifically, the temperature must cool down significantly and the $[Cl^-]$ and $[NO_3^-]$ must both become smaller. It takes a long time in realization 142 to overcome the large negative value indicated by Equation O-3.

The time histories of the chemical conditions and ΔE at every node for every realization cannot reasonably be shown. However, the time histories of the mean of all the nodes in a single bin can be shown. The values for the CSNF WPs in bin 3 are shown to represent the range of values for ΔE, with Realization 142 highlighted. Figure O-3 shows the value of ΔE, averaged over all of the 1,300 nodes for this bin. Notice that the mean ΔE for realization 142 is the last to go above zero. As mentioned previously, the large negative value for the parameters shown in Equation O-3 keeps ΔE low. The highest curves on Figure O-3, which have large positive values for the parameters in Equation 3, are never close to zero. Thus, localized corrosion never occurs in these realizations.

O4. IMPLEMENTATION IN TSPA-LA MODEL

Localized corrosion affects only those modeling cases in which the drip shield (DS) could fail to function within 12,000 years. The events and processes that could lead to DS failure include general corrosion of the DS, igneous intrusions, and seismic events. Section 6.3.5.2.3 discusses each of the modeling cases and indicates that localized corrosion is not modeled directly in any of the cases because of the low incidence of initiation within the first 10,000 years. This Localized Corrosion Initiation Uncertainty Analysis supports the low incidence argument.

INTENTIONALLY LEFT BLANK

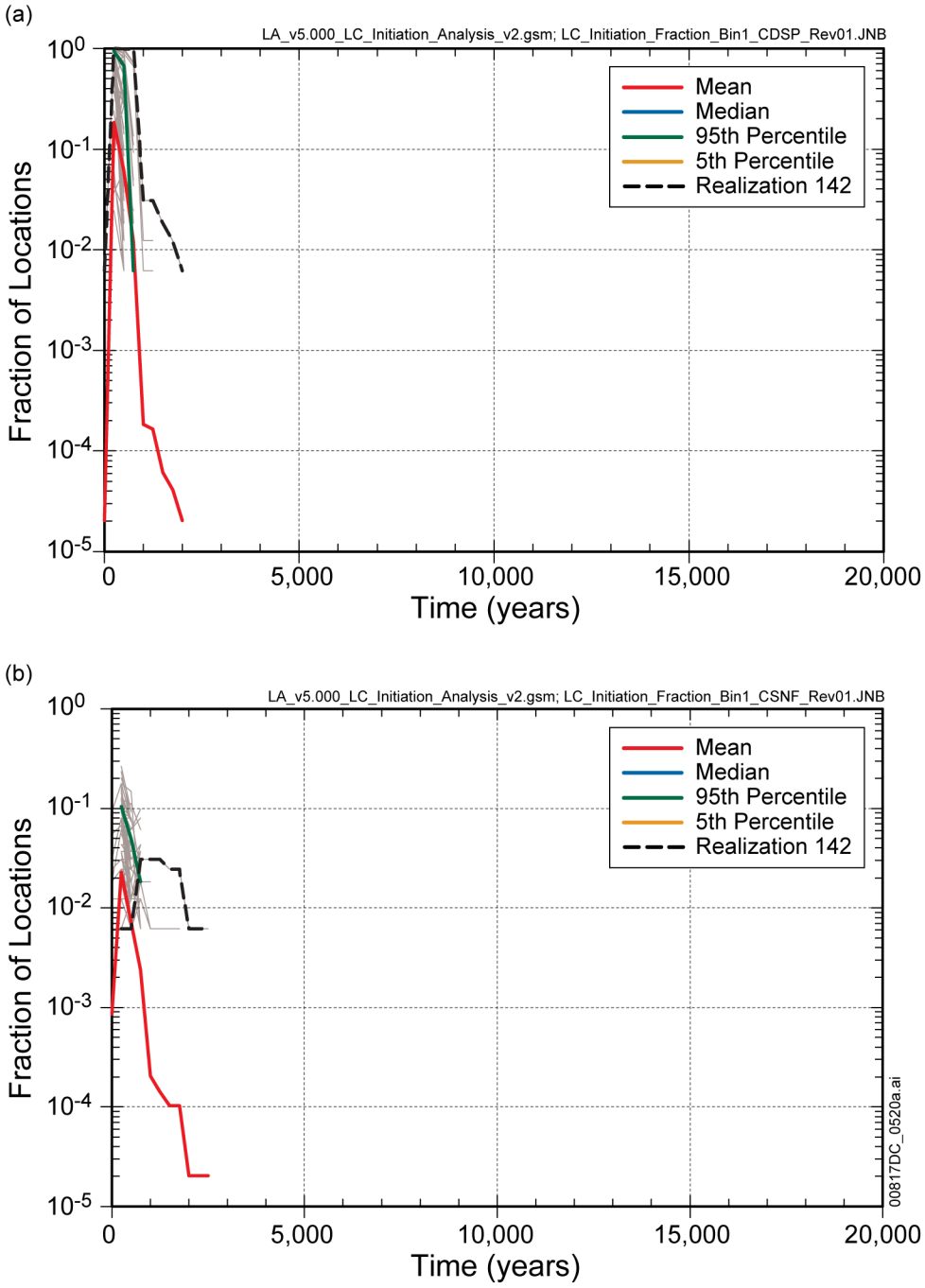

Source: Output DTN: MO0709TSPALOCO.000 [DIRS 182994].

Figure O-1. Fraction of Locations with the Potential for Localized Corrosion Initiation: (a) Bin1, CDSP; (b) Bin1, CSNF; (c) Bin2, CDSP; (d) Bin2, CSNF; (e) Bin3, CDSP; (f) Bin3, CSNF; (g) Bin4, CDSP; (h) Bin4, CSNF; (i) Bin5, CDSP; and (j) Bin5, CSNF

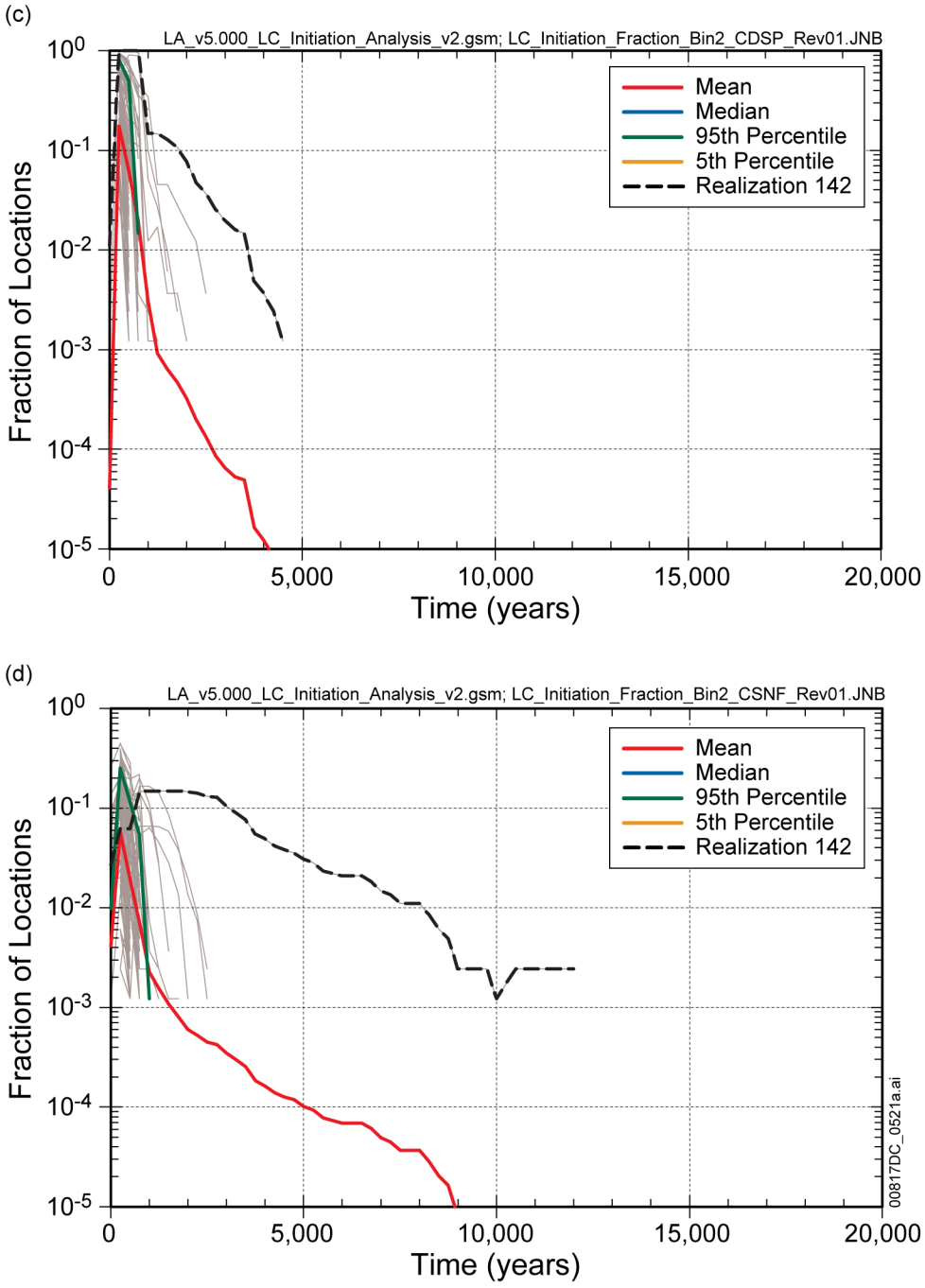

Source: Output DTN: MO0709TSPALOCO.000 [DIRS 182994].

Figure O-1. Fraction of Locations with the Potential for Localized Corrosion Initiation: (a) Bin1, CDSP; (b) Bin1, CSNF; (c) Bin2, CDSP; (d) Bin2, CSNF; (e) Bin3, CDSP; (f) Bin3, CSNF; (g) Bin4, CDSP; (h) Bin4, CSNF; (i) Bin5, CDSP; and (j) Bin5, CSNF (continued)

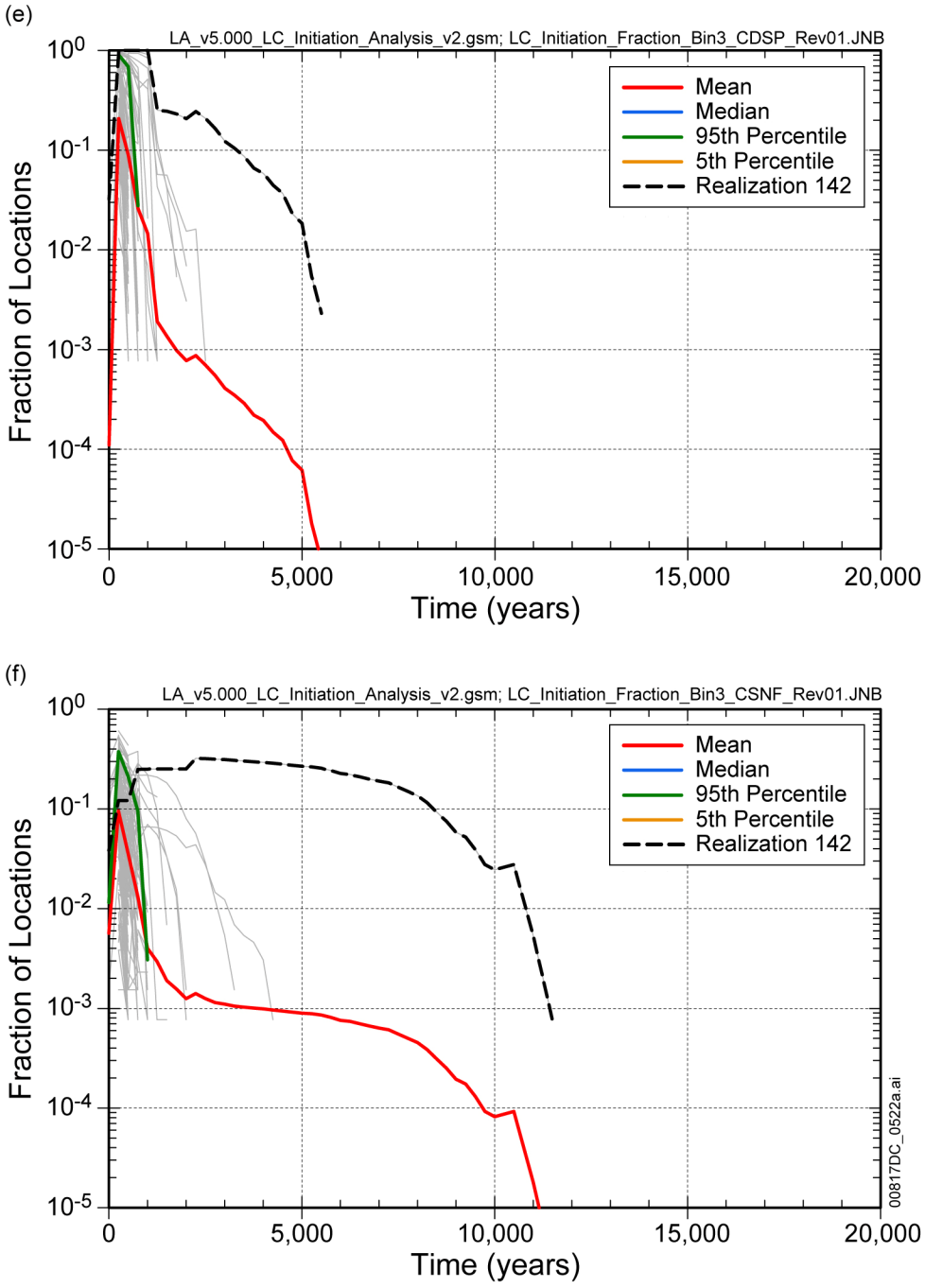

Source: Output DTN: MO0709TSPALOCO.000 [DIRS 182994].

Figure O-1. Fraction of Locations with the Potential for Localized Corrosion Initiation: (a) Bin1, CDSP; (b) Bin1, CSNF; (c) Bin2, CDSP; (d) Bin2, CSNF; (e) Bin3, CDSP; (f) Bin3, CSNF; (g) Bin4, CDSP; (h) Bin4, CSNF; (i) Bin5, CDSP; and (j) Bin5, CSNF (continued)

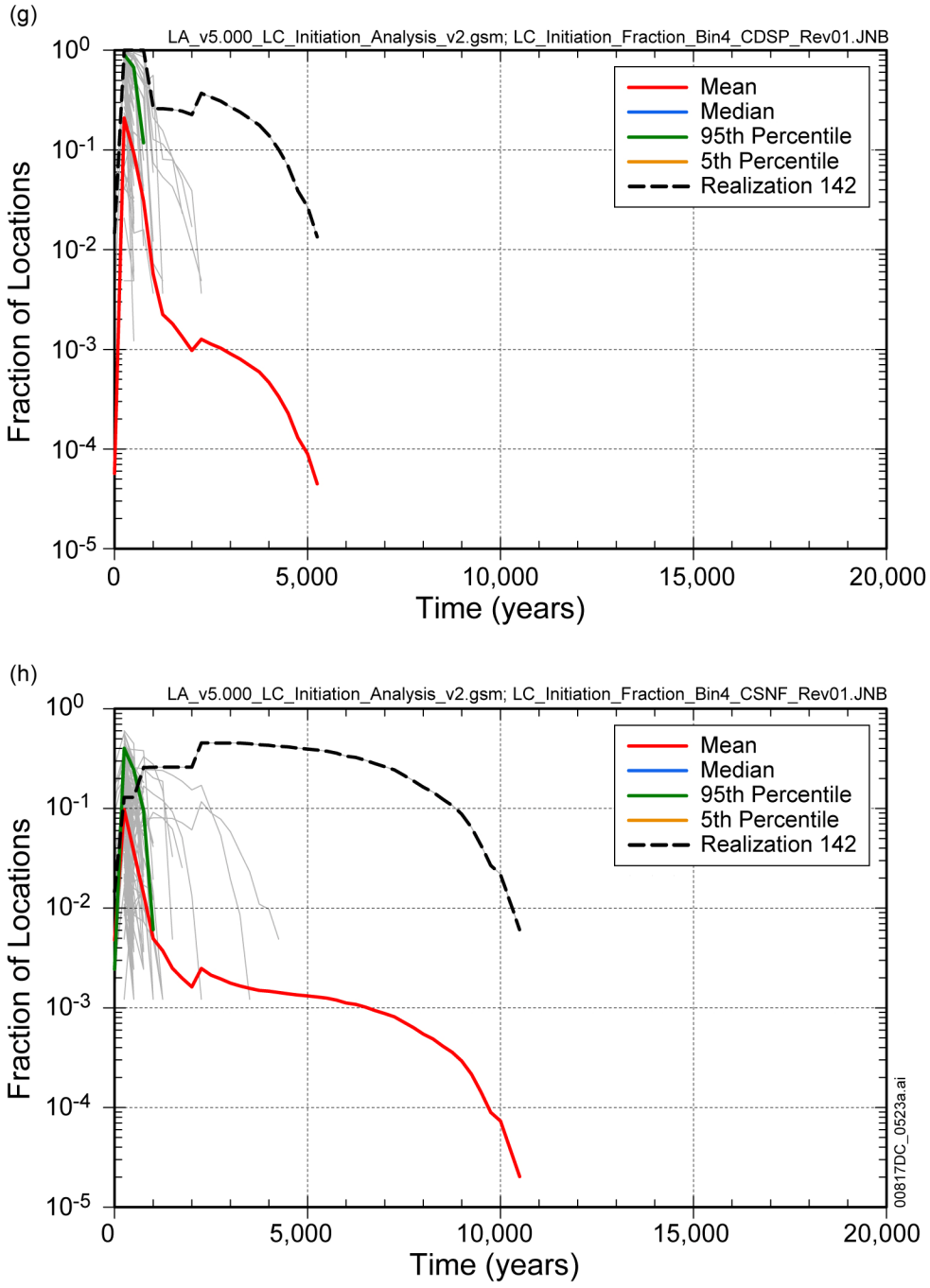

Source: Output DTN: MO0709TSPALOCO.000 [DIRS 182994].

Figure O-1. Fraction of Locations with the Potential for Localized Corrosion Initiation: (a) Bin1, CDSP; (b) Bin1, CSNF; (c) Bin2, CDSP; (d) Bin2, CSNF; (e) Bin3, CDSP; (f) Bin3, CSNF; (g) Bin4, CDSP; (h) Bin4, CSNF; (i) Bin5, CDSP; and (j) Bin5, CSNF (continued)

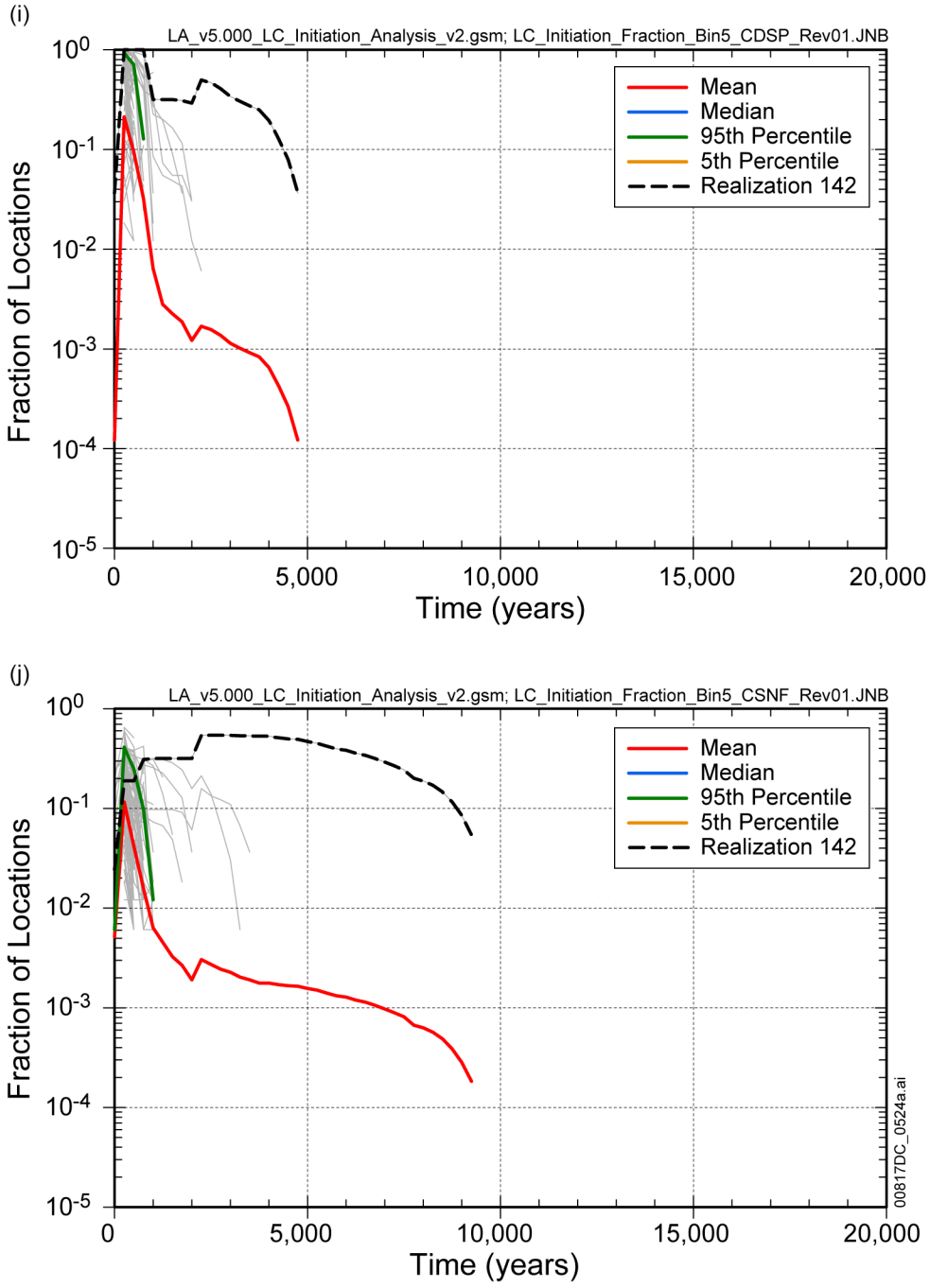

Source: Output DTN: MO0709TSPALOCO.000 [DIRS 182994].

Figure O-1. Fraction of Locations with the Potential for Localized Corrosion Initiation: (a) Bin1, CDSP; (b) Bin1, CSNF; (c) Bin2, CDSP; (d) Bin2, CSNF; (e) Bin3, CDSP; (f) Bin3, CSNF; (g) Bin4, CDSP; (h) Bin4, CSNF; (i) Bin5, CDSP; and (j) Bin5, CSNF (continued)

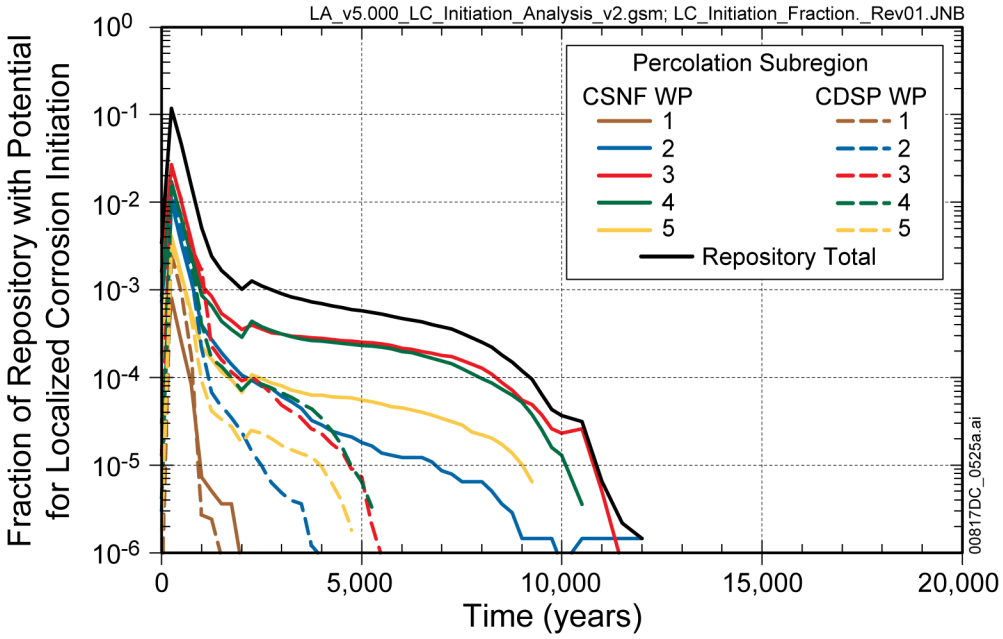

Source: Output DTN: MO0709TSPALOCO.000 [DIRS 182994].

Figure O-2. Fraction of Locations in Each Percolation Subregion with the Potential for Localized Corrosion Initiation

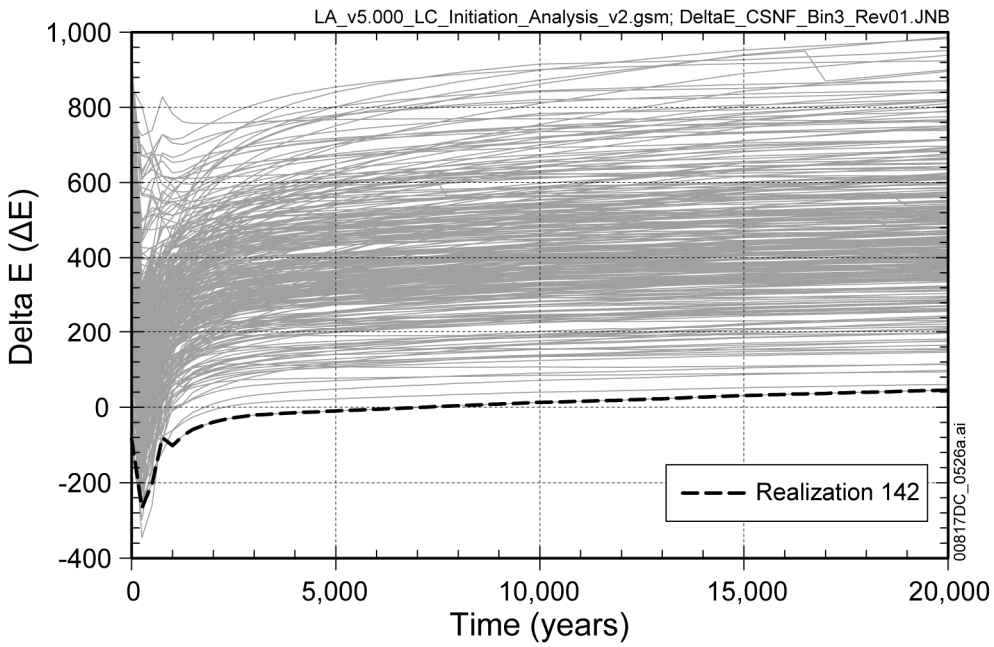

Source: Output DTN: MO0709TSPALOCO.000 [DIRS 182994].

Figure O-3. Average Delta E for Percolation Subregion 3, CSNF, for 300 Epistemic Realizations

INTENTIONALLY LEFT BLANK

APPENDIX P
IMPACT ASSESSMENTS

P1. INTRODUCTION

The post-model development activities following the completion of the TSPA-LA Model (Version 5.0) identified several issues related to errors in implementation, identification of undocumented conservatisms, and updates to parameter values. These issues are addressed here as per the review criteria outlined in Sections 2.1.4 and 2.3.5.2.1 of the *Technical Work Plan for: Total System Performance Assessment FY 07-08 Activities* (SNL 2008 [DIRS 184920]). In addition, this appendix includes an evaluation of the sensitivity of mean annual dose with respect to a fixed igneous event frequency (Section P.14), which is not documented elsewhere. Not all identified issues that are evaluated fall in the category of errors, as some of the issues are presented to only evaluate the degree of conservatism from the modeling choices made during the model development phase.

P2. INVENTORY AND SEEPAGE FRACTION

P2.1 ISSUE

Inventory for ^{36}Cl, ^{79}Se, and ^{126}Sn was omitted in the 10,000-year simulation modeling cases and thus not included in the dose calculations. In addition, the seepage fractions applied for the 10,000-year simulations are based on the post-10,000-year climate.

P2.2 ISSUE DESCRIPTION

The inventories for ^{36}Cl, ^{79}Se, and ^{126}Sn were zeroed out in the 10,000-year simulations but were included for the 1,000,000-year simulations. As a result, the mean annual dose is under predicted for the 10,000-year simulations in all modeling cases except for Volcanic Eruption Modeling Case, where the radionuclide inventories are correct.

The seepage fractions for the 10,000-year simulations are based on the post-10,000-year climate instead of the glacial-transition climate, which could lead to small error in estimating the number of waste packages (WPs) in the dripping environment.

P2.3 IMPACT ASSESSMENT

The impact from these errors is anticipated to be negligible to the mean annual dose because: (a) the three omitted radionuclides do not significantly contribute to the total dose at 10,000 years as determined based on the 1,000,000-year simulations, where the inventory of these radionuclides were included (Figures 8.2-2, 8.2-4b, 8.2-6b, 8.2-8b, 8.2-12b, and 8.2-14b); (b) the change in seepage fraction based on the glacial-transition climate versus the post-10,000-year climate is estimated to be small, leading to a small decrease in the number of waste packages (WPs) assigned to the dripping environment.

The impact evaluation was conducted by correcting the two errors and running the modeling cases for the 10,000-year time period. The impact evaluation for each modeling case is provided in detail below:

<u>Waste Package Early Failure (EF) Modeling Case</u>

The mean annual dose for the impact evaluation case is compared to the base case on Figure P-1a. The impact evaluation case shows a small increase (<10 percent) in the mean annual dose for small time periods due to inclusion of the inventory of the three radionuclides. Note that ^{36}Cl and ^{79}Se are among the top six dose contributors in the first 10,000 years (Figure P-1b). The effect of reduction in seepage fraction by 22.5 percent for the impact evaluation case (Table P-1) is not discernable as the drip shield (DS) remains intact throughout the simulation and the transport out of the WP is still diffusive. Thus, even though there is lesser probability of WP being placed in the dripping environment (based on seepage fraction) the diffusive mass release out of the WP would not change appreciably and any small perturbations due to change in boundary conditions in the engineered barrier system (EBS) would be overshadowed by the dispersion effects in the unsaturated zone (UZ) and saturated zone (SZ). The expected dose calculations are not affected from change in seepage fraction (Equation 6.1.2-13), as the dose is summed over both dripping and non-dripping environments.

Drip Shield Early Failure (EF) Modeling Case

The mean annual dose for the impact evaluation case is compared to the base case on Figure P-2a. The impact evaluation case shows a small decrease in the mean annual dose even though the three radionuclides are included (Figure P-2b). The mean annual dose is typically lower by about 22 percent in the impact evaluation case. This is due to the reduction in the seepage fraction since the total seepage fraction also changed by about 22 percent in the impact evaluation case (see total of last column in Table P-1). Note that there is no localized corrosion-related early failure modeled for WP in a non-dripping environment and, thus, the only release in this modeling case is from the localized corrosion of WPs in a dripping environment. Consequently, the seepage fraction is used as a weighting factor in the expected dose calculations as shown by Equation 6.1.2-14, and thus has a linear effect on the mean annual dose.

Seismic Fault Displacement (FD) Modeling Case

The mean annual dose for the impact evaluation case is compared to the base case on Figure P-3a. The impact evaluation case shows a small decrease (of about 5 percent) in the mean annual dose even though the three radionuclides are included (Figure P-3b). The contribution of the three added radionuclides is less than 2 percent to the mean annual dose. This increase is offset by a larger decrease due to the change in the seepage fraction where the percolation subregion weighted average seepage fraction reduced by about 10 percent in the impact evaluation case (Table P-2). As a result, the number of WPs that are exposed to the seepage are reduced, leading to lower advective mass flux. The mean annual dose does not reduce in proportion to the reduction in seepage fraction (as was the case for the Drip Shield EF Modeling Case) because the water flux through the WP is scaled down by the fractional breach area while the breach area is small. In such cases, the release is dominated by diffusion out of the WP and thus the overall effect on the mean annual dose from reduction in seepage fraction is non-linear.

Seismic Ground Motion (GM) Modeling Case

The mean annual dose for the impact evaluation case is compared to the base case on Figure P-4a. The mean annual dose for the impact evaluation case shows a gradual increase with time from about 1 percent at 500 years to over 7 percent by 10,000 years. This is primarily due

to the dose contribution from the three included radionuclides whose dose is also increasing with time (Figure P-4b). Specifically, ^{36}Cl and ^{79}Se are the fourth and fifth largest dose contributors with a contribution of about 10 percent to the total dose.

Because the DSs remain intact and the WP breaches are only stress corrosion cracks in this modeling case, releases from the WP are diffusive and insensitive to the seepage fraction. Therefore, even though the effect on seepage fraction is appreciable for this modeling case, with the average (area weighted) reduction of over 55 percent (Table P-3), the dose is not significantly influenced. The seepage fraction reduction is greater compared to other modeling cases because the base-case calculations have the effect of drift degradation included that occur past 10,000 years (up to 1,000,000 years), which leads to a greater number of locations undergoing seepage. The impact evaluation case is not affected by this, as drift degradation from seismic activity in the first 10,000 years is not considered (Section 7.3.2.6.1.3), and thus the seepage fraction is the same as for the nominal conditions (as shown in Table P-1). So even though there are fewer WPs being placed in the dripping environment (based on seepage fraction) the overall diffusive mass releases out of the WPs is not appreciably affected due to the presence of small crack areas, although the boundary concentrations in the invert may have changed. Any small perturbations due to changes in boundary conditions in the EBS are likely to be overshadowed by the dispersion effects in the UZ and SZ. Thus, mean annual dose is only affected by the added radionuclides.

Igneous Intrusion Modeling Case

The mean annual dose for the impact evaluation case is compared to the base case on Figure P-5a. The mean annual dose for the impact evaluation case is marginally higher (by <4 percent) compared to the base case. The contribution of the three included radionuclides to the mean annual dose is negligibly small (Figure P-5b).

The seepage fraction effect is not seen in this modeling case, as all WPs see percolation flux following the igneous intrusion. There is no nominal corrosion-related WP failure prior to the igneous event in the 10,000-year simulation and, thus, the seepage fraction correction has no effect prior to the igneous event. The marginal increase in the mean annual dose is likely related to the inclusion of the three radionuclides.

P3. WASTE PACKAGE DAMAGE FROM SEISMIC EVENTS

P3.1 ISSUE

Conservative treatment of WP damage from seismic events following the first breach due to nominal corrosion processes.

P3.2 ISSUE DESCRIPTION

The probability of seismic damage is provided for two end-member states of the WP—one with intact internals and one with fully degraded internals. In the base case, once any WP is breached by a nominal process in a given percolation subregion (e.g., from first occurrence of stress corrosion cracks located on the outer lids) the probability of seismic damage is switched from the intact internals abstraction to the fully degraded internals abstraction, which increases the chance

of seismic damage occurring while the DS is intact. This probability is then applied to all the WPs in the given percolation subregion, which is conservative, as most of the WPs have not yet failed by the nominal processes and should be using the intact internals damage probability. As a result, most WPs fail earlier and acquire greater damage area than expected.

P3.3 IMPACT ASSESSMENT

The impact of this conservative implementation is anticipated to vary with time, as it only occurs in situations where the breach from nominal corrosion occurs earlier than the seismic damage event. Since nominal breaches do not occur in the first 10,000 years, the seismic modeling cases that are run for the 10,000-year compliance duration are not affected. The only modeling case where this has an effect is in the Seismic GM Modeling Case run for the 1,000,000-year simulation duration. Even in this case, the CDSP WPs are generally not impacted because the seismic damage is likely to occur earlier than the nominal corrosion failure: the nominal corrosion failures from stress corrosion cracks do not occur until after 100,000 years while the probability of seismic damage on CDSP WPs has a mean value of around 0.36 in 100,000 years (output DTN: MO0709TSPAWPDS.000 [DIRS 183170]). In contrast, the probability of commercial spent nuclear fuel (CSNF) WPs failing from seismic events is low, with a mean value of around 0.006 in 100,000 years (output DTN: MO0709TSPAWPDS.000 [DIRS 183170]), and thus the nominal corrosion failures are likely to cause the first damage for CSNF WPs. Consequently, the impact of this conservative treatment in likely to occur only for CSNF WPs.

The nominal corrosion failures for CSNF WPs do not start until after 100,000 years and only about 5 percent of realizations would have initiated CSNF WP failures by 200,000 years. Thus, the impact of the conservative treatment of applying degraded internals abstraction following nominal corrosion failure is likely to occur past 100,000 years and likely to last for up to about 400,000 years as by then the majority of the realizations (about 50 percent) would have had some WP failures by nominal corrosion, irrespective of the seismic damage. In the period between 100,000 and 400,000 years, the conservatism is likely to have the maximum impact between 200,000 years and 300,000 years. This is because in this time period the DSs are intact and thus any nominal corrosion failure of any WP in a given percolation subregion would lead to usage of seismic damage abstraction for the “degraded internals under intact DS” for all WPs in the percolation subregion. Since the probability of damage is fairly high from this abstraction (Figure 6.6-10b and Figure 6.6-10c) there is a good chance of failing the WPs and thereby releasing the radionuclides. Following DS failures (typically past 250,000 years), the probability of damage decreases as the WP is likely to be surrounded by rubble and the seismic damage abstraction for the WP with “degraded internals surrounded by rubble” is used (Figure 6.6-15a and Figure 6.6-15b).

Because the seismic damage is likely to cause stress corrosion cracking (SCC), the breach area on the WP would be very small initially, and then grow with each seismic-damage event, but the overall area would still remain small compared to the WP surface area, and thus the release rate out of the WP would be limited. Since non-sorbing radionuclides such as ^{99}Tc and ^{129}I are the major dose contributors and since the WP release would be diffusive (as no advection can occur through the stress corrosion cracks) the breach area along with the number of failed WPs would predominantly control the mass release. The impact of the current implementation is likely to

cause the mean annual dose to be significantly higher in the timeframe of 200,000 and 300,000 years compared to the case where the conservatism is removed. The impact is anticipated to be small at later times.

P4. OUTER BARRIER FAILURE FLAG IN SEISMIC MODEL

P4.1 ISSUE

WP outer barrier failure flag is triggered when the inside-out corrosion of the WP is initiated in the Seismic GM Modeling Case, which could be earlier than the actual breach time from seismic damage or nominal corrosion.

P4.2 ISSUE DESCRIPTION

The inside-out corrosion initiation time for the WP is approximated by pre-calculating the breach time from a seismic event using a conservative calculation and then passing this time to Waste Package Degradation Model (WAPDEG). But this time is also used, by error, to trigger the WP outer barrier failure flag which could be much earlier than the appearance of the first actual breach (crack or patch opening area). Since the downstream waste form and transport submodels use this flag to initiate the waste form degradation and transport processes inside the WP they get started earlier than intended. Once the WP breach occurs (either by nominal corrosion or by seismic damage) the release rates could be higher than expected due to build-up of mass in solution prior to the breach.

P4.3 IMPACT ASSESSMENT

The impact of this error is anticipated to be negligibly small, as most realizations would have either a nominal corrosion failure or seismic event failure before the pre-calculated inside-out corrosion initiation time. Thus, in most realizations, the outer barrier failure flag trigger time and the first breach times will occur simultaneously leading to correct calculations. This is because even though the pre-calculated inside-out corrosion initiation times are based on conservative calculations, they still lead to initiation times, in most realizations, that are either later than the actual breach times from nominal corrosion failures or at the same time as the breach time calculated from the actual seismic calculations.

For CDSP WPs, only about 14 percent of realizations have inside-out corrosion initiation times earlier than the actual seismic damage time, while for CSNF WPs only about one percent of realizations have inside-out corrosion initiation times earlier than the actual seismic damage time (output DTN: MO0709TSPAWPDS.000 [DIRS 183170], file v5.000_GS_9.60.100_StandAlone_9krlz.gsm in folder Seismic_9k_Rlz). Even in these realizations, the time difference between the outer barrier failure flag trigger time and the actual breach time may not always be large, as the nominal corrosion is accelerated from the initiation of inside-out corrosion leading to rapid failure.

It should be noted that in these few realizations, even though the outer barrier failure is triggered earlier and waste form degradation processes and transport processes inside the WP start, there is no mass release from the WP until the WP is truly breached. So the mass release time to the UZ and SZ is unchanged. Since the breach area is small due to the presence of only stress corrosion

cracks, the diffusive releases out of the WP would be controlled by the breach area rather than by the concentration gradient. Thus, the release rates would be small and the mass would be depleted slowly. The overall effect of the error on the mean annual dose is likely to be negligibly small.

P5. INVERT CHEMISTRY

P5.1 ISSUE

In-package chemistry applied in the invert after the DS is failed without considering flow through the WP.

P5.2 ISSUE DESCRIPTION

Currently the in-package chemistry computed for the corrosion products domain is applied to the invert after the DS is failed, without considering whether there is flow through the WP or not. The direction provided by *Engineered Barrier System: Physical and Chemical Environment* (EBS P&CE) (SNL 2007 [DIRS 177412], Table 6.15-1) was to only apply the in-package chemistry from the corrosion products domain of the WP to the invert when there was flow through the WP after the DS is failed. In all other cases, the chemistry equilibrated to the invert temperature, relative humidity, and Pco_2 as described by the EBS P&CE model was supposed to be applied.

P5.3 IMPACT ASSESSMENT

The impact on the mean annual dose from this error is anticipated to be negligible, as this error would only occur in situations where the DS has failed while the WP only has SCC opening areas (leading to no flow through the WP). This situation is only possible in the Nominal Modeling Case and in the Seismic GM Modeling Case. But even in these cases, because the DS failure is not expected until past 200,000 years, any releases prior to DS failure are not impacted. Furthermore, past 200,000 years, benign chemical conditions are anticipated in both the WP and invert due to near-ambient temperatures, and, thus, the difference in the in-package chemistry (from the corrosion products domain) and the chemistry calculated from the EBS P&CE model will be small. In addition, the two radionuclides that control the mean annual dose for the majority of the simulated time period beyond 200,000 years, in both modeling cases are ^{99}Tc and ^{129}I, which are not affected by the chemistry. Once the general corrosion patches appear and the flow through the WP initiates, the calculations become correct once again.

Because of the above arguments, this error is anticipated to have negligible impact on the mean annual dose.

P6. WELD VOLUME

P6.1 ISSUE

Incorrect weld volume is used in computing the probability of manufacturing defects as a factor of π was omitted from the WP circumference calculation.

P6.2 ISSUE DESCRIPTION

The weld volume is an input to the CWD software (STN: 10363-2.0-00 [DIRS 162809]) that is used to compute the cumulative probability of a manufacturing defect conditional on the probability for the non-detection of weld defects. The calculated value is then used as an input in the WAPDEG code for calculating the time of WP failure from SCC or by general corrosion.

The Poisson intensity parameter for the average number of defects per closure weld is given by

$$\lambda = DF \cdot V \cdot \lambda_c \cdot \frac{\lambda_s \cdot H(t)}{\left(1 - \exp(-\lambda_s \cdot t)\right)} \quad \text{(Eq. P-1)}$$

where,

DF is the fraction of defects capable of propagation;

V is the weld volume;

λ_c is the Poisson intensity before detection;

λ_s is the parameter for a truncated (at the weld thickness) exponential distribution for weld sizes before detection;

t is weld thickness; and

H(t) is the conditional probability that the defect is not detected.

Inspection of the above equation shows that correcting the weld volume (V) by a factor of π will also increase the value of λ by a factor of π (about 3.14).

Based on the Poisson intensity parameter, the CWD software returns a value of *q*, the probability of one or more defects per closure lid weld, as:

$$q = 1 - \exp(-\lambda) \approx \lambda \quad \text{for } \lambda << 1 \quad \text{(Eq. P-2)}$$

P6.3 IMPACT ASSESSMENT

This error impacts only those modeling cases where nominal corrosion processes are considered. Thus, only the Nominal Modeling Case and the Seismic GM Modeling Case are likely to be affected. In order to evaluate the impact on the value of *q* (the probability of one or more defects per closure lid weld), a standalone model that was derived from the base case and uses the same random seed (and hence the same sampling) was run for the 300 realizations to sample epistemic uncertainties. This was run twice, once with the uncorrected (original) weld volume and then once with the corrected weld volume, for both CDSP and CSNF WPs. The distribution of *q* (from 300 realizations) was compared for the two cases and it was found that the probabilities increased by about a factor of three for the impact evaluation case, indicating approximately three times more probability of having one or more defects per closure lid weld (per WP).

The mean probability of one or more defects per closure weld lid per CDSP WP increased from about 1.2×10^{-4} to 3.8×10^{-4} and that for the CSNF WP increased from about 1.1×10^{-4} to

3.4×10^{-4} (output DTN: MO0709TSPALAMO.000 [DIRS 182981]. For either WP type, the expected number of weld flaws per WP is significantly smaller than one. On the other hand, there are about six incipient cracks per patch expected on the closure lid patches (Section 6.3.5.1.2), which would lead to about 252 cracks per CDSP WP and about 228 cracks per CSNF WP. Because the main contribution to WP failure due to cracking comes from the presence and growth of incipient cracks and not weld flaws, the error in the weld volume is estimated to have negligible impact on the diffusive area, however it is possible that the first breach time could be earlier in some WPs due to occurrence of cracks from weld flaws. The overall impact on the mean annual dose is anticipated to be negligible.

P7. CRACK FAILURE OPENING

P7.1 ISSUE

The nominal crack failure opening area incorrectly calculated once the elapsed time is greater than the seismic damage time.

P7.2 ISSUE DESCRIPTION

After a seismic event that causes damage, the opening area calculation per failed WP from nominal stress corrosion cracks is incorrectly divided by the cumulative fraction of first crack failures on the WP. This results in an overestimation of the opening area as the cumulative fraction is small (<<1) early on and increases gradually to unity.

P7.3 IMPACT ASSESSMENT

The error can only impact the Seismic GM Modeling Case and would appear only after WP has undergone seismic damage. Note that prior to the seismic damage the calculated nominal crack area is calculated correctly. Because the total opening area from cracks per failed WP that occurs as a consequence of seismic damage (vibratory ground motion) is at least an order of magnitude greater than the area from the nominal SCC, correcting the error is not going to affect the transport area for diffusion calculations. The mean damaged areas for CSNF and CDSP WP are shown on Figures 6.6-12 and 6.6-13 under intact DS.

Because of the above arguments, this error is anticipated to show no to negligible impact on the mean annual dose for the Seismic GM Modeling Case.

P8. DEGRADATION START TIME

P8.1 ISSUE

Degradation processes inside the WP could start before the breach from an igneous event under certain aleatory configurations of specified igneous event times. This is not consistent with the treatment in other modeling cases.

P8.2 ISSUE DESCRIPTION

Two calculations for the igneous event time are currently made in the model. One is based on randomly sampling the event time (from a log-uniform distribution) to be used for the unified sampling case (no separation of aleatory and epistemic uncertainty) and the other is based on specifying the event time to be used in the compliance calculations (by separation of aleatory and epistemic uncertainty). An error occurs in connection with the WAPDEG subroutine as the sampled event time is passed to WAPDEG even when the event time is specified. This could result in failing all WPs in realizations where the sampled event time is prior to the specified event time. As a result, the degradation processes inside the WP could be triggered earlier than the actual event. The breach area, however, is calculated correctly and is based on the breach occurring either from the specified event time or from the nominal corrosion processes. In cases where nominal corrosion has not breached the WP, the breach area remains zero prior to the specified event time.

P8.3 IMPACT ASSESSMENT

This error only occurs in the Igneous Intrusion Modeling Case and is anticipated to have negligible impact on the mean annual dose. This is because all waste forms are modeled to degrade instantaneously after the igneous intrusion and thus starting the degradation processes inside the WP prior to the specified igneous event is likely to have negligible impact.

In realizations where the sampled event time is earlier than the specified event time and where the nominal corrosion processes could cause the WP to breach prior to the specified event time, the calculations would not be correct, as it would over predict the number of failed WPs. But such situations are only possible in very few realizations and unlikely to occur before 200,000 years, as in most realizations the breach from nominal corrosion processes typically do not occur prior to this time. The impact on mean annual dose is likely to be negligible.

P9. THRESHOLD RUBBLE VOLUME

P9.1 ISSUE

Threshold rubble volume (per drift length) that is used for determining when the nonlithophysal drifts undergo collapse is incorrect. It is currently using the value of 5 m^3/m while the correct value is 0.5 m^3/m.

P9.2 ISSUE DESCRIPTION

The threshold rubble volume (per drift length) is used to calculate the time when the drifts in the nonlithophysal locations should be considered collapsed for the purpose of determining the degraded-drift seepage flux. A similar calculation is done for the lithophysal locations but the threshold rubble volume is calculated correctly for the lithophysal locations.

P9.3 IMPACT ASSESSMENT

This error only occurs in the Seismic GM Modeling Case that is run for the 1,000,000-year duration, where the rubble volume resulting from multiple seismic events is calculated inside the

drift. For other modeling cases in the Seismic Scenario Class, the rubble volume is specified and is always greater than the threshold value of 5 m^3/m. Thus, reducing the threshold is not going to affect the outcome.

In the Seismic GM Modeling Case, the drift rubble calculations for the lithophysal zones are used in the nonlithophysal zones for the DS fragility calculations based on the rockfall loads. This is a conservative treatment, as the rockfall volume from the lithophysal zones is greater than that for the nonlithophysal zones (Figure 6.6-7) leading to greater probability of DS failure. Thus, this error does not affect the DS failure times in the nonlithophysal zones.

The threshold rubble volume for the nonlithophysal drift is used in the seepage calculations (for the percolation subregion) to determine when the seepage flux should be changed from the intact drift seepage value to the degraded drift seepage value. Nominal seepage values are used under intact drift conditions but after drift collapse the percolation flux at the base of the PTn is used for the nonlithophysal locations. This switch to percolation flux would occur earlier due to lowering of the threshold rubble volume. But the effects are likely to be very small, as only about 16 percent of the repository is in the nonlithophysal zone. For the five percolation subregions (from 1 to 5), the nonlithophysal fraction is 0.32, 0.24, 0.17, 0.04, and 0.11, respectively. The greatest change in seepage flux is likely to occur in percolation subregion 1, but because it only occupies 5 percent of the repository area the contribution to the overall mass release from the EBS is negligibly small. The actual change in the seepage flux is estimated to be relatively small in all percolation subregions, leading to negligible impact on the mean annual dose.

P10. UNINTENDED CORRELATION OF UNCERTAIN PARAMETERS

P10.1 ISSUE

Base-case TSPA-LA Model contains an inadvertent perfect correlation between two uncertainty parameters: WRIP_beta_rand_a and PCE_Delta_pCO2_a.

P10.2 ISSUE DESCRIPTION

The WRIP_beta_rand_a uncertainty parameter is used to sample a probability value (uniform between 0 and 1) such that when the Water-Rock Interaction Parameter is sampled from a beta distribution at every timestep, it samples from the same probability level in a given realization. The water-rock interaction parameter is used in the P&CE calculations for computing the appropriate invert chemistry.

The PCE_Delta_pCO2_a uncertainty parameter (uniform between -1 and 1) is used in scaling the ambient P_{CO2} in the drift between the minimum and maximum values to compute the drift P_{CO2}.

These two parameters got inadvertently correlated when one of the stochastic elements that was initially created was copied into another submodel to create the other stochastic element, thereby retaining the same local random seed.

P10.3 IMPACT ASSESSMENT

The two uncertainties, generally affect different abstractions, one in terms of water-rock interaction and the other in terms of drift P_{CO2} calculations. However, there is some indirect interaction between the two parameters. The maximum P_{CO2} value that is used in calculating the final drift P_{CO2} is a function of the water-rock interaction parameter. Even though some relationship, if any, may be present, the effect of this correlation on downstream calculations is likely to be weak. This is because: (a) the WRIP_beta_rand_a is used to only determine the probability value and not the actual value of the water-rock interaction parameter, which itself could vary at each timestep due to changes in the mean and standard deviations (SD); and (b) the calculations for the drift P_{CO2} and invert chemistry are further modified by considering other uncertainties, thus diluting the already-weak interaction. As a result, the unintentional correlation is likely to have negligible impact on the mean annual dose.

P11. UNCERTAINTY IN URANIUM SOLUBILITY

P11.1 ISSUE

The uncertainty associated with fluoride concentration in calculating the uranium solubility for the CSNF WPs is incorrectly calculated in the Igneous Intrusion Modeling Case.

P11.2 ISSUE DESCRIPTION

The GoldSim selector elements U_Eps_2_Hi_IStr and U_Norm_Hi_IStr calculate the uncertainty associated from variations in fluoride concentration (ε2 and N) in the uranium solubility for CSNF waste form domain (CSNF Cell 1) and for the CSNF corrosion products domain (CSNF Cell 2) (see Section 6.3.7.5.2). The values that are used under certain sets of P_{CO2} and pH conditions were mistakenly set to their CDSP counterparts. The correct values should be set to U_Eps_2_Boltwoodite_CSNF_High and U_Boltwoodite_CSNF_High_N, respectively, instead of U_Eps_2_Boltwoodite_CDSP_High and U_Boltwoodite_CDSP_High_N. In addition, the value of the third switch in the selector U_Norm_Hi_IStr was mistakenly set to U_Boltwoodite_Glass_Low_N. The correct value should be U_Schoepite_CSNF_High_N.

P11.3 IMPACT ASSESSMENT

This error only affects the uranium solubility calculation for the Igneous Intrusion Modeling Case. The duration of the error is likely to be small, as these calculations are only incorrect under high ionic strength conditions (I>0.2 mol/kg), which would last for only a short duration in the simulation due to dilution from flow through the WP. Furthermore, even under limited duration high ionic strength conditions, the calculation is only incorrect when the Na-Boltwoodite solubility is used, which is only applicable under limited P_{CO2} and pH conditions.

Because of the small probability of the error and its short duration, its effect is not likely to have an impact on the total mass transported out to the UZ and SZ. As presented on Figure 8.2-8 and discussed in Section 8.2.3.1, uranium is not a major contributor to the mean annual dose in the Igneous Intrusion Modeling Case and thus the effect of this error, if any, will be negligibly small.

P12. IONIC STRENGTH FOR HIGH-LEVEL WASTE GLASS DOMAIN

P12.1 ISSUE

During model calculations, for conditions where there is flow through the WP (exceeding a threshold of 0.1 L/yr), the ionic strength for the high-level waste (HLW) glass domain is always determined for flowing conditions, while it should be selecting the minimum between the ionic strength calculations for the flowing conditions and non-flowing conditions as described in *In-Package Chemistry Abstraction* (SNL 2007 [DIRS 180506], Section 6.10.9.1[a]).

P12.2 ISSUE DESCRIPTION

Two ionic strength abstractions are implemented in TSPA that are applicable to HLW waste form subdomain (CDSP Cell 1a): one that is based on relative humidity when there is no flow through the WP (referred as vapor influx case), and the other that is based on the flow rates and the time since WP failure (referred as liquid influx case). For conditions when there is no flow through the WP or where the flow through the WP is less than the threshold of 0.1 L/yr, the vapor influx based calculations are to be used. For flowing conditions, (equaling or exceeding threshold of 0.1 L/yr), the ionic strength should be based on choosing the minimum value after evaluating the ionic strength from both abstractions (SNL 2007 [DIRS 180506], Section 6.10.9.1[a]). The implementation error occurs in the latter case, where the ionic strength calculated for the liquid influx case is always used without evaluating the minimum.

P12.3 IMPACT ASSESSMENT

The implementation error is only applicable to ionic strength calculations in the HLW waste form subdomain of the EBS Transport Model and does not affect the ionic strength calculations for the downstream transport subdomains. Furthermore, it is only an issue when there is flow through the WP that equals or exceeds the threshold of 0.1 L/yr. But even here, for the majority of the time, the calculations would be correct, as under flowing conditions it is most likely that the minimum ionic strength would be calculated from the liquid influx-based abstractions rather than from the vapor influx-based abstraction. Thus the error, even if it occurs, would only occur for very short duration.

The most likely ionic strength for the liquid influx case typically ranges from 0.001 to about 0.1 mol/kg (see Table 6.3.7-11), while that for the vapor influx case typically ranges from about 0.13 mol/kg at relative humidity of 99.8 percent (a reasonable high value in the simulation) to 2.6 mol/kg at relative humidity of 95 percent (a reasonable low value at the start of transport) (Table 6.3.7-9 and Equation 6.3.7-1). The range of most likely ionic strength value for the liquid influx case is lower than that for the vapor influx case. However, because of the uncertainties that are computed independently for the two abstractions, the final values could either increased or decreased somewhat and thus there is a small chance that the current calculation may not be correct. But the duration of this condition is likely to be small, if it occurs, because the ionic strength typically decreases with increasing flow rates.

The ionic strength is used in the solubility model to determine the applicable uncertainty range and in the colloid-facilitated transport model to determine the colloid stability. Both models are unlikely to be affected for the most part, as they are only sensitive to variations across certain

ionic strength boundaries: the primary uncertainty in solubility model (ε_1) is affected when ionic strength goes above 1 mol/kg, while the colloid stability is typically affected above 0.1 mol/kg. Crossing these boundaries by taking the minimum from the vapor influx and liquid influx abstraction is unlikely. The overall effect on the mean annual dose is likely to be negligibly small, if any.

P13. EFFECT ON SEEPAGE FROM WASTE PACKAGE LENGTH CHANGE

P13.1 ISSUE

The seepage abstraction for the TSPA-LA Model uses an average WP length (including gap spacing) of 5.1 m. However, the average length of a WP (including gap spacing) should be about 5.6 m (DTN: MO0702PASTREAM.001_R0 [DIRS 179925]).

P13.2 ISSUE DESCRIPTION

The average WP length used in the seepage abstraction is 5.0 m (SNL 2007 [DIRS 181244], Table 4.1-1), which was the rounded length of the 44-BWR and 21-PWR WPs considered in previous designs. This length formed the basis for defining the model domain length used in the Seepage Model for Performance Assessment seepage simulations (BSC 2004 [DIRS 167652]). In other words, the Seepage Model for Performance Assessment model results, such as seepage rate or seepage percentage, represent the seepage conditions predicted for a drift section comprising one 5.0-m-long WP plus the 0.1-m gap spacing between WPs. With the introduction of the transportation, aging, and disposal (TAD) canisters for commercial spent nuclear fuel (CSNF), which are about 5.85-m long each (SNL 2007 [DIRS 179394], Table 4-3), the average length of all WPs plus gap increases to about 5.614 m (DTN: MO0702PASTREAM.001_R0 [DIRS 179925]).

P13.3 IMPACT ASSESSMENT

The Seepage Model for Performance Assessment provides the mean and SD of the distribution of seepage rates (kg/WP/yr) over a large range of capillary strengths, permeabilities and percolation fluxes. The seepage dynamically linked library (DLL) used in the TSPA-LA Model uses these rates, along with percolation fields, thermal histories at each WP location, and sampled values for mean capillary strength and mean permeability, to determine seepage rates (kg/WP/yr) at each location and time in each realization, and computes the seepage fraction (fraction of WP locations at which seepage occurs) at each time in each realization.

The Seepage Model for Performance Assessment is a three-dimensional continuum representation of a fractured rock system used to calculate drift seepage at Yucca Mountain. The three-dimensional calculational domain for the model is 10-m high, 4-m wide, and 2.4384-m long (BSC 2004 [DIRS 167652], Figure 6-1). This domain takes advantage of model symmetry and spatial correlation lengths to represent a system based on a drift diameter of 5.5 m and a WP length of 5.1 m with a smaller domain. Rock above and around the drift is also represented in the model. Because the model uses a no-flow vertical boundary along the drift axis, and also only represents a part of the WP length, seepage rates from the model are scaled up by a factor of

4.183, which represents the ratio between the considered drift area (5.5 m × 5.1 m) and the modeled drift area ((5.5 m / 2)*2.4384 m).

The seepage rates for an average WP length of 5.614 m can be estimated by scaling the Seepage Model for Performance Assessment results for an average WP length of 5.0 m. As noted in *The Seepage Model for PA Including Drift Collapse* (BSC 2004 [DIRS 167652]), the limited size of the calculational domain was chosen to allow for the use of a fine mesh at the same refinement as the SCM, while containing a reasonable number of cells that would not make the computational time too long. The cell dimensions in the vertical plane perpendicular to the drift axis are 0.1 m by 0.1 m and cell lengths parallel to the drift axes are about 0.3 m each (Section 6.3.1 of [DIRS 167652]). The vertical boundaries, perpendicular to the drift axis and along the drift centerline are appropriate due to symmetry. The main issue for a heterogeneous system is the domain length versus spatial correlation length (Section 6.3.1 of [DIRS 167652]). The lengths of the flow domain in the direction of the drift axis (2.4384 m) and normal to the drift axis (4 m) are 8 times and 13 times the spatial correlation length (0.3 m), respectively. Since the length of the flow domain in the direction of the drift axis is 8 times the correlation length, the no flow boundaries perpendicular to the drift axis are considered appropriate, and should not have significant effect on flow results. Because the no-flow boundaries have little effect on flow results, the model adequately represents any WP length longer than the model dimensions along the drift axis, as long as the results are scaled by the ratio of the chosen WP length to the modeled WP length. Thus, seepage rates for an average WP length of 5.614 m can be estimated by scaling the Seepage Model for Performance Assessment results for an average WP length of 5.0 m. This scaling would increase the mean and SD of the distribution proportionally (by a factor of 5.614 / 5.1 = 1.10).

The seepage fraction is computed in the Seepage DLL as the fraction of locations at which seepage exceeds the threshold of 0.1 kg/WP/yr. Since seepage rates increase when the average WP length is increased, the seepage fraction may also increase, because the seepage rate at some locations may increase from just less than the threshold to greater than the threshold. Current TSPA-LA software does not support a numerical evaluation of the degree to which the seepage fraction may increase when average WP length increases. However, sensitivity analyses conducted in *Abstraction of Drift Seepage* (SNL 2007 [DIRS 181244]) provide some insight into the degree that seepage fraction may change.

Abstraction of Drift Seepage (SNL 2007 [DIRS 181244], Section 6.8.2) reports the results of a sensitivity analysis that varied the distribution of the flow-focusing factor. The flow-focusing factor increases (or decreases) the local percolation flux to account for variability in flow at the scale of a few drift diameters. The distribution of flow focusing conserves the total water volume in the model domain; if percolation flux is increased at one location, this increase is offset by a corresponding decrease at other locations. The base distribution of flow focusing ranges between approximately 0.1 and 5 (SNL 2007 [DIRS 181244], Section 6.6.5.2.3), which introduces significant variability in local percolation flux. Sensitivity case 6a computes seepage results when the flow focusing was fixed at a constant value of 1 (no adjustment to local percolation flux) rather than sampled from the base distribution. This sensitivity case illustrates the effect on seepage fraction of increasing percolation flux at locations that have small fluxes. Because these locations are also the locations at which seepage is likely to be small, the effect on seepage fraction of increasing percolation flux at these locations is similar to the effect of

increasing the seepage flux at these locations. *Abstraction of Drift Seepage* (SNL 2007 [DIRS 181244], Table 6-12[a]) shows that using a constant value of 1 for the flow-focusing factor increases the seepage fraction by less than 3 percent over the first three climate states. Therefore, it is expected that the seepage fraction would not increase substantially by increasing the average WP length by 10 percent.

Because seepage rates increase proportionally with increased WP length, and seepage fraction is not anticipated to increase substantially, the net effect of increasing WP length on annual dose is to increase seepage rates in a percolation bin by approximately 10 percent. As demonstrated in Section P.17, annual dose may increase in proportion to relatively small changes in seepage rates. Therefore, the overall effect of increasing the average WP length used in the seepage abstraction is minor.

P14. IGNEOUS EVENT PROBABILITY

P14.1 ISSUE

Evaluate the effect on mean annual dose from the Igneous Intrusion and Volcanic Eruption Modeling Cases with the probability of the igneous event set to 10^{-7} per year. Note that this is purely a sensitivity analysis and not due to any error in the implementation.

P14.2 ISSUE DESCRIPTION

Since the impact assessment involves changing only the igneous event frequency, the mean annual dose can be calculated using EXDOC_LA V2.0 [DIRS 182102] software by applying a constant igneous event probability (λ_I) of 10^{-7} per year instead of sampling 300 values from a cumulative distribution function (CDF) (ranging from 1.38×10^{-11} to 7.76×10^{-7} per year) for the base case.

For the Igneous Intrusion Modeling Case, the expected annual dose is given by Equation 6.1.2-16, which is reproduced here:

$$\overline{D}_{II}(\tau|\mathbf{e}_i) = \int_0^{\tau} D_{II}(\tau|[1,t],\mathbf{e}_i)\lambda_{I,i}dt \qquad \text{(Eq. 6.1.2-16)}$$

In this sensitivity analysis, $\lambda_{I,i}$ is set to 10^{-7} per year for all 300 $\mathbf{e}_i$.

For the volcanic eruption case the expected annual dose is given by Equation 6.1.2-18, which is reproduced here:

$$\overline{D}(\tau|\mathbf{e}_i) = pE\,\lambda_{I,i}\,\overline{N}_{IE}\,\overline{F}\int_{U_{IE}}\left[\int_0^{\tau} D_{IE}(\tau|[1,t,1,\mathbf{u}],\mathbf{e}_i)dt\right]d_U(\mathbf{u})dU \qquad \text{(Eq. 6.1.2-18)}$$

where,

pE is the probability that an igneous event includes one or more eruptive conduits that intersects waste (= 8.314×10^{-2})

$\lambda_{I,i}$ is the frequency of igneous events for realization $\mathbf{e}_i$

$\overline{N}_{IE}$ is the mean number of WPs affected by an eruptive conduit

$\overline{F}$ is the mean fraction of WP content ejected into the atmosphere.

In this sensitivity analysis, because $\lambda_{I,i}$ is set to 10^{-7} per year the $pE \times \lambda_{I,i}$ is set to a constant value of 8.314×10^{-9} for all 300 $\mathbf{e}_i$. The value of pE is calculated by multiplying the probability of an eruption, given that a dike intersects the repository (= 0.28 [Section 6.5.2]) by the probability of one or more WPs hit by conduits originating from the dike (1-0.703 = 0.297 [Table 6.5-3]).

The calculations are done for the 10,000-year and 1,000,000-year simulations for both modeling cases.

P14.3 IMPACT ASSESSMENT

The comparison of the mean annual dose for the sensitivity analyses with the base case are shown on Figures P-6 and P-7. The mean annual dose increased by a factor of about six (ranging from 4.12 to 6.96 over the timesteps for the four cases), when the probability of the igneous event was set to 10^{-7} per year. This linear increase is expected, as the igneous event probability of 10^{-7} per year is about six times the mean of the distribution of $\lambda_{I,i}$ for the base case (mean value of approximately 1.67×10^{-8} per year).

P15. LONGITUDINAL DISPERSIVITY IN 1-D SZ TRANSPORT MODEL

P15.1 ISSUE

The epistemic uncertainty distribution for longitudinal dispersivity that is used in the 1-D SZ Flow and Transport Model, which is implemented using the pipe pathways, produces unrealistically large values of dispersivity in some realizations that are not supported by the scientific literature. This effect is primarily due to the unbounded log-normal distribution that is used to define the uncertainty in longitudinal dispersivity.

P15.2 ISSUE DESCRIPTION

The log-normal distribution for the longitudinal dispersivity (α_L), implemented in the 1-D SZ Flow and Transport Model for the base case, is unbounded with Mean [$\log_{10}(\alpha_L)$] = 2.0 and SD [$\log_{10}(\alpha_L)$] = 0.75. The sampled value is further adjusted by increasing it by one order of magnitude as it leads to better agreement between the SZ 1-D Transport Model and SZ Site-Scale (3-D) Transport Model results. As a result, sometimes the final values calculated become larger than are physically possible. For example, the largest value computed is 370 km, which is greater than 15 times the length scale of approximately 20 km for flowpaths in the SZ and well beyond any reasonable value tabulated in the literature.

P15.3 IMPACT ASSESSMENT

The 1-D SZ transport model is used to compute the dose for the listed radionuclides that are also shown by decay chain: $^{235}U \rightarrow {}^{231}Pa$, $^{233}U \rightarrow {}^{229}Th$, $^{230}Th \rightarrow {}^{226}Ra$, and ^{232}Th. The dose from ^{227}Ac and ^{228}Ra is calculated by assuming secular equilibrium with ^{231}Pa and ^{232}Th, respectively. In the base cases, transport of all these radionuclides are affected by the unrealistically high longitudinal dispersivity as it leads to earlier arrival of the mass and higher initial concentrations at the RMEI leading to higher early dose. Of the radionuclides taken from the 1-D SZ transport model, none are important to the mean annual dose in any of the modeling cases for the 10,000-year simulations. Thus, all modeling cases run for 10,000 years will be negligibly impacted.

For the 1,000,000-year simulations, the only significant dose contributor modeled using the 1-D SZ transport model is ^{226}Ra. It is important in those modeling cases where there is rapid transport of ^{226}Ra (along with its parent radionuclides) through the WP to the UZ and SZ without much decay. ^{226}Ra is the top dose contributor in the Igneous Intrusion Modeling Case for the majority of the simulation (Figure 8.2-5b). It is second highest dose contributor in the Seismic FD Modeling Case (Figure 8.2-14b) and second or third highest for the two Early Failure Modeling Cases (Figures 8.2-4b and 8.2-6b). Bounding the longitudinal dispersivity at the upper end is likely to have the greatest effect on the Igneous Intrusion Modeling Case as ^{226}Ra is the highest dose contributor. However, even here, the impact on mean annual dose would be relatively small because only a few realizations (epistemic vectors) have the unrealistically high longitudinal dispersivity values, while most realizations have the values within the physical range. ^{226}Ra has a relatively short half-life of 1,600 years compared to the transport times through the SZ (SNL 2008 [DIRS 183750], Figure 6-14[a]). Thus, most of the mass that is released from the WP and UZ will be decayed while being transported through the SZ pipe pathways, even accounting for the high dispersivity values.

To evaluate the impact of using unrealistically high longitudinal dispersivity, the log-normal distribution was truncated at the upper end at two SDs from the geometric mean and the sampled value was directly used without adjusting it further. The upper bound was provided by the subject matter expert (DTN: SN0710PASZFTMA.003_R0 [DIRS 183485]) bearing in mind that the two SD upper bound would cover about 98 percent of the area under the standard normal curve. As a result, the maximum value possible is 3.16 km, which is considered reasonable for the transport distances in the SZ. The impact of the updated dispersivity range was evaluated for the Igneous Intrusion Modeling Case, where maximum effect is likely to be seen. Note that only 26 percent of the realizations in the base case have longitudinal dispersivity values greater than the maximum value of 3.16 km, and thus the impact is likely to be small. A comparison of the mean annual dose for the base case and the impact evaluation case is shown on Figure P-8. The mean annual dose from the impact evaluation case shows a reduction of about 25 percent to 30 percent for the majority of the simulation. Figure P-9 shows the effect on ^{226}Ra dose where the reduction is over 60 percent, with greater percentage reduction (over 80 percent) prior to 200,000 years. The effect is somewhat non-linear on ^{226}Ra dose compared to the number of realizations that are impacted, because almost all of the ^{226}Ra release out of the SZ in the impact evaluation case comes from decay of ^{234}U to ^{230}Th, which decays to ^{226}Ra while being transported through the pipe pathways. Because ^{230}Th has a much larger K_d in the SZ (ranging from 1,000 to 10,000 mL/g) compared to ^{226}Ra (ranging from 100 to 1,000 mL/g) (Table 6.3.10-2) and has much larger half-life (about 75,400 years), the transport of ^{230}Th (and to

some extent ^{234}U) through the 1-D SZ transport model ultimately controls the ^{226}Ra dose (Figure P-9). The major radionuclides contributing to the mean annual dose are shown on Figure P-10 for the impact evaluation case. Here, the ^{226}Ra dose contribution drops, as anticipated, from being the top contributor to the third highest contributor, with ^{242}Pu and ^{237}Np becoming the two highest contributors. The overall impact on the mean annual dose is relatively small with a reduction of 25 percent to 30 percent.

P16. GLASS DEGRADATION RATE

P16.1 ISSUE

The HLW glass degradation rate calculation for the Igneous Intrusion Modeling Case uses the degradation model that was developed for nominal conditions instead of applying an instantaneous degradation, as described in Section 5.3.1.

P16.2 ISSUE DESCRIPTION

The HLW glass degradation rate for the Igneous Intrusion Modeling Case uses the glass degradation model that is applicable for nominal conditions (valid up to 300°C) and computes the dissolution rate by holding the temperature at a maximum value of 300°C for all times while the WP temperature from igneous intrusion is greater than 300°C. The intended rate should have been an arbitrarily chosen high value (>>1 per year) that results in instantaneous degradation of HLW glass, following an igneous event.

P16.3 IMPACT ASSESSMENT

Two glass dissolution rate calculations are made at every timestep in the HLW glass degradation model, one for an acidic solution and the other for an alkaline solution and then the higher rate is selected for the given timestep. However, when the temperatures are above 100°C, the in-package pH is set to 10 and the dissolution rate for alkaline solution is used. The equation for dissolution rate calculation is presented by Equation 6.3.7-8, which is reproduced here:

$$rate_G = k_E 10^{\eta \bullet pH} \exp(-E_a / RT) \qquad \text{(Eq. 6.3.7-8)}$$

where

$rate_G$ = absolute HLW glass dissolution rate ($g/m^2/d$)

k_E = rate coefficient ($g/m^2/d$)

η = pH dependence coefficient (dimensionless)

E_a = effective activation energy (kJ/mol)

R = universal gas constant (8.14E-03 kJ/mol/K)

T = temperature (K).

The parameter values for k_E, η, and E_a are presented in Table 6.3.7-32. For the alkaline solution, the mean value for k_E is 11,585 g/m^2/day, while η and E_a are constant values of 0.49 and 69 kJ/mol, respectively.

The calculated dissolution rate is converted into a fractional degradation rate by multiplying with the specific surface area of glass (fixed value of 2.7×10^{-3} m^2/kg) and by the glass exposure factor that accounts for the higher effective surface area of the glass log resulting from cracking of the HLW glass after it is poured into the canister (mean value of 8.3).

Since the WP temperature is set at a maximum value of 300°C for times when the calculated temperature from igneous intrusion is above it, and since the pH is set at 10 while the WP temperatures are above 100°C, the mean fractional degradation rate following the igneous event time can be calculated using the mean values of the uncertain parameters. The mean fractional degradation rate is calculated to be about 3.9 per year. This results in instantaneous degradation of the HLW glass (for all practical purposes) on an average. Considering the lower bound (most likely values) of the uncertain distributions (k_E = 28.2 g/m^2/day and glass exposure factor = 4) results in fractional degradation of 0.0045 per year. This results in degrading almost all of the HLW glass in about 200 years, which is less than one time-step length in the TSPA simulations for the 1,000,000-year calculations and thus instantaneous for all practical purposes.

Since the HLW glass degradation is nearly instantaneous even by using the degradation model developed for the nominal conditions, there is no impact anticipated on the mean annual dose even by explicitly modeling instantaneous degradation following the igneous event. Furthermore, since CSNF is degraded instantaneously following the igneous event and because it holds most of the total radionuclide mass in the repository, the dose contribution from CSNF releases is likely to control the mean annual dose. Any small changes in the degradation rate for HLW glass are unlikely to have an impact on the mean annual dose.

P17. SEEPAGE FLUX AFTER DRIFT COLLAPSE

P17.1 ISSUE

The seepage flux in the lithophysal zones following the drift collapse may be under predicted in some realizations due to error in estimating the bounding values.

P17.2 ISSUE DESCRIPTION

The seepage flux (a volumetric flux) for the lithophysal zones following the drift collapse is doubled compared to the intact drift seepage flux, based on the assumption of doubling the drift diameter following the drift collapse in the lithophysal zones. This value is then compared to the theoretical maximum, which is calculated by multiplying the percolation flux with the plan area equal to drift diameter times the WP length of 5.1 m. If the calculated seepage flux exceeds the theoretical maximum, the maximum value is taken. However, the plan area for calculating the theoretical maximum flux is not doubled following the drift collapse. This results in under predicting the maximum flux, which may in turn result in under predicting the seepage flux following the drift collapse. The seepage fractions are not affected as the number of repository locations that see seepage at the end of simulation remain unchanged even after drift collapse.

P17.3 IMPACT ASSESSMENT

The error is anticipated to only have an impact on the Seismic GM and Seismic FD Modeling Cases as drift collapse occurs in only those modeling cases. There is no impact on the 10,000 year Seismic GM Modeling Case, as drift collapse is not considered. In the 1,000,000-year Seismic GM Modeling Case, the impact of the error is estimated to be small, as the transport through the WP is only diffusive for the majority of the simulation due to the presence of stress corrosion cracks. Only after enough general corrosion patches appear on the WP would the advective flux be significant. But since the average number of patches on the failed WP is less than 1 percent by 700,000 years, the start of advective flux is not likely to have an appreciable impact on dose. Furthermore, the diffusive flux is expected to remain the dominant transport process even later than 700,000 years until large number of patches have formed. The impact of this error is likely to be negligibly small on the mean annual dose.

For the Seismic FD Modeling Case, complete drift collapse occurs following the seismic event and based on the breach area all of the seepage flux could go through the WP. The amount of increase in seepage flux from this error and its impact on mean annual dose is evaluated by running a 300-realization case, where the epistemic and aleatory uncertainties are sampled per realization (in a unified manner for computational convenience), and then comparing the output from the Seepage DLL for the impact evaluation case with the uncorrected case (called base case). The results indicate that the mean seepage flux increases, as anticipated, for the impact evaluation case for all percolation subregions (Table P-4) in proportion to the lithophysal rock fraction in the percolation subregion. The area weighted increase in mean seepage flux at 1,000,000 years is about 22 percent. The mean seepage flux for percolation subregion 3 (the largest percolation subregion) is compared for the two case (Figure P-11). The comparison shows that the increase in seepage rate is fairly constant (around 20 percent) for the majority of the simulated time but increases slightly with increasing seepage rates. Since the area weighted mean seepage flux increased by about 22 percent at 1,000,000 years, it is anticipated that the advective flux of radionuclides, whose concentration remains at the solubility limits, would also increase by about the same amount. The mean annual dose comparison for the two cases is presented on Figure P-12. It shows an increase of about 20 percent. This is because ^{242}Pu is the major dose-controlling radionuclide and its concentration is solubility-controlled in the EBS and hence its dose increases by about 20 percent (Figure P-12). For radionuclides that do not have

solubility limits, the increased seepage flux would have negligible impact on the mass flux. The overall impact on mean annual dose is relatively small.

P18. UNSTABLE IRON OXYHYDROXIDE COLLOIDS

P18.1 ISSUE

Minimum iron oxyhydroxide colloid concentration is being applied even under stable conditions due to error in calculating the ionic strength threshold for colloid stability calculations.

P18.2 ISSUE DESCRIPTION

The iron oxyhydroxide (or steel degradation) colloid concentration for the EBS Transport Model is determined by first evaluating the stability of colloids under given pH and ionic strength conditions at each timestep as shown on Figure 6.3.7-11d. If the ionic strength is less than the ionic strength threshold (for a given pH), the iron oxyhydroxide colloids are considered to be stable and the colloid concentration is sampled from a distribution (Table 6.3.7-65). However, if the ionic strength is higher than the ionic strength threshold, a constant minimum value of 1×10^{-6} mg/L is applied. The equation for computing the ionic strength threshold for the pH between 4.5 and 8.4 is shown by Equation 6.3.7-18, which is reproduced here:

$$I_{threshold} = -0.013 \times pH + 0.11 \qquad \text{(Eq. 6.3.7-18)}$$

The coefficient term of -0.013 is incorrectly entered as -0.13 in the database. As a result of this error, the ionic strength threshold becomes negative over the pH range of 4.5 to 8.4 leading to unstable iron oxyhydroxide colloids, thus under predicting the colloid concentration, which is set to a minimum value of 1×10^{-6} mg/L.

P18.3 IMPACT ASSESSMENT

The error is expected to have a negligible impact on the mean annual dose for all modeling cases. This is because in the modeling cases where there is no flow through the WP, the ionic strength is likely to be greater than the maximum threshold of about 0.05 mol/kg for iron oxyhydroxide colloids (Figure 6.3.7-11d). The most likely in-package ionic strength for the vapor-influx case, based on Equation 6.3.7-1 and Table 6.3.7-9, ranges from about 0.13 mol/kg at relative humidity of 99.8 percent (a reasonable high value in the simulation) to 2.6 mol/kg at relative humidity of 95 percent (lower bound for initiating transport). Even considering the uncertainty, which could reduce the ionic strength by half, the values are still likely to be greater than the threshold value of about 0.05 mol/kg, leading to continued instability of the iron oxyhydroxide colloids, irrespective of the error.

In the modeling cases, where the flow through the WP exceeds 0.1 L/yr such that in-package chemistry is determined by liquid-influx case, the ionic strength values are likely to be less than the ionic strength threshold (at a given pH) for the majority of the realizations leading to under prediction of colloid concentrations. But since iron oxyhydroxide colloid concentrations are relatively small even under stable conditions (mean value of about 1.5 mg/L from the stainless steel degradation; Table 6.3.7-65) the majority of the transport is likely to be in the dissolved state leading to negligible impact on the mean annual dose. Since the Igneous Intrusion

Modeling Case has the highest dose contribution among the modeling cases where there is flow through the WP, such as the FD Modeling Case and Drip Shield EF Modeling Case (compare Figures 8.2-5, 8.2-8, and 8.2-14), the impact of the error is evaluated for this modeling case.

The impact is evaluated by running a 300-realization simulation, where the epistemic and aleatory uncertainties are sampled per realization (in a unified manner for computational convenience), and then the mean annual dose is compared to the uncorrected case (called base case), which is also run in a similar fashion. As shown on Figure P-13, the impact on mean annual dose is negligible, even though the dose contribution from plutonium that is irreversibly sorbed on the colloids has increased. This is because the dissolved plutonium controls the mean annual dose. The impact of the correction is greater for the ^{242}Pu mass compared to ^{239}Pu mass that is irreversibly associated with the colloids. This is because the majority of the ^{239}Pu mass irreversibly associated with colloids is due to contribution from the mass irreversibly associated (embedded) with HLW glass waste form colloids as compared to the mass that is irreversibly associated with the iron oxyhydroxide colloids. In contrast, ^{242}Pu mass in the HLW glass inventory is negligibly small (compared to ^{239}Pu mass) and thus ^{242}Pu that is irreversibly associated with the iron oxyhydroxide colloids dominates over ^{242}Pu mass irreversibly associated with the HLW glass waste form colloids, leading to greater change as a result of the correction. The overall impact on the mean annual dose is negligibly small.

P19. DOE SPENT NUCLEAR FUEL MASS RELEASE

P19.1 ISSUE

In the Igneous Intrusion Modeling Case, the number of WPs assigned for computing the DOE spent nuclear fuel (DSNF) mass in the non-dripping environments are not correctly calculated following the igneous event.

P19.2 ISSUE DESCRIPTION

Following the igneous event, the number of WPs assigned to the non-dripping environment is incorrectly set to be the same as the number of WPs assigned to the dripping environment. As a result, the DSNF mass available for release is incorrectly computed based on the explicit calculations performed using the discrete change element in GoldSim. There is no effect on the CSNF or HLW mass calculations, as the GoldSim Source element is used leading to a static number of WPs that are determined at the start of the simulation.

P19.3 IMPACT ASSESSMENT

The impact of the error on the Igneous Intrusion Modeling Case is likely to be negligibly small, as total DSNF inventory itself represents a small part of the total inventory in the repository (based on information in Tables 6.3.7-5 and 6.3.7-1). But since the error is restricted to only non-dripping environments, the impact would be even smaller. Table P-1 (second column) shows the seepage fraction that is applied prior to the igneous event, and based on that, the majority of the WPs would fall into the non-dripping environment. After the igneous event, due to the error, the number of WPs assigned to the non-dripping environment, are set to be the same as those for the dripping environment, resulting in a decrease of the number WPs in the non-dripping environment, thus under-representing the DSNF mass. The decrease in the number

of WPs for non-dripping environments would vary by each percolation subregion, but the weighted average reduction (weighted by the area of each percolation subregion) would be about 31 percent. Considering that the weighted non-dripping area prior to the igneous event is about 60 percent, thus the maximum under estimation in total mass out of the EBS would be about 19 percent (= 0.31 × 0.6). In actuality, the under estimation would be even smaller, as different radionuclides would be affected differently based on the proportion of their mass in the DSNF inventory compared to the HLW and CSNF inventory. Since the major dose contributors for this modeling case are expected to be ^{99}Tc, ^{239}Pu, ^{242}Pu, and ^{237}Np (Figure P-10), and because contribution of DSNF inventory is less than 2 percent of the total inventory for these radionuclides, the impact of the error is likely to be negligible.

P20. GOLDSIM SOFTWARE ERROR

P20.1 ISSUE

Incorrect mass amounts could be calculated by the Source and Pipe elements (special GoldSim elements) in the Contaminant Transport module of GoldSim software when decay chains have feedback loops.

P20.2 ISSUE DESCRIPTION

In the TSPA-LA Model, the decay chain feedback loops are utilized in the EBS transport-related cell pathways to model kinetic sorption-desorption processes (with both forward and backward rate constants) in the WP. Since the Source elements are used in the EBS transport submodel and the Pipe elements are used in the UZ and SZ transport submodels, the calculated mass fluxes could be affected by the error. Note that the Volcanic Eruption Modeling Case is not affected by this error as the transport calculations are done through external DLLs.

P20.3 IMPACT ASSESSMENT

Since the error was discovered, the software vendor (GoldSim Technology Group) has corrected the software problem and released a service pack update (GoldSim Version 9.60 Service Pack 3). To evaluate the impact of the error, all modeling cases (except for the Volcanic Eruption Modeling Case) were rerun with the corrected software by simulating 300 realizations, where the epistemic and aleatory uncertainties are sampled per realization (in a unified manner for computational convenience). The results, which are summarized in Table P-5, indicate minor dose differentials on a per realization basis, with up to a ±5 percent change. The impact on mean annual dose is likely to be even smaller over most of the simulated duration. For the purpose of illustration, the impact on mean annual dose for the Seismic GM Modeling Case and the Igneous Intrusion Modeling Case (the two cases with highest mean annual dose for the 1,000,000-year simulation duration) are shown on Figures P-14 and P-15. In these figures, the base case refers to the uncorrected case while the impact evaluation case refers to the case where the error has been corrected. In both modeling cases, the mean annual dose remains practically unchanged. The impact of this error is categorized to be small for all modeling cases.

P21. UNSATURATED ZONE TRANSPORT THROUGH FAULT ZONE

P21.1 ISSUE

Transport through the fault zones of the UZ transport model could be delayed for some radionuclides that are generated from the decay of the parents and whose sorption properties differ widely from their parents. Note that this issue has been documented in Condition Report (CR) 11572.

P21.2 ISSUE DESCRIPTION

The conceptual model for the transport of dissolved or reversibly sorbed radionuclides through the UZ fault zones is different from the remainder of the UZ in two aspects: (1) the fault zones utilize a dual-permeability transport model that considers advection and dispersion without any fracture-matrix diffusive interaction, and (2) the sorption in the fault zones is simulated for both the fracture and the matrix continuum. The manner in which the particle-tracker subroutine for transport in the fault zones is implemented may sometimes cause an unexpected delay in the transport of daughter species. The delay is caused by the fact that when a parent species particle decays to a daughter species particle within a given grid-block cell, the effect of the change in sorption coefficient is not manifested until the daughter species particle enters the next cell. In other words, the sorption coefficient for the parent species is continuously applied to the daughter species while the daughter species resides in the cell where it was generated. This could sometimes result in a significant delay of the daughter species if the sorption coefficient of the parent species were to be much greater. This delay could affect the transport of species, such as ^{237}Np and ^{226}Ra, whose respective parents, ^{241}Am and ^{230}Th, have much greater sorption coefficients (Table 6.3.9-2). The effects on transport are likely to be small for those daughter species whose sorption coefficients are not very different from their parents and would result in faster transport for those daughter species whose sorption coefficients are greater than those of the parents, which is conservative.

P21.3 IMPACT ASSESSMENT

The impact on the mean annual dose from this error is anticipated to be small as only about 7 percent of the repository nodes in the UZ transport model are considered as fault nodes (39 fault nodes out of 560 nodes) and, thus, a small fraction of the total mass released from the EBS will be passed through the faults. Furthermore, it should be noted that the anomalous behavior occurs only for those daughter species that are generated from the decay of the parents in the fault-zone cell while they reside in that cell. Correct sorption coefficients are applied to the daughter species once they move into a different cell or when they are injected directly in the fault zones.

To evaluate the impact of the error, the Seismic GM Modeling Case and the Igneous Intrusion Modeling Case, the two cases with the highest mean annual dose for the 1,000,000-year simulation duration, were rerun for 300 realizations such that the epistemic and aleatory uncertainties are sampled per realization in a unified manner for computational convenience. For the impact evaluation, the transport characteristics of the fault zones were modified so that the conceptual model for transport through the fault pathways is made similar to the rest of the UZ transport model, thus allowing for the fracture-matrix diffusive interaction and no sorption in the

fracture continuum of the fault zones. This is an acceptable alternative conceptualization besides being somewhat conservative. In this approach, the sorption properties of the daughter species are applied correctly while they reside in the cell where they were generated.

The mean annual dose comparison plots for the Seismic GM Modeling Case and the Igneous Intrusion Modeling Case are shown on Figures P-16 and P-18. The mean annual dose remains practically unchanged with a small increase (< 5 percent) for the impact evaluation case in the majority of the simulation. Among the major dose contributing radionuclides, the dose for ^{226}Ra and ^{237}Np is affected, as anticipated (Figures P-17 and P-19). The overall impact of the error on the mean annual dose for all modeling cases is categorized to be small (< 5 percent).

The sensitivity analyses of radionuclide transport presented in Appendix K are also unlikely to be affected including those analyses that investigate the uncertainty in transport of ^{239}Pu and ^{237}Np through the UZ. This is because (a) the mass transported through the UZ fault nodes represents a small fraction of the total mass transported through the UZ, and (b) the mass of ^{239}Pu and ^{237}Np entering the UZ fault nodes from EBS is likely to be much higher than that produced in the UZ fault nodes from the decay of their parents, ^{243}Am and ^{241}Am, respectively, due to small initial mass of ^{243}Am in the emplaced inventory and fast decay rates of ^{241}Am compared to slow transport through the EBS due to sorption.

P22. OTHER MINOR IMPLEMENTATION ERRORS

P22.1 ISSUE

Other minor implementation errors that have been discovered since running the compliance case are grouped and addressed here.

P22.2 ISSUE DESCRIPTION

The implementation errors whose effects are unlikely to have any impact on the dose are grouped together and addressed in Table P-6. They are unlikely to affect the radionuclide releases appreciably in our judgment but are documented for future correction.

P23. SUPERFICIAL CHANGES

P23.1 ISSUE

Several suggested changes to the model file structure are tracked in a model status log.

P23.2 ISSUE DESCRIPTION

Several nice-to-have changes are proposed in the model status log that will make the TSPA Model file more transparent and consistent with the conceived code architecture.

P23.3 IMPACT ASSESSMENT

There is no impact from these as these are only superficial (cosmetic) changes and do not affect the calculations.

P24. SUMMARY

The issues presented in this appendix are summarized in Table P-7 with their anticipated impact on the mean annual dose for the modeling cases discussed in the preceding sections. Since most of the issues evaluated are estimated to have negligible to small impact (except for the issue discussed in Section P3), the combined effect of correcting the errors is expected to be small as well on the mean annual dose for all modeling cases. The impact of the issue discussed in Section P3 is estimated to cause appreciable decrease in the mean annual dose for some period of time (typically between 200,000 and 300,000 years) in only the Seismic GM Modeling Case for the 1,000,000-year duration. In none of the issues evaluated does the mean annual dose increase appreciably (by a factor of two or more) above the base-case results presented in Section 8. In fact, in most cases, it decreases. Thus, the confidence in the base-case results as an estimator of the mean annual dose to the reasonably maximally exposed individual (RMEI) can be maintained, and the validation activities performed on the base-case results remain applicable.

Table P-1. Comparison of Mean Seepage Fraction for Various Percolation Subregions for Nominal Conditions

Percolation Subregion	Seepage Fraction – Base Case	Seepage Fraction – Impact Analysis	Percent Change from Base Case	Percolation Subregion Weighting	Percent Weighted Change in Seepage Fraction
1	0.125	0.088	-29.0	0.05	1.45
2	0.340	0.230	-32.1	0.25	8.03
3	0.437	0.329	-24.6	0.4	9.85
4	0.436	0.384	-11.7	0.25	2.93
5	0.494	0.466	-5.54	0.05	0.27
Total					22.53

Source: Output DTNs: MO0709TSPAREGS.000 [DIRS 182976] – for base case; MO0709TSPALAMO.000 [DIRS 182981] – for impact analysis.

Table P-2. Comparison of Mean Seepage Fraction for Various Percolation Subregions for Seismic Fault Displacement Modeling Case

Percolation Subregion	Seepage Fraction – Base Case	Seepage Fraction – Impact Analysis	Percent Change from Base Case	Percolation Subregion Weighting	Percent Weighted Change in Seepage Fraction
1	0.467	0.431	-7.78	0.05	0.389
2	0.649	0.558	-14.08	0.25	3.52
3	0.719	0.636	-11.59	0.4	4.64
4	0.704	0.661	-6.06	0.25	1.52
5	0.751	0.734	-2.38	0.05	0.12
Total					10.18

Source: Output DTNs: MO0709TSPAREGS.000 [DIRS 182976] – for base case; MO0709TSPALAMO.000 [DIRS 182981] – for impact analysis.

Table P-3. Comparison of Mean Seepage Fraction for Various Percolation Subregions for the Seismic Ground Motion Modeling Case

Percolation Subregion	Seepage Fraction – Base Case	Seepage Fraction – Impact Analysis	Percent Change from Base Case	Percolation Subregion Weighting	Percent Weighted Change in Seepage Fraction
1	0.464	0.088	-81.0	0.05	4.05
2	0.647	0.230	-64.4	0.25	16.1
3	0.718	0.329	-54.2	0.4	21.7
4	0.704	0.384	-45.4	0.25	11.4
5	0.752	0.466	-38.0	0.05	1.9
Total					55.1

Source: Output DTNs: MO0709TSPAREGS.000 [DIRS 182976] – for base case; MO0709TSPALAMO.000 [DIRS 182981] – for impact analysis.

Table P-4. Comparison of Mean Seepage Flux (m^3/yr) at 1,000,000 years for Various Percolation Subregions for the Seismic Ground Motion Modeling Case

Percolation Subregion	Seepage Flux – Base Case	Seepage Flux – Impact Analysis	Percent Change from Base Case	Percolation Subregion Weighting	Percent Weighted Change in Seepage Flux
1	0.096	0.098	1.76	0.05	0.09
2	0.350	0.400	14.3	0.25	3.58
3	0.523	0.635	21.3	0.4	8.53
4	0.547	0.723	32.2	0.25	8.06
5	0.748	0.964	28.8	0.05	1.44
Total					21.7

Source: Output DTN: MO0709TSPALAMO.000 [DIRS 182981].

Table P-5. Quantitative Evaluation of the Impact of GoldSim Software Error on Various Modeling Cases Based on Dose

Number	Modeling Case	Duration (years)	Percent Realizations with a Dose Change (%)	Typical Difference (for at least 90% of realization) (%)
1	Nominal	10,000	0	0
2	Nominal	1,000,000	97	±3
3	EF DS	10,000	28	±3
4	EF DS	1,000,000	87	±0.5
5	EF WP	10,000	2.3	0
6	EF WP	1,000,000	43	±2
7	Igneous	10,000	93	±2.2
8	Igneous	1,000,000	100	±5
9	Seismic GM	10,000	7.3 (88 showed zero dose)	±1
10	Seismic GM	1,000,000	96	±4
11	Seismic FD	10,000	21	±1.3
12	Seismic FD	1,000,000	93	±3
13	Human Intrusion	1,000,000	99	-5.2 to +1

Source: Output DTN: MO0709TSPALAMO.000 [DIRS 182981].

Table P-6. Discussion of Other Minor Implementation Errors

	ISSUE DESCRIPTION	ANTICIPATED IMPACT
1	Drift-wall condensation incorrectly turned off in the non-dripping environments.	This error should have negligible or no impact in all modeling cases. Because drift-wall condensation occurs for at most 2,000 years (Section 6.3.3.2.3) and because the DS remains intact throughout this period in all modeling cases except Drip Shield EF Modeling Case, the release from any failed WP should be negligibly impacted. In the Drip Shield EF Modeling Case since the WP is always modeled to be located in the dripping environment (Section 6.4.1.3), there should be no impact.
2	Inconsistent half-lives applied to ^{79}Se and ^{126}Sn for calculations performed using GoldSim elements and those used by the UZ and SZ transport models implemented through DLLs.	The ^{79}Se half life in GoldSim is set at 290,000 years while that in the UZ and SZ transport model is set at 295,000 years. The ^{126}Sn half life in GoldSim is set at 230,000 years while that in the UZ and SZ transport model is set at 250,000 years. These inconsistencies are minor, as they occur only in the second significant digit. Since the dose contribution from ^{79}Se and ^{126}Sn is at least an order of magnitude lower than some of the other radionuclides (see Figures P-1 to P-5), the impact on the mean annual dose would be negligible.
3	In the calculations to determine the time of first seismic damage to the WP, the abstraction for WP failure under intact DS is considered while the DS is intact. This calculation should not be used after either the DS plate or DS framework has failed. However, this calculation ignores the DS framework failure and only considers the DS plate failure to determine whether to use this abstraction or not.	It should be noted that this error only affects the 1,000,000-year Seismic GM Modeling Case because the DS remains intact in the 10,000-year modeling case. Since the DS framework failure (average failure time of 100,000 years) occurs earlier than the DS plate failure (average failure time of 250,000 years), there is a possibility of predicting the WP failure time earlier than intended in the time duration where the DS framework has failed but the DS plate is intact. This error may have an impact on estimating first failure time for only CDSP WPs as the probability of WP failure under intact DS is generally greater than the probability of failure under failed DS that is surrounded by rubble. Even here, the probability of occurrence of this error is small as the DS framework lasts up to 100,000 years on an average, during which time CDSP WPs that are likely to fail from seismic damage would have failed in majority of the realizations (~70%). For CSNF WPs there is no impact anticipated, as the probability of failure under intact DS is much smaller than the probability of failure under the failed DS that is surrounded by rubble. As a result, this error is likely to have only a negligible impact on the mean annual dose.
4	The calculation for the time of first seismic damage may be incorrect if the WP damage is from the first seismic event.	This error only appears when the first seismic event causes the damage to the WP or leads to rockfall. Since seismic events occur on an average of every 2,330 years (inverse of specified annual rate of 4.287×10^{-4} yr^{-1}), only those realizations would be impacted where the WP damage or rockfall occurs within 2,330 years (on an average). There are only five such realizations in the 9,000 realization seismic ground motion base case where the damage should have occurred from the first seismic event but did not occur due to the error. The impact of this error is negligible. No other modeling cases are affected.

Table P-6. Discussion of Other Minor Implementation Errors (Continued)

	ISSUE DESCRIPTION	ANTICIPATED IMPACT
5	The HLW glass derived waste form colloid concentrations are overestimated under conditions when the waste form colloids are unstable.	This error occurs only when the conditions are unstable for the generation of glass waste form colloids. Since the maximum concentration of HLW glass waste form colloids, under stable conditions, is itself small (maximum of 2 mg/L and a mean of 0.3 mg/L) the mass transported on colloids will be negligibly small compared to that transported in the dissolved phase. Thus, this overestimation would have negligible impact on the mean annual dose. Furthermore, the unstable conditions generally occur when the ionic strength is greater than 0.4 mol/kg, which are typical while there is no flow through the WP. Since the transport mechanism is diffusion when there is no flow and because the diffusion coefficient of colloids is much smaller compared to the dissolved species (by at least two orders) no appreciable mass can be carried by the colloids.
6	The element that integrates the mass released from the WP in the Human Intrusion Scenario integrates the mass flux rate computed for the previous timestep over the next timestep using the next timestep length. It should instead integrate the mass flux rate computed for the given timestep over that timestep length.	This error would only have an impact when the timestep length is changing as the integrated mass would change. Since the intrusion time is set at 200,000 years in the Human Intrusion Scenario and because there is no change made in the timestep length for the remaining simulation duration, the calculations are not affected. The only impact is one timestep delay in passing the mass to the UZ borehole pathway while the dose magnitudes remain unaffected. Since this is a highly stylized modeling case, with a selected intrusion time, the one timestep delay is not important to the overall system results and does not affect the dose values.
7	The implemented range of two uncertain parameters used in determining the number of monolayers of adsorbed water for corrosion products as part of the EBS Transport submodel is different from their intended ranges.	The stochastic elements FHH_Isotherm_k_CP_a and FHH_Isotherm_s_CP_a are sampled to determine the value for parameters *k* and *s* that are used in the water adsorption isotherm for corrosion products to determine the number of sorbed layers of water (Section 6.3.4.3.2 of the *EBS Radionuclide Transport Abstraction*, SNL 2007 [DIRS 177407]), which is eventually used in computing the saturation under conditions when there is no flow through the WP. The uniform distribution ranges used, as specified in the DTN: SN0703PAEBSRTA.001_R3 [DIRS 183217] (modified from Table 8.2-4 of the *EBS Radionuclide Transport Abstraction*, SNL 2007 [DIRS 177407]) are: FHH_Isotherm_k_CP_a: 1.048 – 1.370 FHH_Isotherm_s_CP_a: 1.525 – 1.852 The correct ranges, as intended in Section 6.3.4.3.2 of the *EBS Radionuclide Transport Abstraction*, (SNL 2007 [DIRS 177407]) are: FHH_Isotherm_k_CP_a: 1.030 – 1.326 FHH_Isotherm_s_CP_a: 1.493 – 1.799 The difference in the two ranges is small compared to their uncertainty ranges and thus the effect on calculating the number of monolayers of adsorbed water and saturation of corrosion products is likely to be negligible, leading to negligible impact on the mean annual dose.

Table P-6. Discussion of Other Minor Implementation Errors (Continued)

	ISSUE DESCRIPTION	ANTICIPATED IMPACT
8	The K_d range for sorption of Np on the Uranium mineral colloids in the EBS is not correct.	The K_d range for sorption of Np on the uranium colloids is given by a log-uniform distribution ranging from 10 to 500 mL/g (Table 6.3.7-64). The lower bound value of 10 mL/g was incorrectly set to 1 mL/g during the implementation. The impact of this reduction in the lower bound is anticipated to be negligible as the Np mass carried by the uranium colloids is likely to be small (even with the corrected values) compared to the mass carried by other colloid types and in the dissolved phase. Considering the mean uranium colloid concentration of about 6 mg/l (based on cumulative distribution function given in Table 6.3.7-64) and the maximum Np K_d of 500 mL/g, and multiplying the two would lead to a value of about 3×10^{-3}, which represents the ratio of Np mass on the uranium colloids to the mass in the dissolved phase in given water volume. This indicates that the predominant mechanism for Np transport is in the dissolved phase. The impact of this error is anticipated to be negligible, if any, on the mean annual dose.
9	In the Human Intrusion Modeling Case, the mass irreversibly associated with colloids that is released to the SZ is not partitioned into the fast transport fraction and the slow transport fraction.	In the Human Intrusion Modeling Case, the mass irreversibly associated with the waste form colloids (referred as "Ic") and the iron oxyhydroxide colloids (referred as "If") from the WP and passed through the UZ borehole needs to be combined together and repartitioned based on the fast fraction, before passing the mass to SZ. This needs to be done in such a way that only a small fraction (0.00168) travels unretarded (fast) while the rest of the mass travels with some retardation (slowly). The impact of this error is anticipated to be small as the relative contribution from fast and slow traveling mass fraction cannot be fully differentiated due to large timesteps employed in the TSPA-LA Model past 200,000 years (when the human intrusion is modeled). Thus, even though the relative contribution of Ic and If species could vary, the combined mass flux from the mass irreversibly associated with colloids is not anticipated to change. As a result, the impact on the mean annual dose is anticipated to be negligible.
10	In the UZ transport model, the correct minimum value for the selenium K_d for vitric rock units was supposed to be 0 mL/g. However, the minimum value after natural log transformation was set to 0, which is equivalent to K_d of 1 mL/g.	The impact of this error is anticipated to be negligible as the mean K_d value remains largely unchanged (reduced by 0.8%) when the minimum value is corrected. Furthermore, ^{79}Se is not a large contributor to dose.
11	For the UZ transport model, the uranium K_d for zeolitic rock unit has an error at probability level of 1. It was incorrectly set to 20 mL/g instead of 30 mL/g.	The impact of this error is anticipated to be negligible as the mean K_d value would change from 5.25 mL/g to 7.75 mL/g. This small increase is unlikely to affect the transport of uranium through the UZ. Furthermore, the current error is conservative as it leads to lowering the uranium K_d in the UZ matrix.

Table P-6. Discussion of Other Minor Implementation Errors (Continued)

	ISSUE DESCRIPTION	ANTICIPATED IMPACT
12	The concentration limit for plutonium and americium mass irreversibly sorbed on the iron oxyhydroxide colloids in the invert is incorrectly based on the stability criteria for the waste form domain instead of the corrosion products domain.	The error would only have an impact if the irreversible colloid concentration in the invert is nearing the concentration limit in the invert, which is an unlikely condition due to fast transport rates out of the invert compared to the incoming transport rate. Even if the conditions conducive to error occur, they would remain for a short time period compared to the simulation time. The impact of this error is expected to be negligible on the mean annual dose.
13	The time-dependent increase in the diffusive area from nominal corrosion of the WP outer barrier should be removed from the stylized Human Intrusion Modeling Case.	Ignoring the time-dependent increase in diffusive area from nominal corrosion processes (by either SCC or general corrosion patches) on the WP for the Human Intrusion Modeling Case is unlikely to affect the diffusive release out of the WP as only about 5% of the realizations would have some SCC failures by 200,000 years, the time when the human intrusion event is modeled. Following the event, the patch area equal to the drill stem area is applied to the WP for both diffusive and advective release. The patch area applied is large enough to cause large diffusive releases. Since the general corrosion patches do not occur until very late times (>400,000 years), any small increases in diffusive area from SCCs is unlikely to affect the diffusive flux. The impact of this error is likely to be negligibly small on the mean annual dose.
14	In calculating the first damage time for the WP due to seismic ground motion, the possibility of failure from puncture was not considered.	The first damage time calculations only evaluate the failures caused by seismic-induced SCCs or by nominal corrosion processes (nominal SCC or general corrosion). However, there is a small probability that punctures could occur earlier under certain conditions. The conditions, for puncture failure require that the DSs have failed and the WPs are surrounded by rubble. Under these conditions the probability of puncture varies as a function of PGV, but the probabilities remain low even at high PGVs (Figure 6.6-17). First failures from puncture damage are only likely to occur late in time when the WP has a reduced thickness (Figure 7.3.2-15). The number of realizations where puncture occurs before seismic-induced SCCs would be small since there is a higher probability of damage from seismic-induced SCCs (Figure 6.6-15). Note that this error only occurs in the Seismic GM Modeling Case run for 1,000,000 years. There is no effect on the Seismic GM Modeling Case run for 10,000 years as the conditions conducive to puncture do not occur. Analysis of a stand-alone model for WP degradation that includes both nominal and seismic degradation processes (output DTN: MO0709TSPAWPDS.000 [DIRS 183170]; file v5.000_GS_9.60.100_StandAlone_9krlz.gsm in folder Seismic_9k_Rlz) showed that 63 out of 9,000 realizations could have first damage from punctures. The impact of this on the mean annual dose is likely to be negligible as only 0.7% of the realizations would be affected and the effects are likely to be late (after the DSs are failed and the WPs have thinned).

Table P-6. Discussion of Other Minor Implementation Errors (Continued)

	ISSUE DESCRIPTION	ANTICIPATED IMPACT
15	The temperature and relative humidity modifications may be incorrectly applied after rubble fills the drifts as a result of degradation due to seismic ground motion.	The percolation subregion representative temperature and relative humidity time histories under nominal conditions (from MSTHM abstraction) are modified once the drifts become filled with rubble as a result of drift degradation from seismic ground motion. These modifications (deltas) are applied by adding to or subtracting from the representative temperature and relative humidity datasets. Twelve possible delta combinations, from four infiltration scenarios over three host-rock thermal conductivity cases (Section 6.3.2.2), are considered in the TSPA-LA Model for each percolation subregion and for each fuel type. However, in order to limit the computational burden, only eight delta combinations are actually calculated: six delta combinations for CSNF and two delta combinations for HLW. The six delta combinations for CSNF are then mapped to 12 possible delta combinations for the CSNF fuel type in each percolation subregion. Similarly, the two delta combinations for HLW are then mapped to 12 possible delta combinations for the HLW fuel type (CDSP WP) for each percolation subregion. Due to an implementation error, some of the combinations are incorrectly matched and the data are incorrectly read from the look-up tables. This could sometimes result in incorrect modifications of representative temperature and relative humidity time histories for the given percolation subregion and a given fuel type. In addition, some of the data sets used in the modification of temperatures (called temperature deltas) have been entered in a sequence that is different compared to the relative humidity deltas resulting in internal inconsistency once the modifications are made. Note that the error is only possible in the two modeling cases in which rubble fills the drifts, the Seismic GM Modeling Case run for 1,000,000 years and the Seismic FD Modeling Case. The impact of this error on the mean annual dose for either modeling case is likely to be negligible as the variation in the delta among various combinations is small. Thus, even though incorrect values may be applied, they would not result in any appreciable deviations from the corrected time history profiles. Furthermore, the magnitude of the modification is itself small relative to the actual temperature and relative humidity values even at the maximum initial values (the magnitudes of the deltas decrease with time). As a result, the downstream models affecting radionuclide transport are unlikely to be appreciably impacted by this error. The impact of the error on localized corrosion initiation is also evaluated based on the Localized Corrosion Initiation Uncertainty Analysis described in Appendix O. The five realizations (out of 300) that have early rubble fill times (within 12,000 years) all have conditions that are not conducive to localized corrosion initiation, even accounting for slightly incorrect temperature and relative humidity. One realization (Realization 142), which has conditions favorable for localized corrosion until 12,000 years, has a rubble fill time greater than 100,000 years, by which time localized corrosion is not favored. It is concluded that there is no impact of this error on the localized corrosion initiation.

Table P-6. Discussion of Other Minor Implementation Errors (Continued)

	ISSUE DESCRIPTION	ANTICIPATED IMPACT
16	Drift-wall condensation flux is being applied even after the igneous intrusive event, when the drifts are all assumed to be filled with magma.	The drift-wall condensation model is applicable only under nominal conditions and does not apply once the drifts are degraded from seismic ground motion or filled with magma following the igneous intrusion. However, it is being incorrectly applied even after the igneous intrusion. The impact of the error is restricted to the first 2,000 years only because the drift-wall condensation can only occur in the first 2,000 years (Section 6.3.3.2.3). As a result, the water flux through the WP could be higher than the percolation flux leading to increased advective mass flux of radionuclides for realizations when the igneous intrusion occurs within the first 2,000 years. But because the probability of having an igneous event in the first 2,000 years is negligibly small (mean value of 3.3×10^{-5}) the effect on expected dose of this additional mass flux is small. The impact of the error is evaluated to be negligible.

Table P-6. Discussion of Other Minor Implementation Errors (Continued)

	ISSUE DESCRIPTION	ANTICIPATED IMPACT
17	The WP temperatures could sometimes fall below the lower range of validity of the abstractions provided for computing in-package chemistry, HLW glass degradation rate, and dissolved concentration limits in the TSPA-LA Model.	An assessment of the range of validity shows that most of the validity ranges specified for the process models and abstractions included in the TSPA-LA Model are honored (see output DTN: MO0709TSPALAMO.000 [DIRS 182981]). However for three submodels (discussed below) that are included in the 1,000,000-year performance calculations the representative WP temperatures could fall below the lower limit specified by the abstractions; the minimum waste package temperature noted in the TSPA-LA Model is about 17°C for the 1,000,000 year simulation period. The lower temperature limit for the range of applicability of the In-Package Chemistry Abstraction (SNL 2007 [DIRS 180506]) is 25°C. Without an alternate implementation for low temperature conditions, the TSPA-LA Model applies the In-Package Chemistry Abstraction at temperatures below 25°C. Given that the In-Package Chemistry Abstraction for pH and ionic strength includes uncertainty to account for higher temperatures, the application of abstraction at lower temperatures is anticipated to produce results that are within the range of uncertainty captured in the abstractions for pH and ionic strength. The lower temperature limit for the range of applicability of the HLW Glass Waste Form Degradation Abstraction (BSC 2004 [DIRS 169988]) is 20°C. Without an alternate implementation for low temperature conditions, the TSPA-LA Model applies the HLW glass waste form degradation rate model at temperatures below 20°C. The lower temperature limit was determined by the ranges considered in the experimental results used to validate the rate model (BSC 2004 [DIRS 169988], Section 7.3) which showed that the Arrhenius relationship for glass degradation rate is maintained between 20°C and 90°C. This relationship is not anticipated to change between 17°C and 20°C and therefore unlikely to have any effect on mass transport calculations. The lower temperature limit for the range of applicability of the Dissolved Concentration Limits Abstraction (SNL 2007 [DIRS 177418]) is 25°C. Without an alternate implementation for low temperature conditions, the TSPA-LA Model applies the Dissolved Concentration Limits Abstraction at temperatures below 25°C. Because actinides have retrograde solubility (SNL 2007 [DIRS 177418], Section 6.3.3.3), it is possible that dissolved concentration limits below 25°C could be higher than those implemented in the TSPA-LA Model. But because the Dissolved Concentration Limits Abstraction includes additional uncertainty to account for differences in temperature conditions (SNL 2007 [DIRS 177418], Section 6.3.3), it is anticipated that any small effects from extrapolation would produce results that are within the range of uncertainty captured in the abstractions for dissolved concentration limits. For the 10,000 year simulations the temperatures remain within the range of validity.

Table P-6. Discussion of Other Minor Implementation Errors (Continued)

	ISSUE DESCRIPTION	ANTICIPATED IMPACT
18	Drift-wall condensation flow only occurs in the non-lithophysal regions of the repository.	The drift wall condensation abstraction states that drift wall condensation should cease after the drift has collapsed. Drift collapse is only modeled in the Seismic Scenario Class. In the Seismic Scenario Class, drift collapse occurs in the lithophysal regions of the repository; thus the fraction of WPs that are exposed to drift wall condensation is limited to the fraction of WPs in the non-lithophysal region. However, this limit was not properly implemented in the TSPA-LA Model. As a result, in all but the Igneous Intrusion modeling case, drift wall condensation was limited to the fraction of WPs in the nonlithophysal region and therefore was underestimated in the TSPA-LA Model. Because drift wall condensation only increases the flux in the repository for the first 2,000 years, the dose impact can only occur in the modeling cases that fail WPs in the first 2,000 years and have radionuclide transport in the first 2,000 years. The implementation is correct for the Seismic Ground Motion and Seismic Fault Displacement modeling cases and the Igneous Intrusion Modeling Case. The Nominal Scenario Class and Human Intrusion Scenario do not have failures in the first 2,000 years and thus are not affected. The EF WP modeling case does have WP failures in the first 2,000 years, but the DS remains intact so any additional condensation flux is not anticipated to change transport out of the EF WP. The flux through a failed WP in the EF DS modeling case could be increased by drift wall condensation. As a result, WP releases could also be increased, leading to a higher expected dose in the EF DS modeling case. Contributing less than 2.5% to the total mean dose, the EF DS modeling case is not a significant contributor to the total dose from the repository. The impact of the error is evaluated to be negligible.

Table P-7. Impact Assessment Summary Table

Issue/Section No.	Issue Description	Anticipated Impact
P2.	Inventory for ^{36}Cl, ^{79}Se, and ^{126}Sn was omitted in the 10,000-year simulation modeling cases and the seepage fractions applied for the 10,000-year simulations are based on the post-10,000-year climate.	Negligible
P3.	Conservative treatment of WP damage from seismic events following the first breach due to nominal corrosion processes.	Significant between 200,000 and 300,000 years
P4.	WP outer barrier failure flag is triggered when the inside-out corrosion of the WP is initiated in the Seismic GM Modeling Case, which could be earlier than the actual breach time.	Negligible
P5.	In-package chemistry applied in the invert after the DS is failed without considering flow through the WP.	Negligible
P6.	Incorrect weld volume is used in computing the probability of manufacturing defects.	Negligible
P7.	Nominal crack failure opening area incorrectly calculated once the elapsed time is greater than the seismic damage time.	Negligible
P8.	Degradation processes inside the WP could start before the breach from an igneous event under certain aleatory configuration of specified igneous event times.	Negligible
P9.	Threshold rubble volume (per drift length) that is used for determining when the non-lithophysal drifts undergo collapse is incorrect. It is currently using the value of 5 m^3/m while the correct value is 0.5 m^3/m.	Negligible
P10.	Unintended perfect correlation between two uncertainty parameters: WRIP_beta_rand_a and PCE_Delta_pCO2_a.	Negligible
P11.	The uncertainty associated with fluoride concentration in calculating the uranium solubility for the CSNF WPs is incorrectly calculated in the Igneous Intrusion Modeling Case.	Negligible
P12.	The ionic strength for the HLW glass domain, for conditions where there is flow through the WP always chooses the ionic strength determined for flowing conditions.	Negligible
P13.	The seepage abstraction uses an average WP length (including gap spacing) of 5.1 m. However, the average length of a WP (including gap spacing) should be about 5.6 m.	Small (≤10%)
P14.	Evaluate the mean annual dose from the Igneous Intrusion and Volcanic Eruption Modeling Cases with the probability of the igneous event set to 10^{-7} per year. Note that this is purely a sensitivity analysis and not due to any error in the implementation.	None
P15.	The distribution for longitudinal dispersivity that is sampled produces unrealistically large values in the 1-D SZ flow and transport model.	Small (<30%)
P16.	The HLW glass degradation rate calculation for the Igneous Intrusion Modeling Case uses the degradation model that was developed for nominal conditions instead of applying an instantaneous degradation	Negligible
P17.	The seepage flux in the lithophysal zones following the drift collapse may be under predicted in some realizations due to error in estimating the bounding values.	Small (~20%)
P18.	Minimum iron oxyhydroxide colloid concentration is being applied even under stable conditions due to error in calculating the ionic strength threshold for colloid stability calculations.	Negligible
P19.	In the Igneous Intrusion Modeling Case, the number of WPs assigned for computing the DSNF mass in the non-dripping environments are not correctly calculated following the igneous event.	Small (<6%)

Table P-7. Impact Assessment Summary Table (Continued)

Issue/Section No.	Issue Description	Anticipated Impact
P20.	GoldSim software error where incorrect masses could be calculated by the Source and Pipe elements (special GoldSim elements) when decay chains have feedback loops.	Small (<5%)
P21.	Delay in transport for some radionuclides through the fault zones in the UZ transport model.	Small (<5%)
P22.	Other minor implementation errors that have been discovered since running the compliance case are grouped and addressed (Table P-6).	Negligible
P23.	Several suggested changes to the model file structure are tracked in a model status log.	None

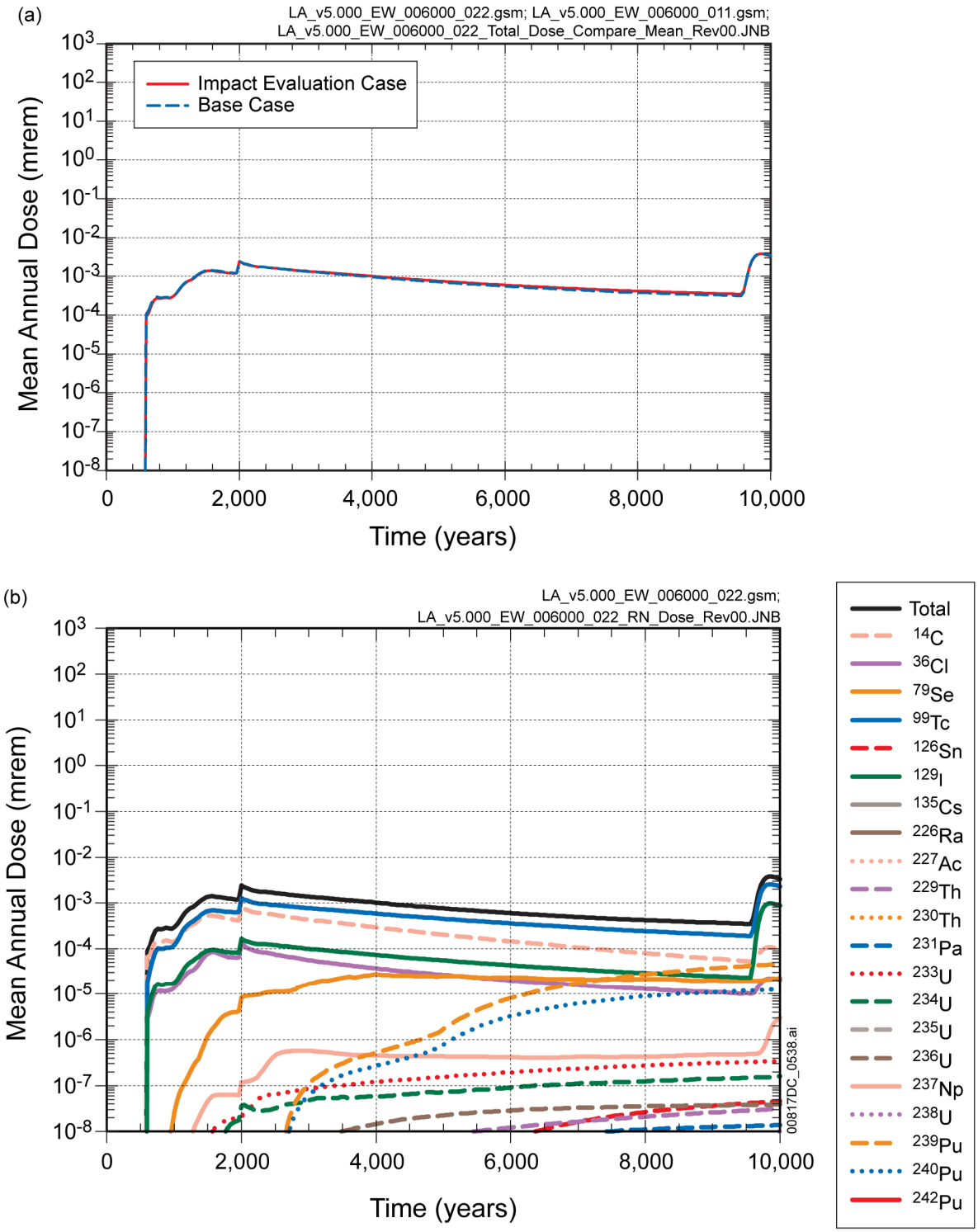

Source: Output DTNs: MO0709TSPALAMO.000 [DIRS 182981]; and MO0709TSPAREGS.000 [DIRS 182976].

Figure P-1. (a) Comparison of the Mean Annual Dose for the Impact Evaluation Case with the Base Case for the Waste Package EF Modeling Case and (b) Major Radionuclide Dose Contributors for the Corrected Case

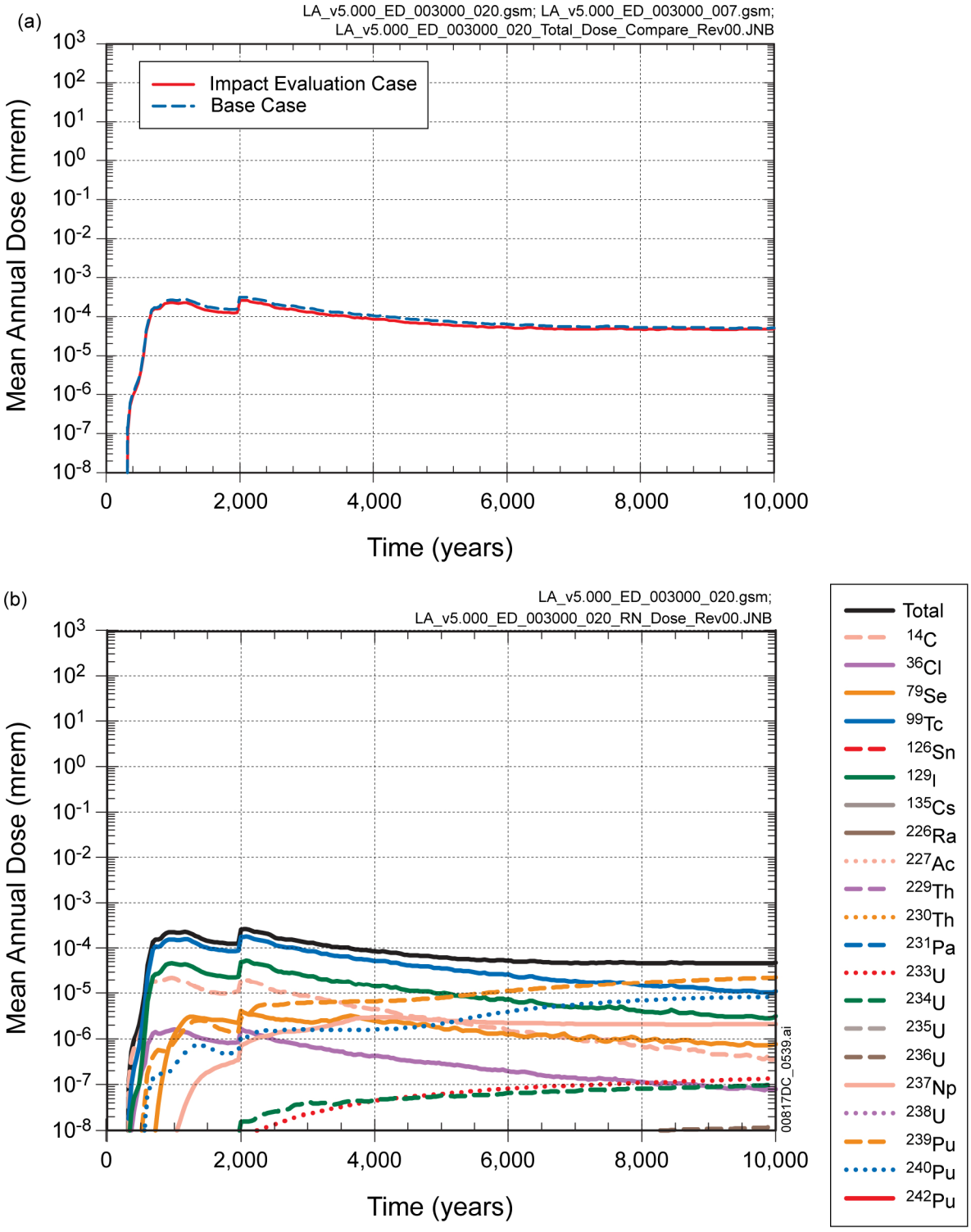

Source: Output DTNs: MO0709TSPALAMO.000 [DIRS 182981]; and MO0709TSPAREGS.000 [DIRS 182976].

Figure P-2. (a) Comparison of the Mean Annual Dose for the Impact Evaluation Case with the Base Case for the Drip Shield EF Modeling Case and (b) Major Radionuclide Dose Contributors for the Corrected Case

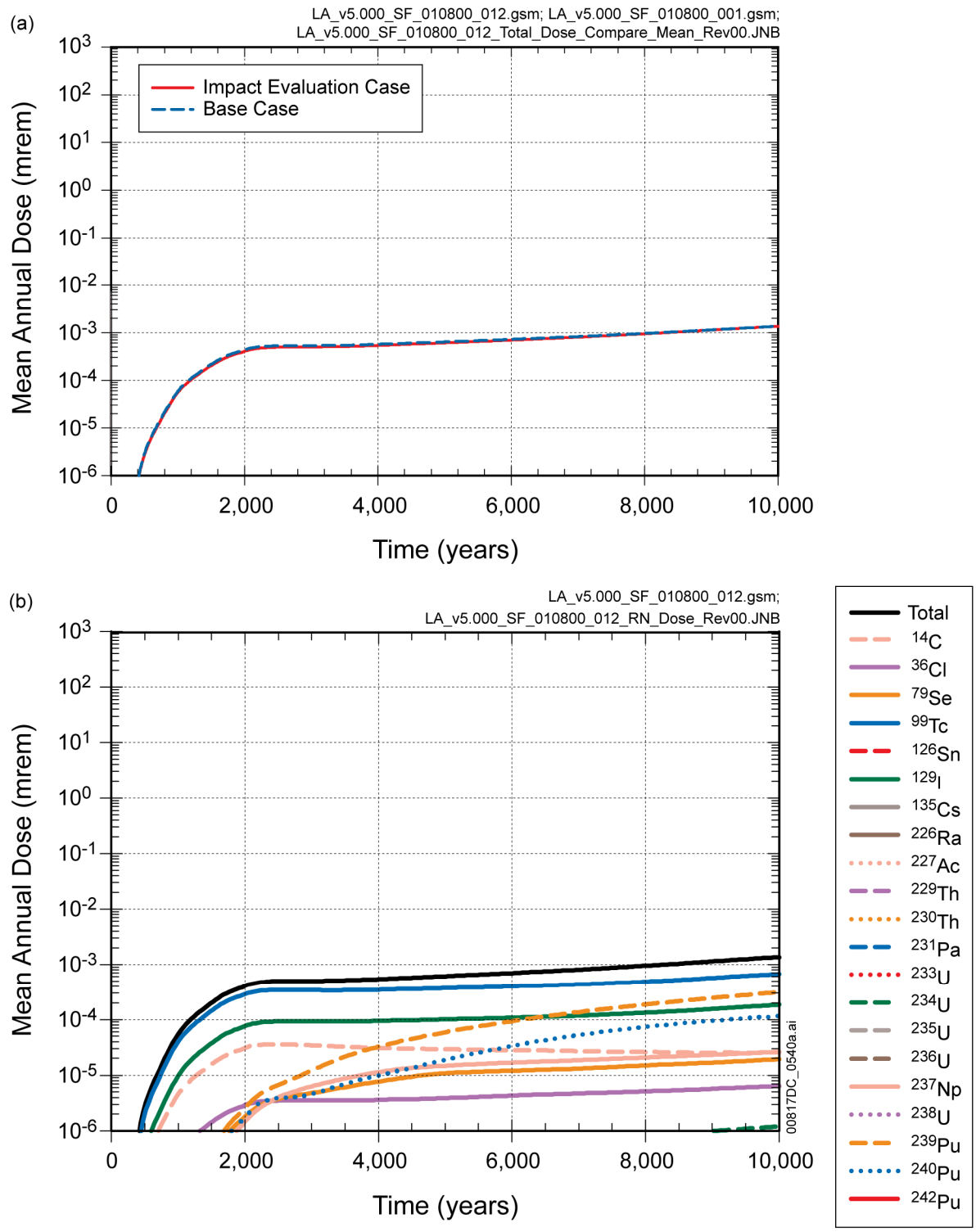

Source: Output DTNs: MO0709TSPALAMO.000 [DIRS 182981]; and MO0709TSPAREGS.000 [DIRS 182976].

Figure P-3. (a) Comparison of the Mean Annual Dose for the Impact Evaluation Case with the Base Case for the Seismic FD Modeling Case and (b) Major Radionuclide Dose Contributors for the Corrected Case

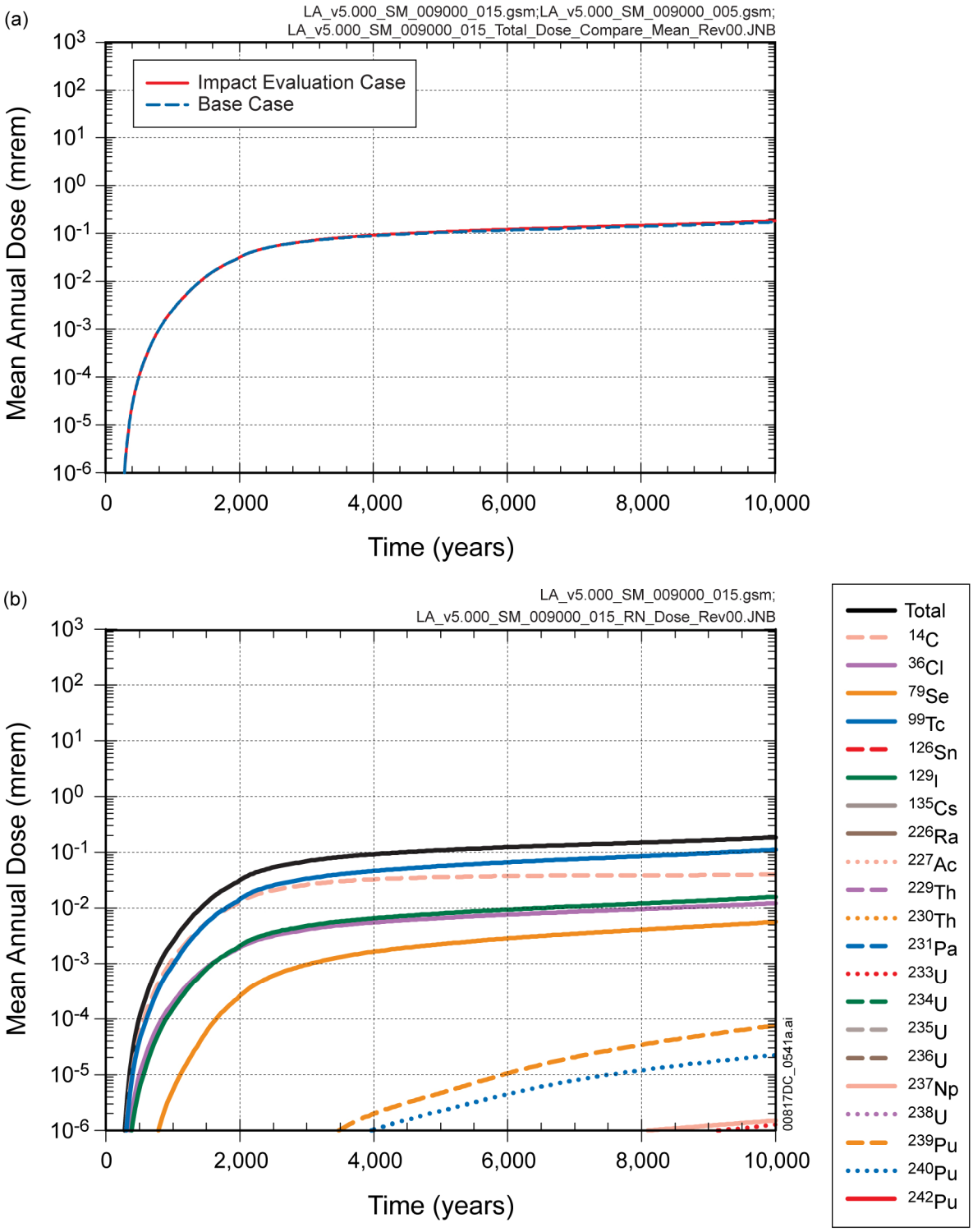

Source: Output DTNs: MO0709TSPALAMO.000 [DIRS 182981]; and MO0709TSPAREGS.000 [DIRS 182976].

Figure P-4. (a) Comparison of the Mean Annual Dose for the Impact Evaluation Case with the Base Case for the Seismic GM Modeling Case and (b) Major Radionuclide Dose Contributors for the Corrected Case

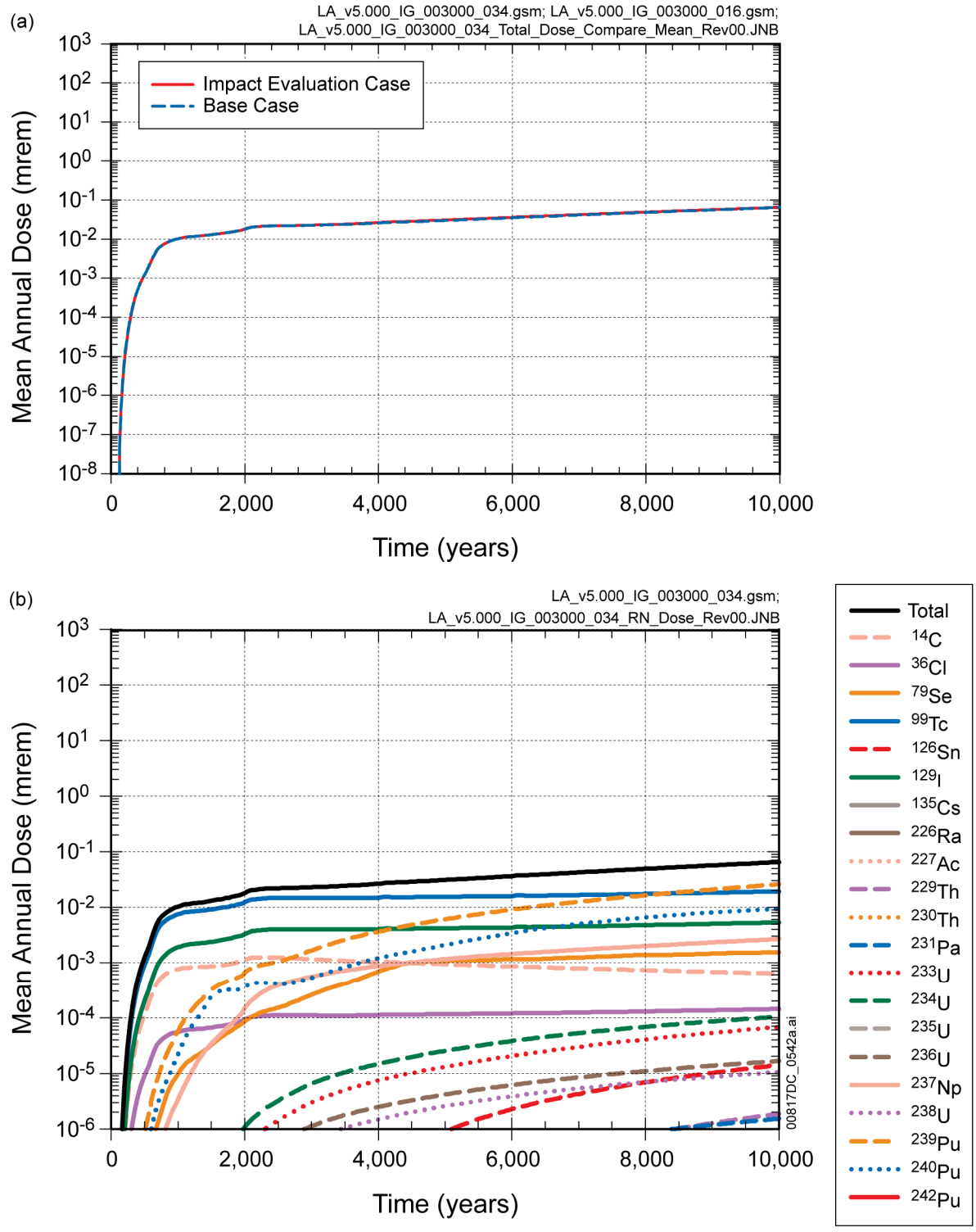

Source: Output DTNs: MO0709TSPALAMO.000 [DIRS 182981]; and MO0709TSPAREGS.000 [DIRS 182976].

Figure P-5. (a) Comparison of the Mean Annual Dose for the Impact Evaluation Case with the Base Case for the Igneous Intrusion Modeling Case and (b) Major Radionuclide Dose Contributors for the Corrected Case

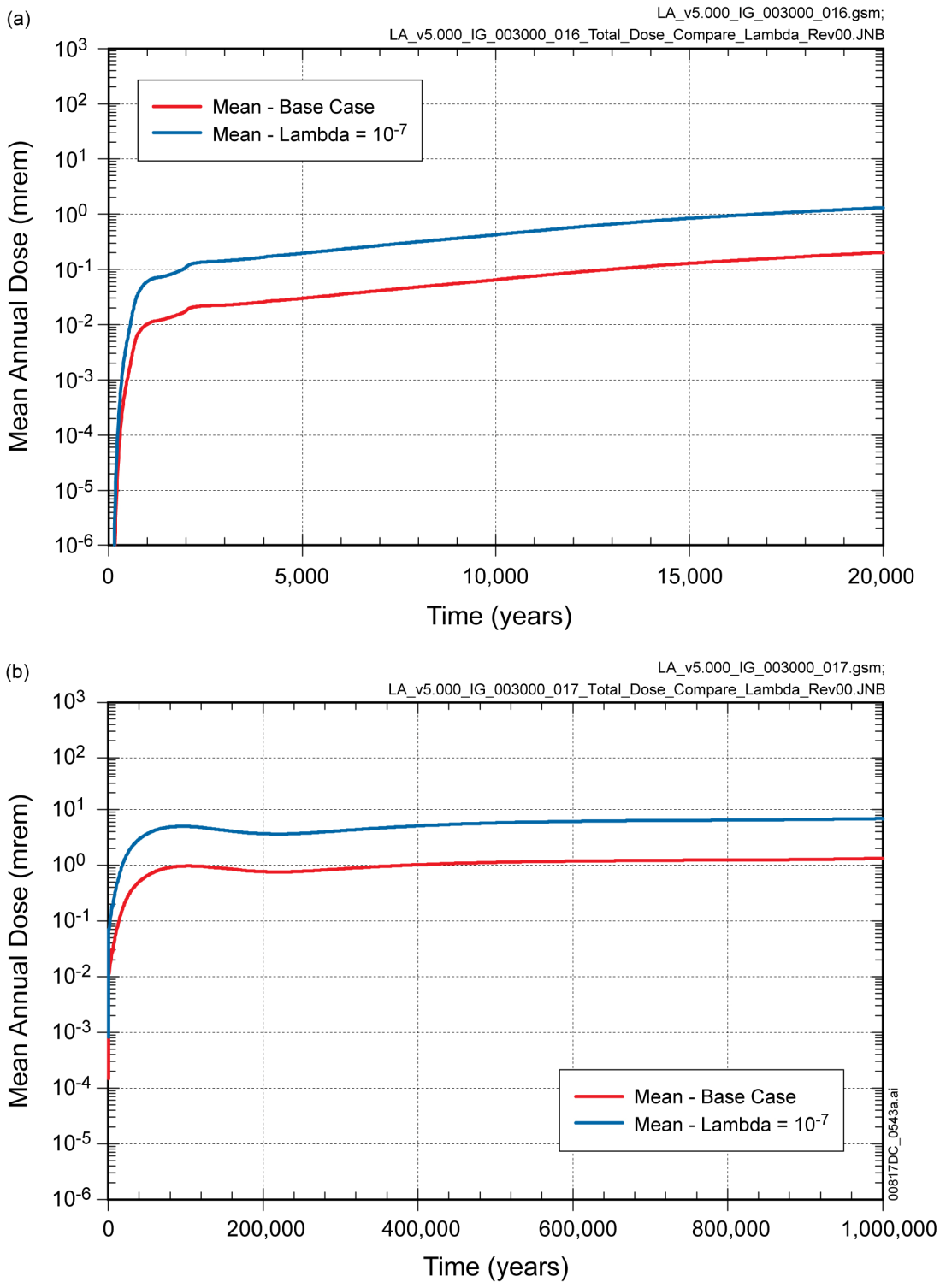

Source: Output DTNs: MO0709TSPALAMO.000 [DIRS 182981]; and MO0709TSPAREGS.000 [DIRS 182976].

Figure P-6. Mean Annual Dose for the Igneous Intrusion Modeling Case: Base Case and Probability of the Igneous Event set to 10^{-7} per year for (a) 20,000 Years and (b) 1,000,000 Years

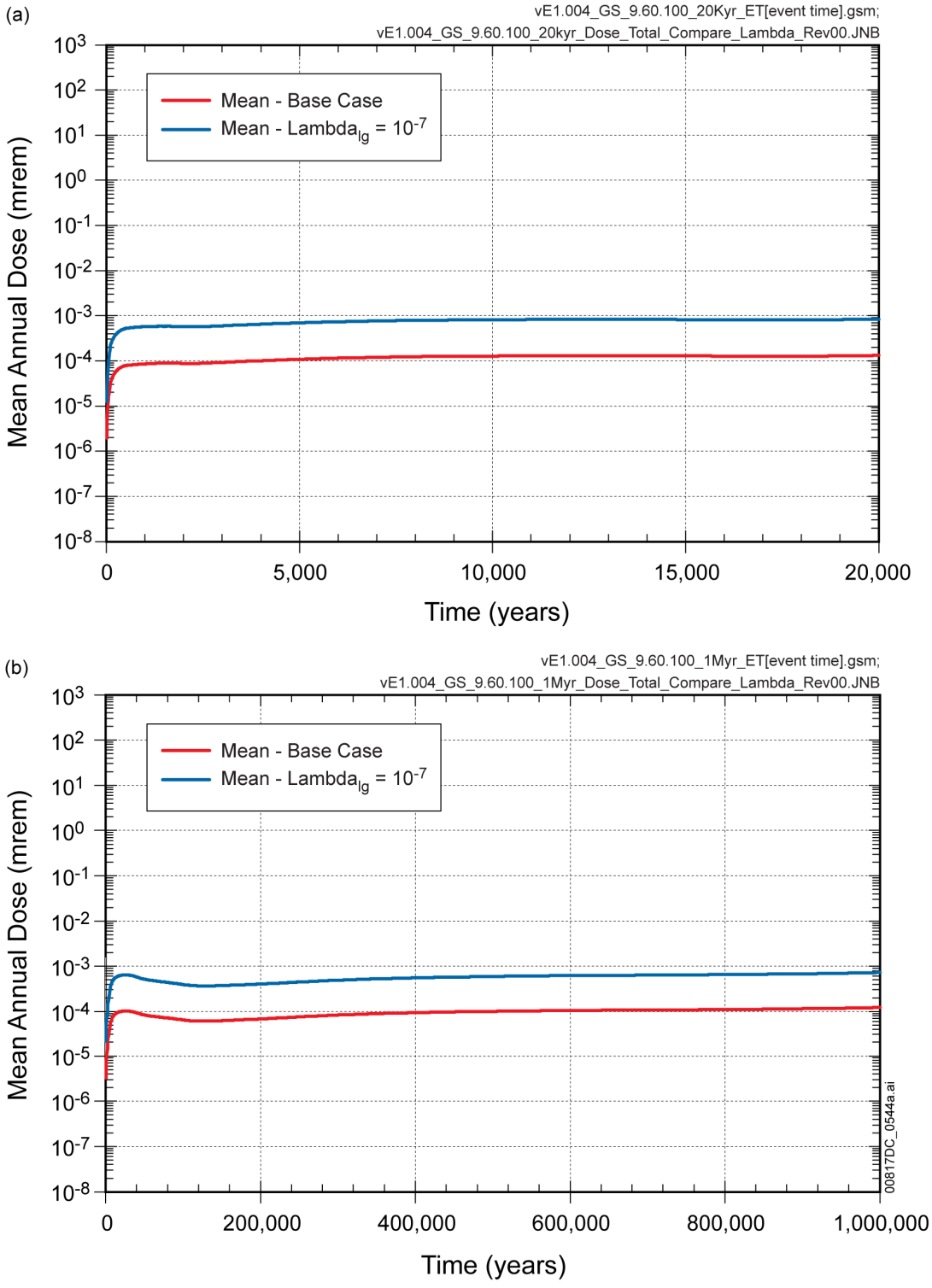

Source: Output DTNs: MO0709TSPALAMO.000 [DIRS 182981]; MO0709TSPAREGS.000 [DIRS 182976].

Figure P-7. Mean Annual Dose for the Volcanic Eruption Modeling Case: Base Case and Probability of the Igneous Event set to 10^{-7} per year for (a) 20,000 Years and (b) 1,000,000 Years

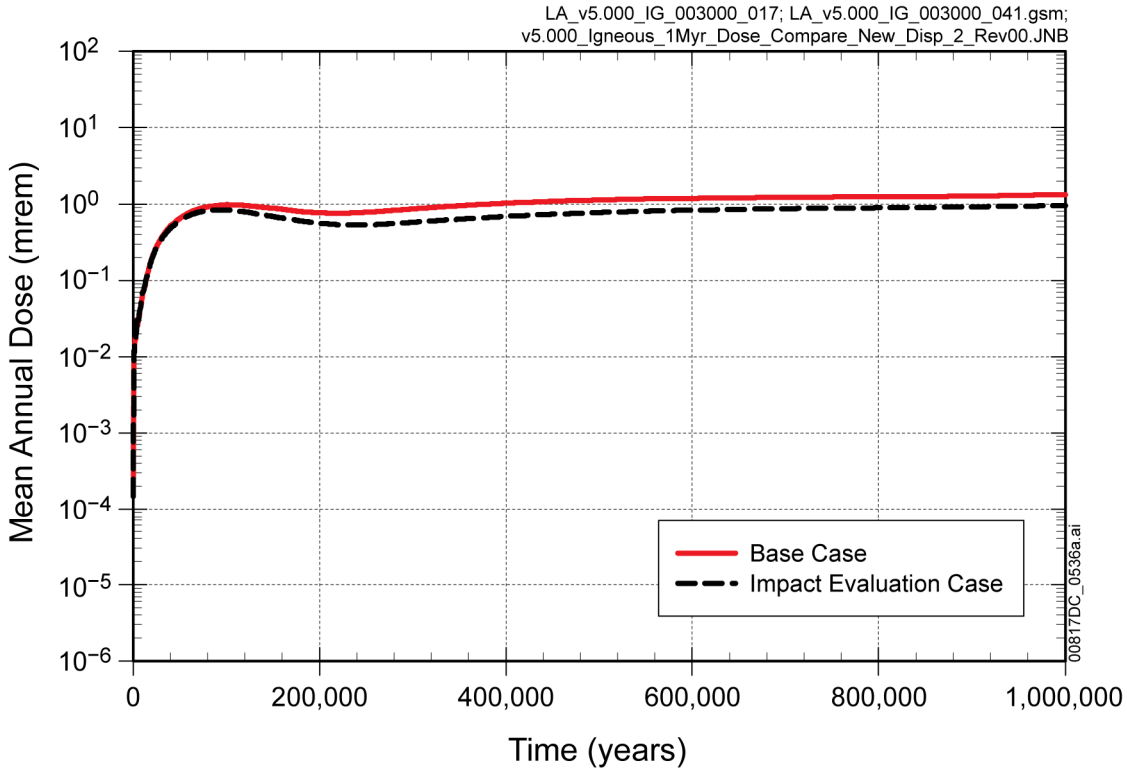

Source: Output DTNs: MO0709TSPALAMO.000 [DIRS 182981]; and MO0709TSPAREGS.000 [DIRS 182976].

Figure P-8. Mean Annual Dose Comparison for the Base Case and the Impact Evaluation Case with Updated Longitudinal Dispersivity for the Igneous Intrusion Modeling Case

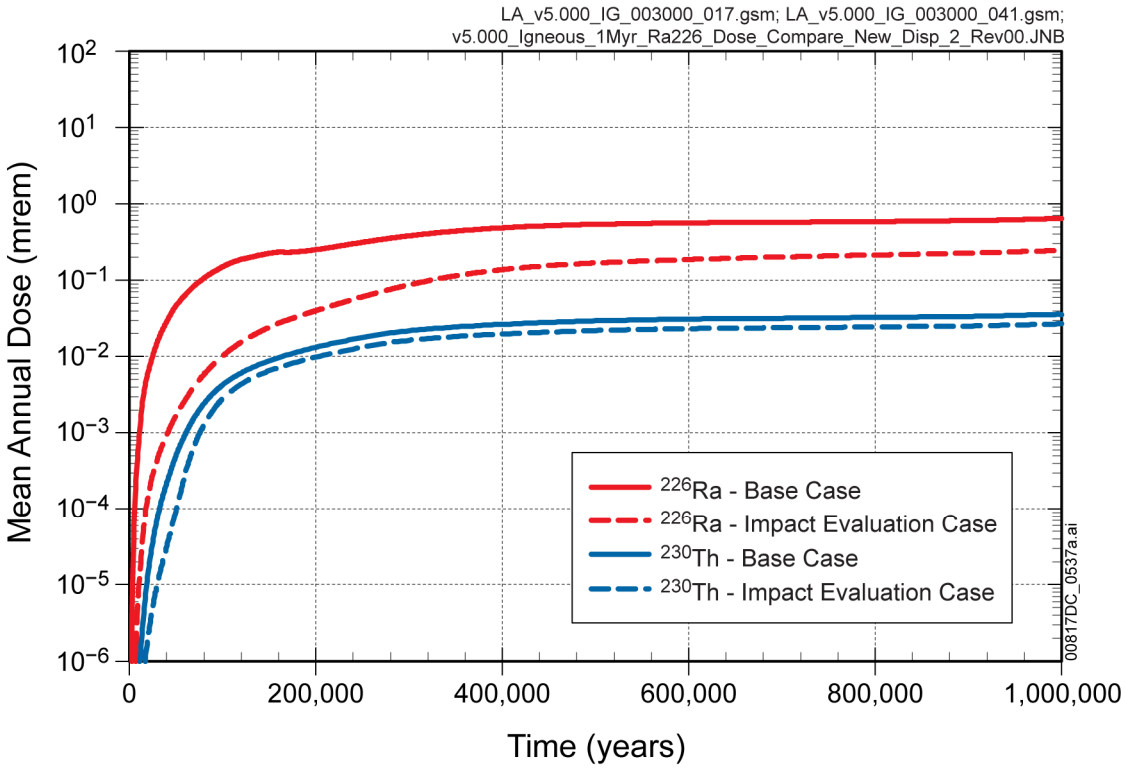

Source: Output DTNs: MO0709TSPALAMO.000 [DIRS 182981]; and MO0709TSPAREGS.000 [DIRS 182976].

Figure P-9. Comparison of Mean Annual Dose Contribution from ^{226}Ra and ^{230}Th for the Base Case and the Impact Evaluation Case with Updated Longitudinal Dispersivity for the Igneous Intrusion Modeling Case

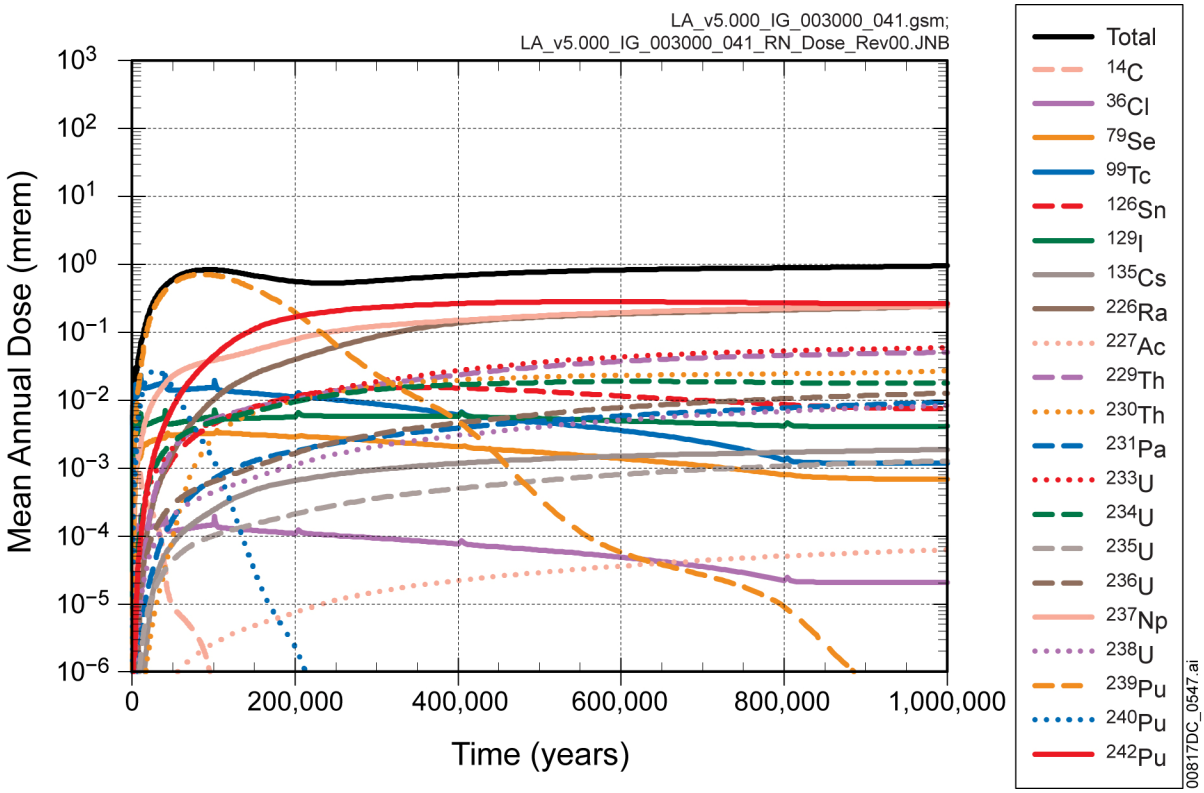

Source: Output DTN: MO0709TSPALAMO.000 [DIRS 182981].

Figure P-10. Major Radionuclide Dose Contributors for the Impact Evaluation Case with Updated Longitudinal Dispersivity for the Igneous Intrusion Modeling Case

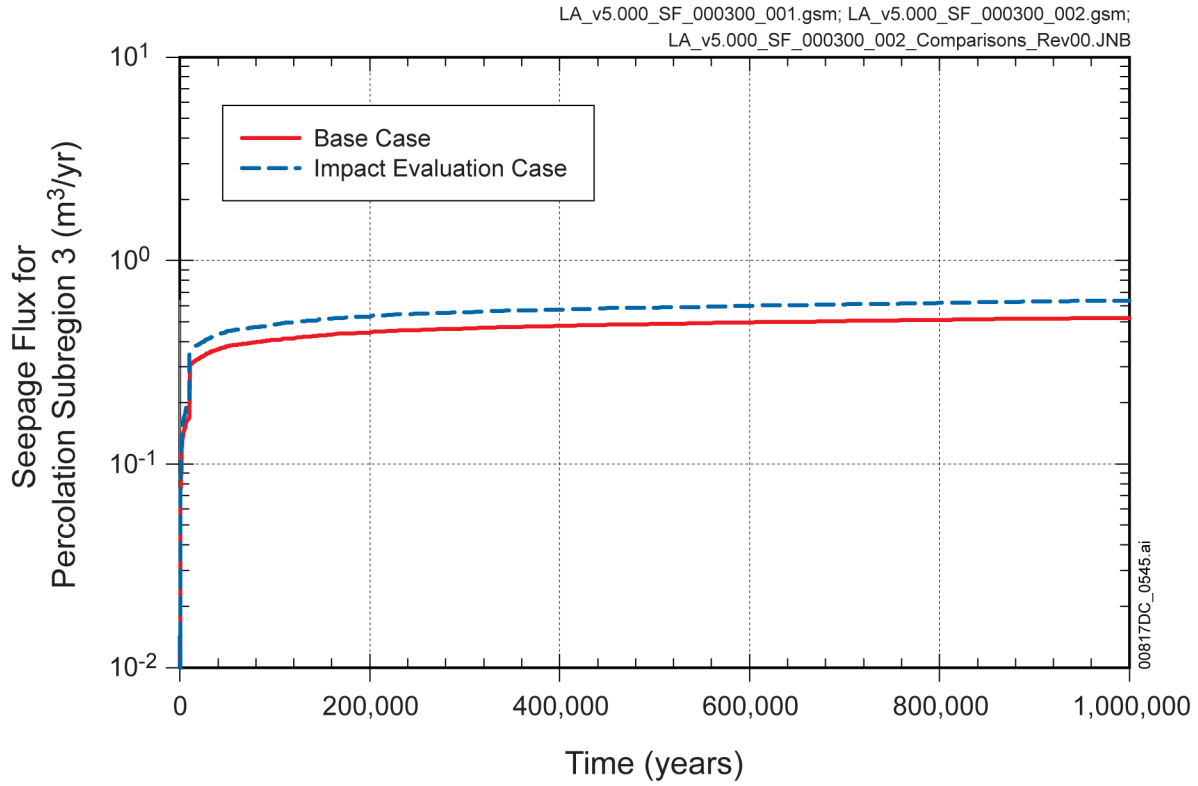

Source: Output DTN: MO0709TSPALAMO.000 [DIRS 182981].

Figure P-11. Mean Seepage Flux Comparison for Percolation Subregion 3 for the Base Case and the Impact Evaluation Case for the Seismic FD Modeling Case

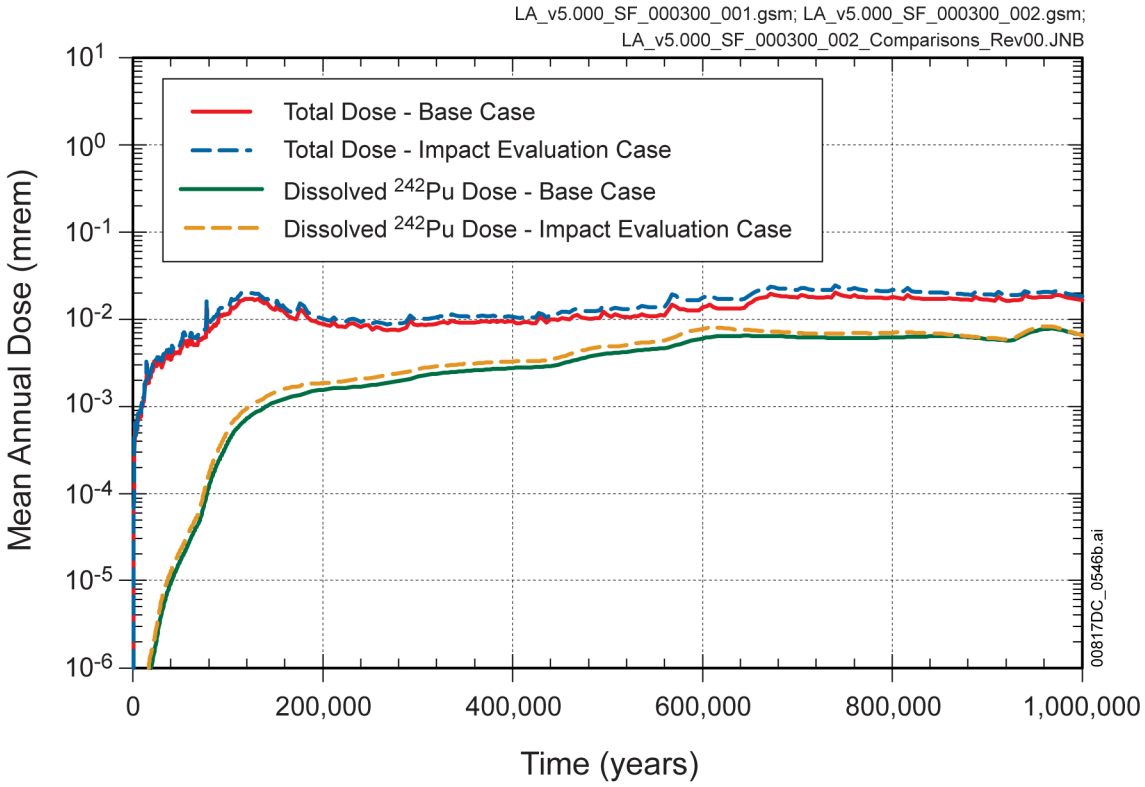

Source: Output DTN: MO0709TSPALAMO.000 [DIRS 182981].

Figure P-12. Mean Annual Dose Comparisons for the Base Case and the Impact Evaluation Case for the Seismic FD Modeling Case

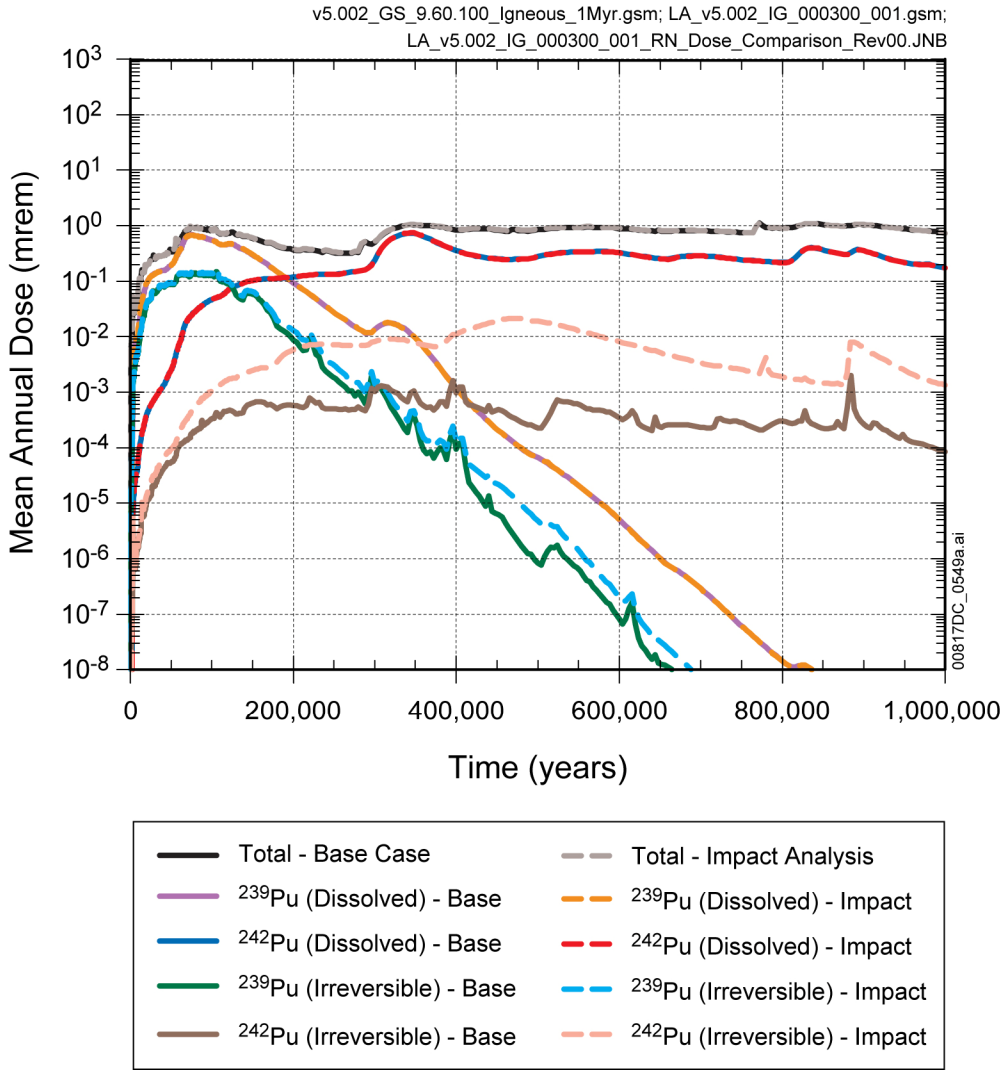

Source: Output DTN: MO0709TSPALAMO.000 [DIRS 182981].

Figure P-13. Mean Annual Dose Comparisons for the Base Case and the Impact Evaluation Case for the Igneous Intrusion Modeling Case

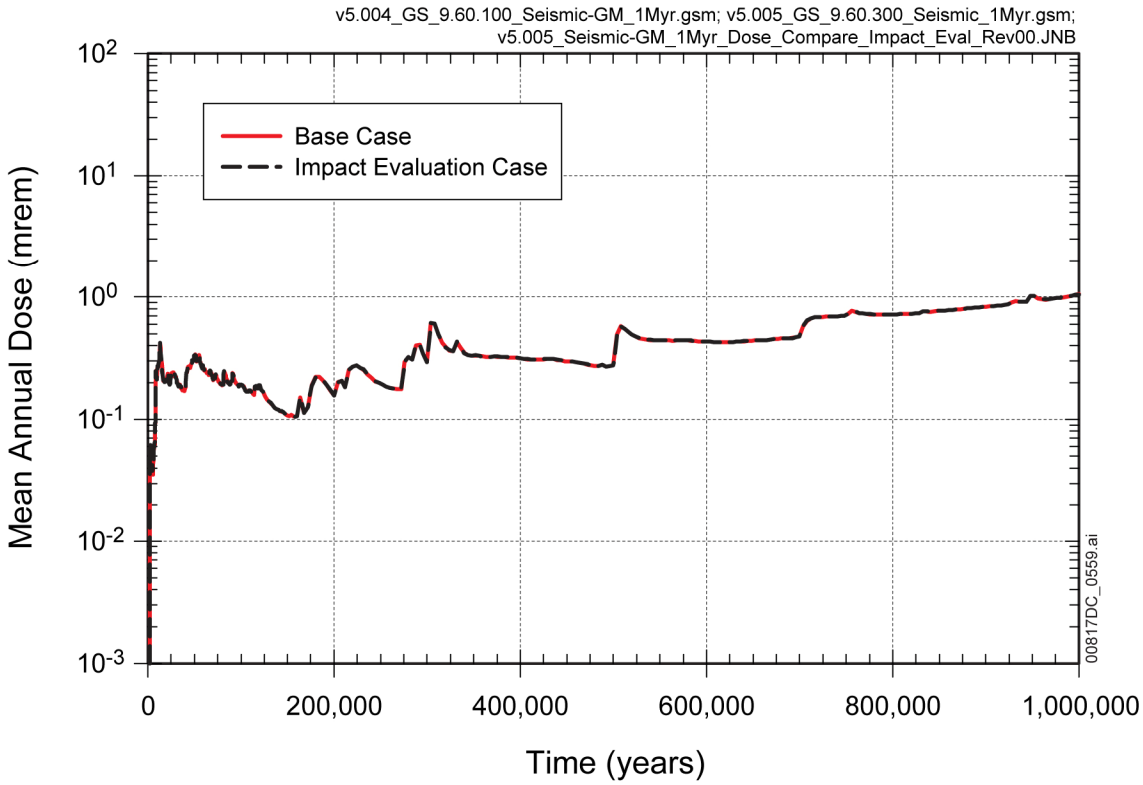

Source: Output DTN: MO0709TSPALAMO.000 [DIRS 182981].

Figure P-14. Mean Annual Dose Comparisons for the Base Case and the Impact Evaluation Case for the Seismic Ground Motion Modeling Case to Evaluate the Impact of the GoldSim Solver Error

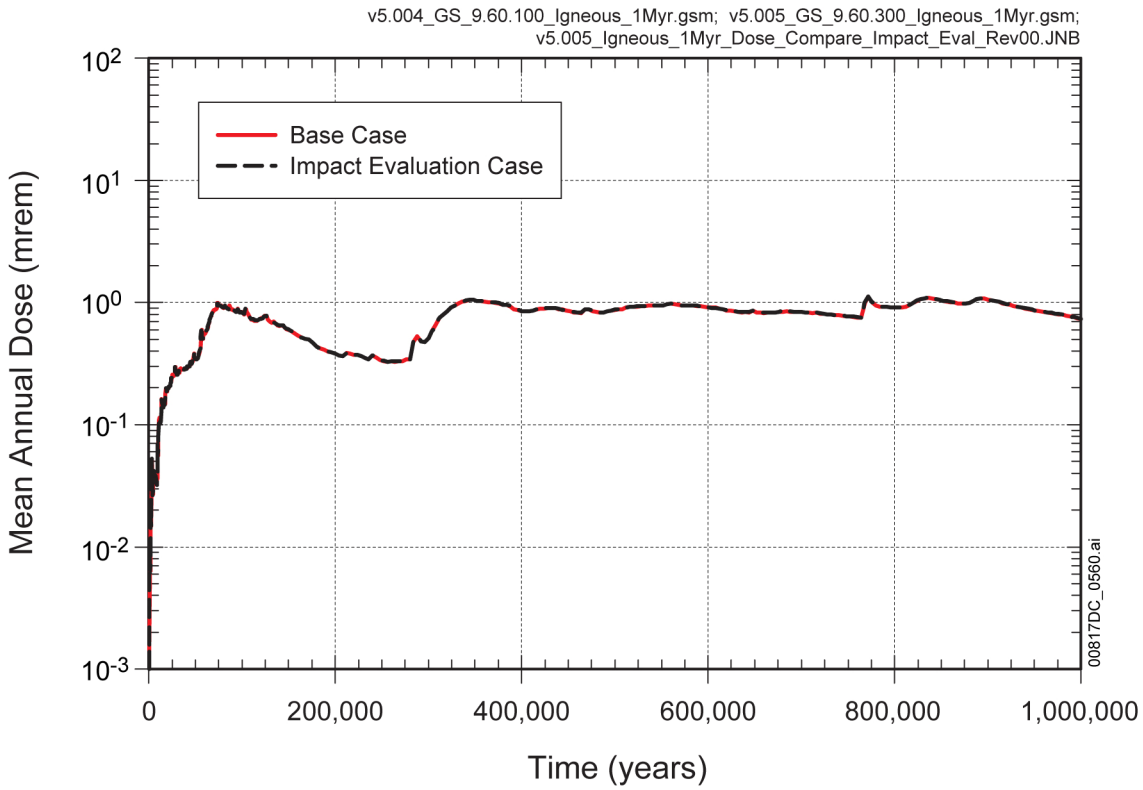

Source: Output DTN: MO0709TSPALAMO.000 [DIRS 182981].

Figure P-15. Mean Annual Dose Comparisons for the Base Case and the Impact Evaluation Case for the Igneous Intrusion Modeling Case to Evaluate the Impact of the GoldSim Solver Error

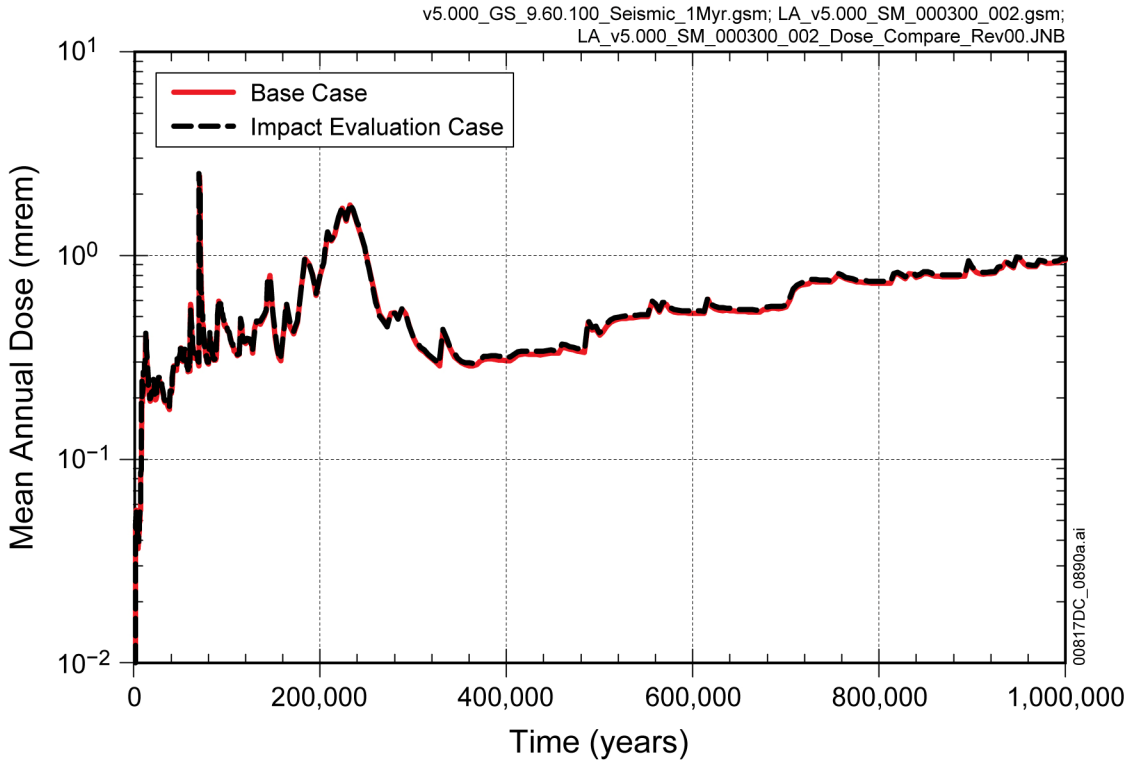

Source: Output DTN: MO0709TSPALAMO.000 [DIRS 182981].

Figure P-16. Mean Annual Dose Comparisons for the Base Case and the Impact Evaluation Case for the Seismic GM Modeling Case to Evaluate the Impact of UZ Transport Delay of some Radionuclides through the Fault Zones

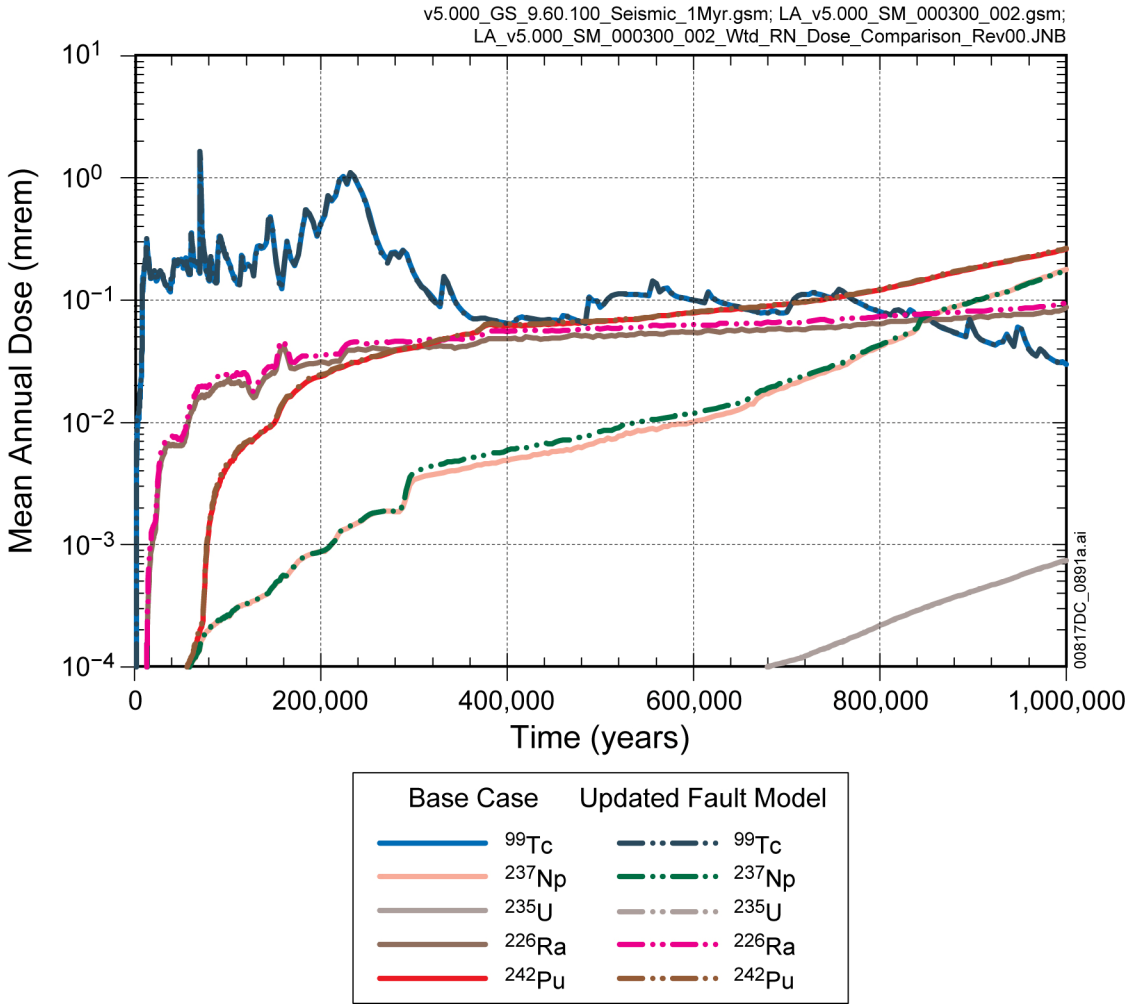

Source: Output DTN: MO0709TSPALAMO.000 [DIRS 182981].

Figure P-17. Mean Annual Dose Comparisons of Major Radionuclides for the Base Case and the Impact Evaluation Case for the Seismic Ground Motion Modeling Case to Evaluate the Impact of Unsaturated Zone Transport Error through the Fault Zones

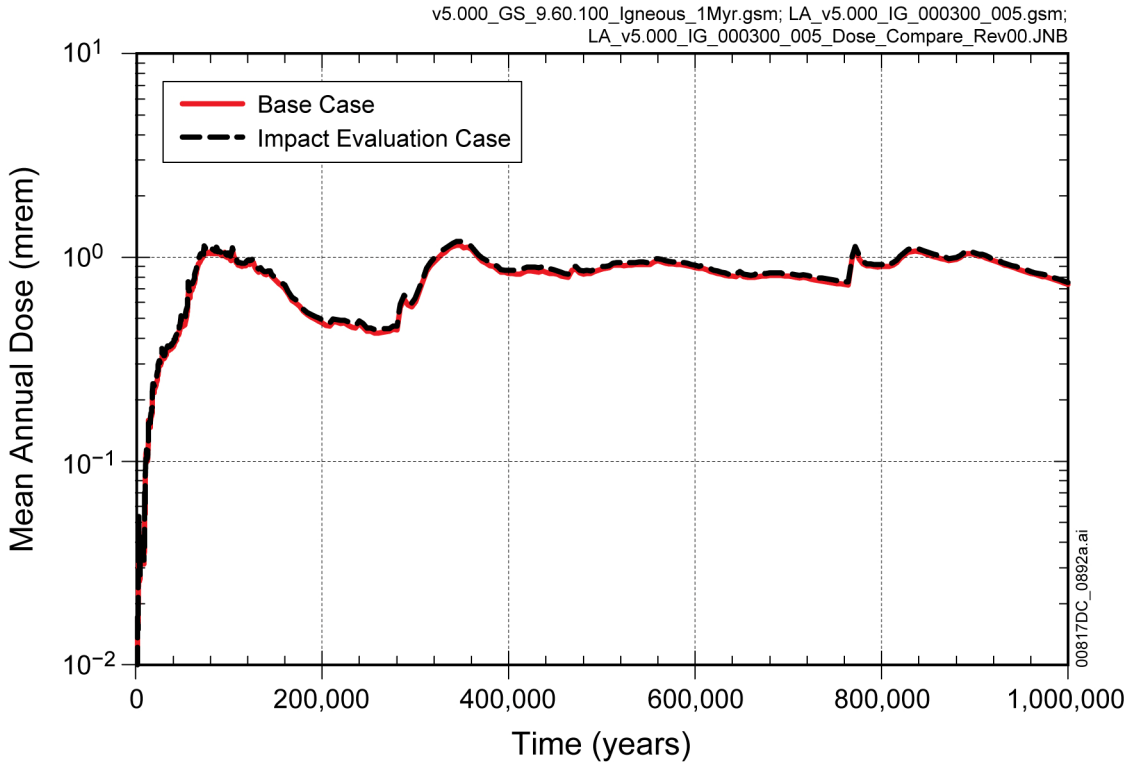

Source: Output DTN: MO0709TSPALAMO.000 [DIRS 182981].

Figure P-18. Mean Annual Dose Comparisons for the Base Case and the Impact Evaluation Case for the Igneous Intrusion Modeling Case to Evaluate the Impact of Unsaturated Zone Transport Error through the Fault Zones

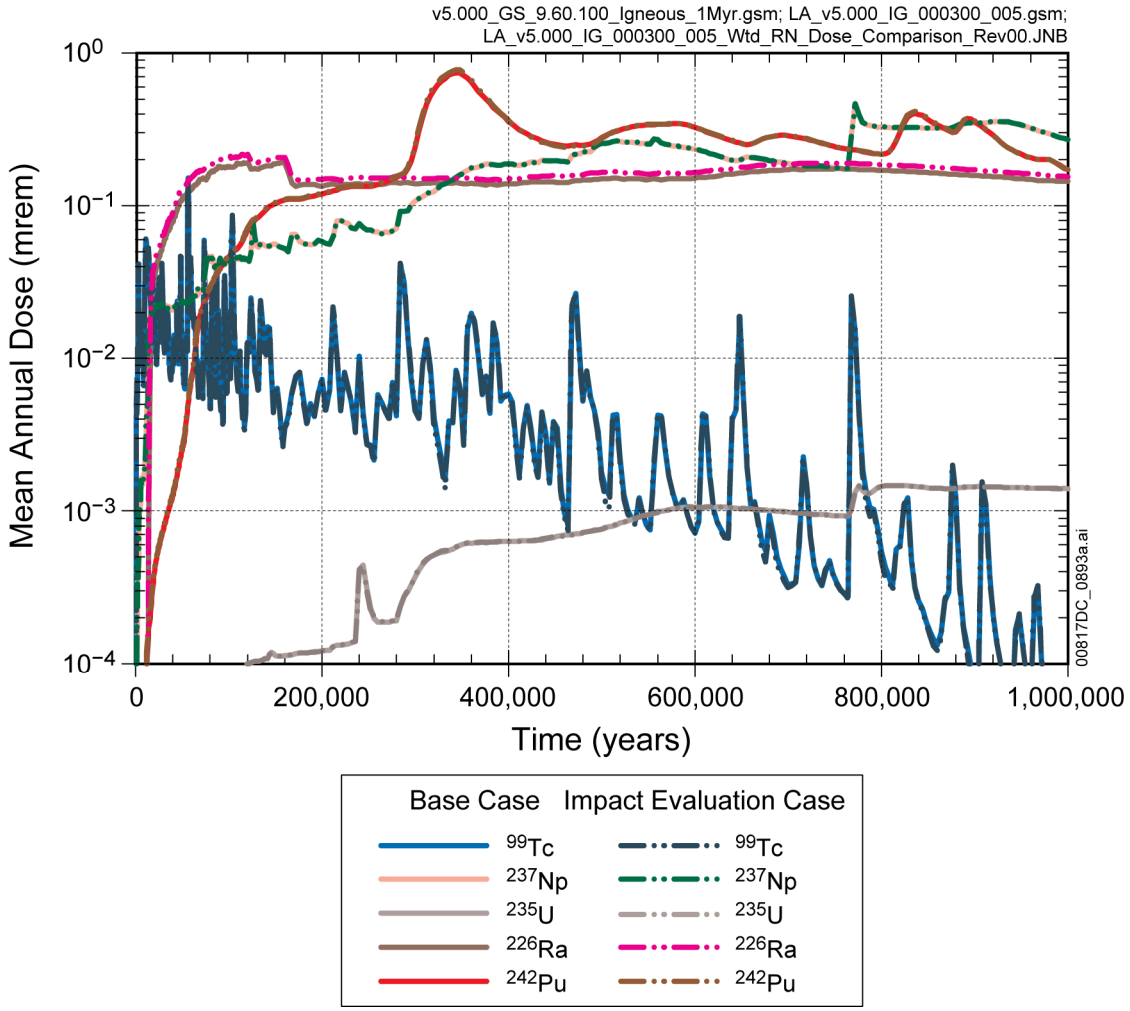

Source: Output DTN: MO0709TSPALAMO.000 [DIRS 182981].

Figure P-19. Mean Annual Dose Comparisons of Major Radionuclides for the Base Case and the Impact Evaluation Case for the Igneous Intrusion Modeling Case to Evaluate the Impact of Unsaturated Zone Transport Error through the Fault Zones

INTENTIONALLY LEFT BLANK